Advanced Motion Corrected Reconstruction Techniques for Magnetic Resonance Imaging

Lima Da Cruz, Gastao Jose

Awarding institution:
King's College London

King's College London

Advanced Motion Corrected Reconstruction Techniques for Magnetic Resonance Imaging

Gastão José Lima da Cruz

Supervised by
Dr. Claudia Prieto
Dr. David Atkinson
Professor Tobias Schaeffter

Thesis submitted to King's College London
for the degree Doctor of Philosophy
April 2016

Abstract

Magnetic Resonance Imaging (MRI) is a powerful imaging modality with excellent soft tissue contrast and high spatial resolution without the need for ionising radiation. However, the acquisition process is inherently slow, which imposes practical constraints on the modality. Scan times are particularly long in three-dimensional high spatial resolution imaging. This difficulty has recently been alleviated by accelerated acquisitions, combined with Parallel Imaging or Compressed Sensing reconstructions.

Patient motion is one of the major obstacles in clinical MRI, as physiological motion is typically faster than the acquisition process. Motion occurring during a scan will corrupt the acquired data and introduce image artefacts in the reconstructed image. Unavoidable types of motion such as respiratory motion must be considered for a successful MR examination. The problem of respiratory motion is most predominant in abdominal and cardiac imaging. To tackle this concern, motion corrupted data is commonly rejected using the so-called gated data acquisition. However, scan times are increased further as rejected data needs to be re-acquired. A more efficient approach to this problem is to acquire motion corrupted data and attempt to correct this data afterwards.

Novel approaches for respiratory motion correction are developed in this thesis. The proposed framework estimates complex, non-rigid motion from the data itself. The motion information is then incorporated into the reconstruction to remove motion-related artefacts.

This non-rigid motion correction framework is adapted to three different applications: 3D accelerated abdominal imaging, 3D coronary lumen and vessel wall imaging, and 3D whole-heart water/fat imaging. In the first application, the framework is combined with Parallel Imaging and Compressed Sensing to enable high acceleration factors. The proposed method reduced scan times by 2.6x when compared with the gated acquisition while maintaining similar image quality. In the second application, the framework is combined with interleaved image navigators to add high temporal resolution motion correction. This method also presented similar coronary lumen quality to the gated, despite a 1.6x reduction in scan time. Additionally, it presented significantly superior vessel wall quality when compared to translation correction. In the third application, the framework is combined with Parallel Imaging, Compressed Sensing and interleaved image navigators. Initial results indicate the proposed approach produces significantly superior water and fat images than translation correction.

Acknowledgements

The works in this dissertation would not have been possible without the help of Dr. Claudia Prieto, Dr. David Atkinson and Professor Tobias Schaeffter. Their advice, guidance and knowledge were fundamental for this thesis. I'd like to thank Dr. Steffen Petersen and Dr. Freddy Odille for their careful analysis and suggested corrections of this thesis.

I also need to thank all the people in our KCL group for all their help over the last three years: Rene, Markus, Usman, Teresa, Jedrek, Jack, Christian, Lucilio, Matt, Arian, Rui, Francesco, Mazen, Camila, Torben, Giovanna, Isabel, Andreia, Dan, Nick, Bram, Sebastian, Dregely, Radhouene, Alberto, Devis, Marta and Schirmer to name a few. You all make St. Thomas a great place to do research. Thanks to all my guinea pigs (i.e. volunteers) for all their time spend inside the scanner. I owe a lot of people a lot of favours. Thanks especially to Christoph, Andy and Ghislain for answering all of my MR questions. There were a lot of questions.

I am grateful to my mother for everything. Thanks to all my friends and family that supported me through ups and downs, specially Franco, Mel, Daniel, Rita, Alex and Milho. And finally thank you, Stephanie Walker, for being there, always.

The works in this dissertation where supported by the EPSRC (grant EP/H046410/1) and the MRC (grant MR/L009676/1).

Contents

List of Tables

List of Figures

Chapter 1

Introduction

Magnetic resonance imaging (MRI) is a medical imaging modality capable of three-dimensional (3D) imaging with high spatial resolution. MRI does not require ionising radiation, excels at imaging of soft tissues and provides both anatomical and functional information. Additionally, this modality has flexible image contrast, which has enabled many imaging applications in diagnostic medicine. However, the MR acquisition is a slow process, particularly in 3D. This limitation leads to a practical trade-off between scan time, resolution and field-of-view.

Significant efforts in the MR field have focused on alleviating the scan time requirements. An MR scan can be accelerated by acquiring only a fraction of the data, collecting so-called undersampled datasets. However, an image reconstructed from an undersampled dataset will contain aliasing artefacts, also known as ghosting. Parallel Imaging was a ground-breaking development that enabled significant scan time re-

ductions in exchange for a small penalty in signal-to-noise ratio. This method accelerates the acquisition, but then uses prior information from coil sensitivities to reconstruct an alias-free image. Compressed Sensing is a more recent development that exploits compressibility as prior information to enable even higher acceleration factors. Faster pulse sequences have been developed, hardware has significantly improved and efficient sampling strategies have been introduced. Regardless, the MR acquisition times remain slower than physiological motion, making this image modality sensitive to motion related artefacts.

Motion occurring during an MR experiment creates ghosting (image replicas) and blurring artefacts in the reconstructed image, which compromise diagnostic value. Patients are typically instructed to remain still, but some types of motion are unavoidable, such peristalsis, respiratory and cardiac motion. Abdominal and cardiac imaging are particularly challenging due to the presence of respiratory motion (as well as cardiac motion in the latter). Breath-hold acquisitions can minimize respiratory motion but are not always possible, particularly in 3D acquisitions. In this case the so-called respiratory gating is used, which minimizes motion by rejecting data outside a pre-defined gating window. Naturally, this approach extends scan time as rejected data must be re-acquired. Gating also requires a measurement of the respiratory position, which is typically obtained with additional

MR data using the so-called navigator echo. Developments on motion estimation have enabled navigators from the data itself (so-called self-navigation) and more accurate motion measurements have been obtained using low resolution image navigators.

In this thesis, the problem of scan time acceleration and respiratory motion is tackled by incorporating motion correction directly into fully sampled or undersampled reconstructions. Correcting motion corrupted data is more efficient than discarding and re-acquiring corrupted data and therefore motion correction can achieve reduced scan times. This thesis presents novel methods to estimate and correct the complex, non-rigid respiratory motion occurring during abdominal or whole-heart cardiac imaging. The framework developed incorporates Parallel Imaging and Compressed Sensing, enabling high spatial resolution motion correction of undersampled data in abdominal imaging. The method is further combined with image navigators to enable additional high temporal resolution motion correction in coronary vessel wall imaging and coronary water/fat imaging. The organization of this thesis is described below.

Chapter 2 introduces the problem of motion in MRI. A brief description of abdominal MR applications is given, followed by respiratory motion in abdominal imaging and the current methods used to deal with it. Cardiac imaging is also introduced, followed by a description of cardiac-induced and respiratory-induced motion in cardiac imaging,

as well as the current clinical practice to deal with these problems. Finally, a brief overview on general solutions to the problem of motion in MRI is given.

Chapter 3 provides the physical description of the MR acquisition. The mechanisms behind the MR signal generation are described, followed by a description of selected MR acquisition sequences relevant to the thesis.

Chapter 4 provides the mathematical description of the MR reconstruction. The reconstruction problem is introduced and studied as an inverse problem. Advanced reconstruction methods relevant to the thesis are described, followed by a description of the effects of motion in an MR image, as well as methods to correct for it.

Chapter 5 makes a comparison between image-based motion correction and reconstruction-based motion correction for abdominal imaging. A framework for motion estimation from the data itself is introduced and applied to both motion correction methods. Both approaches are studied in simulations and in vivo for abdominal respiratory motion correction.

Chapter 6 combines the reconstruction-based motion correction framework introduced in Chapter 5 with compressed sensing to deal with accelerated acquisitions. A novel approach is introduced to correct motion in undersampled data using motion estimated from the under-

sampled data itself and demonstrated in vivo for abdominal respiratory motion correction.

Chapter 7 extends and adapts the framework introduced in Chapter 5 for coronary vessel wall imaging. The proposed approach acquires two high resolution images interleaved with a low resolution image navigator. This method combines high temporal resolution translational corrections with high spatial resolution non-rigid corrections to address respiratory-induced motion of the heart. The proposed approach is studied in vivo for coronary lumen and coronary vessel wall imaging.

Chapter 8 combines the approach in Chapter 7 with compressed sensing and applies respiratory motion correction for 3D whole-heart water/fat coronary imaging at 3 Tesla. Initial results of the proposed approach are demonstrated in vivo for water/fat coronary imaging.

Chapter 9 summarizes the contributions and findings of the works developed in this thesis. Future work on motion correction and other topics in the MR field are also discussed.

Chapter 2

The problem of motion in MRI

The medical utility of Nuclear Magnetic Resonance (NMR) was noted since its' inception in 1971. Today, Magnetic Resonance Imaging (MRI) has applications in virtually every organ in the human body. One limitation of this modality are the long scan times, which typically lead to session durations upwards of 30 minutes. Patient motion during the scan results in image artefacts that compromise image quality. This chapter will introduce the clinical use of abdominal and cardiac imaging, which pertain to works in this thesis. The effect of motion in these examinations will be discussed, along with the current solutions to estimate, compensate and correct motion.

2.1 Abdominal Imaging

The first patient MRI scan in 1980 included an abdominal scan that was used to diagnose a liver abnormality [129]. Nowadays, abdominal MR encompasses imaging of the liver, biliary system, kidneys, adrenal glands, pancreas, bowel and all the vascular systems associated. In

particular, MRI is increasingly becoming the preferred modality to image the liver in clinical pratice. [131].

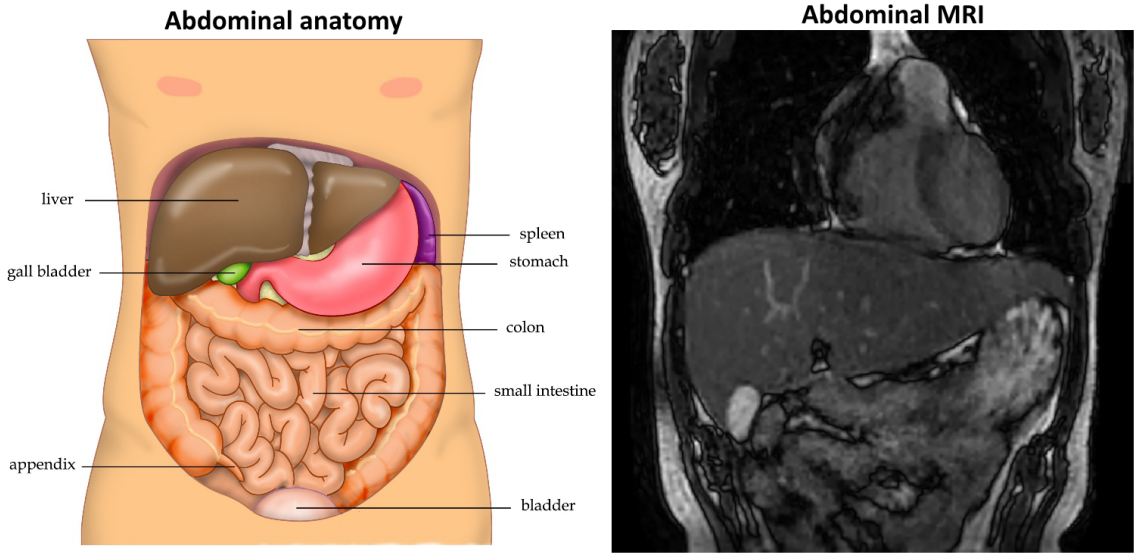

Figure 2.1: **Left**: Diagram of the major organ structures in the abdomen. **Right**: Abdominal MR image in the coronal orientation. Adapted from [209].

Figure 2.1 depicts the major organs in the abdominal anatomy, alongside with a coronal slice of abdominal MR image. In the MR image, the anatomy is visible in great detail, including small organs and vascular structures. The native contrast mechanism in MR are based in Proton Density (PD), T_1 relaxation and T_2 relaxation to generate PD-weighted, T_1-weighted and T_2-weighted images, respectively. Advanced techniques like Diffusion Weighted Imaging (DWI) or Phase Contrast (PC) manipulate physiological motion to produce contrast and exogenous contrast agents are also commonly used to produce Contrast Enhanced (CE) images. One of the advantages of MR is the ability to generate images with different tissue contrast using different pulse sequences. Hence, it is possible to optimize image properties to facilitate a given diagnosis. Several pathologies in the liver and

associated MR applications are listed bellow:

- **Simple liver cysts** appear as lesions with smooth thin walls, containing fluid and with no internal features. The cysts appear hypo-intense in T_1-weighted images and hyper-intense in T_2-weighted images relative to the liver. The fluid leads to increased signal intensity in T_2 imaging, which helps differentiate from cystic metastases [208]. No significant enhancement is observed with gadolinium.

- **Hemangiomas** are solid benign lesions with similar contrast properties to simple liver cysts. Dynamic contrast enhanced (DCE) MRI (post injection of Gadolinium based contrast agent) can be used to characterize the hemangioma into three different patterns: smaller than 1.5 cm, larger than 1.5 cm or larger than 6 cm [194]. Hemangiomas present similar T_1 and T_2 contrast, albeit less intense than cysts in T_2 imaging. Under T_1 with gadolinium, Hemangiomas may show nodular discontinuous enhancement and retain contrast in delayed imaging.

- **Focal nodular hyperplasia** (FNH) is a type benign liver lesion associated with vascular malformations. 80% of FNH are classified as histology-classic: these are relatively iso-intense in both T_1 and T_2, however they include central scars that are hypo-intense in T_1 images and hyper-intense in T_2 images [103]. When DCE-MRI is used, the FNH will show homogeneous enhancement in

the arterial phase, followed by late enhancement of the central scar. The remaining 20% are classified as histology-nonclassic: they lack the central scar and thus are invisible in T_1 and T_2 imaging.

- **Adenoma** is a rare benign liver growth, however they may lead to haemorrhage and can potentially evolve into a malignant form. Contrast in T_1 images depend on the lipid and haemorrhage presence: lipid signal is decreased in out-of-phase acquisitions, whereas haemorrhage leads to high signal. In T_2 imaging, hepatic adenomas appear as heterogeneous lesions with a mix of hyper- and hypo-intense locations [76].In DCE, the adenoma can have early enhancement during the arterial phase, but it typically appears hypo-intense during the hepatocyte phase [189].

- **Hepatocellular carcinoma** (HCC) is the most common type of liver cancer, commonly caused by chronic viral hepatitis (types B or C) and alcohol intake. HCC has a linear development from regenerative nodules into dysplastic nodules (without HCC and then with HCC) into finally HCC and MRI is commonly used to differentiate these stages [69]. HCCs are typically hypo-intense in T_1 and moderately hyper-intense in T_2 imaging. They also appear bright during the arterial phase in DCE and wash out during the equilibrium phase. Dysplastic nodules, for instance, do not washout easily during the equilibrium phase and have a

lower signal in T_2-weighted images.

- **Intrahepatic cholangiocarcinoma** (IHCC) is another type of liver cancer. These tumours are slightly hypo-intense in T_1 and moderately hyper-intense in T_2 and DWI, although this will depend on the content of the growth. IHCC typically display progressive enhancement after the arterial phase [10]. Ultra-delayed images may present enhanced scar tissue [231].

- **Liver metastases** are cancerous tumours that have spread to the liver from a different organ or system. They typically appear moderately hypo-intense in T_1 images, moderately hyper-intense in T_2 images (although darker than benign lesions) and hypo-intense with DWI at high b-values. The contrast may vary with the properties of the tumour, however DCE can be used to characterize it further [194]. Small (< 1.5 cm) lesions tend to enhance uniformly, whereas large lesions (> 1.5 cm) present a transient rim enhancement which can be used to distinguish from hemangioma [184].

- **Fatty liver disease** is a condition where fat accumulates in liver cells typically associated with excessive alcohol consumption or a high lipid diet. Although treatable, fatty liver can lead to HCC. Acquiring in-phase and out-of-phase images with Gradient Echo will reveal signal loss for the out-of-phase images in fatty locations [81]. The geometry of the deposit also allows it to be distinguished

from both benign and malignant tumours [13].

- **Cirrhosis** is a condition where the functionality of the liver is affected due to persistent liver damage. Scarring will appear hypo-intense in T_1 and hyper-intense in T_2. Regenerative nodules may be present and will typically display the opposite contrast [65]. In DCE, there are no significant peaks during the arterial or venous phases, but a progressive enhancement culminating in a peak during the equilibrium phase. Cirrhotic livers may change in size [46], which is easily detectable with most sequences.

- **Hemochromatosis** is a condition that causes iron accumulation in the body and particularly in the liver. This condition can be studied with standard T_2 imaging with various echo times as iron susceptibility effects will cause increasing signal loss with longer echo times [171].

From the list above, it can be seen that several scans are required for accurate detection and characterization of liver pathologies. Recent guidelines by the American College of Radiology recommend several sequences for a complete liver examination: a T_2 or short-tau-inversion recovery (STIR) image in axial and/or coronal planes, a gadolinium enhanced dynamic T_1 image in 2D or 3D (although high resolution 3D is preferable) using in-phase and out-of-phase imagine, and potentially a diffusion weighted sequence in the axial plane using single shot echo planar imaging [2].

2.1.1 Abdominal Respiratory Motion

All of the sequences above are sensitive to respiratory motion, which may cause ghosting and blurring artefacts. Respiratory inspirational motion is caused by contraction of the diaphragm and expansion rib cage muscles [225]. The exhalation motion occurs due to diaphragm and rib cage muscle relaxation. The two processes are mechanically different, leading to respiratory hysteresis as observed in several studies [109, 221]. It is known that the motion pattern generated depends on the subject's position [55], breathing depth [190] and varies greatly between subjects [111]. Nonetheless, the diaphragm is the main force that drives respiratory motion, causing other surrounding organs to move in tandem.

During normal breathing, foot-head (FH) motion of the diaphragm has been reported to be in the range of 10-30 mm [54, 90], with anterior-posterior (AP) and left-right (LR) motion approximately 5 and 6 times smaller, respectively [112]. Motion in the lung away from rigid structures has been measured to be approximately 12 mm in FH, with approximately 2 mm in both LR and AP [188]. Left and right kidney presented average motions of 11 and 13 mm in FH (respectively), 4.4 and 6.1 mm in AP, 1.7 and 1.4 mm in LR according to the study in [27]. The same study also evaluated spleen and liver motion: 13 and 13 mm (respectively) in FH, 5.0 and 5.2 in AP, 2.5 and 2.1 in LR. Liver motion in particular has been analysed in several studies [47, 175, 193]

with good reproducibility. The work in [175] used image registration, measuring liver motion in the range of 12-26 mm, 1-12 mm and 1-3 mm in FH, AP and LR, respectively, in addition to small rotational motion (inferior to 1.5 degrees). The same study detected non-rigid motion components up to 19 mm with an average difference of 6 mm when compared to a rigid motion model. Abdominal respiratory motion is complex in nature, with non-rigid relationships between different organs [175, 211]. Nonetheless, several techniques have been proposed to minimize respiratory motion artefacts in MR.

2.1.2 Dealing with Abdominal Respiratory Motion

A simple solution to minimize respiratory motion is to divide the scan time into one or more 15-20 second segments and acquire each during a breath-hold. Breath-hold scans generally achieve very good suppression of motion artefacts, however they are not possible in every case. Although commonly used for 2D acquisitions, this may not be a viable strategy in 3D due to time constraints. Breath-hold cooperation can be difficult in elderly or paediatric patients. Furthermore, multiple breath-holds are not guaranteed to be in the same respiratory position, which can lead to misregistration problems [186] in addition to possible drift during the breath-hold [94]. Additionally, normal physiology is compromised during a breath-hold; for instance, atypical blood signal can occur during breath-hold imaging [121]. Naturally, breath-hold

examination time is increased as the patient requires instructions and rest time between breath-holds.

It is also possible to minimize respiratory motion by estimating and compensating for it. Respiratory gating is an alternative *motion compensation* technique that does not require breath holding. The method monitors the respiratory position to avoid introducing motion artefacts. This is achieved by only accepting acquired data during a specific respiratory phase (commonly end-expiration) within a pre-defined *gating window*. Typically, a gating window of 5 mm or less is preferred to minimize the motion during the acquisition. The downside of this approach is a loss in *scan efficiency*, the ratio of accepted data to acquired data, due to data rejection. Increases in scan time of 30% to 50% are expected when respiratory gating is employed [62]. The first studies with respiratory gating were performed in the 80's and since then the method has become standard clinical practice. Figure 2.2 shows results of one of the early experiments with respiratory gating.

The respiratory gating technique requires knowledge of the current motion state, usually obtained with external monitoring devices or from MR data. Respiratory bellows are a type of external devices commonly used to monitor respiratory motion [62]. This device typically comes in the form of a belt that is strapped around the patient, measuring pressure changes due to respiratory motion. This information is fed to the scanner in real-time and converted into a one-dimensional

respiratory signal to enable respiratory gating. However, external devices only provide a relative and indirect motion measurement.

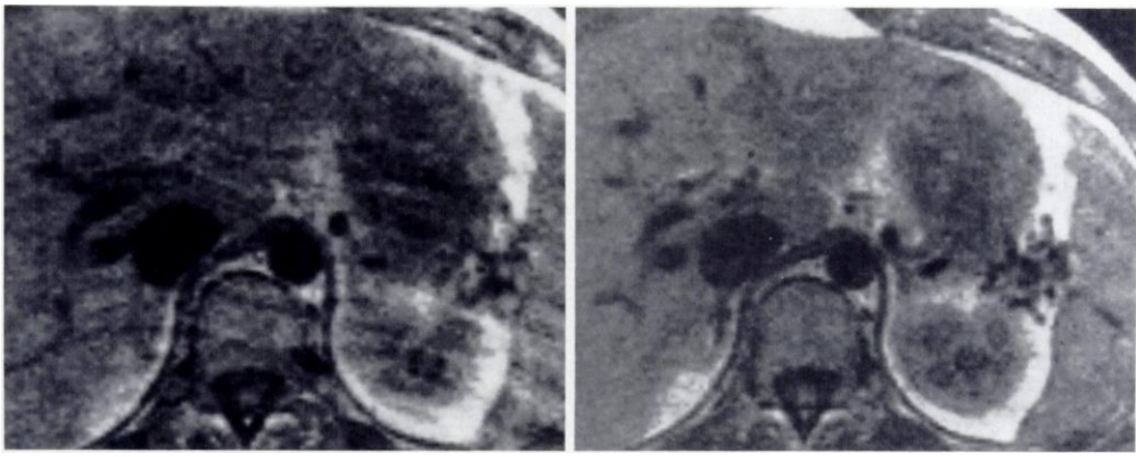

Figure 2.2: **Left:** Axial motion corrupted abdominal image. **Right:** Axial respiratory gated abdominal image. Note a significant reduction in blurring and ghosting artefacts. Taken from [62].

Respiratory information can also be measured directly from MR data using so-called navigators [61]. Navigators acquire a small amount of MR data shortly before or after the acquisition of each k-space segment and use this information to measure the respiratory position in real time. Navigator information is commonly obtained from a column of moving tissue, usually the dome of the right hemi-diaphragm, allowing measurement of foot-head (FH) motion. This excitation can be performed with a 2D radio-frequency (RF) pulse (the so-called pencil beam navigator) or with a combination of a 90° RF excitation and an oblique 180° RF refocusing. The corresponding signal is then reconstructed to provide a 1D projection of the lung-liver interface which correlates to the respiratory position of that tissue. The respiratory position can be obtained from the 1D signal using edge-

detection, cross-correlation or least-squares methods [216]. Usage of a diaphragmatic navigator to perform respiratory gating is shown in Figure 2.3, depicting the location of the pencil-beam (a-c), as well as the 1D projection of this interface through time (d) and the final respiratory signal (e).

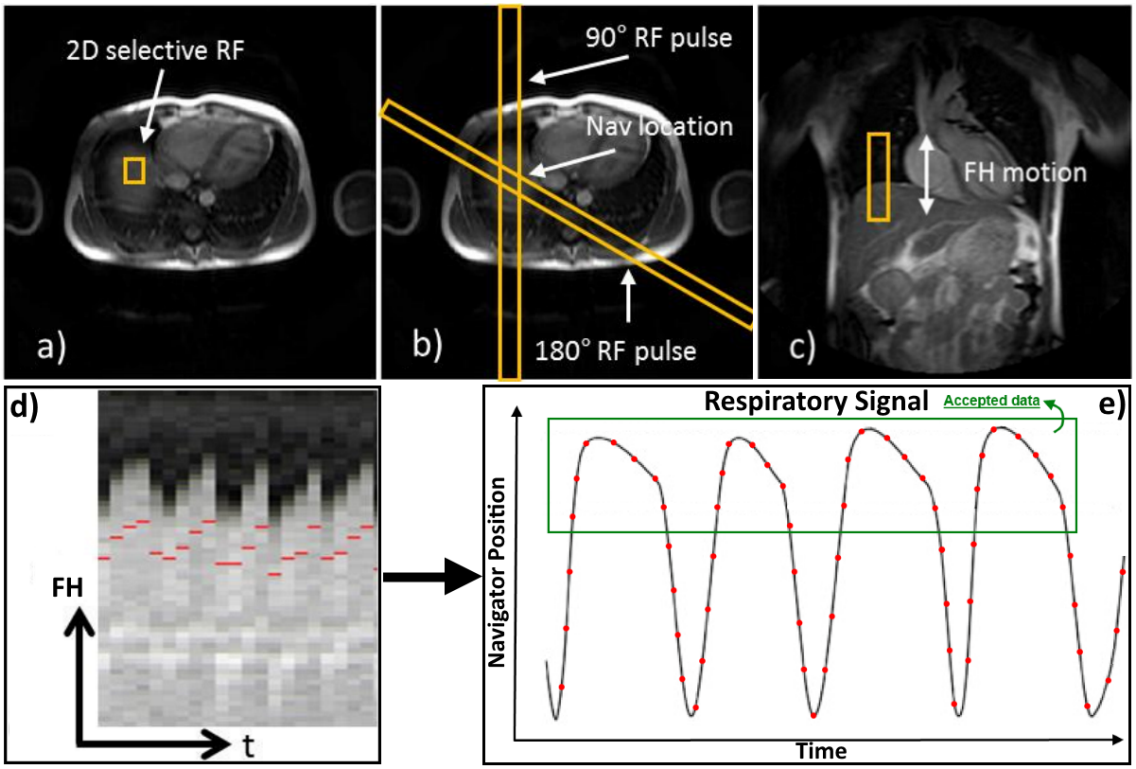

Figure 2.3: A respiratory navigator may be acquired with a 2D selective RF pulse (**a)**) or a combination of a 90° RF and 180° RF pulses (**b)**), monitoring foot-head (FH) motion of tissue in the liver-lung boundary (**c)**). Repeated acquisitions through time measure the foot-head variation of this boundary (**d)**), from which a respiratory signal can be derived (**e)**). Respiratory gating is then applied by only accepting data within a given gating window. Adapted from [84].

Gating deals with motion by minimizing motion to a small gating window. Regardless, respiratory motion information can also be used to correct the data and further improve image quality. For example, if the diaphragmatic translational motion of each MR data point is known, motion artefacts can be reduced by correcting the MR data

before reconstructing the image. This *motion correction* technique is known as *tracking*. Figure 2.4 shows an example of an early study using respiratory navigation information to correct translational motion in abdominal imaging. This approach can correct residual motion within a gating window, further reducing motion artefacts. However, correcting for moving tissue might introduce artefacts in static tissue, since the translation correction is global. Translational motion or even rigid motion is insufficient to fully capture the abdominal deformations due to respiratory motion, as described before. The limitation of the translational model is apparent in Figure 2.4, where the spine appears out of focus in the corrected image.

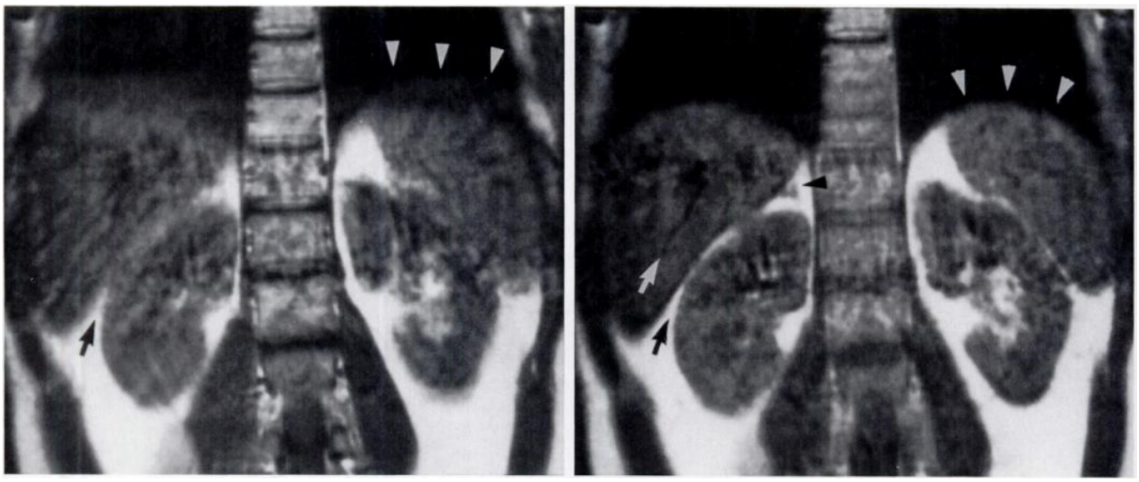

Figure 2.4: **Left:** Motion corrupted coronal abdominal image. **Right:** Translational corrected coronal abdominal image. A significant improvement in image quality can be seen in the (moving) diaphragm and the kidneys, however note the increased blurring in the (static) spine. Taken from [61].

Breath-hold imaging (usually in 2D imaging) and FH respiratory gating with translation correction (usually in 3D imaging) are commonly used for motion compensation in abdominal MRI. However, breath-hold might not always be possible and respiratory gating is inefficient,

typically doubling the scan time. Current methods for motion compensation only provide an approximation model of the complex non-rigid abdominal motion. Nonetheless, it is possible to compensate for complex abdominal motion without a penalty in scan time, as it is demonstrated in several works in this thesis.

2.2 Cardiac Imaging

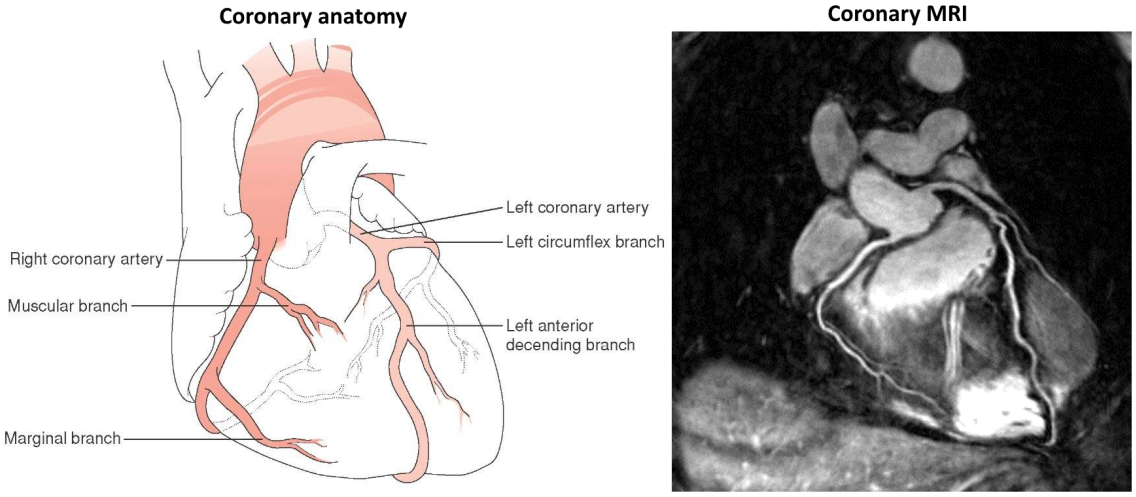

Figure 2.5: **Left:** Diagram of the major vessels in the coronary anatomy. **Right:** Reformated coronary lumen MR image. Adapted from [229].

Cardiovascular magnetic resonance (CMR) imaging has had a slow development due to the difficulties associated with respiratory-induced and cardiac-inducted motion. Clinical applications for CMR have increased in recent years due to several technical advancements in the field. Today, several anatomical and functional protocols are part of standard clinical practice. Recent developments have even enabled imaging of the coronaries, although this is not yet common practice.

Figure 2.5 shows a simple diagram of the coronary arteries and a corresponding reformatted coronary lumen MR image.

A wide range of applications have been developed over the years, allowing CMR to compete with transthoracic echocardiogram (TTE), X-ray computed tomography (CT), positron emission tomography (PET) and single photon emission computed tomography (SPECT). A few of these applications are listed bellow:

- **Valvular heart disease** refers to defects in any of the heart valves. Doppler TTE is the first-line technique, however, CMR may be used if quantification is required or the acoustic window is weak. Balanced steady-state (b-SSFP) free-precession cine images can be used to evaluate thickness and motion of the valve. Left and right ventricular (LV and RV, respectively) function, mass and volume can be accessed with multi-slice cine to detect functional abnormalities and obtain quantitative measures of cardiac function. Gradient echo is also used and excels at detecting turbulent flow. Phase-contrast (PC) imaging is used to obtain velocity mapping, which provides measurements of flow and stroke volume.

- **Congenital heart disease** are structural anomalies in the heart, present at birth. A variety of CMR techniques can be used for this problem [70]. Black blood imaging can be used to visualize the anatomy. Gadolinium enhanced b-SSFP angiography is used

to see vascular problems in the pulmonary arteries/veins or the aorta and cine imaging can be used to evaluate function. Late gadolinium enhancement (LGE) can detect a variety of congenital defects as it highlights scarred and dead tissue. Additionally, perfusion imaging using a coronary vasodilator can reveal regions of low blood supply due to coronary stenosis. PC imaging is also used to detect stenosis or regurgitation defects [11].

- **Myocardial ischemia** typically refers to a restriction in the blood supply to the heart. Stress perfusion CMR can be used as an alternative to SPECT, with similar performance [185]. This is achieved with adenosine (vasodilator) and contrast enhancement to locate regions of decreased blood supply. Cine imaging may also be used to detect abnormal wall motion in the heart, indicating local ischemia. CMR is also used to study myocardial viability, the presence of living myocytes and the recovery potential of damaged regions in the heart, although PET is regarded as the gold standard for this problem [41]. Damaged tissue can be visualized with LGE. The transmurality of the scar across the wall of the myocardium can be measured to determine the prognosis of revascularization. Myocardial scar may also be detected with tagging MR. Finally, low dose dobutamine (cardiac stimulant) has also been used to detect scarred tissue, since the contraction of healthy tissue will increase, whereas scarred tissue

will not.

- **Myocardial Infarction**, the so-called heart attack, occurs when the blood flow to the heart ceases, commonly due to coronary artery disease. Ischemia will then cause death of heart muscle, which can lead to further complications. T_1-weighted LGE is the main technique to diagnose this disease due to high accuracy and sensitivity [105]. It can be used to quantify scar tissue, assess viability and evaluate thrombus. Death or damage to myocytes (muscle cells) allow contrast agents to permeate and accumulate freely in regions of abnormal tissue, causing it to appear very bright. Additionally, microvascular obstructions (dead tissue cut-off from blood supply) will appear very dark with this technique. T_2-weighted imaging can also be used to detect myocardial edema (fluid accumulation), differentiating between chronic and acute infarction [1]. Multiple slice b-SSFP cines can also be used to determine ventricular and valvular function.

- **Cardiomyopathy** is an intrinsic myocardial dysfunction associated with structural defects in the heart muscle, particularly in the left ventricle. CMR is used to characterize the various types of this disease, although the protocol varies with the suspect myopathy. The most common variants are dilated (enlarged heart cavity leads to reduced cardiac output) and hypertrophic (thickening of the ventricular wall obstructs blood flow). Dilated

cardiomyopathy may be studied with black blood imaging, where enlarged cardiac chambers or thin myocardial walls will be visible [5]. Coronary angiography is used to rule out coronary artery disease and late enhancement imaging can evaluate the degree of fibrosis [7]. Hypertrophic cardiomyopathy is characterized primarily by LV wall thickening, which can be visualized in black blood images. Cine imaging enable assessment of LV systolic function, which can be studied further with PC imaging [130]. LGE is also useful to study ventricular wall thickness and detect scarring that occurs in thicker regions [139]. Stress perfusion has also been recently proposed for this problem [158].

- **Coronary artery disease** (CAD) refers to the narrowing and hardening of the coronary arteries, due to atherosclerosis (plaque accumulation). This will reduce and potentially block blood flow to the heart, causing several of the conditions described above and potentially death. CAD was the number one cause of death in 2013 [114] and significant effort has been devoted to early diagnosis. X-ray angiography is commonly used for CAD imaging. Recent studies have shown that MRI can provide similar measurements in the proximal section of the coronaries [164]. Coronary magnetic resonance angiography (CMRA) is a challenging technique. High resolution 3D b-SSFP sequences are used to capture the full coronary tree in detail. Fat suppression methods are re-

quired, as the vessels are embedded in epicardial fat [134], and T_2 preparation pulses are commonly employed to improve contrast between the vessels and the myocardium [24, 28]. CMRA has recently undergone a paradigm shift towards imaging of the vessel wall. A recent study has shown that vessel wall imaging can detect pre-clinical atherosclerosis whereas classic lumen imaging will not [107]. Vessel wall images were initially obtained using double inversion black blood sequences, but subtraction-based approaches have been recently proposed [6].

Most of the studies described above, and particularly the protocols for CMRA, are sensitive to motion. If no bulk patient motion is present, the dominant sources of motion will be cardiac-induced motion and respiratory-induced motion.

2.2.1 Cardiac-induced Motion

The heart is divided into four chambers: the left and right atria receive blood into the heart; the left and right ventricle pump blood out of the heart. The heart undergoes a cyclical motion as part of its' function to pump blood. This cardiac cycle can be broadly divided into a systolic (compression) phase lasting approximately 400 ms and a diastolic (relaxation) phase that takes typically between 200 and 800 ms [222]. Several studies on the form of cardiac-induced motion have been performed [101, 159, 160], particularly the compression of the left ventri-

cle (responsible for pumping oxygenated blood to the body). Results show a strong longitudinal component (up to 13 mm near the base), accompanied by significant scaling (approximately 5 mm average) and rotation (up to 10 degrees in the apex) components. Cardiac-induced coronary motion has also been studied under breath-hold [4], revealing predominant anterior posterior (AP) motion (approximately 11.4 mm average), as well as foot-head (FH) motion (approximately 9.2 mm average) and left-right (LR) motion (approximately 9.1 mm average). The motion amplitude in the right coronary artery (RCA) is typically twice the amplitude in the left coronary artery (LCA).

2.2.2 Dealing with Cardiac-induced Motion

Cardiac-induced motion is commonly resolved with the aid of an electrocardiogram (ECG), a technique that records the electrical activity of the heart. ECG provides an electrical signal derived from the myocardium's electrophysiology. The characteristics of this signal contain rich information about the structure and function of the heart, making the ECG a very useful diagnostic tool. In the context of cardiac-induced motion, the ECG is used to track the major events in the cardiac cycle: atrial systole is mapped by the P-wave, the so-called QRS complex maps the beginning of the ventricular systole and the remainder of the ventricular systole is mapped by the T-wave. A schematic of an ECG signal can be seen in Figure 2.6.

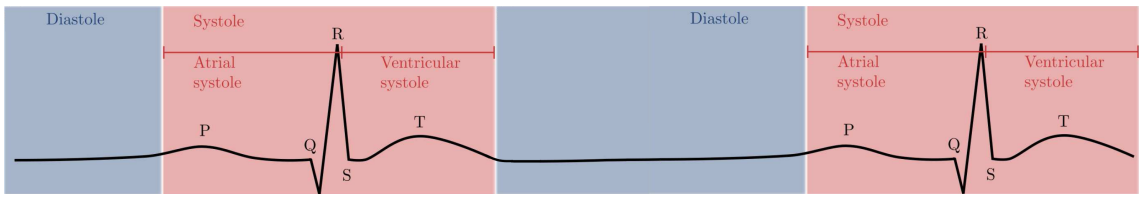

Figure 2.6: Diagram of an ECG signal of the cardiac cycle. The P-wave marks the beginning of atrial systole when blood is transferred from the atria to the ventricles. The QRS complex marks the beginning of ventricular systole (extending throughout the T-wave) when blood is pumped to the rest of the body. Data acquisition typically takes place during diastole (both atrial and ventricular), as the heart has relatively little motion for an extended period of time. Adapted from [110]

The R wave in the ECG is used to identify the beginning of the systole and the acquisition timing is adjusted to coincide with the diastole, when cardiac motion is minimal. Cardiac motion is assumed to be periodic, enabling data acquisition to be split over multiple cardiac cycles. Each subset of the data is acquired during diastole in an *acquisition window* of typically 100 ms or less. This so-called *cardiac triggering* is one of the most common solutions to freeze cardiac-induced motion. Data acquisition is split over several cardiac cycles, enabling imaging of a given cardiac phase. The optimal *trigger delay* (time lapsed from the R wave to the beginning of data acquisition) is known to be subject dependent [219], but the optimal timing can be determined by cine imaging. A limitation of cardiac triggering is its sensitivity to variations in cardiac frequency [203]. Arrhythmia rejection techniques discard data when sudden changes in the heart rate are detected (approximately $\pm$ 20%), reducing motion artefacts at the expense of increased scan time.

Cardiac gating uses ECG information to label data continuously ac-

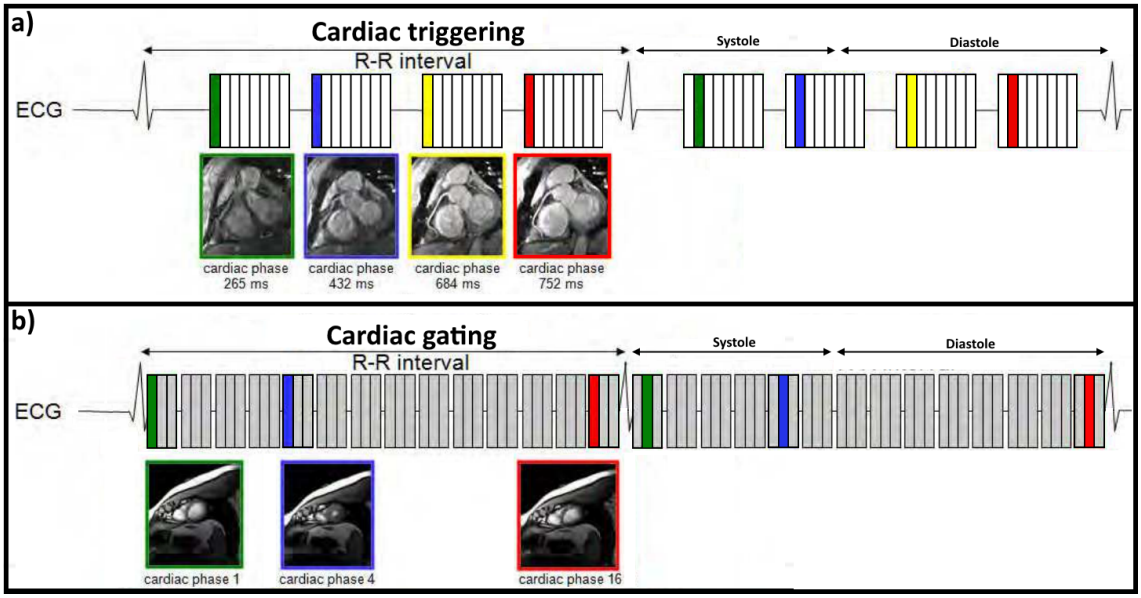

Figure 2.7: **a)** Schematic for cardiac triggering. Different amount of motion artefacts are present depending on the trigger delay. Mid-diastole acquisition minimizes cardiac induced motion. Note that only one of these cardiac phases would be imaged in a real acquisition. **b)** Schematic for cardiac gating. Data is continuously acquired and labelled according to its' cardiac phase. Adapted from [145].

quired during the cardiac cycle. These data can be grouped into different cardiac phases (with temporal resolution of ≈30 ms) retrospectively to resolve cardiac-induced motion [117], which yields a cine image of the heart. Figure 2.7 depicts an example of cardiac triggering and cardiac gating. Note in a) that acquiring data during systole can result in motion artefacts, whereas these are significantly reduced in a mid-diastolic acquisition (approximately 750 ms after the R wave). Cardiac gating sorts data depending on the relative delay to the R wave, enabling imaging of different cardiac phases.

ECG gating and triggering have been very successful in dealing with cardiac-induced motion, however residual cardiac motion may remain even when these techniques are employed. Studies have shown sig-

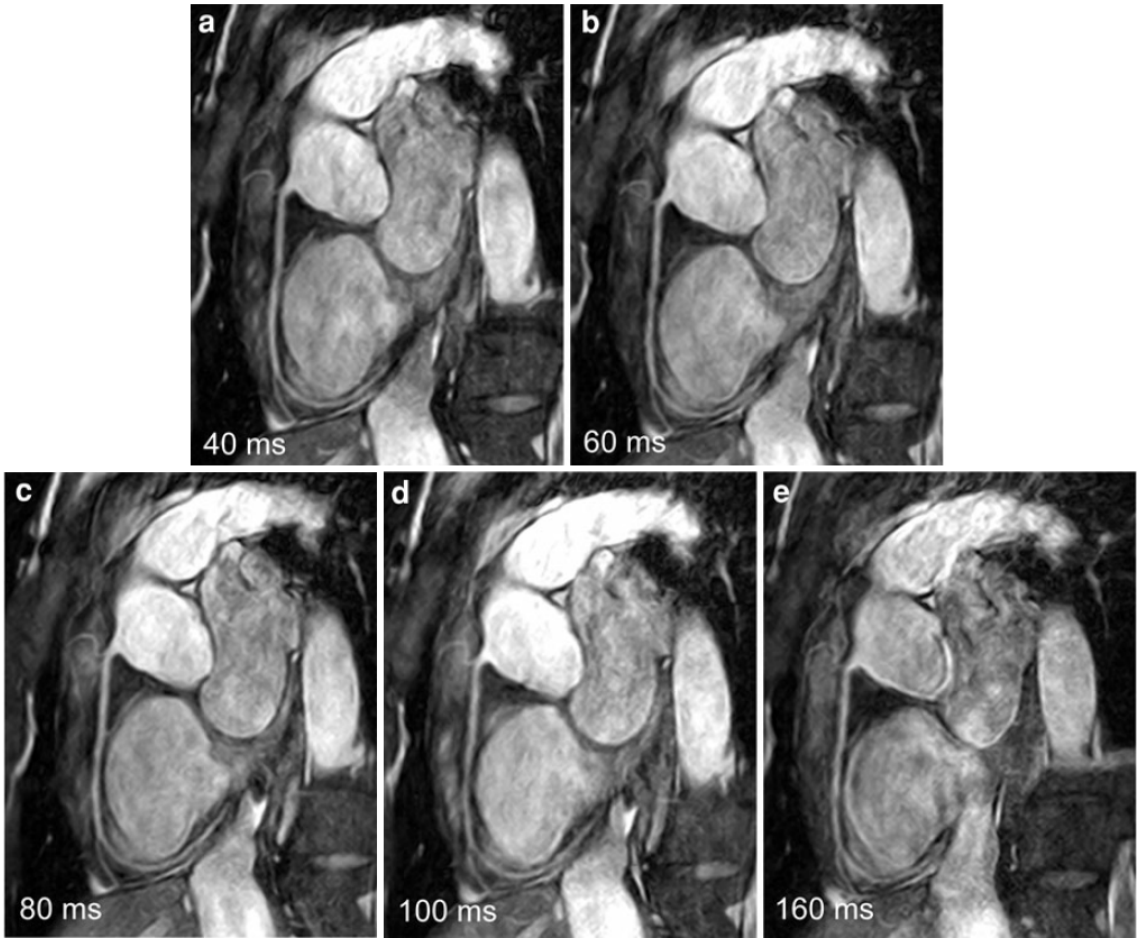

Figure 2.8: Right coronary artery image acquired with different acquisition windows. Optimal image quality is obtained for the smallest window (40 ms). Motion artefacts are introduced with wider windows, however acceptable image quality is obtained for windows up to 100 ms. Significant motion artefacts are seen with an acquisition window of 160 ms. Taken from [21].

nificant motion even during diastole: longitudinal velocities of approximately 140 mm/s and radial velocities up to 51 mm/s. Thus, significant cardiac-induced motion may be present (as well as residual respiratory motion), depending on the size of the acquisition window. Figure 2.8 shows images of the RCA acquired with different acquisition windows. Increasing window size introduces motion artefacts; an acquisition window less than 100 ms is desired for acceptable image quality. The obvious advantage of increasing the acquisition window

is a reduction in scan time. The periodicity of the cardiac cycle in conjunction with small acquisition windows is typically sufficient to suppress most of the cardiac motion, hence cardiac motion correction is seldom used.

2.2.3 Respiratory-induced Motion

Respiratory-induced motion of the heart has been studied for many years. One of the first studies, using X-rays, determined the FH heart motion to be approximately half that of the diaphragm (with diaphragmatic motion in the range of 10 to 20 mm) [22]. These results were replicated in MRI several years later, suggesting that the FH heart motion is 0.6 of the FH diaphragm motion, on average [217]. Additional studies have confirmed inter and intra-subject variability on this relationship, as well as the presence of hysteresis [142, 205]. More recent studies have revealed non-rigid components in respiratory-induced motion in FH, AP and LR [137, 191]. Respiratory-induced motion is a more challenging problem than cardiac-induced motion. The periodicity of respiratory motion is less predictable and the motion cannot be fully described by simple models (e.g. translation or affine) due to its' complexity and amplitude. Despite this limitation, gating and tracking have gained popularity in clinical practice, as a good reduction in motion artefacts is achieved whilst adding minimal complexity to the acquisition and processing.

2.2.4 Dealing with Respiratory-induced Motion

Initial CMR experiments featured breath-hold imaging [200]. CMR faces similar breath-hold challenges to abdominal MR, namely the extension in scan time, compromise of normal physiology and the reproducibility of the breath-hold position [95]. Respiratory-induced cardiac motion compensation uses similar techniques to respiratory abdominal motion compensation, namely gating and tracking.

Respiratory gating, also known as the accept-reject algorithm (ARA) [176], is commonly used with a 5 mm gating window to accept data only during end-respiration when the heart motion due to breathing is minimal. For translational tracking correction, a standard scaling factor of 0.6 is used to relate FH diaphragmatic and heart motion [53, 202]. However, additional methods have been proposed to derive subject-specific correction factors [205].

Initial comparisons between respiratory gating with 2 mm gating window and breath-hold reported no significant differences [151]. However, more recent studies have demonstrated that respiratory gating with larger windows is inferior to breath-hold imaging, presenting decreased accuracy in detection of coronary artery stenosis [173]. Images comparing the breath-hold and gating approaches are shown in Figure 2.9.

Figure 2.9: **a)** CMRA using breath-hold. **b)** CMRA using respiratory gating with a 2 mm gating window. Respiratory gating achieves comparable image quality to breath-hold imaging. In both cases an acquisition window of 160 ms was used. Taken from [21]. **c)** Breath-hold CMRA in a different study, indicating the presence of coronary artery stenosis. **d)** Respiratory gating in the same study with a gating window larger than 2 mm. Stenosis is also visible, albeit with decreased image quality. Taken from [173].

Diaphragmatic respiratory navigators are also commonly used to estimate respiratory motion, however this approach does has several limitations. Variations in the breathing motion, respiratory hysteresis and the fact that motion is indirectly measured (i.e. a diaphragmatic surrogate is used) are all sources of error in respiratory-induced cardiac motion estimation. Additionally, the commonly used diaphragmatic navigator only measures 1D FH motion and does not consider more

complex motion or additional dimensions, which have been shown to occur in the heart.

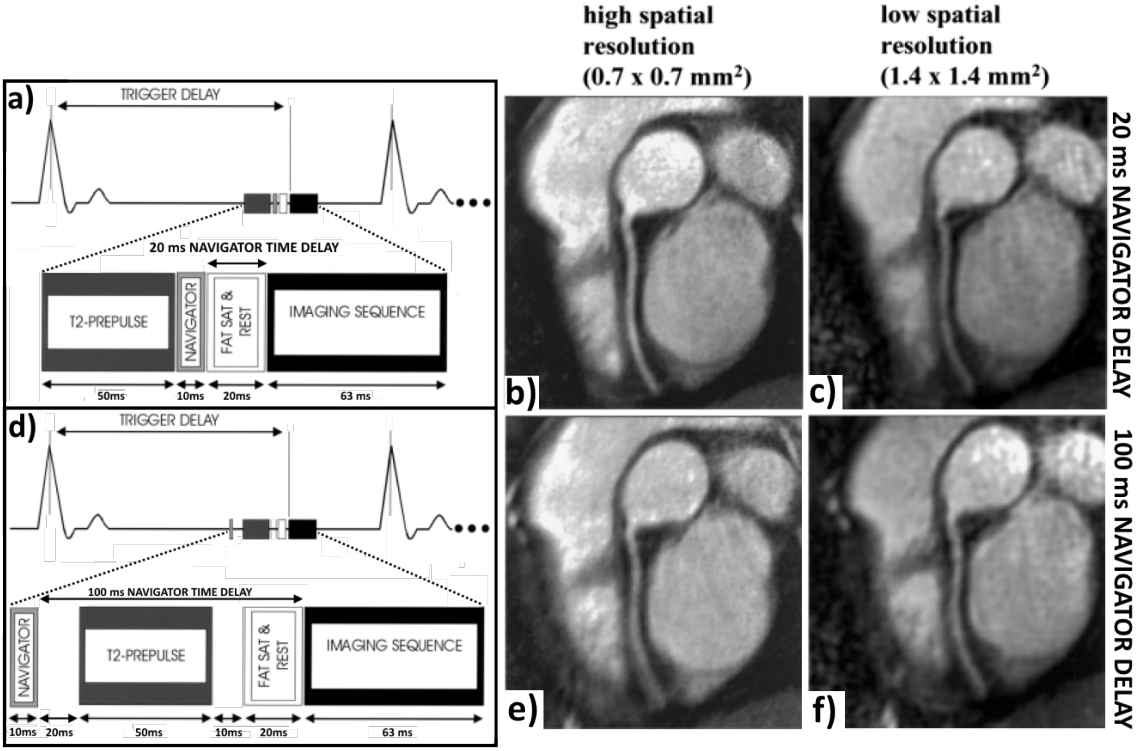

Figure 2.10: **a)** Schematic of a CMRA acquisition with a 20 ms navigator time delay. The T_2 preparation and fat saturation pulses are required for adequate coronary visibility. **b)** Reformated CMRA image acquired with a 20 ms navigator delay and 0.7 x 0.7 mm resolution. **c)** Reformated CMRA image acquired with a 20 ms navigator delay and 1.4 x 1.4 mm resolution. **d)** Schematic of a CMRA acquisition with a 100 ms navigator time delay. **e)** Reformated CMRA image acquired with a 100 ms navigator delay and 0.7 x 0.7 mm resolution. **f)** Reformated CMRA image acquired with a 100 ms navigator delay and 1.4 x 1.4 mm resolution.

When respiratory gating (or tracking) is used, it is important that the time delay between the motion measurement and data acquisition be made small. Spuentrup and colleagues in [199] analysed the impact of the navigator timing in a respiratory gated and tracked CMRA acquisition. The results, shown in Figure 2.10, indicate a loss in image quality (notably sharpness and contrast) when the navigator delay is increased from 20 ms to 100 ms. The effect is visible at a spatial

resolution of 1.4 x 1.4 mm, but is more severe at 0.7 x 0.7 mm resolution. Note that the navigator measurement may be taken before or after (or both) the data acquisition, although only the former enables prospective corrections.

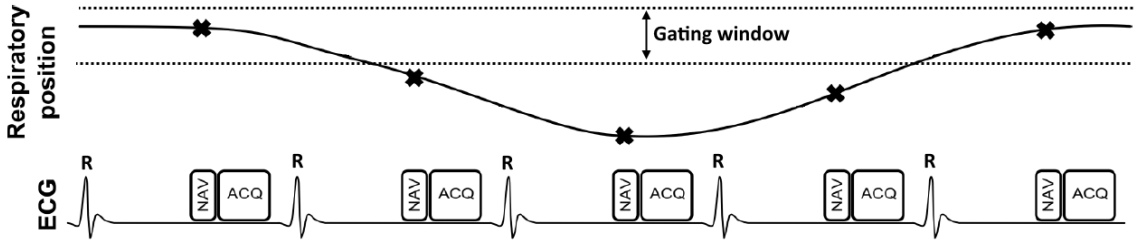

Figure 2.11: Schematic of a CMR acquisition using cardiac triggering and respiratory gating (without pre-pulses). A motion measurement (NAV) with navigator echoes, self-navigation or image navigation is acquired once per heartbeat. This information is used to determine if data is within the end-expiration gating window to be accepted. A small segment of the data is acquired shortly after (ACQ) if the navigator measurement lies inside the gating window. The duration of the acquisition window and the size of the gating window determine the amount of residual cardiac-induced and respiratory-induced motion. Adapted from [84].

Cardiac triggering and respiratory gating are commonly employed to compensate motion in CMR, in combination with tracking to further correct the data. A schematic of such an acquisition in shown in Figure 2.11. ECG triggering can minimize cardiac-induced motion, however only 100 ms (typically) in each heartbeat are used for imaging. Respiratory gating minimizes respiratory-induced motion, however only data within 5 mm (typically) in the end-expiration phase is accepted. Translational tracking only provides an approximate correction, as respiratory-induced heart motion is known to have non-rigid components [137]. Both triggering and gating methods significantly increase scan times, particularly in high resolution 3D acquisitions. For ex-

ample, a 1x1x2 mm resolution dataset can take over 20 minutes to acquire (using a b-SSFP sequence and with a heart rate of 60 beats per minute), if both these methods are used to compensate for motion. These limitations have prompted the MR community to develop further techniques for motion estimation, compensation and correction.

2.3 Strategies for motion minimization

The commonly used respiratory gating, cardiac triggering and translational tracking techniques have been introduced in the previous sections. However, numerous techniques have been developed over the last 30 years to help minimize different types of motion, in different MR applications. Some of the main approaches developed in the field are summarized bellow:

- **Motion estimation: navigation strategies**
  - *Higher dimensional navigators* allow more complex motion estimation than provided by the 1D FH signal produced by the standard pencil-beam navigator. 2D [71, 220] and 3D [223] navigators have been introduced to capture rigid-body motion in some brain applications. Naturally, these approaches come with an increased complexity in the acquisition and processing steps.

- *Self-navigation* is a navigator technique that uses the image data itself to estimate motion [115], without an additional dedicated navigator acquisition. Self-navigation does not require the additional planning and avoids interference between navigation and imaging, like signal saturation or disruption of the steady state [182]. However, self-navigation typically use 1D signals that correspond to projections of the full image volume and therefore will include static tissue. Recent developments have yielded methods that allow 1D self-navigation for the cardiac and respiratory signals from the data itself [49, 155].
- *Image navigators* (iNAV) have recently been proposed to provide real-time low-resolution images at every heart-beat [88, 187]. This technique allows motion to be estimated from the heart directly, instead of a diaphragmatic surrogate. Additionally, iNAVs contain 2D (or 3D) motion information that allows direct estimation of rotation or non-rigid motion components.

- **Motion Compensation: gating strategies**
  - *Diminishing Variance Algorithm* (DVA) is an advanced gating technique focused on minimizing the variance of the accepted respiratory amplitude [177, 178] to improve resistance to respiratory drifts. A free-breathing (motion corrupted)

dataset is initially acquired. Following, the data segments with the highest displacement are repeatedly re-acquired (effectively reducing the variance), until a pre-defined variance threshold or time limit is reached.

- *Phase Encoding with Automatic Window Selection* (PAWS) is another gating variant that features multiple gating windows, also known as bins [98]. PAWS' strategy is to initialize data acquisitions in multiple bins, covering the range of the respiratory signal. The sampling strategy is defined to be complementary in neighbouring bins, allowing an image to be reconstructed using data from contiguous bins. A recent study in CMRA found PAWS to be superior to DVA and ARA [144].
- *Retrospective gating* methods have also been introduced where 5x the standard amount of data is acquired, but then only the subset of data with minimal motion is used for reconstruction [118]. This approach is more robust in the presence of respiratory drift, whereas prospective gating requires a predefined gating window and is susceptible to low efficiencies (or even scan abortions) if the respiratory pattern changes significantly during the acquisition. However, this approach requires 5x the scan time of a free-breathing acquisition.

- **Motion Compensation: sampling strategies**

- *ROPE, COPE and HOPE* stand for Respiratory [12], Centrally [79] and Hybrid [99] (respectively) Ordered Phase Encoding. These methods rely on re-ordering the data sampling strategy to produce more benign motion artefacts (artefacts that are unlikely to be mistaken for pathologies, e.g. noise-like or incoherent artefacts). The strategy is to acquire low frequency data in similar motion states, reducing motion ghosting artefacts. However, residual blurring and high frequency motion artefacts are likely to be present with these approaches.
- *Non-Cartesian sampling* typically uses spiral and radial data sampling patterns which naturally average low frequency information in the image [72, 93, 162]. Additionally, the artefacts tend to be more benign, commonly smeared over the image in a less coherent way, reducing the apparent motion artefacts.

- **Motion Compensation: data-based strategies**

  - *Averaging* multiple free-breathing datasets can be used to reduce motion artefacts. The resulting image will correspond predominantly to the object in the most common motion states, with smaller incoherent contributions from the less popular motion states. This technique can reduce ghosting artefacts, at the expense of additional scan time, however

blurring artefacts are likely to remain.

– *Parallel Imaging* can be used for motion minimization. Motion corrupted data may be discarded and Parallel Imaging [169] used to recover missing data [37]. This enables motion compensation at some minor expense in signal-to-noise (SNR) ratio.

- **Motion Compensation: Signal suppression strategies**

  – *Spatial saturation bands* allow signal from moving tissue (e.g. blood flow) to be suppressed, effectively preventing motion artefacts that would otherwise be generated. Additional magnetic field radio frequency (RF) pulses are applied prior to data acquisition to null the signal entering the volume to be imaged. The downside of this approach is an increase in specific absorption rate (SAR) and measurement time. A variant of this method can also be used as a form of contrast, for example black blood MRI [140].

  – *Gradient moment nulling* is a technique useful in suppressing signal loss and ghosting artefacts originating from near-constant velocity tissues [128]. The nuclear spins responsible for signal generation will precess with a frequency proportional to the magnetic gradient, a spatially variant magnetic field. The data acquisition is typically designed to keep all spins focused (on the same rotational phase) when the data

is read. However, moving spins will precess at different frequencies and will not refocus when expected, resulting in phase discontinuities and signal loss. Constant-velocity moving spins can be refocused if the first moment of the gradients are null at specific times, particularly the centre of the readout, which is the mechanism behind gradient moment nulling. The following chapter will give additional background on MR Physics required to describe this approach in finer detail. Note that this phase accrual is the mechanism responsible for the contrast in DWI and PC.

- **Motion Correction: prospective and retrospective**

  – *Prospective motion correction* refers to a class of methods that estimate and correct motion during the acquisition. If a given motion measurement can be processed in real-time, the parameters of the magnetic fields involved (gradients, RF pulses, frequencies, phases) can be adjusted to prospectively correct each data segment [141]. In CMR, subject-specific affine models have been introduced for prospective motion correction [132]. Many motion measurement approaches have been proposed, including in-bore cameras [127] and compatible ultrasound systems [66], in addition to the navigation approaches described before. Prospective motion correction avoids opening gaps in k-space (the frequency space where

the data is acquired), as well as the sampling of redundant frequency information. This is a limitation of retrospective motion correction, discussed in greater detail in Chapter 4. This approach is limited in the amount of motion information that can be processed in a timely fashion and may cause distortions in the main magnetic field [97]. Additionally, prospective motion correction is limited to affine corrections.

– *Retrospective motion correction* corresponds to the complementary class of methods that correct motion after the acquisition. This is commonly achieved by modifying the data before or during the reconstruction with the appropriate mathematical corrections [123]. It is also possible to retrospectively correct for motion without previous motion measurements, using a class of algorithms known as autofocus [9, 44, 122]. Autofocus will iteratively make changes to the data, aiming to minimize entropy-based metrics [135] that correlate with the absence of ghosting artefacts. This approach can be seen as a form of self-registration. Retrospective motion correction is performed if prospective corrections is not possible in a timely fashion or if full non-rigid motion correction (beyond the affine model) is required. The general solution for non-rigid motion correction in MRI is a retrospective method that iteratively corrects the data during the image reconstruction [14]. This method is at the heart of several

works developed in this thesis and will be described further in Chapter 4.

Chapter 3

MR acquisition

The imaging mechanics behind nuclear magnetic resonance (NMR) are discussed in this chapter. A general introduction to the physics of the modality is given, along with a description of signal encoding methods and selected pulse sequences related to the work in this thesis. This chapter is based on content from the books in references [18, 29, 40]. Detailed descriptions of the topics in this chapter can be found therein.

3.1 MR physics

Magnetic Resonance Imaging (MRI) is based on manipulating naturally occurring magnetic fields in the human body. The key physical property exploited in MRI is the intrinsic angular momentum, also known as spin. This momentum generates a measurable magnetic dipole in atomic nuclei with an odd number of elements. For example, the hydrogen nucleus (^1H) is a common target, due to its strong magnetic moment and high abundance in the body in the form of water (H_2O). Three external magnetic fields are involved in the imaging

process: a static magnetic field $\mathbf{B_0}$, a magnetic field rotating at radio frequency $\mathbf{B_1}$ and a set of spatially varying magnetic field gradients $\mathbf{G}$.

3.1.1 Static field $\mathbf{B_0}$

Consider a population of static (i.e. no magnetic field present) ^1H with an isotropic spatial distribution of magnetic moments. In this natural configuration, the magnetic moments average out to zero and the macroscopic magnetization is null (Figure 3.1a). However, in the presence of an external static magnetic field $\mathbf{B_0}$ spins will align with this magnetic field, either in a parallel (up) or anti-parallel (down) orientation (Figure 3.1b).

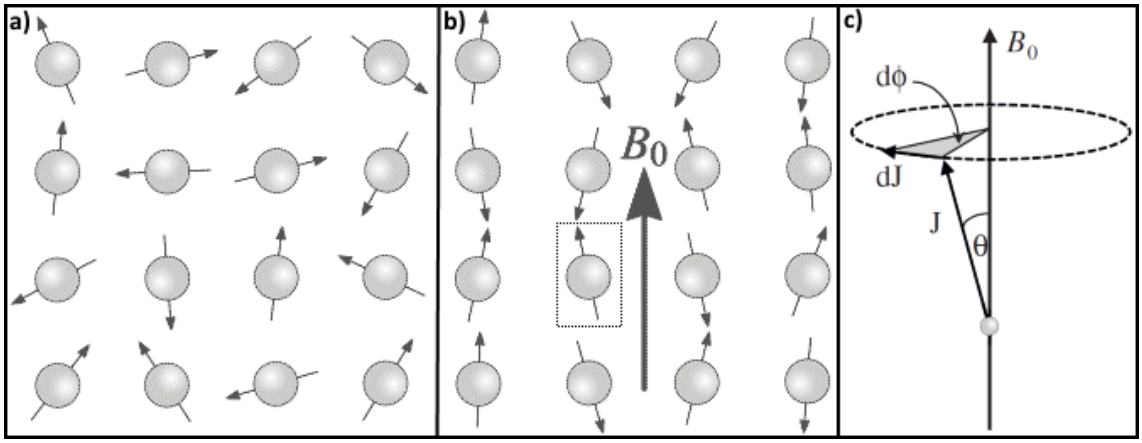

Figure 3.1: **a)** An ensemble of spins with magnetic moments in random orientations with no external magnetic field present. **b)** The same set of spins aligns into parallel and anti-parallel directions of the external magnetic field $\mathbf{B_0}$. **c)** Diagram of the classical mechanics of the precession for the selected spin in **b).** Adapted from [170] .

In this arrangement, a spin with magnetic moment $\boldsymbol{\mu} = \gamma\mathbf{J}$ will precess about $\mathbf{B_0}$ with angular momentum $\mathbf{J}$. The rate of change of the angular momentum is given by:

$$\left|\frac{d\mathbf{J}}{dt}\right| = \gamma \left|\mathbf{J} \times \mathbf{B_0}\right| = \gamma J B_0 sin\theta \tag{3.1}$$

where γ is the gyromagnetic ratio for a given atomic species. Noting that $d\phi/dJ = Jsin\theta$ (Figure 3.1c) allows the derivation of the Larmor frequency:

$$\boldsymbol{\omega}_0 = \frac{d\phi}{d\mathbf{J}} \cdot \frac{d\mathbf{J}}{dt} = \gamma \mathbf{B}_0 \tag{3.2}$$

In the presence of $\mathbf{B_0}$, the ensemble of spins will not be equally distributed between "up" and "down" states. In fact, the number of spins in the up (N_{up}) and down (N_{down}) states will follow a Boltzmann distribution:

$$\frac{N_{\text{up}}}{N_{\text{down}}} = exp(\frac{\Delta\epsilon}{kT}) \tag{3.3}$$

where $\Delta\epsilon$ is the energy difference between the states, k is the Boltzmann constant and T is the temperature of the system. This energy difference can be obtained via De Broglie's wave equation:

$$\Delta\epsilon = \hbar\omega_0 = \gamma\hbar B_0 \tag{3.4}$$

where $\hbar$ is Planck's constant divided by 2π. At body temperature ($\approx$315K) and typical field strengths ($\approx$1.5T) $\gamma\hbar B_0 << kT$ and equa-

tion (3.3) can be approximated by:

$$\frac{N_{\text{up}}}{N_{\text{down}}} = 1 + \frac{\gamma \hbar B_0}{kT} \tag{3.5}$$

Using the values above, this fraction corresponds to approximately 5 parts per million (ppm), meaning that for every million spins in the "down" state there will be additional 5 spins in the "up" state. Since the magnetic contributions of all other spins will cancel out, the only measurable net magnetization $\mathbf{M}$ comes from these 5 spins. However, $\mathbf{M}$ will be of the order of μT, which remains undetectable since it will be aligned with the main field $\mathbf{B_0}$.

3.1.2 Rotating field $\mathbf{B_1}$

To measure the net spin magnetization induced by $\mathbf{B_0}$, this magnetization is tipped to the perpendicular plane, using a magnetic field $\mathbf{B_1}$ rotating at the Larmor frequency:

$$\boldsymbol{B}_1(\boldsymbol{t}) = B_1 \; cos\omega_0 t \; \mathbf{x} - B_1 \; sin\omega_0 t \; \mathbf{y} \tag{3.6}$$

Substituting $\mathbf{B} = \mathbf{B_0} + \mathbf{B_1}$ with $\mathbf{B_0} = B_0\mathbf{z}$ in equation (3.1) produces the system of equations:

$$\begin{aligned} dM_x/dt &= \gamma(M_y B_0 + M_z B_1 \; sin\omega_0 t) \\ dM_y/dt &= \gamma(M_z B_1 \; cos\omega_0 t - M_x B_0) \\ dM_z/dt &= \gamma(-M_x B_1 \; sin\omega_0 t - M_y B_1 \; cos\omega_0 t) \end{aligned} \tag{3.7}$$

With the magnetization initially aligned with $\mathbf{B_0}$ (i.e. $\mathbf{M}(0) = M_0\mathbf{z}$) the solution for $\mathbf{M}$ can be written as:

$$\begin{aligned} M_x(t) &= M_0\ sin\omega_1 t\ sin\omega_0 t \\ M_y(t) &= M_0\ sin\omega_1 t\ cos\omega_0 t \\ M_z(t) &= M_0\ cos\omega_1 t \end{aligned} \tag{3.8}$$

with $\omega_1 = \gamma B_1$. The trajectory parametrized by equation (3.8) is depicted in Figure 3.2a. The magnetization is continuously tipped from the $\mathbf{z}$ direction to the transverse plane, which is easily seen in the frame of reference of the rotating field $\mathbf{B_1}$ (Figure 3.2b). At B_0 values of 1-10 T, ω_0 will be of the order of MHz, a radio frequency (RF) in the electromagnetic spectrum. Thus, these short-lived B_1 fields are also referred as RF pulses. A 90° RF pulse will completely tip the magnetization onto the $\mathbf{x}-\mathbf{y}$ plane, although arbitrary flip angles $\alpha = \omega_1 t$ can also be used.

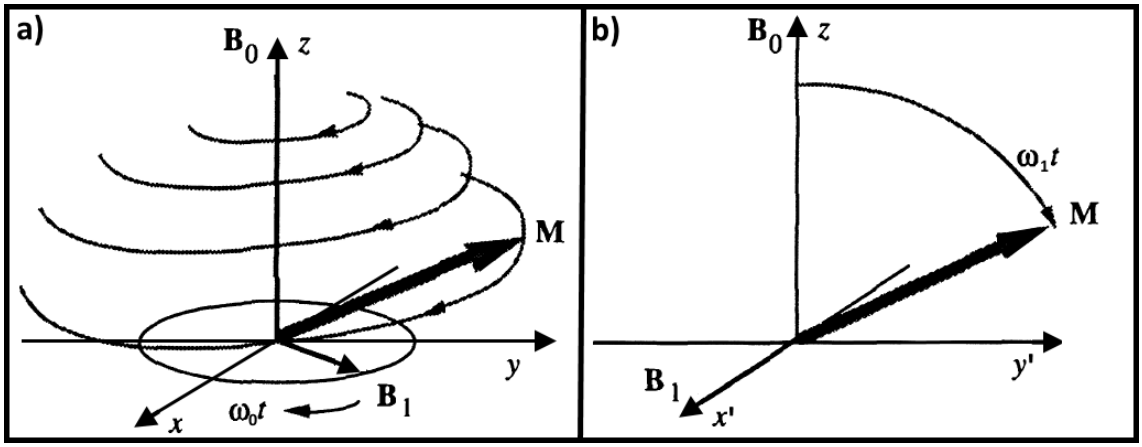

Figure 3.2: **a)** A $\mathbf{B_1}$ field rotating at the Larmor frequency in the transverse ($\mathbf{x}-\mathbf{y}$) plane to $\mathbf{B_0}$ will cause the magnetization to spiral down into the transverse plane. **b)** The same effect seen from the rotating frame of $\mathbf{B_1}$. After time t the magnetization $\mathbf{M}$ will tip towards $\mathbf{y'}$ by an angle $\alpha = \omega_1 t$.

At this point there exists a detectable magnetization which is proportional to M_0. However, this magnetization is not permanently locked in a coherent state in the transverse plane.

3.1.3 Signal relaxation

The (RF) pulse acts as a perturbation on a system of spins that relaxes back to equilibrium once the pulse has terminated. Two independent mechanisms are responsible for this process: spin-lattice relaxation and spin-spin relaxation. Spin-lattice relaxation accounts for the energy exchange between the excited spins and their surroundings (the lattice), which is in equilibrium. This mechanism describes the recovery of M_z:

$$M_z(t) = M_0(1 - exp(-t/T_1)) \tag{3.9}$$

where, T_1 is the time it takes the M_z to reach approximately 63% of M_0 (Figure 3.3a). T_1 values for most tissues of interest are in the range of [100,2000] ms. Spin-spin relaxation accounts for the energy exchange between each other which causes spins to precess slightly faster or slower. Over time the spins will dephase and the overall measurable transverse magnetization M_{xy} will decrease:

$$M_{xy}(t) = M_0 exp(-t/T_2) \tag{3.10}$$

where T_2 is the time it takes M_{xy} to decay to approximately 37% of its initial value (Figure 3.3b). Most tissues of interest contain T_2 values in the range of [50,500] ms. In practice, inhomogeneities in the magnetic field accelerate spin-spin relaxation into the so called $T_2^* < T_2$. The tissue dependency of T_1 and T_2 forms two of the main sources of contrast in MRI. Spin-lattice relaxation depends on the B_0 field strength, whereas spin-spin relaxation is mostly insensitive.

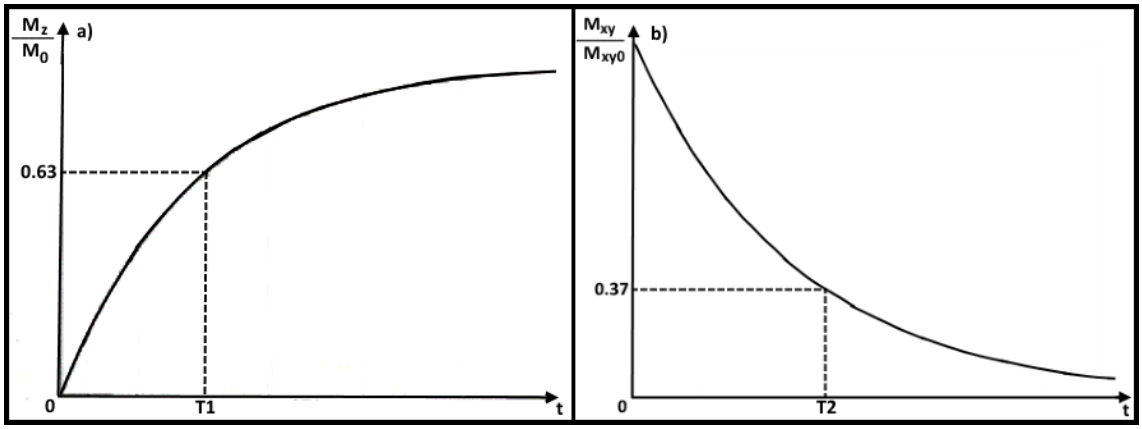

Figure 3.3: **a)** Recovery of M_z magnetization with characteristic time T_1 after a 90° pulse. **b)** Decay of M_{xy} magnetization with characteristic time T_2 after a 90° pulse.

The effects of T_1 and T_2 relaxation can be introduced in equation (3.7) to produce the Bloch equations:

$$\begin{aligned} dM_x/dt &= \gamma(M_y B_0 + M_z B_1 \ sin\omega_0 t) - M_x/T_2 \\ dM_y/dt &= \gamma(M_z B_1 \ cos\omega_0 t - M_x B_0) - M_y/T_2 \\ dM_z/dt &= \gamma(-M_x B_1 \ sin\omega_0 t - M_y B_1 \ cos\omega_0 t) - (M_z - M_0)/T_1 \end{aligned} \tag{3.11}$$

If a 90° RF pulse is applied and then switched off, then $B_1(0) = 0$ and

the solution of equation (3.11) may be written as:

$$\begin{aligned} M_x(t) &= (M_x(0)\ cos\omega_0 t + M_y(0)\ sin\omega_0 t)exp(-t/T_2) \\ M_y(t) &= (M_y(0)\ cos\omega_0 t - M_x(0)\ sin\omega_0 t)exp(-t/T_2) \\ M_z(t) &= M_z(0)\ exp(-t/T_1) + M_0[1 - exp(-t/T_1)] \end{aligned} \tag{3.12}$$

In $\mathbf{B_1}'s$ rotating frame of reference $M_x(0) = M_z(0) = 0$ and $M_y(0) = M_0$, allowing the result in (3.12) to be simplified:

$$\begin{aligned} M_{xy}(t) &= M_0\ exp(i\omega_0 t)\ exp(-t/T_2) \\ M_z(t) &= M_0[1 - exp(-t/T_1)] \end{aligned} \tag{3.13}$$

The signal from M_{xy} is often known as the free induction decay (FID). According to Faraday's law, this oscillating magnetization M_{xy} will induce a proportional voltage in any nearby receiver coil: $E = -d\Phi/dt$, where Φ is the flux through the coil. By noting that $dM_{xy}/dt = M_{xy}(i\omega_0 t - t/T_2)$ it can be shown that the signal of the entire sample is proportional to:

$$S(t) = \int_V M_0(\mathbf{r})\ exp(-i\omega_0 t)\ exp(-t/T_2)d\mathbf{r} \tag{3.14}$$

where the integral is taken over the entire volume of magnetization.

3.1.4 Spatial gradients G

The $\mathbf{B_0}$ and $\mathbf{B_1}$ fields enable measurements of the magnetization weighted by the properties of the local tissue, however the spatial source of the signal remains unresolved. This issue is addressed with spatial linear magnetic gradients $\mathbf{G}$. The magnetic gradient $\mathbf{G}$ shares the same direction as $\mathbf{B_0}$, but its amplitude varies linearly in space. Consider that the spins are now under the effect of $\mathbf{B}(\mathbf{r},\mathbf{t}) = \mathbf{B_0} + \mathbf{G}(\mathbf{t}) \cdot \mathbf{r}$. Inputting $\mathbf{B}(\mathbf{r},\mathbf{t})$ in equation (3.2) produces a spatially dependent Larmor frequency:

$$\omega(r,t) = \omega_0 + \gamma \mathbf{G}(\mathbf{t}) \cdot \mathbf{r} \tag{3.15}$$

During the application of the spatial gradient, the spins will accrue a spatially dependent phase:

$$\phi(t) = \omega_0 t + \gamma \int_0^t \mathbf{G}(\mathbf{t}') \cdot \mathbf{r} dt' = \omega_0 t + 2\pi \mathbf{k}(\mathbf{t}) \cdot \mathbf{r} \tag{3.16}$$

Demodulating equation (3.14) by ω_0 and neglecting T_2 relaxation produces:

$$S(t) = \int_V M_0(\mathbf{r})\ exp(-2\pi i \mathbf{k}(\mathbf{t}) \cdot \mathbf{r}) d\mathbf{r} \tag{3.17}$$

Note that equation (3.17) represents a Fourier Transformation. Thus,

the signal measured in an MR experiment corresponds to the frequency spectrum of the spatial distribution of the magnetization. In practice the FID signal is rarely used, instead the magnetization further manipulated to produce signal echoes.

3.2 Pulse sequences and pre-pulses

As shown in the section above, various types of magnetic fields ($\mathbf{B_0}$, $\mathbf{B_1}$ and $\mathbf{G}$) are required in an MR experiment. The interaction between fields can be depicted in a so called pulse sequence diagram (Figure 3.4a). Most pulse sequences use three types of spatial gradients: a slice selection gradient ($\mathbf{G_{SS}}$), a phase encoding gradient ($\mathbf{G_{PE}}$) and a frequency encoding gradient ($\mathbf{G_{FE}}$). In Figure 3.4a, these correspond to $\mathbf{G_z}$, $\mathbf{G_y}$ and $\mathbf{G_x}$, respectively.

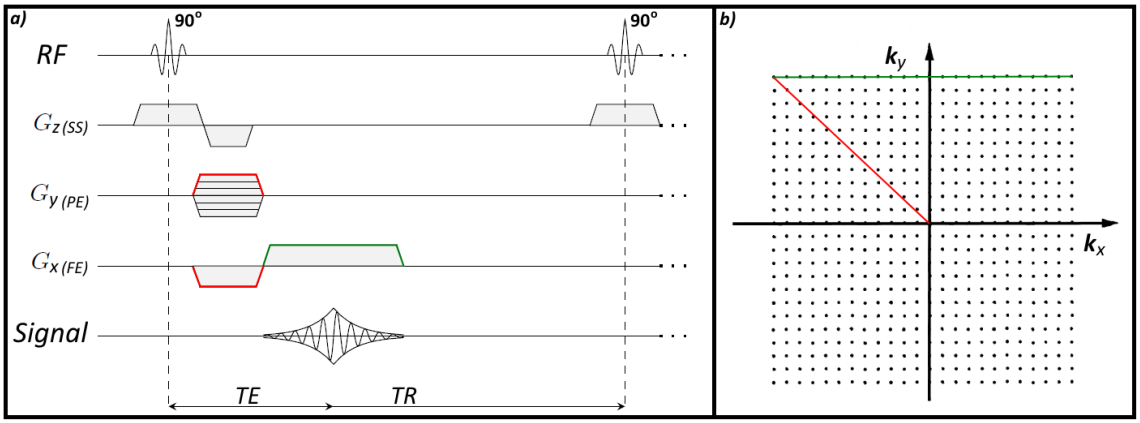

Figure 3.4: **a)** Gradient Echo pulse sequence diagram. **RF**: Rotating $\mathbf{B_1}$ field. $\mathbf{G_z}$: gradient along **z** performing slice selection. $\mathbf{G_y}$: gradient along **y** performing phase encoding. $\mathbf{G_x}$: gradient along **x** performing frequency encoding. **Signal**: Measurable signal produced. TE is the echo time, TR is the repetition time. **b)** Corresponding Cartesian trajectory traversed in k-space by the gradient echo sequence in **a)**. Note that only the points in green are acquired during this TR.

$\mathbf{G_{SS}}$ is used simultaneously with the RF pulse. It can be seen from

equations (3.8) and (3.15) that only the spins in a slab $\Delta_{SS} = \Delta\omega/\gamma G_{SS}$ will be flipped to the transverse plane, where $\Delta\omega$ is the bandwidth of the RF pulse. This approach has the benefit of immediately reducing the spatial encoding to a two-dimensional (2D) problem. Note that while $\mathbf{G_{SS}}$ is active, the spins will experience further de-phasing due to their spatially dependent precession frequency. This effect is refocused by the $\mathbf{G_{SS}}$ negative lobe in Figure 3.4, designed to have a gradient moment of half the previous positive lobe.

Following, the excited 2D slab will experience a second spatial gradient, $\mathbf{G_{PE}}$. According to (3.16) and (3.17), $\mathbf{G_{PE}}$ will create linear relation between phase and spatial location, thus *phase-encoding* the signal. Finally, as the signal is measured, a final $\mathbf{G_{FE}}$ is applied to *frequency-encode* the signal by relating the spins current precession frequency to its spatial location. The $\mathbf{G_{FE}}$ negative lobe pre-winds the phases in order to create an echo at time *TE*. Note that at $t = TE$ the de-phasing effects of all gradients (apart from phase encoding) balance out. It can be easily seen from equation (3.17) that phase and frequency encoding correspond to the same encoding task. The only difference is the timing relative to signal readout; thus phase encoding is essentially a pre-emptive frequency encoding. When the recipe above is played out, a slice-selected, spatially-encoded signal echo is produced at time TE. A time TR after the initial RF pulse, the sequence is repeated multiple times with different $\mathbf{G_{PE}}$ values to

spatially encode the remaining locations in the 2D excited slab.

3.2.1 Gradient Echo

The diagram in Figure 3.4a is an example of a Gradient Echo (GE) sequence, one of two main families of pulse sequences. In Gradient Echo, the echo is formed with bipolar gradients. In Figure 3.4b we can see the corresponding trajectory generated by $\mathbf{G_{PE}}$ and $\mathbf{G_{FE}}$ in the so called "k-space". Note that the vector $\mathbf{k}$ was implicitly defined in equation (3.16) as $\mathbf{k} = \gamma/2\pi \int_0^t \mathbf{G}(\mathbf{t}')dt'$. $\mathbf{k}$ exists in the reciprocal space of the proton density (the "image-space"), the same space where the MR signal data is acquired [40].

The Spoiled Gradient Echo (SGE) is a commonly used GE sequence that uses additional gradients to de-phase (spoil) the transverse magnetization after the readout. An RF pulse with incremental phase (i.e. applied in a slightly different direction than x') can also be used for magnetization spoiling. Repeating the sequence will cause the magnetization to reach a steady-state [18]:

$$M_{xy}^{GE}(\alpha) = M_0 \frac{sin\alpha(1 - exp(-TR/T_1))}{1 - cos\alpha\ exp(-TR/T_1)}\ exp(-TE/T_2^*) \qquad (3.18)$$

The refocusing done by the gradients cannot correct for field inhomogeneities and thus this sequence has a T_2^* contrast. Additionally, the

signal depends on the flip angle α, which can be used to manipulate contrast. The maximum signal obtained at the so called Ernst angle $\alpha' = cos^{-1}(exp(-TR/T_1))$ is:

$$M_{xy}^{GE}(\alpha') = M_0\sqrt{(1-E_1^2)}\; exp(-TE/T_2^*) \tag{3.19}$$

where $E_{1,2} = exp(-TR/T_{1,2})$.

3.2.2 Spin Echo

There is a second type of sequence, known as Spin Echo (SE), where additional RF pulses are used to produce a signal echo. In Spin Echo, a 180° RF pulse is used to flip the magnetization in the transverse plane, effectively reversing the phase. The spins will naturally re-phase, although adequate gradient fields must be used to balance any gradient de-phasing effects prior to the 180° RF pulse. Figure 3.5a shows an example of a Spin Echo sequence. Note the additional de-phasing gradients (known as "crushers" or "spoilers") surrounding the 180° RF pulse used to eliminate potential transverse magnetization created by $\mathbf{B_1}$ inhomogeneities. In this example the phase encoding and frequency encoding are performed by two gradients. This combination of $\mathbf{G_y}$ and $\mathbf{G_x}$ gradients will create a radial trajectory, as can be seen in Figure 3.4b. It can be shown that a 180° RF pulse will convert M_{xy} into M_{xy}^*. Introducing M_{xy}^* in equation (3.17) reveals

that this corresponds to changing $\mathbf{k(t)}$ to $-\mathbf{k(t)}$. This spin echo effect is depicted in the k-space representation of Figure 3.5b in the form of an instantaneous warp through k-space. Gradient Echo sequences are typically faster, although Spin Echo sequences are more robust to magnetic field inhomogeneities.

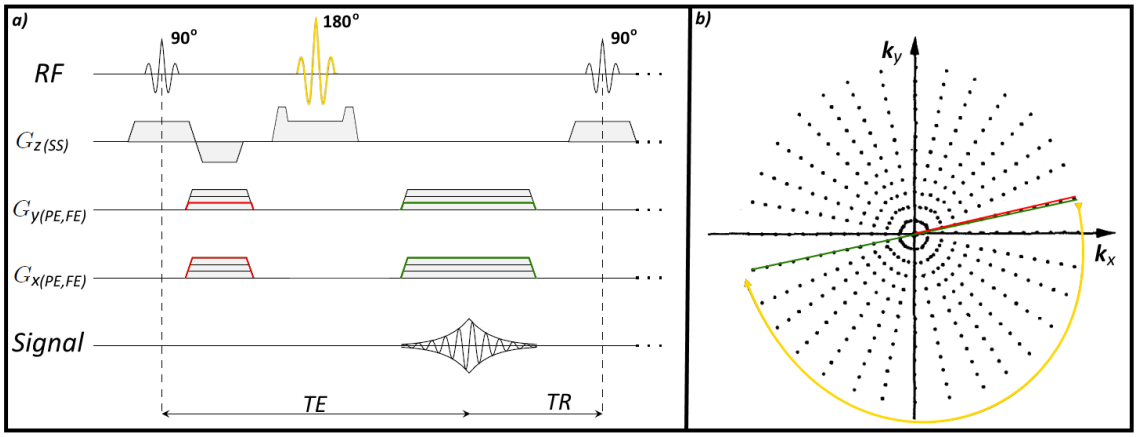

Figure 3.5: **a)** Spin Echo pulse sequence diagram. **RF**: Rotating $\mathbf{B_1}$ field. $\mathbf{G_z}$: gradient along **z** performing slice selection. $\mathbf{G_y}$: gradient along **y** performing frequency and phase encoding. $\mathbf{G_x}$: gradient along **x** performing frequency and phase encoding. **Signal**: Measurable signal produced. TE corresponds to the echo time, TR corresponds to the repetition time. **b)** Corresponding radial trajectory traversed in k-space by the spin echo sequence in **a)**. Note that the trajectory travelled during phase encoding (red) partially overlaps with the one travelled during frequency encoding (green). The 180 °RF pulse moves the **k** vector to its' opposite position in k-space.

Assuming that spoiler gradients are applied after the readout to eliminate transverse magnetization, the signal obtained using 90°and 180°RF pulses is given by [18]:

$$M_{xy}^{SE}(\pi/2) = M_0(1 - E_1(2exp(TE/2T_1) - 1))\ exp(-TE/T_2) \quad (3.20)$$

3.2.3 b-SSFP

Balanced steady state free precession (b-SSFP) sequence shares some traits with GE and SE sequences. The b-SSFP has a high signal-to-noise (SNR) ratio and contrast proportional to T_2/T_1 which provides good muscle/blood contrast. For these reasons, it is commonly used in cardiac MRI. In this sequence, gradients are played out symmetrically about the TE time point. When the b-SSFP is repeated with a $TR << T_{1,2}$ the magnetization will converge to a steady state where excitations from different TRs add constructively at $TE = TR/2$ via so called coherence pathways. The transient state has a typical duration of $5T_1$, however additional $\alpha/2$ RF pulses can be used to catalyse the magnetization onto the steady-state [20]. An example b-SSFP sequence and corresponding k-space travel path is depicted in Figure 3.6.

RF pulses in the b-SSFP typically have alternating signs. This will shift the signal profile by 180° such that "on-resonant" spins will have high signal, which would not be the case otherwise. The signal dependence on phase accrued within each TR is characteristic of the b-SSFP and is at the source of the "banding artifacts" commonly seen with this sequence. The b-SSFP signal using alternated phase RF pulses can be written as [20]:

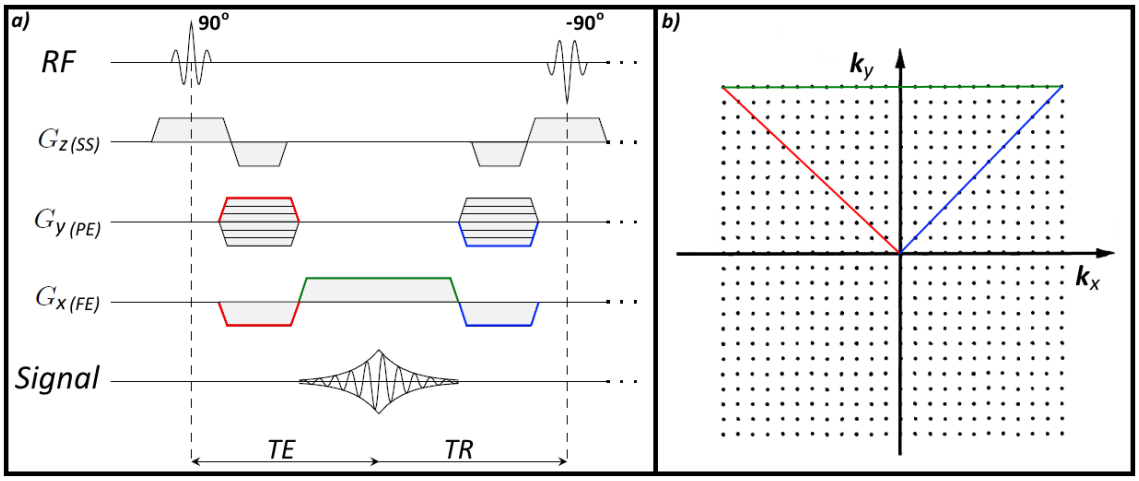

Figure 3.6: **a)** b-SSFP pulse sequence diagram. **RF**: Rotating $\mathbf{B_1}$ field. $\mathbf{G_z}$: gradient along **z** performing slice selection. $\mathbf{G_y}$: gradient along **y** performing phase encoding. $\mathbf{G_x}$: gradient along **x** performing frequency encoding. **Signal**: Measurable signal produced. TE corresponds to the echo time, TR corresponds to the repetition time. Note that all gradient effects are balanced out within each TR. **b)** Corresponding trajectory traversed in k-space starts and ends at the centre of k-space within each TR.

$$M_{xy}^{b-SSFP}(\alpha) = M_0 \frac{(1-E_1)\ sin\alpha}{1-(E_1-E_2)\ cos\alpha - E_1E_2}\ exp(-TE/T_2) \quad (3.21)$$

The optimum flip angle for a given tissue is:

$$\alpha' = cos^{-1}(\frac{E_1-E_2}{1-E_1E_2}) \quad (3.22)$$

which, neglecting the T_2 term, leads to a signal magnitude of:

$$M_{xy}^{b-SSFP}(\alpha') = M_0\sqrt{\frac{1-E_1^2}{1-E_2^2}} \approx \frac{1}{2}M_0\sqrt{\frac{T_2}{T_1}} \quad (3.23)$$

In equation (3.23) we can see that the b-SSFP can produce a steady state signal of 50% of the total magnetization (the highest steady

state signal to date). The T_2/T_1 contrast dependency is also clear in equation (3.20). The contrast in the b-SSFP depends on T_2 instead of T_2^*, even though no refocusing pulses are used. This happens because an RF pulse with arbitrary flip angle α will partially behave like a 180° RF pulse. T_2^* weighting is introduced as the TE deviates from the symmetry point ($TR/2$) [180].

3.2.4 T2-preparation

T_1 and T_2 are the two main mechanisms of contrast in MRI as they present significantly different values for different tissues. One way of manipulating image contrast is to manipulate the weighting of the magnetization. In coronary magnetic resonance angiography (CMRA), the so called $T_2Preparation$ (T_2prep) [28] is commonly used to improve contrast between coronary blood and the myocardium. A T_2Prep is described by the following sequence of RF pulses:

$$90^\circ_x \rightarrow \tau \rightarrow 180^\circ_y \rightarrow \tau \rightarrow 90^\circ_{-x} \tag{3.24}$$

where τ corresponds to the time elapsed between pulses. This pulse sequence tips the magnetization to the transverse plane (90°_x), using a refocusing pulse (180°_y) to create a Spin Echo at time 2τ. At this point in time, the magnetization with a weighting of $exp(-2\tau/T_2)$ will be tipped back onto the longitudinal axis (90°_{-x}). Thus, any MR experi-

ment done at this point will measure a magnetization with additional T_2 contrast. The T_2prep duration (2τ) can be changed to control the amount of T_2 weighting, with additional refocusing pulses to minimize de-phasing due to inhomogeneities. This pre-pulse typically includes a spoiler gradient after 90°_{-x} to eliminate magnetization that is not returned to the longitudinal axis.

3.2.5 Fat suppression

The presence of ^1H in the body is not limited to water molecules. It is also present in body fat, mostly in the form of triglyceride molecules. Due to the different chemistry, water and fat protons will experience different amounts of electromagnetic shielding from their electrons. This shield reduces the effective B_0 experienced by the molecule, which will reduce the precession frequency by a proportional amount (equation (3.2)). For a simplified fat model, this so called chemical shift corresponds to 3.3 ppm [60], which amounts to a 210 Hz and 420 Hz lower frequency, for $B_0 = 1.5T$ and $B_0 = 3T$, respectively. Frequency-encoded fat protons will be spatially displaced after reconstruction due to resonating at a slightly different frequency than water protons. Additionally, fat tissue features small T_1 values which gives fat very high signal in many sequence types. In the presence of motion, strong fat ghosts appear. All these effects create image artefacts that conceal the anatomy and deteriorate the diagnostic value of the image. For

these reasons, several MR scans feature some form of fat suppression. The low T_1 can be used for fat suppression using a so called Short Tau Inversion Recovery (STIR) [36]. STIR uses a 180° RF pulse to tip the magnetization onto $-\mathbf{z}$, where it will experience T_1 decay:

$$M_z(t) = M_0(1 - 2exp(-t/T_1)) \tag{3.25}$$

Thus, an imaging sequence starting at the inversion time $TI = T_1^{fat} ln(2)$ will have zero fat signal. An alternative approach known as FatSat [80] uses the resonance frequency offset (i.e., the difference between water and fat resonant frequencies) to saturate fat signal. This is achieved by applying a 90° RF pulse with a small bandwidth centred around the fat frequency, followed by a spoiler gradient. An imaging sequence starting immediately after will not contain fat signal. This approach is faster than STIR, but also more susceptible to magnetic inhomogeneities. SPectral Inversion Recovery [102] (SPIR) combines these ideas by employing a fat spectrally selective RF pulse in the range of 100-180° , followed by transversal crusher gradients. Due to (unavoidable) imperfections in the RF pulse, a fraction of the magnetization will experience a 180° pulse and relax into the transversal plane by the time the imaging excitation pulse is applied. A fraction of the magnetization will experience a 90° pulse, which gets de-phased by crushing. Finally, some magnetization will experience a 0° RF pulse and the associated fat signal will be present at the time of acquisition.

3.2.6 Water-Fat separation

Despite the potential to introduce image artefacts, fat information can be useful in some cases. For example, fat imaging has shown diagnostic potential in liver cancer [195] and cardiac fat infiltration [35]. It is possible to achieve fat suppression without sacrificing fat information using so called Water-Fat separation techniques.

Dixon [56] proposed one of the first Water-Fat separation techniques. Due to the chemical shift, water and fat spins will precess at different frequencies. At time t, water and fat protons produce the signal:

$$M_{xy}(t) = M_{xy}^{water} + M_{xy}^{fat} exp(i\omega_{\Delta} t) \tag{3.26}$$

where ω_{Δ} is the difference in resonance frequency. Acquiring two images at TEs where the fat has de-phased by $n2\pi$ and $n2\pi + \pi$ will generate two images where the water and fat are in-phase (IP) and out-of-phase (OP), respectively:

$$\begin{aligned} IP &= M_{xy}^{water} + M_{xy}^{fat} \\ OP &= M_{xy}^{water} - M_{xy}^{fat} \end{aligned} \tag{3.27}$$

The water and fat images follow immediately from addition and subtraction of IP and OP:

$$\begin{aligned} 2M_{xy}^{water} &= IP + OP \\ 2M_{xy}^{fat} &= IP - OP \end{aligned} \tag{3.28}$$

The above, so called Two-Point Dixon, does not account for B_0 inhomogeneities and tissue susceptibilities. This can be addressed by introducing a spatially dependent off-resonance term (ω_{off} in the signal model $M_{xy}(t) = (M_{xy}^{water} + M_{xy}^{fat}\ exp(i\omega_{\Delta}t))\ exp(i\omega_{off})\ t$. A common solution to solve for this additional variable is to acquire the signal at three echo times, known as the Three-Point Dixon [108]. Note that the Dixon method does not require magnetization to be exactly in and out of phase.

Chapter 4

MR reconstruction

This chapter describes how to obtain an image of the object from the signal acquired during an MR experiment, a process known as *image reconstruction*. The chapter introduces reconstruction fundamentals, a description of reconstruction as an inverse problem and some advanced reconstruction methods available in MR. The treatment below assumes the reconstruction of an isotropic volume (for simplicity), but it is valid in the general case. Additional information on the topics covered in this chapter may be found in [8, 82, 119].

4.1 MR Reconstruction fundamentals

MR reconstruction, i.e. the process of reproducing an object from a signal obtained in an MR experiment, is not a straightforward operation. Some choices for the acquisition must be made, which fundamentally determine image characteristics such as the field-of-view or

the resolution.

4.1.1 Cartesian sampling

As shown in Chapter 3, the MR signal equation (2.17) corresponds to the Fourier transform of the magnetization:

$$S(\mathbf{k}) = \int_V M_0(\mathbf{r})\ exp(-2\pi i \mathbf{k}\cdot\mathbf{r}) d\mathbf{r} = \mathfrak{F}\{M_0(\mathbf{r})\} \tag{4.1}$$

where $M_0(\mathbf{r})$ is the magnetization at point $\mathbf{r}$ in space, and $\mathbf{k}$ is a vector position in the Fourier space of the image. The magnetization, henceforth referred as the *image*, can be reconstructed via the inverse Fourier transform $M_0(\mathbf{r}) = \mathfrak{F}^{-1}\{S(\mathbf{k})\}$. Usually, this can be efficiently done with the popular Fast Fourier Transform (FFT) [48]. However, there is a practical limitation in that equation (4.1) implies a continuous (and infinite) sampling of k-space. In order to achieve reasonable scan times, a discrete and finite number of samples is acquired. The sampling process can be expressed as a multiplication with a Dirac comb function III(k):

$$S(\mathbf{k_n}) = S(\mathbf{k})\ \mathrm{III} = S(\mathbf{k}) \sum_{n=-\infty}^{+\infty} \delta(\mathbf{k} - n\boldsymbol{\Delta}_\mathbf{k}) \tag{4.2}$$

where $\boldsymbol{\Delta}_\mathbf{k}$ is the spacing between samples. Noting that:

$$\mathfrak{F}^{-1}\left\{\sum_{n=-\infty}^{+\infty}\delta(\mathbf{k}-n\boldsymbol{\Delta}_{\mathbf{k}})\right\}=\frac{1}{\boldsymbol{\Delta}_{\mathbf{k}}}\sum_{n=-\infty}^{+\infty}\delta(\mathbf{r}-\frac{n}{\boldsymbol{\Delta}_{\mathbf{k}}}) \tag{4.3}$$

and invoking the convolution theorem, it can be shown that the reconstructed image from finite sampling corresponds to:

$$M_0(\mathbf{r_n})=\frac{1}{\boldsymbol{\Delta}_{\mathbf{k}}}\sum_{n=-\infty}^{+\infty}M_0(\mathbf{r}-\frac{n}{\boldsymbol{\Delta}_{\mathbf{k}}}) \tag{4.4}$$

Equation (4.4) indicates that it is possible to reconstruct an image from a finite number of samples, however image information is replicated with periodicity $\boldsymbol{\Delta}_{\mathbf{k}}{}^{-1}$ and scaled by $\boldsymbol{\Delta}_{\mathbf{k}}{}^{-1}$. Let the support of the image be contained inside a given field-of-view (FOV) of $2\mathbf{r_{max}}$. Then, according to equation (4.4), the minimum FOV where replicas do not overlap is:

$$\mathbf{r_{max}}=\frac{1}{2\boldsymbol{\Delta}_{\mathbf{k}}} \tag{4.5}$$

If the equation above is not respected and $\boldsymbol{\Delta}_{\mathbf{k}} > 2\mathbf{r}_{\mathbf{max}}^{-\mathbf{1}}$, then the replicas will overlap. This effect, known as *aliasing*, can cause the reconstructed image to differ significantly from the original object because the signal is *undersampled*. The nature of the aliasing artefacts will depend on the sampling pattern. A structured pattern like the Cartesian example above will create clear replicas of the object, commonly referred as *ghosting*. Generally, the less structured the pattern,

the more incoherent the aliasing artefacts. A signal respecting equation (4.5) is characterized as *fully sampled* and enables an alias-free reconstruction.

Note that equation (4.2) still involves an infinite summation. The number of samples is limited to a range $\mathbf{k_{max}}$ to allow for a feasible acquisition time. Limiting the number of samples is equivalent to multiplying by a rectangular function $\Pi(k)$:

$$S^{\Pi}(\mathbf{k_n}) = S(\mathbf{k}) \sum_{n=-\infty}^{+\infty} \delta(\mathbf{k} - n\mathbf{\Delta_k}) \Pi(\frac{\mathbf{k}}{2\mathbf{k_{max}}}) \tag{4.6}$$

Noting that $\mathfrak{F}^{-1}\{\Pi\} = sinc$, the final reconstruction can be written as:

$$M_0^{\Pi}(\mathbf{r_n}) = \frac{1}{\mathbf{\Delta_k}} \sum_{n=-\infty}^{+\infty} M_0(\mathbf{r} - \frac{n}{\mathbf{\Delta_k}}) * 2\mathbf{k_{max}} sinc(2\mathbf{k_{max}}\ \mathbf{r}) \tag{4.7}$$

Convolution with the *sinc* function leads to the well-known Gibbs artefact in regions of the image with high frequency information. The maximum frequency sampled $\mathbf{k_{max}}$ determines the maximum spatial resolution that can be resolved. Equation (4.7) shows that the reconstruction is interpolated by a *sinc* function. If the spatial resolution ($\mathbf{\Delta r}$) is defined as the effective point spread function of the filter used, then:

$$\mathbf{\Delta r} = \frac{1}{sinc(0)} \int_{-\infty}^{+\infty} sinc(2\mathbf{k_{max}}\ \mathbf{r}) d\mathbf{r} = \frac{1}{2\mathbf{k_{max}}} \tag{4.8}$$

The effects of finite sampling are depicted in Figure 4.1 for an example boxcar function. By comparing M_0 and $M_0^{\Pi}(\mathbf{r_n})$ it can be seen that there are some fundamental limitations when reconstructing an image from a finite and discrete dataset.

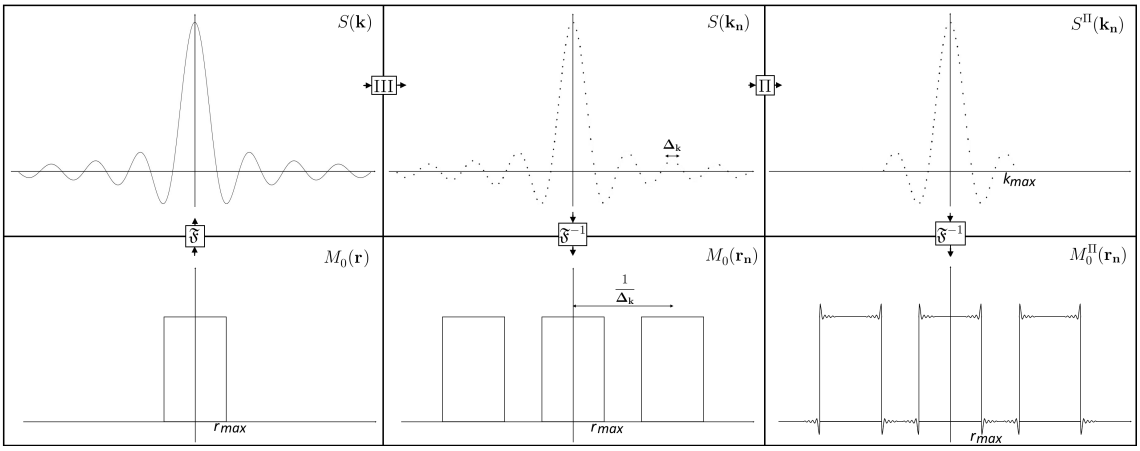

Figure 4.1: Example reconstruction of a boxcar function $M_0(\mathbf{r})$. A feasible acquisition requires that the acquired data $S(\mathbf{k})$ be discretized into $S(\mathbf{k_n})$ and cropped into $S^{\Pi}(\mathbf{k_n})$. These operations are responsible for the image replicas (and aliasing when $\mathbf{\Delta_k} > 2\mathbf{r_{max}^{-1}}$) in $M_0(\mathbf{r_n})$ and Gibbs ringing in $M_0^{\Pi}(\mathbf{r_n})$, respectively.

Equations (4.5) and (4.8) are both instances of the Nyquist-Shannon sampling theorem and impose important sampling constraints. Equation (4.5) shows that the spatial sampling frequency $\mathbf{\Delta_k}^{-1}$ determines the size of the object (FOV) that can be reconstructed, absent aliasing. However, $\mathbf{\Delta_k}^{-1}$ is proportional to the number of samples (which is proportional to the number of phase encoding steps and thus scan time) required for the MR experiment.

Equation (4.8) indicates that the maximum spatial frequency sampled

dictates how well the object can be resolved in image space, i.e. the image resolution. Achieving higher $\mathbf{k_{max}}$ also requires additional phase-encoding steps and hence additional scan time. If $N_{samples} = \frac{2\ \mathbf{k_{max}}}{\mathbf{\Delta k}}$ is defined as the total number of samples acquired in k-space, then a trade-off between FOV and resolution can be established:

$$N_{samples} = \frac{FOV}{\Delta \mathbf{r}} \tag{4.9}$$

4.1.2 Reconstruction as an Inverse Problem

The problem of MR reconstruction can be stated as a linear inverse problem. Using the quadrature rule, the integral in equation (4.1) can be discretized into a finite sum:

$$\int_{-\mathbf{r_{max}}}^{+\mathbf{r_{max}}} M_0(\mathbf{r})\ exp(-2\pi i \mathbf{k}\cdot\mathbf{r}) d\mathbf{r} \approx \sum_{j=1}^{n} M_0(\mathbf{r_j}) exp(-2\pi i \mathbf{k}\cdot\mathbf{r_j}) \mathbf{\Delta r} \tag{4.10}$$

which can be written as a system of linear equations $\mathbf{s} = \mathbf{Fm}$, where $\mathbf{s}$ corresponds to the acquired k-space data, $\mathbf{F}$ is the Fourier operator and $\mathbf{m}$ is the image to be reconstructed. The MR reconstruction then amounts to inverting this system. This is recognized as a linear problem of the type $\mathbf{Ax} = \mathbf{b}$, where $\mathbf{A}$ is some known operator (e.g. Fourier transform), $\mathbf{b}$ is some known vector (e.g. acquired data) and

$\mathbf{x}$ is the unknown vector (e.g. the reconstructed image).

The difficulty of an inverse problem is characterized by the Hadamard conditions. The problem is said to be *well-posed* if it satisfies *solution existence*, *solution uniqueness* and *solution stability*:

- *solution existence*: The operator must be consistent with the data and a solution must exist. This is rarely a problem in MR reconstruction: if the operator is inconsistent, then the problem can be reformulated as a least squares. That is, if $\mathbf{Ax} = \mathbf{b}$ has no solution, then a good approximation for $\mathbf{x}$ can be obtained by solving $min_{\mathbf{x}}||\mathbf{Ax} - \mathbf{b}||_2^2$. This is commonly done to provide a solution in the presence of errors in the operator or noise in the acquired data.

- *solution uniqueness*: If a solution exists, it is the only one. This condition has a significant impact in MR reconstruction. Due to the finite sampling requirements discussed in the previous section, there are many possible images consistent with the acquired data. For example, the set of images $\hat{M}_0(\mathbf{r}) = M_0(\mathbf{r}) + exp(2\pi i \boldsymbol{\Delta}_{\mathbf{k}}\mathbf{r}\ \mathbf{k_{hf}})$ with $\mathbf{k_{hf}} > \mathbf{k_{max}}$ are all feasible reconstructions for $\mathfrak{F}^{-1}\left\{S^{\Pi}(\mathbf{k_n})\right\}$. In practice, this ambiguity is resolved by nulling all $\mathbf{k_{hf}}$, a process known as *zero-filling*. However, if not enough data are acquired (i.e. $\boldsymbol{\Delta}_{\mathbf{k}} \geq 1/2\mathbf{r_{max}}$), then the reconstructed image can differ significantly from the actual object. In this case, the image replicas (equation (4.4) and Figure 4.1) will overlap with the true image,

resulting in *aliasing*.

- *solution stability*: Small perturbations to $\mathbf{b}$ should produce small perturbations to the solution $\mathbf{x}$, i.e., $\mathbf{b} + \mathbf{\Delta b} \approx \mathfrak{F}^{-1}\{\mathbf{x} + \mathbf{\Delta x}\}$. This is not true for the Fourier transformation, which suffers from noise amplification when the data is not fully sampled. Consider $\mathbf{\Delta x} = Asin(2\pi \mathbf{k_{hf}} \mathbf{x})$. According to the Riemman-Lebesque lemma, we have $\lim_{k_{hf} \to \infty} \int_{-\infty}^{+\infty} \mathbf{\Delta x}\, exp(-2\pi i \mathbf{k}.\mathbf{x} d\mathbf{x}) = 0$. This means that high frequency information of arbitrarily high magnitude may be added to $\mathbf{x}$ without producing a measurable difference in $\mathbf{b}$. Conversely, this means that small perturbations in $\mathbf{b}$ (like noise) can produce large perturbations in $\mathbf{x}$ during the reconstruction. *Uniqueness* and *stability* are both closely connected to how well the inverse problem can be solved. *Uniqueness* is violated if there are not enough equations to determine all the unknown variables, meaning the system is underdetermined. *Stability* is violated when these equations contain redundant information, effectively also making the system underdetermined.

According to the description above, MR reconstruction from discrete samples does not satisfy *uniqueness* or *stability*, meaning that a perfect reconstruction is out of reach. However, if appropriate conditions are met (e.g. equations (4.5) and (4.8)) then it is possible to recover an approximation of the true image with negligible differences. Additionally, the *uniqueness* and *stability* conditions can be managed with

the use of additional information, a process known as *regularization.*

4.1.3 Solution of the Inverse Problem

The previous section determined that the problem of MR reconstruction amounts to solving the following linear system:

$$\mathbf{Fm} = \mathbf{s} \tag{4.11}$$

where $\mathbf{m}$ is the (vectorized) unknown image, $\mathbf{F}$ is the acquisition model and $\mathbf{s}$ is the (vectorized) MR signal. In practice, a solution for $\mathbf{m}$ is found by seeking the minimum of the residual $\mathbf{r} = \mathbf{Fm} - \mathbf{s}$ in the least square sense, that is:

$$f(\mathbf{m}) = min_{\mathbf{m}}||\mathbf{Fm} - \mathbf{s}||_2^2 \tag{4.12}$$

The minimum of $f(\mathbf{m})$ is found by setting its derivative to zero:

$$\begin{aligned} &\nabla f(\mathbf{m}) = 0 \\ &\mathbf{m} = (\mathbf{F^H F})^{-1}\mathbf{F^H s} \end{aligned} \tag{4.13}$$

where H denotes the conjugate transpose. Although direct inversion of $(F^H F)^{-1}$ is not always computationally feasible, fast solutions can usually be achieved with iterative methods. A simple iterative solution

is the gradient descent where each step taken is orthogonal to the previous one:

$$\begin{aligned} \mathbf{m^{i+1}} &= \mathbf{m^i} - \alpha \nabla f(\mathbf{m^i}) \\ \nabla f(\mathbf{m}) &= 2\mathbf{F^H}(\mathbf{Fm} - \mathbf{s}) \end{aligned} \tag{4.14}$$

where α is the step size (a function of $\nabla f(\mathbf{m})$) and i denotes the iteration number. Note the practical advantage of this approach: it only requires $\mathbf{F}$ and $\mathbf{F^H}$. Additionally, the matrices $\mathbf{F}$ and $\mathbf{F^H}$ need not be explicitly assembled: the corresponding functions (e.g. FFT for the Cartesian case) are sufficient.

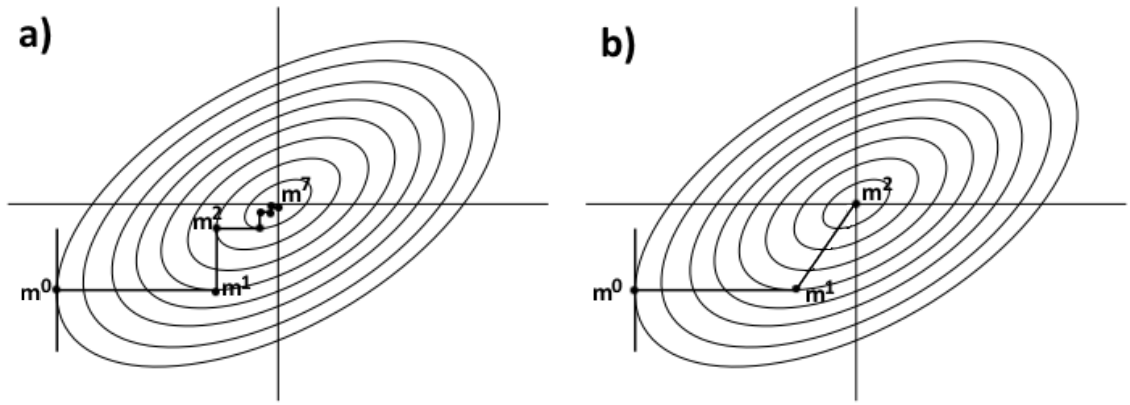

Figure 4.2: **a)** Convergence of the gradient descent. **b)** Convergence of the Conjugate gradient. The contours depict points with the same residual.

The Conjugate Gradient (CG) [89] is a more efficient and commonly used iterative approach for this type of problem. Since the CG method requires that the operator being inverted is symmetric and positive-definite, it is typically applied to the normal equation $(\mathbf{F^H F})\mathbf{m} = \mathbf{F^H s}$. The advantage of CG is that each step in the space of the operator is taken in an orthogonal direction to all previous search directions (Fig-

ure 4.2). This means that convergence is much faster, as no redundant steps are performed. The search directions are an orthonormal basis build on the so-called Krylov subspace:

$$\mathfrak{K}^{\mathrm{i}} = span\left\{F^H s, (F^H F)F^H s, (F^H F)^2 F^H s, ..., (F^H F)^{i-1} F^H s\right\} \tag{4.15}$$

Each iteration of the CG updates the solution along decreasing eigenvalues of $(\mathbf{F^H F})^i$ [83]. Late iterations are associated with small eigenvalues (high frequency information) which are more likely to produce amplified noise in the solution. For this reason, the number of iterations in CG is commonly used to regularize the solution. Alternatively, a stopping criteria can also be enforced based on the l2-norm of the residual, i.e., $||\mathbf{r}^i||_2^2/||\mathbf{r}^0||_2^2 < \epsilon$.

In practice, an MR experiment will always have some amount of noise σ, i.e. $\mathbf{Fm} = \mathbf{s^{true}} + \sigma$, where $\mathbf{s^{true}}$ corresponds to a noise free measurement. Using the Singular Value Decomposition (SVD) of the operator $\mathbf{F}$, it can be shown that:

$$\frac{||\mathbf{m^{true}} - \mathbf{m}||_2}{||\mathbf{m^{true}}||_2} \leq \frac{\tau_{max}}{\tau_{min}} \frac{||\sigma||_2}{||\mathbf{s^{true}}||_2} = C(\mathbf{F}) \frac{||\sigma||_2}{||\mathbf{s^{true}}||_2} \tag{4.16}$$

where τ denotes a singular value of $\mathbf{F}$ and the ratio of the singular values is known as the condition number C. The condition number

is a measure of the *stability* of the problem: the higher the condition number the more ill-conditioned the problem is. When this is the case, additional information can be incorporated into the problem in the form of *regularization*.

4.1.4 Stabilization of the Inverse Problem

There are several strategies available to improve the stability of the inversion and guarantee a successful reconstruction. *Preconditioning* is an approach to solve:

$$\mathbf{M^{-1}}(\mathbf{F^H F})\mathbf{m} = \mathbf{M^{-1}F^H s} \tag{4.17}$$

where $\mathbf{M}$ is an invertible matrix that approximates $\mathbf{F^H F}$. In this case, $\mathbf{M^{-1}}(\mathbf{F^H F}) \approx \mathbf{I}$, leading to $C(\mathbf{M^{-1}}(\mathbf{F^H F})) \ll C(\mathbf{F^H F})$. If $(\mathbf{F^H F})$ is ill-conditioned (which is often the case, since $C(\mathbf{F^H F}) = C^2(\mathbf{F})$), then the rate of convergence can be improved by solving an equivalent problem with a lower condition number [192].

Another stabilization strategy is to *regularize* the inversion with prior information. For instance, it is known that noise will be amplified in the reconstruction. Noise amplification can be suppressed by controlling the norm of the solution image $||m||_2^2$. This is known as Tikhonov regularization and can be formulated as:

$$f(\mathbf{m}) = min_{\mathbf{m}}||\mathbf{Fm} - \mathbf{s}||_2^2 + \lambda^2||\mathbf{m}||_2^2 \tag{4.18}$$

where λ is a scalar that controls the balance between the data consistency term $||\mathbf{Fm} - \mathbf{s}||_2^2$ and the regularization term $||\mathbf{m}||_2^2$. Similar to what was done in equations (4.12) and (4.13) a closed-form solution for this problem is also available:

$$\mathbf{m} = (\mathbf{F^H F} + \lambda^2\mathbf{I})^{-1}\mathbf{F^H s} \tag{4.19}$$

The Tikhonov regularization has the following condition number:

$$C_\lambda(\mathbf{F}) = \frac{\tau_{max}}{\lambda} \tag{4.20}$$

which means that any $\lambda > \tau_{min}$ is associated with an inversion with superior convergence properties. In general, the Tikhonov regularization term can use any linear operation $\mathbf{L}$ in the least squares form of $||\mathbf{Lm}||_2^2$. For example, if a previous estimate of the image $\mathbf{m_0}$ is known, the reconstruction may be regularized via:

$$f(\mathbf{m}) = min_{\mathbf{m}}||\mathbf{Fm} - \mathbf{s}||_2^2 + \lambda^2||\mathbf{m} - \mathbf{m_0}||_2^2 \tag{4.21}$$

An alternative stability strategy, known as sparsity regularization, is to minimize the number of non-zero elements in some transform do-

main of the image. The assumption in this case is that the image has a sparse representation in some domain. This means that the image can be characterized by a small number of non-zero values which implies compressibility. Sparsity regularization can be incorporated into the minimization problem as:

$$f(\mathbf{m}) = min_{\mathbf{m}}||\mathbf{Fm} - \mathbf{s}||_2^2 + \lambda^2||\mathbf{\Psi m}||_0 \tag{4.22}$$

where Ψ is an operator that transforms the image into some sparse domain and $||.||_0$ (L_0-norm) is the pseudo-norm that measures the number of non-zero elements. Unfortunately, minimizing a L_0-norm is a NP-hard problem due to its combinatorial nature, which makes it difficult to solve for practical purposes. However, the solution of L_1-norm (sum of the absolute values) regularized problem is (in general) equivalent to the L_0-norm regularized problem with very high probability [30, 43]. This information can be incorporated into the following optimization problem:

$$f(\mathbf{m}) = min_{\mathbf{m}}||\mathbf{Fm} - \mathbf{s}||_2^2 + \lambda^2||\mathbf{\Psi m}||_1 \tag{4.23}$$

Note that whereas both L_0 and L_1 regularizations promote sparse solutions, this is not necessarily the case for the L_2-norm. Consider a problem of the type $x_1 = Ax_2 + b$, with x_1 and x_2 unknowns. This system is under-determined and therefore has an infinite number of

solutions, depicted in Figure 4.3 (a). Enforcing Tikhonov regularization (L_2) leads to a dense solution because the minimum energy solution is one that attempts to minimize all coefficients (Figure 4.3 (b)). Enforcing L_0 regularization will restrict the solution to the x_1 or x_2 axes. This strategy does enforce a sparse solution on the x_1 axis as shown in Figure 4.3 (c) (and another solution on the x_2 axis not shown), however it is not a practical solution as mentioned above. Enforcing L_1 regularization promotes similar sparse solutions to L_0 as shown in Figure 4.3 (d), with the advantage of being computationally less expensive.

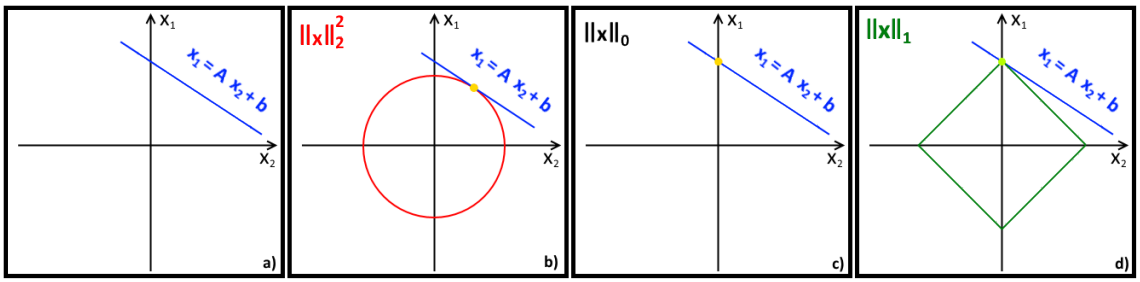

Figure 4.3: **a)** Set of points corresponding to the solution to $x_1 = Ax_2 + b$. **b)** L_2-norm regularization does not promote a sparse solution (yellow point). **c)** L_0-norm regularization promotes a sparse solution (yellow point). L_1-norm regularization also promotes a sparse solution (yellow point).

The solution to equation (4.23) is found by setting $\nabla f(\mathbf{m}) = \mathbf{0}$:

$$(2\mathbf{F^H F m} + \lambda \mathbf{\Psi^H W \Psi})\mathbf{m} = 2\mathbf{F^H s} \tag{4.24}$$

The derivative of $||.||_1$ is not defined at zero. Defining $|m| = \sqrt{m^H m + \epsilon}$, then the diagonal matrix $\mathbf{W}$ has elements:

$$w_i = \sqrt{(\mathbf{\Psi m})_i^H (\mathbf{\Psi m})_i + \epsilon} \tag{4.25}$$

where $0 < \epsilon \ll 1$ and i denotes the diagonal index. Equation (4.24) corresponds to a nonlinear system, since $\mathbf{W}$ depends on $\mathbf{m}$. Non-linear optimization problems can be solved with alternative methods like projection onto convex sets [42] or the nonlinear Conjugate Gradient [52], for instance.

4.2 Advanced reconstructions

This section describes more advanced MR reconstructions pertaining to works in thesis: Non-Cartesian reconstruction is introduced, followed by Parallel Imaging and finally Compressed Sensing reconstructions.

4.2.1 Non-Cartesian Sampling and Reconstruction

The reconstruction formalism presented thus far is based on a Cartesian acquisition. The first MR experiment used in fact a non-Cartesian trajectory [116], at the time known as projection acquisition / projection reconstruction, now referred to as radial. The focus in this section will be on radial trajectories, although the same reconstruction methods for non-uniform fast Fourier transformation (NUFFT) presented here can be applied to spiral or other non-Cartesian trajectories.

Radial trajectories are flow and motion resistant [72], as the sampling pattern generates streaking artifacts instead of coherent replicas of the image. The geometry of the streak artefacts depend on the interaction between the radial sampling pattern and the motion. Depending on the geometry, these streaks can sometimes appear outside the region-of-interest (ROI) of the image. Additionally, the natural oversampling of the central regions of k-space results in signal averaging and a trade-off between aliasing and blurring occurs. Radial trajectories have a fully sampled region in the centre of k-space, even if the entire k-space is not fully sampled (assuming a minimum amount of profiles has been acquired). This is useful, as the fully sampled low frequency data region can be used to estimate coil sensitivity maps for Parallel Imaging [136], phase maps in Partial Fourier [146] or self-navigation [115]. Finally, the radial trajectory allows for a trade-off between resolution and aliasing, as the gap between samples increases with the distance from the k-space centre.

One of the disadvantages of radial trajectories is the need for extra k-space data in a fully sampled acquisition. Consider a radial trajectory, such as the one in Figure 3.5b), where $\Delta\phi$ is the spacing between radial profiles for a 2D k-space. The maximum gap between samples occurs at the edge of k-space, where the Nyquist criterion demands (equation (4.5)):

$$\Delta\phi\ \mathbf{k_{max}} = \frac{1}{2\mathbf{r_{max}}} \tag{4.26}$$

If each spoke covers the range $[-\mathbf{k_{max}}, +\mathbf{k_{max}}]$, then the number of radial samples required:

$$\mathbf{N_r} = \frac{\pi}{\Delta\phi} = 2\mathbf{r_{max}}\mathbf{k_{max}}\pi \tag{4.27}$$

Noting from equations (4.8) and (4.9) that the number of Cartesian samples $\mathbf{N_c} = 4\mathbf{r_{max}}\mathbf{k_{max}}$ it follows that:

$$\mathbf{N_r} = \frac{\pi}{2}\mathbf{N_c} \tag{4.28}$$

meaning that the radial acquisition requires $\approx 57\%$ more profiles than the Cartesian acquisition. On the other hand, the radial trajectory is more robust to undersampling artifacts, as these tend to be more incoherent (i.e. noise-like) and appear mostly on the outer sides of the field of view [181].

Another disadvantage is the need for additional reconstruction steps with considerable computational complexity. The most common reconstruction solution for the non-Cartesian case is to interpolate data onto a Cartesian grid followed by an FFT, a process known as *gridding*. However, a direct interpolation followed by a Fourier transform will cause artifacts, which are managed within the gridding reconstruction

described below.

Let $\mathbf{R}(\mathbf{k}) = \sum_{\mathbf{n}} \delta(\mathbf{k} - \mathbf{k}_{\mathbf{n}}^{\mathbf{nc}})$ denote the locations of the non-Cartesian (**nc**) sampled locations in k-space, such that $\mathbf{S}^{\mathbf{nc}}(\mathbf{k}) = \mathbf{S}(\mathbf{k})\mathbf{R}(\mathbf{k})$ corresponds to the acquired k-space points. The interpolation amounts to a convolution followed by Cartesian sampling, that is:

$$\hat{\mathbf{S}}(\mathbf{k}) = [\mathbf{S}^{\mathbf{nc}}(\mathbf{k}) * \mathbf{C}(\mathbf{k})]\mathbf{III}(\frac{\mathbf{k}}{\mathbf{\Delta k}}) \tag{4.29}$$

where $\mathbf{C}(\mathbf{k})$ is the convolution kernel for the interpolation and **III** is the Cartesian sampling function. However, an FFT applied to $\hat{\mathbf{S}}(\mathbf{k})$ will not produce a good reconstruction. The radial trajectory has more low frequency samples than high frequency samples, which will cause "halo-like" artifacts in the image. This problem is addressed by weighting the samples inversely proportional to their local density in k-space, the so-called *density compensation*. For a general non-Cartesian trajectory, this Density Compensation Function (DCF) can be found using Voronoi diagrams [172] or iteratively refined to find the DCF that has a Dirac delta Point Spread Function (PSF) [163]. In some cases, the DCF can be computed analytically: for example, a 2D radial trajectory has the following density of samples ρ:

$$\rho(\mathbf{k}) = \frac{4N}{\pi \Delta k_r^2} \tag{4.30}$$

where N is the total number of points and Δk_r the distance between samples along the radial direction. The density corrected interpolated k-space is given by:

$$\hat{\mathbf{S}}(\mathbf{k}) = [\mathbf{S^{nc}}(\mathbf{k}) * \frac{\mathbf{C}(\mathbf{k})}{\rho(\mathbf{k})}]\mathbf{III}(\frac{\mathbf{k}}{\mathbf{\Delta k}}) \tag{4.31}$$

A practical problem is that the ideal convolution kernel $\mathbf{C}(\mathbf{k})$ (sinc kernel) is infinite. Naturally, a finite surrogate must be used, however it will cause apodization (signal loss). The problem of finite kernels has been studied and the solution has converged into a Kaiser-Bessel function of the form [92]:

$$K(u) = \frac{\beta}{W}\sqrt{1 - \frac{2u}{W}^2} \;\; with \; u \; \leq W/2 \tag{4.32}$$

where W is the window size and β is a tunable parameter. The Kaiser-Bessel kernel has a good trade-off between residual errors and computational requirements [92] and analytical expressions in both image and k-space domains. Although this kernel will introduce apodization, the effect can be cancelled out by dividing by the Fourier transform of the kernel (deapodization). The reconstructed image is then given by:

$$\hat{\mathbf{M}}(\mathbf{r}) = \mathfrak{F}^{-1}\left\{[\mathbf{S^{nc}}(\mathbf{k}) * \frac{\mathbf{C}(\mathbf{k})}{\rho(\mathbf{k})}]\mathbf{III}(\frac{\mathbf{k}}{\mathbf{\Delta k}})\right\}\frac{\mathbf{1}}{\mathfrak{F}^{-1}\{\mathbf{C}(\mathbf{k})\}} \tag{4.33}$$

This reconstruction however, can still be affected by aliasing. As shown in equations (4.2 - 4.4), convolving k-space data with a Dirac comb function following by a Fourier transformation creates replicas in the image domain. It was also shown in equation (4.5) that there is a minimum FOV that prevents replica overlap and therefore solves the aliasing problem. In the MR experiment additional scan time is required to prevent aliasing, as additional data needs to be acquired. However, in the reconstruction problem the requirement is merely computational. The solution is simply to interpolate into a bigger grid (increasing the sampling density by 2x, for instance), where the replicas no longer overlap with the image and crop the region of interest afterwards. The final non-Cartesian reconstruction will be given by:

$$\hat{\mathbf{M}}(\mathbf{r}) = \mathfrak{F}^{-1}\left\{[\mathbf{S^{nc}}(\mathbf{k}) * \frac{\mathbf{C}(\mathbf{k})}{\rho(\mathbf{k})}]\mathbf{III}(\frac{\alpha\mathbf{k}}{\mathbf{\Delta k}})\right\}\frac{\mathbf{\Pi}(\mathbf{k}/\mathbf{2k_{max}})}{\mathfrak{F}^{-1}\{\mathbf{C}(\mathbf{k})\}} \tag{4.34}$$

where the oversampling factor is given by α and the cropping is done by $\mathbf{\Pi}(\mathbf{k})$.

Shepp-Logan reconstructions with and without the DCF as well as the effect of the oversampled gridding, can be seen in Figure 4.4, showing the necessity of these steps in the non-Cartesian reconstruction. The so-called non-uniform Fast Fourier Transformation (NUFFT) used for non-Cartesian reconstruction has been an active field of research in

recent years [16, 67] and is now readily available for use.

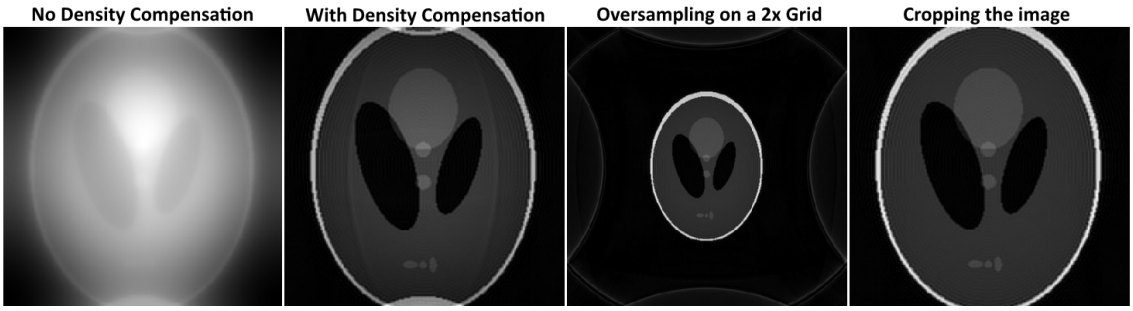

Figure 4.4: Example non-Cartesian reconstruction of a Shepp-Logan phantom with different corrections. Low frequencies are amplified without density compensation and residual aliasing may be visible if no oversampling is performed. Apodization is a more subtle effect not shown here as these images have been deapodized.

4.2.2 Parallel Imaging

In section 4.1.1 it was shown that there is a minimum number of samples required to avoid aliasing (equation (4.5)). If $\mathbf{\Delta_k}$ is too large, then the reconstruction operator will be underdetermined and an alias-free reconstruction is out of reach. This is what happens when the acquisition is accelerated by only acquiring every other line in k-space, for example. If the FOV remains the same, aliasing will be introduced into the reconstruction. An easy way to tackle this problem is to add additional equations to the linear system to resolve these undersampling artefacts.

An MR experiment often uses an array of receiver coils. Parallel Imaging uses the spatial information of these receiver coils to aid image reconstruction. Coils' spatial sensitivity can be incorporated into the signal equation in (4.1):

$$S_j(\mathbf{k}) = \int_V C_j(\mathbf{r}) M_0(\mathbf{r})\ exp(-2\pi i \mathbf{k}.\mathbf{r}) d\mathbf{r} = \mathfrak{F}\{C_j(\mathbf{r}) M_0(\mathbf{r})\} \quad (4.35)$$

where $C_j(\mathbf{r})$ denotes the complex sensitivity for coil j. The corresponding linear system is:

$$\mathbf{AFCm} = \mathbf{s} \quad (4.36)$$

where $\mathbf{A}$ is a logical matrix that determines which k-space samples were acquired, i.e. the sampling pattern, $\mathbf{F}$ is the Fourier operator and $\mathbf{C}$ is a diagonal matrix with the coil sensitivity map. This is a simple formulation of the popular (iterative) SENSitivity Encoding (SENSE) reconstruction [168]. The SENSE encoding matrix $\mathbf{E} = \mathbf{AFC}$ can be easily inverted for simple types of Cartesian sampling. However, this is not true for most sampling patterns with more complex aliasing patterns where an iterative inversion is required. Taking into account the noise correlation between different channels (ψ), the corresponding normal equations may be written as:

$$(\mathbf{C^H F^H A^H} \psi^{-1} \mathbf{AFC})\mathbf{m} = \mathbf{C^H F^H A^H} \psi^{-1} \mathbf{s} \quad (4.37)$$

If the noise levels are negligible, ψ can be approximated as the identity and the image may be reconstructed with the Conjugate Gradient [89].

An example of an iterative SENSE reconstruction is shown in Figure 4.5.

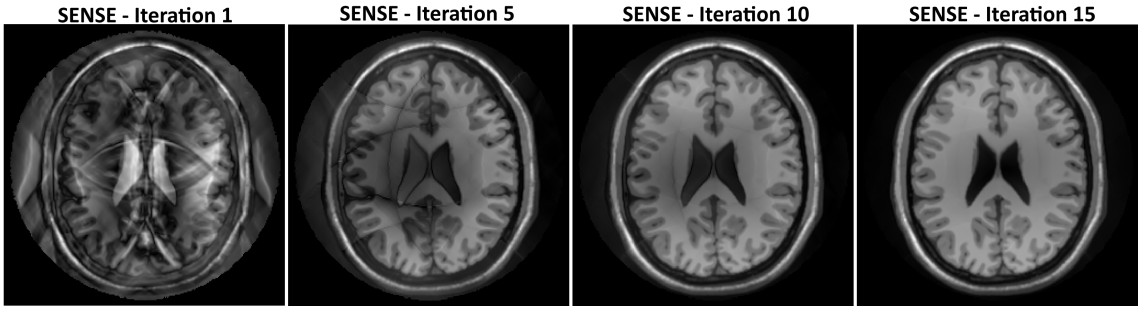

Figure 4.5: Example of an Iterative SENSE reconstruction in different iterations. Note that the first iterations resolve the low-frequency information of the aliasing, the later iterations resolve the higher frequencies. Further iterations could result in noise amplification.

In general, the noise matrix can be removed from equation (4.37) by *pre-whitening*. To do this, a Cholesky decomposition of matrix (ψ) is required:

$$\psi = \mathbf{L}\mathbf{L}^{\mathbf{H}} \tag{4.38}$$

where $\mathbf{L}$ and $\mathbf{L}^{\mathbf{H}}$ are lower triangular and upper triangular matrices. *pre-whitening* amounts to solving the equivalent problem:

$$\mathbf{L}^{-1}\mathbf{AFCm} = \mathbf{L}^{-1}\mathbf{s} \tag{4.39}$$

which we recognize as a form of *preconditioning*. This is equivalent to correcting the coil maps and acquired data:

$$\begin{aligned} \mathbf{C}' &= \mathbf{L}^{-1}\mathbf{C} \\ \mathbf{s}' &= \mathbf{L}^{-1}\mathbf{s} \end{aligned} \tag{4.40}$$

and solving the corresponding system $\mathbf{AFC}'\mathbf{m} = \mathbf{s}'$.

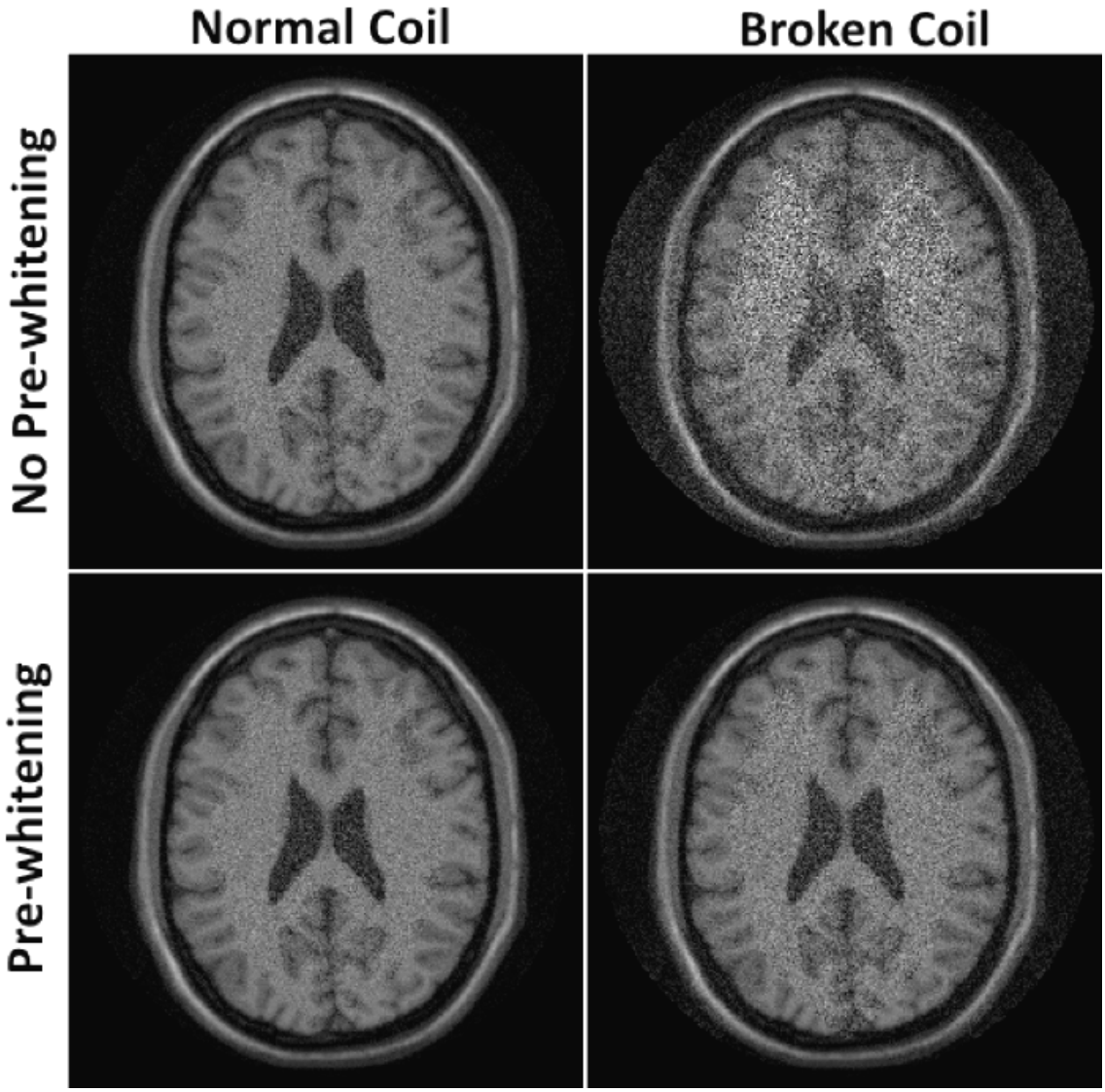

Figure 4.6: Example of a SENSE reconstruction with and without pre-whitening. Severe noise amplification can be seen due to a broken coil. However, pre-whitening regularizes this problem, effectively reducing noise amplification. Taken from [15].

By *pre-whitening*, data is weighted in different channels inversely with their corresponding noise variance. If some channels are very corrupted by noise (due to a broken coil, for instance), then they are

given a lower weight, controlling noise amplification in the reconstruction (Figure 4.6). Additional preconditioning is often enforced in the form of intensity correction. The spatial inhomogeneity of coil sensitivities will cause corresponding intensity variations in the image, which hinders convergence of the reconstruction. This can be accounted for by normalizing the image by the square root sum-of-squares of the coil sensitivities:

$$\mathbf{P} = \frac{\mathbf{1}}{\sqrt{(\sum_{\mathbf{j}} \mathbf{C_j}.\mathbf{C_j^H})}} \tag{4.41}$$

where $\mathbf{C_j}$, corresponds to the sensitivity of the pre-whitened coil j. The final intensity corrected SENSE reconstruction can be written as:

$$(\mathbf{P^H C^H F^H A^H AFCP})\mathbf{m} = \mathbf{P^H C^H F^H A^H s} \tag{4.42}$$

where $\mathbf{s}$ has also been pre-whitened.

In the treatment above it is assumed the coil sensitivity maps are known. In practice, these must estimated during the MR experiment. One approach is to acquire a separate calibration scan [169] that allows the estimation of $\mathbf{C}$. It is also known that coil sensitivities vary slowly in space, meaning that a good estimate can be obtained from low frequency information. Thus, if the centre region of k-space is fully sampled, coil sensitivities may be estimated from the data itself [136, 215].

These strategies avoid potential inconsistencies between pre-scan coil maps and data acquisition. However, enforcing the k-space centre to be acquired imposes constraints on the undersampling patterns of the data acquisition. Additionally, the estimated coil maps are only relative (they are multiplied by an unknown complex function), meaning that the phase information of the reconstructed image may not be preserved. In either case, the noise correlation matrix ψ can be estimated from an MR experiment absent RF excitations [168].

Parallel Imaging has become common practice in clinical MRI, with acceleration factors typically ranging from 2 to 4 times. This section introduced Parallel Imaging through the lens of the SENSE approach. Other popular Parallel Imaging approaches include: SMASH [196], GRAPPA [78] and SPIRiT [126] which enforce the same information in a different formulation. In recent years a popular approach has been introduced that makes use of prior information about the structure of medical images, known as Compressed Sensing.

4.2.3 Compressed Sensing

Compressed Sensing [59] is a technique that explores prior information about MR images to enable faster acquisitions. For instance, Compressed Sensing can break the Nyquist sampling criterion without any Parallel Imaging information. The idea is closely connected to the denoising of sparse signals [43], where, under certain conditions, a signal

can be perfectly recovered from undersampled data.

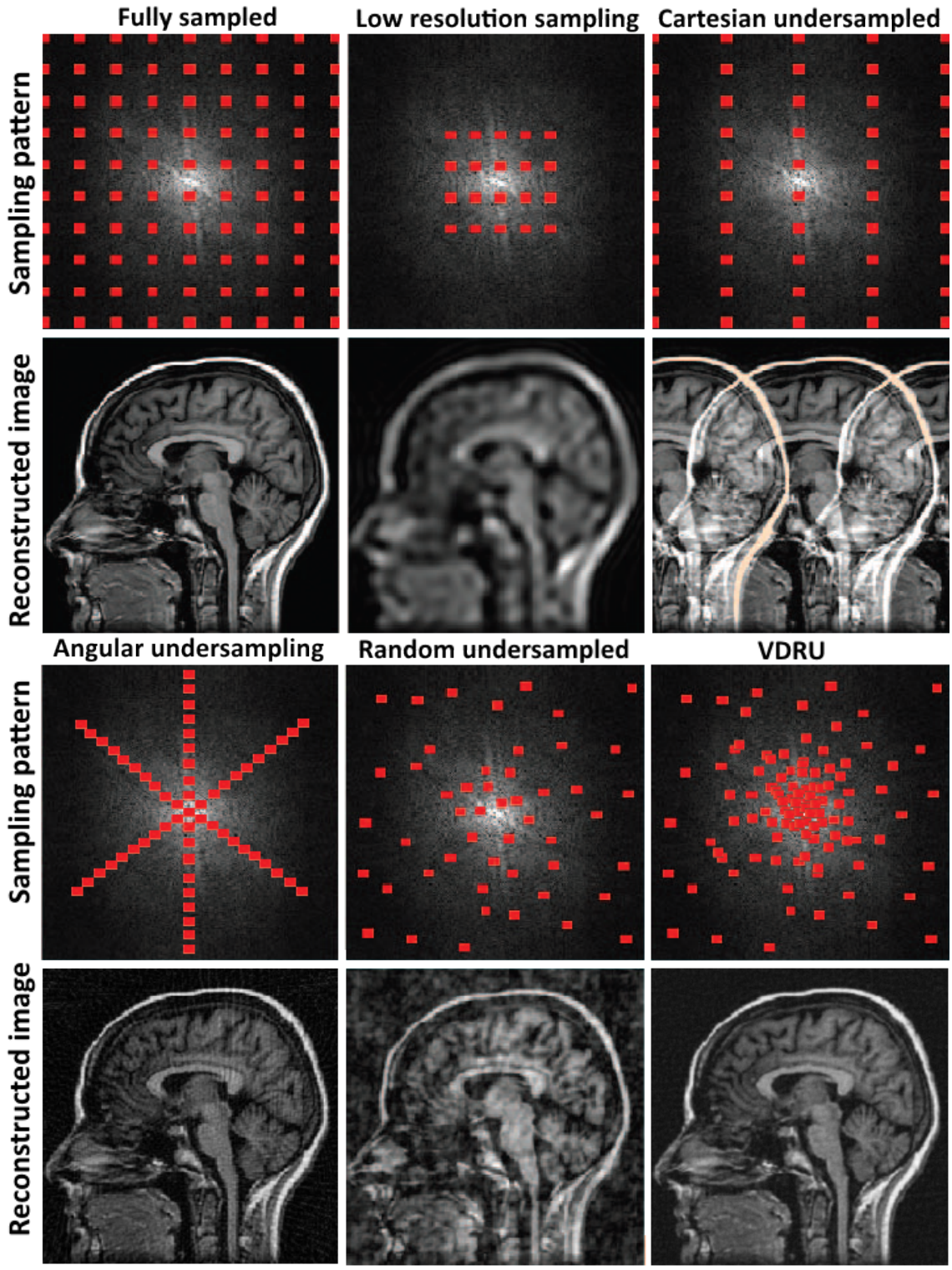

Figure 4.7: Different (schematic) sampling patterns in k-space produce different effects in the reconstructed images. Cartesian undersampling produced image replicas, structured angular undersampling presents more incoherent "streaking" artefacts, random undersampling produces incoherent aliasing with "cloud-like" artefacts, variable density random undersampling (VDRU) produces noise-like aliasing. Adapted from [125].

To make use of Compressed Sensing, the MR undersampling problem must be converted into a denoising problem. In particular, the aliasing resulting from undersampling must display a noise-like behaviour. In practice, noise-like aliasing can be obtained with any trajectory that features a Variable Density Random Undersampling (VDRU) [124], that is, the central regions of k-space should be more densely sampled and the missing points should be randomly distributed.

Different sampling patterns and corresponding reconstructions can be seen in Figure 4.7. Structured patterns like Cartesian undersampling produce coherent artefacts (image replicas), whereas unstructured patterns like random undersampling produce incoherent artefacts. However, note that a noise-like aliasing is only produced with a VDRU patterns. The optimality of VDRU sampling strategies can also be seen using wavelet decomposition [124]: coarse scale (low frequency) components are quite dense, whereas fine scale (high frequency) components are quite sparse (Figure 4.8). Radial trajectories have a natural variable density sampling, therefore incoherent aliasing can be achieved with a pseudo-random angular undersampling, for instance.

The denoising operation is equivalent to L_1-norm minimization, which has been previously discussed as *sparsity regularization* (equation (4.23)). Re-iterating, the Compressed Sensing reconstruction can be written as:

$$\hat{\mathbf{m}} = min_{\mathbf{m}}||\mathbf{Fm} - \mathbf{s}||_2^2 + \lambda^2||\mathbf{\Psi m}||_1 \tag{4.43}$$

where the $\mathbf{\Psi}$ operator transforms the image to some sparse domain.

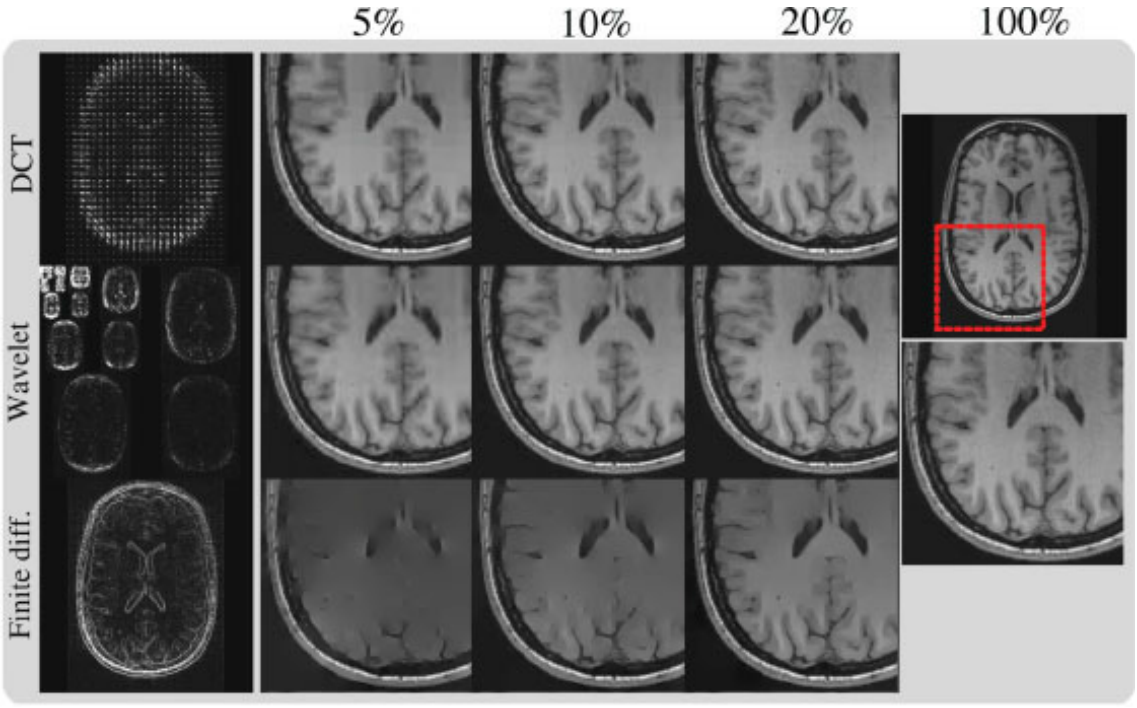

Figure 4.8: Compressed Sensing reconstructions using Discrete Cosine Transform, Wavelet Transform and Finite Differences as sparsifying operators. Reconstructions using 5%, 10%, 20% and 100% of the data are shown. Taken from [124].

For example, angiograms can be considered sparse in their natural domain and thus the identity is an appropriate sparse transformation for that reconstruction. Also recall that equation (4.43) corresponds to a non-linear system and requires a non-linear reconstruction. This non-linear reconstruction is one of the ingredients for Compressed Sensing, the other two being the sparsifying transform and the incoherent sampling.

As mentioned above, incoherent sampling can be obtained by a variety

of trajectories as long as they respect the VDRU requirement. Trajectories like radial [72], variable density spirals [120, 206], G-CASPR [57,166] (Cartesian-Spiral), G-RPE [167] (Cartesian-Radial) or a Variable Density 3D cones (Radial-Spiral), for example, are all capable of producing incoherent undersampling artefacts.

The choice of sparsifying transform is also important. The gradient domain has sparse representations for many types of images. The minimization of the L_1-norm of the gradient is known as Total Variation (**TV**) [210], defined as:

$$\mathbf{TV} = ||\nabla \mathbf{I}||_1 \tag{4.44}$$

where the gradient $\nabla \mathbf{I}$ may be taken over one or more dimensions of the image. Additional sparsifying transforms have also been proposed, such as Wavelets [31], Discrete Cosine [204] and the Temporal Fourier [207] transforms have all been proposed as sparsifying transforms for different applications. Reconstructions using Discrete Cosine Transforms, Wavelets and Finite Differences can be seen in Figure 4.8, demonstrating the high compressibility of a MR brain image. Finally, Dictionaries [39, 63] have also recently been used for the same purpose, creating domains where the image can be represented by a small combination of its elements.

4.3 Motion in MRI

The reconstruction formalism given so far assumes the object being imaged remains static during the MR experiment. When scanning human subjects this is rarely true, due to blood flow, respiratory motion, cardiac motion, peristalsis and bulk body motion, for instance. Intuitively, it is expected that motion will generate a blurring of some sort in the reconstructed image. While this is true, in MRI blurring is commonly accompanied by ghosting artefacts due to inconsistencies in k-space. This section will first introduce a mathematical description of an acquisition corrupted by motion to study the effects of motion in the reconstructed image. The effects of motion on the magnetization (and consequently on the acquired k-space data) are presented, as well as the description of affine motion in k-space. Finally, the model introduced to study motion is used to create a motion corrected reconstruction, capable of correcting for arbitrary motion in MR.

4.3.1 Motion in image space

The effects of motion during the acquisition are often described as *ghosting* and *blurring*. In general, a motion corrupted image can be understood as the superposition of undersampled images in different motion states. The motion corrupted acquisition can be described by the following forward model [14]:

$$\sum_{\mathbf{t}} \mathbf{A_t F U_t m} = \mathbf{s} \tag{4.45}$$

where $\mathbf{A_t}$ denotes the samples acquired at time t and $\mathbf{U_t}$ is the operator that describes the motion that occurred at time t. Fourier transforming both sides of equation (4.45) produces:

$$\begin{aligned} \sum_{\mathbf{t}} \mathbf{F^H A_t F U_t m} &= \mathbf{F^H s} \\ \sum_{\mathbf{t}} \mathbf{m_t} &= \mathbf{m'} \end{aligned} \tag{4.46}$$

where $\mathbf{m_t}$ is the motion warped, undersampled image at time t and $\mathbf{m'}$ corresponds to the motion corrupted image. A naive solution to correct for motion in image space is to invert the motion of $\mathbf{m_t}$ at each point in time:

$$\sum_{\mathbf{t'}} \mathbf{F^H A_{t'} F U_{t'}^{-}} \sum_{\mathbf{t}} \mathbf{m_t} \neq \mathbf{m} \tag{4.47}$$

where $\mathbf{U_t^-}$ applies motion in the opposite direction of $\mathbf{U_t}$. This approach is flawed, as the aliasing in each $\mathbf{m_t}$ will also be warped and is not guaranteed to cancel out. However, it can be shown that the naive solution will work when the aliasing matrix $\mathbf{F^H A_t F}$ and the motion matrix $\mathbf{U_t}$ commute (i.e. motion warping after aliasing is equivalent to aliasing after motion warping). This will be the case if the motion at every aliased location is the same at the location that generates the

aliasing. These matrices will of course also commute if $\mathbf{A_t}$ corresponds to the identity.

4.3.2 Motion in k-space

Motion occurring during the MR experiment can be divided in two groups: motion occurring between phase encoding (PE) steps and motion occurring between RF excitation and readout. The works in this thesis focus on respiratory motion correction, where the latter is approximated as negligible when compared with motion between phase encodes. Thus only motion occurring between PE steps is considered below.

Recall the signal equation given in equation (4.35) for a static magnetization:

$$S_j(\mathbf{k}) = \int_V C_j(\mathbf{r_0}) M_0(\mathbf{r_0})\ exp(-2\pi i \mathbf{k}.\mathbf{r_0}) d\mathbf{r_0} \tag{4.48}$$

where $\mathbf{r_0}$ denotes spatial position at time t_0, constant throughout the acquisition. Under the presence of motion [147], the spatial position of the magnetization can be written as some function of time $\mathbf{r} = f(\mathbf{r_0}, t)$. The coil sensitivities will also be a function of time due to motion of the magnetization. The signal of moving magnetization can be written as:

$$S_j(\mathbf{k},t) = \int_V C_j(f(\mathbf{r_0},t))M_0(f(\mathbf{r_0},t))\ exp(-2\pi i\mathbf{k}.\mathbf{r_0})d\mathbf{r_0} \qquad (4.49)$$

If $f(\mathbf{r_0},t)$ is injective, differentiable, has continuous partial derivatives and a nonzero Jacobian J_f for all $\mathbf{r_0} \in V$ then a substitution between $\mathbf{r}$ and $\mathbf{r_0}$ is applicable. Consider the example where the motion can be described as a translation with constant velocity $\mathbf{v}$, i.e. $f(\mathbf{r_0},t) = \mathbf{r_0} + \mathbf{v}t$. The signal affected by translational motion follows:

$$S_j(\mathbf{k},t) = \int_V C_j(\mathbf{r})M_0(\mathbf{r})\ exp(-2\pi i\mathbf{k}.(\mathbf{r}-\mathbf{v}t))\ |J_f(\mathbf{r_0})|\ d\mathbf{r} \qquad (4.50)$$

For the case of translational motion, $|J_f(\mathbf{r_0})| = 1$. The term $exp(-2\pi i\mathbf{k}.\mathbf{v}t)$ can be extracted from the integral to reveal:

$$\begin{aligned} S_j(\mathbf{k},t) &= exp(-2\pi i\mathbf{k}.\mathbf{v}t)\int_V C_j(\mathbf{r})M_0(\mathbf{r})\ exp(-2\pi i\mathbf{k}.\mathbf{r})\ d\mathbf{r} \\ S_j(\mathbf{k},t) &= exp(-2\pi i\mathbf{k}.\mathbf{v}t)\ S_j(\mathbf{k}) \end{aligned} \qquad (4.51)$$

which is recognized as the Fourier translation theorem. Translational motion in image space will correspond to a phase shift of $exp(-2\pi i\mathbf{k}.\mathbf{r_t})$ in k-space, where $\mathbf{r_t}$ is the position at time t. From the equation above it can be seen that translational motion can create phase discontinuities in k-space. The translation theorem is one of the various known

properties of the Fourier transform: rotations in image space correspond to rotations in k-space, compression (scaling) in image space corresponds to an expansion in k-space (and vice-versa), for example. In fact, there is a complete mathematical description for the effects that affine motion in image space has on the corresponding k-space.

Consider the point $\mathbf{r} = (x, y, z, 1)^T$ in homogeneous coordinates. The 3D affine transformation A_{ff} (which can also be written as a 3x3 matrix) can be written by matrix multiplication of various transformations and an added translation:

$$A_f(\mathbf{r}) = \mathbf{Q}\mathbf{r} + \mathbf{t} = \mathbf{S_{sh}}\mathbf{S_{sc}}\mathbf{R}_\phi\mathbf{R}_\theta\mathbf{R}_\varphi\mathbf{r} + \mathbf{t} = \mathbf{r}' \tag{4.52}$$

where $\mathbf{S_{sh}}$ is the shearing matrix, given by:

$$\mathbf{S_{sh}} = \begin{bmatrix} 1 & h_{xy} & h_{xz} & 0 \\ h_{yx} & 1 & h_{yz} & 0 \\ h_{zx} & h_{zy} & 1 & 0 \\ 0 & 0 & 0 & 1 \end{bmatrix} \tag{4.53}$$

$\mathbf{S_{sc}}$ is the scaling matrix given by:

$$\mathbf{S_{sc}} = \begin{bmatrix} s_x & 0 & 0 & 0 \\ 0 & s_y & 0 & 0 \\ 0 & 0 & s_z & 0 \\ 0 & 0 & 0 & 1 \end{bmatrix} \tag{4.54}$$

the rotations about the 3 different axis $\mathbf{R}_\phi, \mathbf{R}_\theta, \mathbf{R}_\varphi$ are given by:

$$\mathbf{R}_\phi = \begin{bmatrix} 1 & 0 & 0 & 0 \\ 0 & cos(\phi) & -sin(\phi) & 0 \\ 0 & sin(\phi) & cos(\phi) & 0 \\ 0 & 0 & 0 & 1 \end{bmatrix} \tag{4.55}$$

$$\mathbf{R}_\theta = \begin{bmatrix} cos(\theta) & 0 & sin(\theta) & 0 \\ 0 & 1 & 0 & 0 \\ -sin(\theta) & 0 & cos(\theta) & 0 \\ 0 & 0 & 0 & 1 \end{bmatrix} \tag{4.56}$$

$$\mathbf{R}_\varphi = \begin{bmatrix} cos(\varphi) & -sin(\varphi) & 0 & 0 \\ sin(\varphi) & cos(\varphi) & 0 & 0 \\ 0 & 0 & 1 & 0 \\ 0 & 0 & 0 & 1 \end{bmatrix} \tag{4.57}$$

and the translation vector $\mathbf{t}$ is given by:

$$\mathbf{t} = \begin{bmatrix} t_x \\ t_y \\ t_z \\ 1 \end{bmatrix} \tag{4.58}$$

Let $\mathbf{S}'(\mathbf{k}')$ be the Fourier transform of the 3D affine transformed image $\mathbf{M}'_{\mathbf{0}}(\mathbf{r}')$. The relationship between $\mathbf{S}(\mathbf{k})$ and $\mathbf{S}'(\mathbf{k}')$ is given by:

$$\mathbf{S}(\mathbf{k}) = \mathbf{S}'(\mathbf{k}')\frac{exp(2\pi i\mathbf{k}' \cdot \mathbf{t})}{|det(\mathbf{Q})|} \tag{4.59}$$

where $\mathbf{k}' = \mathbf{Q}^{-\mathbf{T}}\mathbf{k}$ and $\mathbf{T}$ denotes the transpose. The equation above is the base for motion correction in k-space. If the motion can be described by an affine model, then it can be compensated by first correcting the k-space and then reconstructing the image. It is worth to note a few points:

- Translational motion does not warp k-space in any way. This gives translational correction a special status (for practical purposes) as it never requires a gridding operation, only a point-wise phase shift.

- The remaining affine matrices have the inverse transpose effect in k-space. This means that k-space will be warped to (potentially) non-Cartesian locations and may require advanced reconstruction

methods. Depending on the sampling strategy and the motion, this could open gaps in k-space (i.e. create unsampled locations).

- The rotation and shear operations are orthogonal with determinant of one, meaning that the intensity normalization depends only on the behaviour of the scaling operation, i.e., $|det(\mathbf{Q})| = |S_x S_y S_z|$.

4.3.3 Motion correction in image-space and k-space

To illustrate motion corruption and motion correction, consider an object that rotates (instantaneously) 90°, halfway (at time t_2) during the acquisition. This problem is depicted in Figure 4.9. For a standard Cartesian undersampling (e.g. the pattern in Figure 4.9(d)), the aliasing and motion matrices will commute if $\mathbf{U_t}(\mathbf{r}) = \mathbf{U_t}(\mathbf{r} + \mathbf{FOV}/\mathbf{R_{us}})$, where $\mathbf{R_{us}}$ contains the undersampling factor for all dimensions. For example, whereas the sampling strategy in Figure 4.9(d) would commute with vertical scaling motion, it would not commute with horizontal scaling motion. Moreover, it does not commute with rotational motion either. Figure 4.9(c) shows the effect of motion on this simulated acquisition. Notably, both blurring and ghosting are visible in the reconstruction shown in Figure 4.9(c). The sampling patterns in Figure 4.9(d) and Figure 4.9(e) produce the aliased views of the object in Figure 4.9(h) and Figure 4.9(i), respectively.

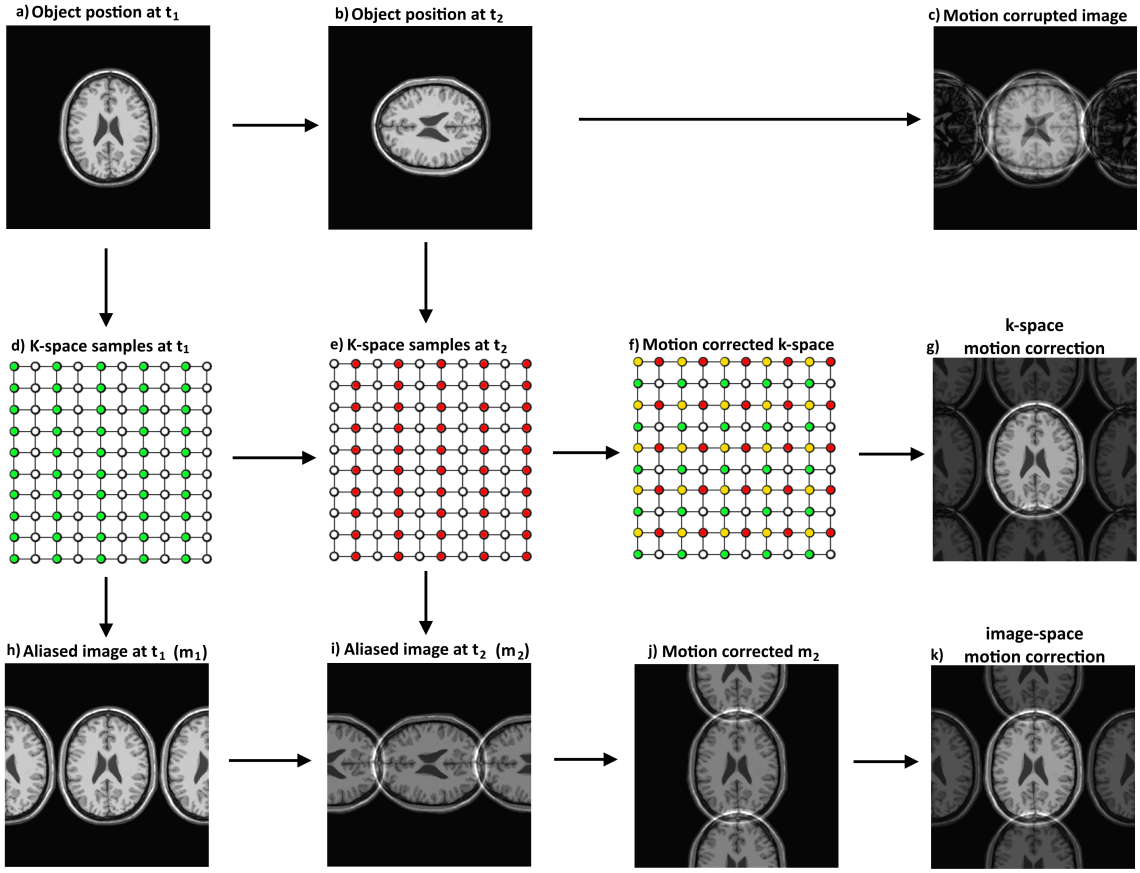

Figure 4.9: **a)** Object motion state during the first half of the acquistion. **b)** Object motion state during the second half of the acquisition. **c)** Reconstructed image contains artifacts due to motion during acquistion. **d)** k-Space samples acquired during the first half of the acquisition. **e)** k-Space samples acquired during the second half of the acquisition. **f)** Motion corrected k-space obtained by rotating the k-space in e). Yellow points correspond to the average of overlapping green and red samples. **g)** k-Space based motion correction, obtained by Fourier transformation of the k-space in f). **h)** Aliased view of the object (m_1) given by Fourier transformation of the k-space in d). **i)** Aliased view of the object (m_2) given by Fourier transformation of the k-space in e). **j)** Motion corrected m_2 obtained by rotation of the image in (i). **i)** Image-space based motion correction, obtained by summing the images in h) and j).

It is clear to see that the motion corrupted image (Figure 4.9(c)) corresponds to the summation of the undersampled images Figure 4.9(h) and Figure 4.9(i). The image-based motion correction shown in Figure 4.9(k) removes some motion artifacts, but some aliasing remains as expected. This correction corresponds to the naive solution in equa-

tion (4.47), which is not guaranteed to work for the general case. Figure 4.9(f) shows the corrected k-space (effective k-space pattern) according to equation (4.59), where yellow locations correspond to the mean value of red and green samples due to overlap. Note that some k-space locations remain undersampled. In general the effective undersampling factor due to motion will be $1 \leq R \leq N_t$, where N_t corresponds to the number of motion states. In this simulation, motion introduces an effective undersampling factor $R \approx 1.33$. This is the source of aliasing present in both Figure 4.9(g) and Figure 4.9(k).

These approaches produce different results because, whereas redundant information can be averaged in k-space (i.e. yellow points), in image space only summation is possible (i.e. yellow samples would be the sum of green and red samples). Despite this advantage, the k-space correction approach is limited to affine corrections as there is no known description of non-rigid motion in k-space.

4.3.4 Motion corrected reconstruction

A general solution to non-rigid motion correction in MRI was introduced by Philip Batchelor in 2005 in the form of the General Matrix Description (GMD) [14]. The key insight of this work is the description of a motion corrupted acquisition as an inverse linear problem, as shown in equation (4.45). Since arbitrary motion in image space can be written as linear transformation matrix, the entire process can be

inverted and the motion-free image recovered. For nearest neighbour interpolation, this motion matrix $\mathbf{U_t}$ will be a permutation matrix. Writing the *ghosting matrix* as $\mathbf{G} = \sum_{\mathbf{t}} \mathbf{A_t F U_t}$, the corresponding normal equation can be written:

$$\mathbf{G^H G m} = \mathbf{G^H s} \tag{4.60}$$

which can be solved with the Conjugate Gradient method. No assumptions are made about the type of motion $\mathbf{U_t}$ or the sampling pattern $\mathbf{A_t}$, hence this method is applicable to any type of motion and any trajectory.

The GMD reconstruction is a more unstable problem than the standard Fourier reconstruction, i.e., $C(\mathbf{G}) \geq C(\mathbf{F})$, as it will typically have less information. There are two reasons for this. If the object leaves the FOV information will be permanently lost, although in practice this is rarely the case. A more common reason for this is that non-translational motion will warp k-space, opening gaps.

This means that during the acquisition, some k-space data will effectively be acquired multiple times, whereas some k-space data will not be acquired (Figure 4.9(f), for example). Thus, the full k-space will be undersampled and the motion corrected reconstruction will contain aliasing. Correspondingly for the problem in Figure 4.9, the GMD will converge to the image in Figure 4.9(g) (before diverging due

to noise amplification). One way to mitigate this problem is simply to acquire more data [147]. A regular (non-motion corrected) reconstruction would simply benefit from increased SNR after averaging the additional data. In the GMD, however, the condition number of the problem will generally improve since the undersampling factor of each shot ($\mathbf{R_t}$) will likely decrease. The effective undersampling factor $\mathbf{R}$ will decrease as well, in addition to improved SNR of some k-space frequencies (consider the case in Figure 4.9 if each shot contained more than 50% of the full data).

Regardless if additional data is acquired, the GMD can be combined with SENSE to further mitigate noise amplification:

$$\sum_{\mathbf{t}} \mathbf{A_t F C U_t m} = \mathbf{s} \tag{4.61}$$

The index $_{\mathbf{c}}$ is explicitly written to remind that there is a summation on the coil dimension in addition to the motion dimension. Thus, the computational complexity of this reconstruction will be proportional to $N_c\ N_t\ \mathcal{O}(FFT)$, where N_c and N_t are number of coil channels and motion states, respectively. A schematic of this encoding operator for a radial sampling strategy is shown in Figure 4.10.

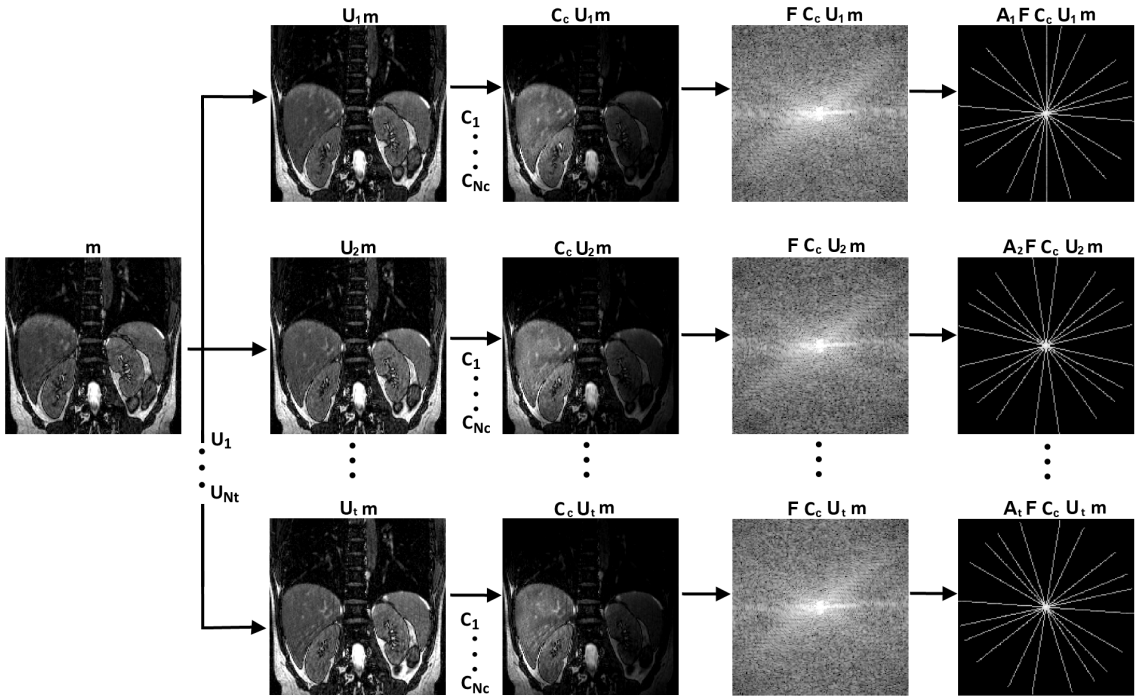

Figure 4.10: Schematic of the encoding operator for a motion corrupted acquisition with multiple coils. During the acquisition, the object $\mathbf{m}$ will be warped to different motion states, becoming $\mathbf{U_t m}$. Each motion state will be weighted by all different coils and have an associated k-space $\mathbf{FCU_t m}$. During the acquisition only a fraction of the k-space will be sampled in a given motion state $\mathbf{A_t FCU_t m}$ and the full motion corrupted data then is given by the sum of these subsets.

A simulation of the example depicted in Figure 4.9 using two coil channels was made and reconstructed with the aforementioned GMD-SENSE reconstruction operator. Results for different iterations of the reconstruction can be seen in Figure 4.11. Note that the final reconstruction is virtually indistinguishable from the ideal (motion free) image, whereas without Parallel Imaging significant alias would remain (Figure 4.9(g)). Normalized root mean square error (NRMSE) was computed (normalized by the mean intensity value of the ideal image) for each image in Figure 4.11. The error decreases with each GMD-SENSE iteration: by the 10th iteration, the error is inferior to

1%.

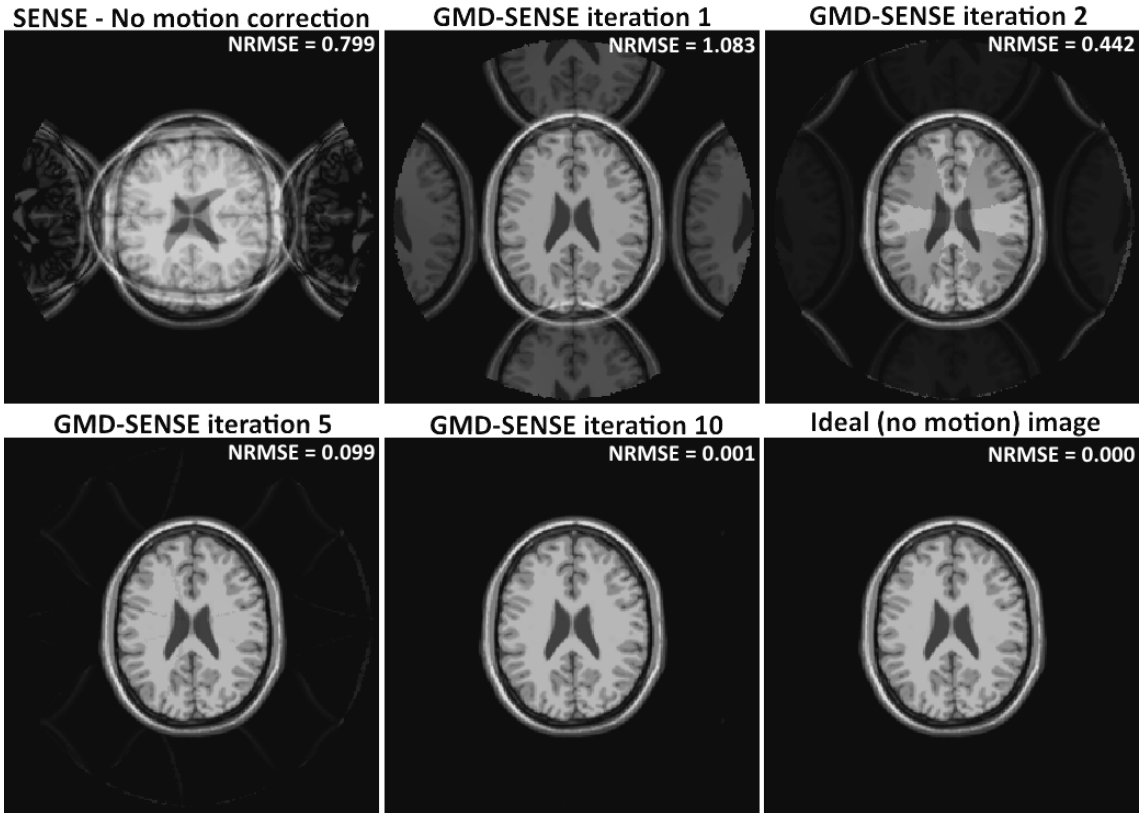

Figure 4.11: GMD-SENSE reconstruction for the example depicted in Figure 4.9 using 2 channels. The GMD-SENSE reconstruction iteratively removes aliasing due to motion, converging to the ideal image. Normalized root mean square error is shown for each image.

Additional information (Parallel Imaging in this case) is required for a successful motion compensated reconstruction even if the k-space is fully sampled. If the acquired k-space is undersampled, then there may not be enough information to guarantee a successful motion corrected reconstruction, even if Parallel Imaging is used. In this case, Compressed Sensing can be incorporated into the previous formalism as:

$$f(\mathbf{m}) = min_{\mathbf{m}}||\sum_{\mathbf{t}} \mathbf{A_t F C U_t m} - \mathbf{s}||_2^2 + \lambda^2||\mathbf{\Psi m}||_1 \tag{4.62}$$

Thus, if the Compressed Sensing conditions are met (namely the incoherent sampling), then it is possible to reconstruct a motion correct image from undersampled data. It is worth to note that the motion corrected reconstruction tends to naturally create incoherent sampling. Due to motion, the effective k-space pattern (Figure 4.9(f)) will be a warped version of the acquired k-space pattern (Figures 4.9(d) and Figure 4.9(e)). Motion effects in k-space are proportional to the distance from the centre, meaning that larger gaps will be created in the high frequency regions of k-space. Thus, with more complex non-rigid motion applied to several motion states, the effective k-space pattern can easily satisfy the VDRU requirement, even if the acquired k-space pattern does not. For affine motion, this effective k-space pattern ($\mathbf{A_{eff}}$) follows immediately from:

$$\mathbf{A_{eff}} = \sum_{t} \mathbf{Q_t^{-T} A_t A_{acq}} \tag{4.63}$$

where $\mathbf{Q_t}$ represents the affine transformation for motion state t, $\mathbf{A_t}$ represents the sampling mask for motion state t and $\mathbf{A_{acq}}$ corresponds to the vectorized acquired k-space sampling mask. For motion beyond affine, the effective k-space pattern can be estimated using the forward model introduced in 4.3.1:

$$\mathbf{A_{eff}} = \sum_t \mathbf{F U_t^H F^H A_t A_{acq}} \tag{4.64}$$

The effective k-space pattern can be used to compute the effective undersampling factor of an acquisition corrupted by motion, which will influence the condition number of the motion corrected reconstruction problem.

The seminal work introduced by Batchelor and colleagues in [14] is the starting point to several works in this thesis. In the following chapters, it will be shown how the GMD can be used to correct respiratory motion in abdominal and cardiac imaging, improving image quality without sacrificing scan efficiency.

Chapter 5

Comparison of non-rigid motion corrected reconstructions for 3D abdominal MRI

5.1 Introduction

Respiratory motion is a major source of artifacts in abdominal imaging, causing ghosting and blurring in the reconstructed image [228] as described in Chapter 2. Breath-hold is commonly employed for 2D imaging, however breath-holding in 3D imaging is difficult without compromising resolution/scan time and therefore a 3D free-breathing acquisition is desired. Free-breathing acquisition is usually performed using respiratory gating techniques [62] using external sensors, navigator echoes or self-gating.

External sensors require additional preparation and provide only a

relative measurement of diaphragm displacement [179]. Navigator echoes do not have these limitations, but can interfere with image acquisition (e.g. disrupting the balanced steady state free precession acquisition [182]). Self-gating techniques [224] extract motion information from the acquired data itself, in general using the central k-space profile. Respiratory gating only accepts data within a small gating window, minimizing motion artifacts at the expense of additional scan time. Moreover, in subjects with highly irregular breathing patterns, drift in respiratory motion can lead to scan termination due to low scan efficiency. Respiratory gating monitors foot-head (FH) translational motion, although it is known that abdominal acquisitions are corrupted by large non-rigid components of motion [112, 175, 197]. Respiratory navigator gating is frequently used to *compensate* for motion. With respiratory gating, only a fraction of the acquired data is accepted for image reconstruction which leads to longer scan times (Figure 5.1(a)). A preferable solution would be to continuously accept data and *correct* for motion during the acquisition (Figure 5.1(b)).

In cardiac imaging several approaches have been proposed for motion compensation. In [68], FH motion is estimated via self-navigation, enabling the estimation of data weighting factors from the distance to a reference respiratory phase. This information is then used in a weighted iterative reconstruction with total variation regularization to reduce respiratory artifacts. More complex 3D affine motion has

been estimated from 3D low resolution image navigators and used to correct the actual acquisition in image space [87]. An alternative approach [154] estimates 3D affine motion from respiratory resolved images and uses it to correct the acquired k-space before reconstructing the image. The work in [166], motion is estimated similarly, but is then corrected directly in the Cartesian reconstruction using the General Matrix Description (GMD) [14]. Additional solutions have been proposed to correct the more complex non-rigid abdominal motion. A pixel-by-pixel translation correction has been used to correct non-rigid motion [44] using local autofocus [9]. This technique requires the acquisition of additional navigator echoes as well as triggering and gating of a portion of the acquired data.

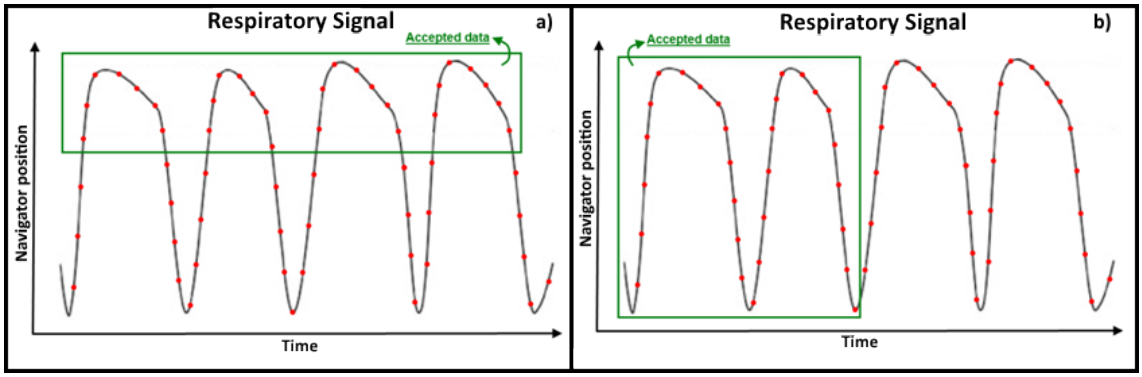

Figure 5.1: **a)** Schematic of acquired data for respiratory gating. Accepted data is limited to a small pre-defined gating window, extending scan time. **b)** Schematic of acquired data for a generic motion correction approach. Motion corrupted data is continuously acquired (quicker scan time) and the data is motion corrected instead.

Recently, a free-breathing motion corrected technique was proposed that estimates 3D non-rigid motion from the data itself. The acquired dataset is grouped onto different positions in the respiratory cycle (so-called *bins*) creating a set of undersampled k-spaces. These

bins are then reconstructed using iterative SENSE [168], to produce a set of respiratory resolved 3D volumes, enabling motion estimation via image registration [34]. This technique, henceforth referred as image-based motion correction (IMC), corrects motion by warping the undersampled bin images to a common respiratory position and averaging different bins [32, 33]. An alternative approach is to use the estimated motion fields to correct the corrupted k-space directly in the reconstruction process, using a general matrix description (GMD) of the acquisition [14]. Both methods use the same information, namely coil sensitivities and motion fields. The IMC approach first uses coil information to reconstruct the undersampled data and then the motion information to combine the reconstructions in image-space. The GMD approach, on the other hand, combines both coil and motion information into one single reconstruction step using the full dataset.

Here I propose to use the GMD approach to correct for motion in free-breathing 3D abdominal MRI using motion estimated from the data itself and compare its performance with the IMC approach. I hypothesize that the IMC approach may present residual aliasing originating from the undersampled bins; additionally, blurring is expected due to the averaging of multiple bins. These effects are not expected in the GMD approach as it operates with lower undersampling factors without data averaging. Five volunteers were scanned and acquired data was reconstructed with the GMD, IMC and respiratory gating

(Gated) methods. These methods are compared using vessel sharpness, liver sharpness, apparent SNR, visual evaluation, scan efficiency and scan time.

5.2 Methods

A common framework for motion estimation (red box in Figure 5.2) is used in order to compare the reconstruction-based (GMD) and image-based (IMC) approaches for motion correction. Estimated motion is used differently in each approach to correct for respiratory motion during the acquisition: the IMC first uses Parallel Imaging to reduce aliasing artefacts in each bin and then combines them by warping and averaging; the GMD combines Parallel Imaging and motion information into one single reconstruction to correct for motion. The framework can be divided in 5 steps: 1) data is acquired with a Golden Radial-Phase Encoding (a Cartesian-Radial hybrid trajectory), enabling flexible reconstructions, 2) the central line of k-space is used to produce a self-navigated respiratory signal and bin data into different respiratory motion states, 3) each undersampled bin is reconstructed independently with non-Cartesian iterative SENSE, 4) non-rigid motion estimation is obtained via image registration of the bins, 5A) the estimated motion is incorporated into the GMD reconstruction, 5B) the estimated motion is used to warped all bins to a common motion state, where they are averaged.

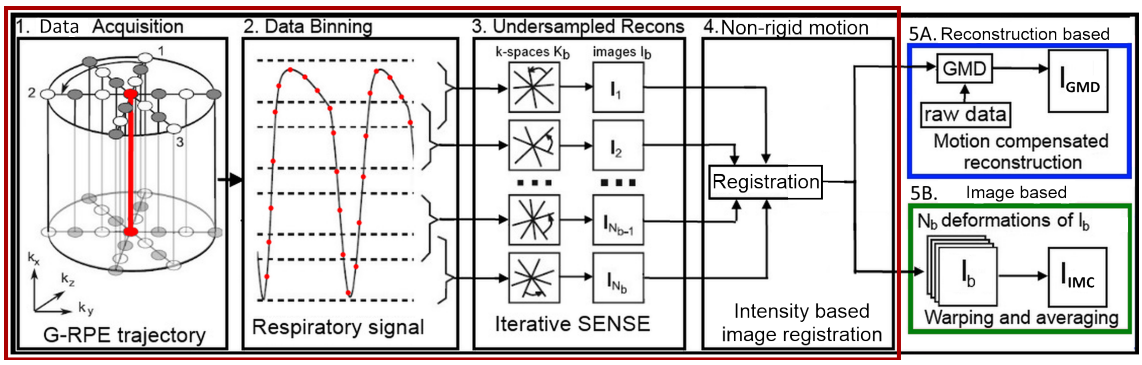

Figure 5.2: Motion estimation framework: **1)** data acquisition with the Golden Radial Phase Encoding (G-RPE) trajectory, **2)** binning data into similar respiratory phases using the self-navigated signal, **3)** reconstructions of undersampled binned data with iterative SENSE, **4)** non-rigid motion estimation via intensity based image registration. **5A)** The motion fields obtained can be used in a reconstruction-based approach (GMD in blue) where motion is corrected during reconstruction or **5B)** in an image-based approach (IMC in green) where bin reconstructions are warped to a common respiratory phase and averaged.

5.2.1 Data acquisition

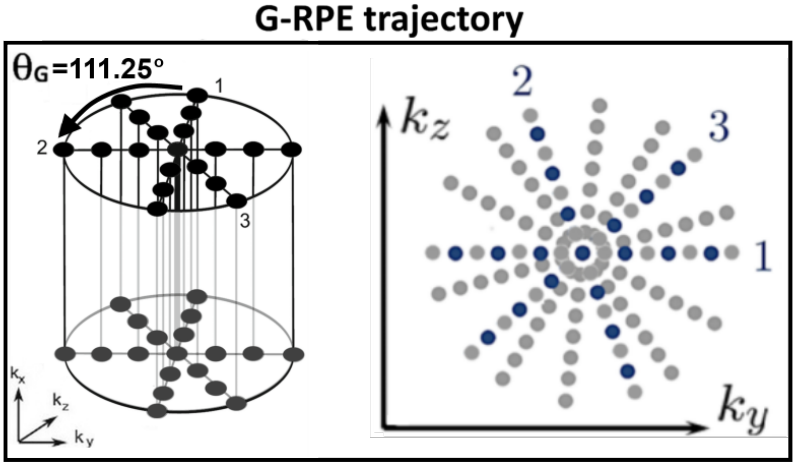

Figure 5.3: Schematic of the G-RPE sampling pattern. **Left:** Sampling pattern obtained by the G-RPE in 3D. The k_x dimension is sampled with a Cartesian readout, while the $k_y - k_z$ is phase encoded along radial spokes. Subsequent spokes are separated by the golden angle $\theta_G = 111.25°$. **Right:** The phase encoding plane $(k_y - k_z)$ can be undersampled along the radial and/or the angular direction, where the blue points correspond to acquired data.

Data is acquired with a Golden Radial Phase Encoding (G-RPE) trajectory [166]. The G-RPE (Figure 5.2.1) combines a Cartesian readout

in k_x with a radial phase encoding order in k_y and k_z. This trajectory has a simple Cartesian readout whilst still benefiting from radial sampling traits like incoherent undersampling artefacts and motion resistance due to repeated sampling of central k-space data. Each radial spoke (numbered in Figure 5.2.1) is acquired with an angular step of 111.25°, guaranteeing a quasi-uniform profile distribution for an arbitrary number of angular profiles. This sampling strategy has the advantage of enabling flexible reconstructions with variable amounts of data. The G-RPE can be undersampled along both radial and angular dimensions as shown in Figure 5.3. The radial sampling enables high acceleration factors otherwise not supported by a standard Cartesian trajectory. Finally, the centre line of k-space (red line) is acquired for every radial spoke. This information can be used for self-navigation, enabling self-gating or binning methods.

5.2.2 Data binning

The set of central k-space lines can be Fourier transformed to provide a set of 1D projections of the entire excited volume through time. An assumption is made that the dominant source of signal variations come from the displacement of the liver-lung boundary. To help guarantee this requirement, only the coil data close to this boundary is used for self-navigation. A respiratory signal is obtained from the set of 1D projections by maximizing the correlation coefficient (CC) between

each projection and a reference projection:

$$CC = \frac{\sum_i (r_i - \bar{r})(p_i - \bar{p})}{\sqrt{\sum_i (r_i - \bar{r})^2 \sum_i (p_i - \bar{p})^2}} \tag{5.1}$$

where r_i and p_i denote the *i-th* pixel in the reference projection r and an arbitrary projection p; the bar ($\bar{}$) denotes the mean value.

The estimated 1D FH respiratory signal (Figure 5.2.2) can be used for respiratory binning. This method has similarities with respiratory gating, but binning separates the data into different groups in the respiratory cycle. The trajectory used (G-RPE) supports variable bin sizes as well as bin overlap due to the golden angle radial strategy. The locations and sizes for the bins were chosen experimentally to balance the bin size and the undersampling factor of each bin.

5.2.3 Undersampled reconstruction

The binning approach divides the acquired data into several independent datasets. Therefore, even if the acquired data is fully sampled the binned data will be undersampled. To minimize undersampling artefacts, each bin is reconstructed using a non-Cartesian iterative SENSE reconstruction [168]. The number of iterations was used as regularization for the reconstruction. This reconstruction step is depicted in Figure 5.2.3: a set of undersampled k-spaces K_b is reconstructed with iterative SENSE to produce the respiratory resolved images I_b.

Reliable motion estimation has been obtained from bins with undersampling factors up to 2x in the radial dimension and 4x in the angular dimension [33]. However, higher undersampling factors may introduce significant aliasing which can compromise the intensity-based image registration and consequently the accuracy of the estimated motion. The non-Cartesian iterative SENSE reconstruction was solved with a Conjugate Gradient algorithm [89].

5.2.4 Non-rigid motion estimation

The set of reconstructed I_b are registered with an intensity-based image registration algorithm [34] to a reference respiratory bin reconstruction (end-exhale). These registrations produce a set of dense non-rigid motion fields, relating each respiratory motion state to the end-exhale motion state.

5.2.5 Reconstruction-based motion correction

Motion can be incorporated into the reconstruction using the formalism introduced in [14]. The forward model for this reconstruction can be written as:

$$\mathbf{K} = \sum_{\mathbf{b}}^{\mathbf{N_b}} \mathbf{A_b F C U_b I_{GMD}} = \mathbf{E I_{GMD}} \tag{5.2}$$

where $\mathbf{I_{GMD}}$ is the reconstructed motion corrected image of matrix size $[N, 1]$, N_b is the number of motion states, $\mathbf{A_b}$ is a diagonal logical matrix of size $[N, N]$ indicating the sampled locations for motion state b, $\mathbf{F}$ is the Fourier transform, $\mathbf{C}$ are the coil sensitivities for all coil channels (matrix size $[N \times N_c, N]$), $\mathbf{U_b}$ is the motion field for motion state b (matrix size $[N, N]$) and $\mathbf{K}$ is the acquired k-space data of matrix size $[N \times N_c, 1]$. N corresponds to the total number of voxels and N_c to the number of coil channels. This is the same formalism introduced in Chapter 4 as SENSE-GMD, which here is simply referred to as GMD. The number of iterations was used as regularization for the GMD reconstruction.

This reconstruction can be reformulated as:

$$\mathbf{E^H}\ \mathbf{K} = (\mathbf{E^H E})\mathbf{I_{GMD}} \tag{5.3}$$

and solved with the Conjugate Gradient method [89], which requires an implementation of the transpose encoding operator:

$$\mathbf{E^H} = \sum_{\mathbf{b}}^{\mathbf{N_b}} \mathbf{U_b^H C^H F^H A_b^H} \tag{5.4}$$

where $\mathbf{H}$ denotes the conjugate transpose. $\mathbf{F^H}$ corresponds to the inverse Fourier transform; $\mathbf{C}$ and $\mathbf{A_b}$ are diagonal matrices, therefore $\mathbf{C^H} = \mathbf{C}^*$ and $\mathbf{A_b^H} = \mathbf{A_b^*}$. In the works in this thesis, the motion ma-

trix is assembled explicitly as a sparse $N \times N$ matrix, enabling fast computation of the motion warp (matrix-vector product of $\mathbf{U_b I}$) and easy access to the transpose motion operator $\mathbf{U_b^H}$.

The form of the motion matrix $\mathbf{U_b}$ will depend on the interpolation scheme used. For nearest neighbour interpolation, $\mathbf{U_b}$ will become a permutation matrix, i.e., the matrix will have only one non-zero entry (with value 1) per row. If more sophisticated interpolation schemes are used, then each row will have several non-zero entries. For instance, if $\mathbf{I_{GMD}}$ is a 2D image and linear interpolation is used, then there will be up to four interpolation weights (w_i^j) per pixel, i.e. up to four non-zero entries per row. An example of such a matrix for this instance is:

$$\mathbf{U_b} = \begin{bmatrix} 0\cdots0 & w_1^1 & w_1^2 & 0\cdots & \cdots0 & w_1^3 & w_1^4 & 0\cdots & \cdots0 \\ 0\cdots & \cdots & \cdots & \cdots0 & w_2^1 & w_2^2 & 0\cdots & \cdots & \cdots0 \\ 0\ 0\ w_3^3 & 0\cdots & \cdots & \cdots & \cdots & \cdots & \cdots & \cdots & \cdots0 \\ \vdots & \ddots & \ddots & \ddots & \ddots & \ddots & \ddots & \ddots & \vdots \\ 0\cdots & \cdots & \cdots & \cdots0 & w_n^1 & w_n^2 & 0\cdots0 & w_n^3 & w_n^4 \end{bmatrix} \tag{5.5}$$

where $w_i^j \in [0,1]\ \forall\ i,j$ and $\sum_j w_i^j = 1\ \forall\ i$. Studying the structure of this matrix reveals some information about the motion of each pixel. The first row of the matrix above indicates that the first pixel was moved to some non-integer location of the Cartesian grid, as four

weights were used. The second pixel was warped to some location exactly between two grid locations (i.e. along a vertical or horizontal line) and therefore only required two interpolation weights. The third pixel was warped to an existing Cartesian grid location and $w_3^3 = 1$. In fact, since w_3^3 occurs in a diagonal entry of the matrix this indicates that the third pixel did not move. The last pixel in the image also has its own location as an interpolation weight (w_n^4), however it is not the only weight in this row. This indicates that the last pixel moved less than one pixel distance.

As mentioned above, explicit construction of $\mathbf{U_b}$ enables efficient computation of the motion warps and provides easy access to $\mathbf{U_b^H}$. However, this implementation can have considerable memory requirements, since N_b matrices of size $[N, N]$ are required for the iterative reconstruction. Fortunately, the memory requirements can be significantly reduced by exploiting the sparse structure of the motion matrices.

5.2.6 Image-based motion correction

The IMC approach uses the motion estimated via registration to warp all bin reconstructions I_b to a common respiratory motion state. The final motion corrected image simply amounts to the average of the warped images:

$$\mathbf{I_{IMC}} = \frac{\sum_{\mathbf{b}}^{\mathbf{N_b}} \mathbf{U_b^- I_b}}{\mathbf{N_b}} \tag{5.6}$$

where $\mathbf{I_{IMC}}$ corresponds to the image-based motion correction, $\mathbf{U_b^-}$ is the inverse motion field (i.e. the motion in the inverse direction, as opposed to the matrix inverse) for motion state b and $\mathbf{I_b}$ are the reconstructed bin images. Elastic motion was estimated as a composition of multiple affine transformations at different scales, using the method in reference [34]. U_b^- was obtained by inversion of the affine transformations, as described in the same paper.

5.3 Experiments

A motion corrupted acquisition was simulated using known a priori motion. The IMC and GMD approaches were used to correct this simulated acquisition to evaluate the hypothesis that the IMC will have residual aliasing. Following, in vivo experiments were performed in five healthy subjects to demonstrate the feasibility of the proposed GMD framework. All iterative reconstructions were solved with a Conjugate Gradient algorithm [89] implemented in MATLAB (The MathWorks, USA). Reconstructions were stopped when the relative residual reached 0.05%. Reconstruction times were approximately, 30 minutes for IMC and 60 minutes for the GMD.

5.3.1 Simulations

One of the in vivo datasets acquired (as described below) was used to simulate a motion corrected image using the GMD and estimated motion fields (describing the non-rigid respiratory motion) as proposed. A coronal slice of this reconstruction was taken as ground-truth (i.e. ideal image without motion) and one estimated motion field was used in the forward model (equation 4.45) to simulate a motion corrupted acquisition with 2 motion states and 4 coil channels. Each coil channel was centred on a different quadrant of the image. A 2D radial trajectory was used for this simulation, similar to the sampling pattern shown on the right side of Figure 5.3. Three different experiments were performed using different undersampling patterns for the whole simulated acquisition: **S1)** 4x radial undersampled, **S2)** 3x radial undersampled and 2x angular undersampled, **S3)** 8x angular undersampled. High undersampling factors were used to highlight the residual aliasing artefacts. Radial undersampling produces more coherent aliasing than angular undersampling, therefore the radial sampling allows us to study how different aliasing patterns and undersampling factors affect the GMD and IMC approaches. Data was divided equally between both motion states along the radial direction: motion state 1 sampled odd points, motion state 2 sampled even points (along the radial direction). The simulated motion corrupted images were reconstructed with no-motion correction (NMC), the reconstruction-based approach

(GMD) using equation (5.2) and the image-based motion correction (IMC) using equation (5.3). IMC and GMD used the ground-truth motion for correction. IMC reconstruction of each motion state was performed using iterative-SENSE with 50 iterations. The GMD reconstruction used 20 iterations.

5.3.2 In vivo experiments

Five volunteers were scanned under free-breathing on a 1.5T Philips scanner using a 32 channel coil. Written informed consent was obtained from all subjects according to institutional guidelines and the study ("Development of novel magnetic resonance techniques using healthy volunteers") was approved by the institutional review board. Data were acquired with a b-SSFP sequence: FOV = 287mm isotropic, resolution = 1.75mm isotropic, TR/TE = 3.0/1.4ms, flip angle = 30, radial undersampling = 2. 820 radial profiles were acquired, corresponding to an oversampling factor of 3.2x in the angular direction. Angular oversampling was used to guarantee that the reconstructed bins I_b (2x radial undersampling, 1.6x angular undersampling on average) had sufficient quality for motion estimation via image registration. However, it incidentally benefits the IMC approach, since it significantly reduces residual bin aliasing propagates to the final image after warping and averaging.

Three reconstructions were performed from the same acquired data: a

5mm self-gated reconstruction (Gated), the image-based IMC and the reconstruction-based GMD. The same number of profiles was used for each of the three reconstructions to allow comparison. 5 bins (2.92±1.00mm) and 723±91 profiles were employed to allow accurate motion estimation. Respiratory outliers (due to deep breaths or errors in self-navigation, for instance) were not binned for either IMC or GMD methods, instead being discarded (2% of the data, on average). Methods were compared using measures of vessel sharpness, liver sharpness and apparent SNR. Vessel sharpness was computed by taking twenty-five 1D profiles along vessels in selected coronary slice and taking the maximum gradient normalized by the maximum intensity of each one, followed by averaging. Liver sharpness was computed in the same way, except the twenty-five 1D profiles were along the lung-liver boundary of a selected coronal slice. Apparent SNR was computed using a region of uniform signal from the liver and a region absent of signal from the lungs, also in a selected coronal slice. Visual scoring of image blurring on a scale from 0 (extreme blurring) to 4 (no blurring) by 6 experts blinded to the method used was also performed. Statistical significance of the automated metrics (liver sharpness, vessel sharpness, and apparent SNR) was evaluated with a two-sided paired t-test (P-value ¡ 0.05); statistical significance of the visual scoring was performed with a Wilcoxon signed rank test (P-value ¡ 0.05).

5.4 Results

5.4.1 Simulations

Results for simulations **S1** using 4x radial undersampling, **S2** using 3x radial undersampling and 2x angular undersampling and **S3** using 8x angular undersampling are shown in Figures 5.4, 5.5 and 5.6, respectively. In each case, the non-motion corrected (NMC) image is shown, as well as intermediate iterations in both the GMD and IMC approaches.

Different types of motion artefacts appear in the NMC images according to the sampling pattern used. In all experiments the IMC successfully removed motion induced blurring. Remaining artefacts were removed with various degrees of success.

S1 has the highest radial undersampling and therefore the highest coherent aliasing. Significant aliasing is present in the independent reconstruction of each motion state (I_1 and I_2) which fails to cancel out with the IMC approach. This is the origin of the significant aliasing artefacts present in the IMC image of Figure 5.4.

S2 (Figure 5.5) features a less aggressive radial undersampling; correspondingly the residual aliasing in each motion state is reduced, as well as the residual aliasing after combining I_1 and I_2. The low angular undersampling in this example generates streak artefacts that

are predominantly resolved with iterative-SENSE in each independent motion state.

S3 (Figure 5.6) is fully-sampled along the radial dimension, but is 8x undersampled along the angular dimension which generates streaking artefacts. Residual streaking artefacts are present in I_1 and I_2 for this example. Combination of both motion states using the IMC approach does not produce significant aliasing in this case, but blurring artefacts are introduced due to the smoothing operation within IMC.

The GMD approach successfully removed motion artefacts in all of the simulations above, producing images with comparable quality to the motion free image. This is due to the fact that the GMD approach uses information more efficiently than the IMC. Consider only the undersampling factor along the radial dimension, which is used to split the data between motion states. Whereas the GMD has an effective undersampling factor $R_{rad} \leq R \leq R_{rad} \cdot N_b$ (where R_{rad} is the radial undersampling factor), the undersampling factor of each motion state reconstruction (I_b) will correspond to $R_{rad} \cdot N_b$. Therefore, in the majority of cases the GMD will be a better conditioned problem than the IMC for each bin.

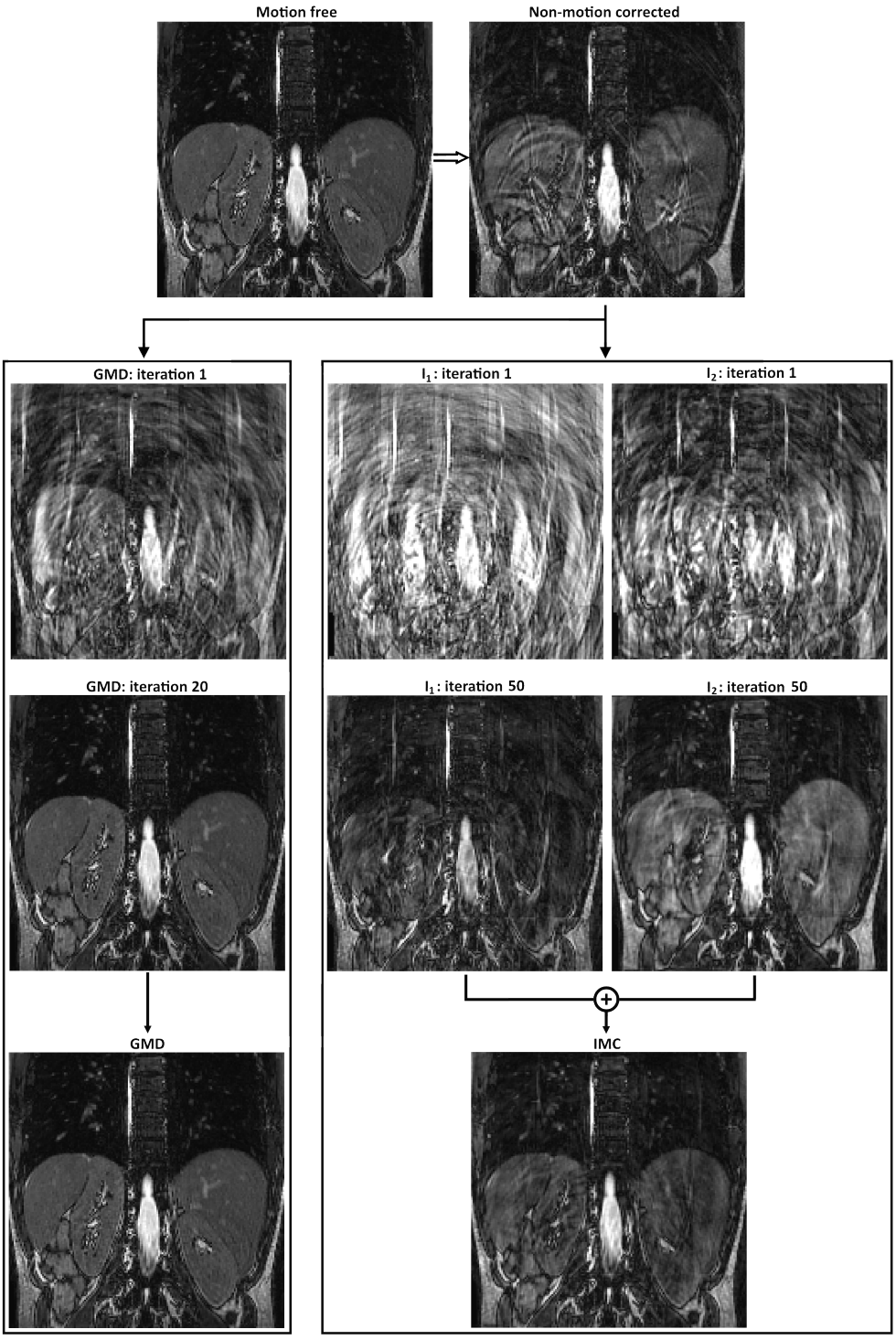

Figure 5.4: Simulation **S1** of a motion corrupted acquisition with non-rigid motion using 2 motion states, 4 coil channels and 4x undersampling along the radial dimension. The simulated acquisition produces the non-motion corrected (NMC) image from the motion-free image. GMD and IMC approaches are shown for the first and final iterations. Motion and blurring is visible in NMC. Although IMC removes most of the blurring artefacts, significant aliasing remains. Residual aliasing in each motion state (I_1 and I_2) does not cancel out after warping and averaging, as seen in the final result (IMC). No visible artefacts are present in the GMD.

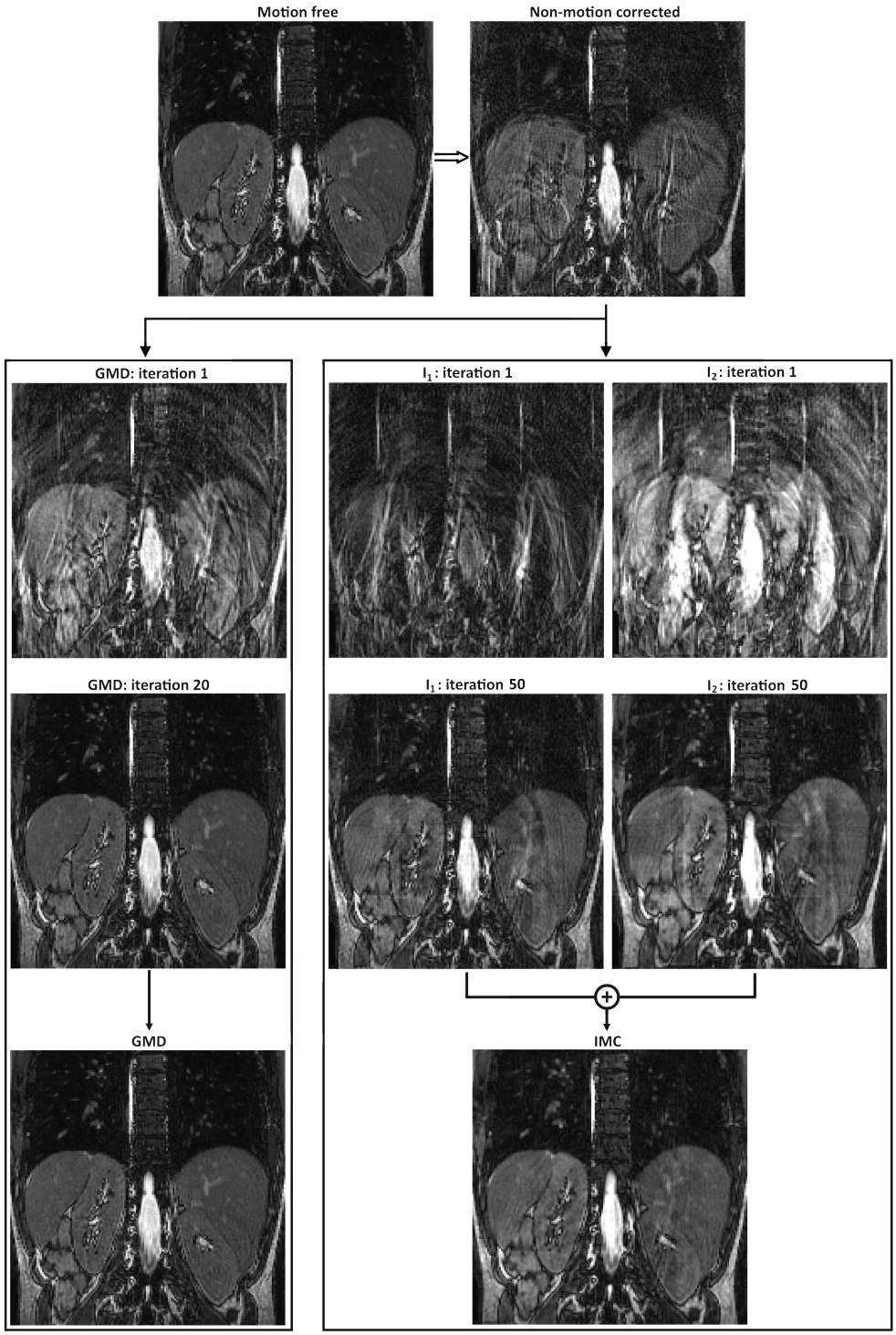

Figure 5.5: Simulation **S2)** of a motion corrupted acquisition with non-rigid motion using 2 motion states, 4 coil channels, 3x undersampling along the radial dimension and 2x undersampling along the angular dimension. The simulated acquisition produces the non-motion corrected (NMC) image from the motion-free image. GMD and IMC approaches are shown for the first and final iterations. Aliasing and blurring is visible in NMC. Most artefacts are removed with IMC, but some aliasing remains. Here, iterative-SENSE is almost sufficient to resolve aliasing artefacts due to undersampling. However, residual aliasing (due to radial undersampling) and streak artefacts (due to angular undersampling) are still present in I_1 and I_2. No visible artefacts are present in the GMD.

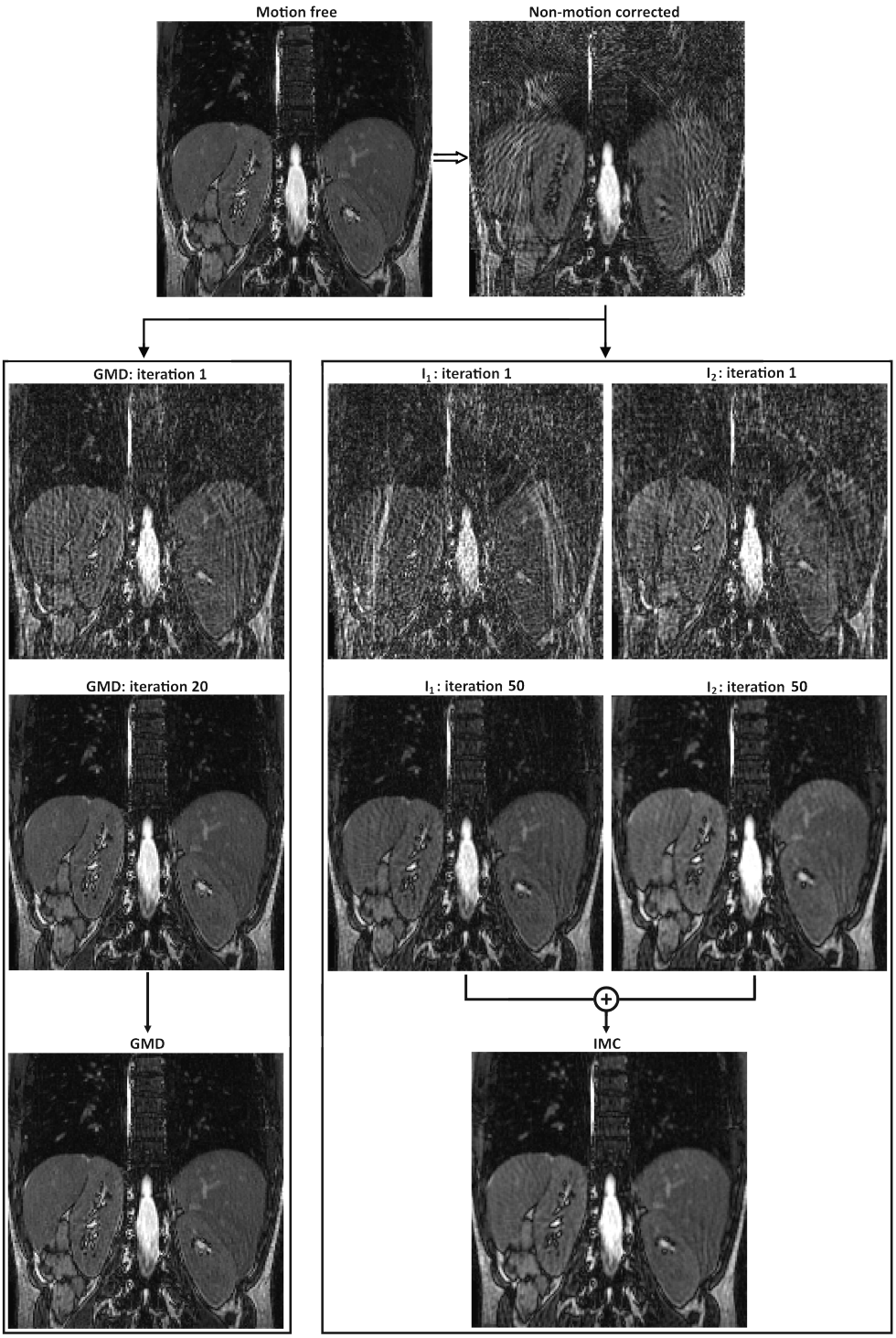

Figure 5.6: Simulation **S3)** of a motion corrupted acquisition with non-rigid motion using 2 motion states, 4 coil channels and 8x undersampling along the angular dimension. The simulated acquisition produces the non-motion corrected (NMC) image from the motion-free image. GMD and IMC approaches are shown for the first and final iterations. Aliasing and blurring is visible in NMC. The angular undersampling leads to strong streaking artefacts that remain in I_1 and I_2 after iterative-SENSE reconstruction. Only minor aliasing remains using the IMC approach, however the blurring effect due to averaging is apparent. No visible artefacts are present in the GMD.

5.4.2 In vivo experiments

Reconstructions results for the Gated, IMC and GMD approaches are shown in Figures 5.7 and 5.8 for volunteers 1 and 2, respectively. The 5 mm Gated reconstruction shows residual motion artefacts. These are further reduced with the IMC and GMD approaches, using 3 mm bins (on average). A shaper reconstruction can be obtained for the GMD, however a higher apparent SNR is obtained with the IMC. No apparent undersampling artefacts are seen in the IMC images, as the low acceleration factors (2x radial undersampling, 1.6x angular undersampling on average) were fully resolved by iterative SENSE.

The respective metrics obtained for Gated, IMC and GMD were as follows: Vessel Sharpness = 0.72±0.09, 0.69±0.08 and 0.77±0.13; Liver Sharpness = 1.10±0.29, 1.09±0.26 and 1.27±0.32; apparent SNR = 10.11±4.02, 14.41±5.86 and 8.51±3.99; visual scoring = 2.73±0.93, 2.28±0.64 and 3.10±0.89; scan efficiency = 63±13%, 88±11% and 88±11%. These results are summarized in the plots presented in Figure 5.8.

The GMD approach obtains the highest sharpness scores, measured in the liver dome, vessels and expert evaluation. The IMC consistently presents the lowest sharpness values, but has the highest apparent SNR. Both motion correction methods significantly reduce scan time from approximately 290 seconds down to approximately 200 seconds,

when compared to the self-gated (Gated) approach.

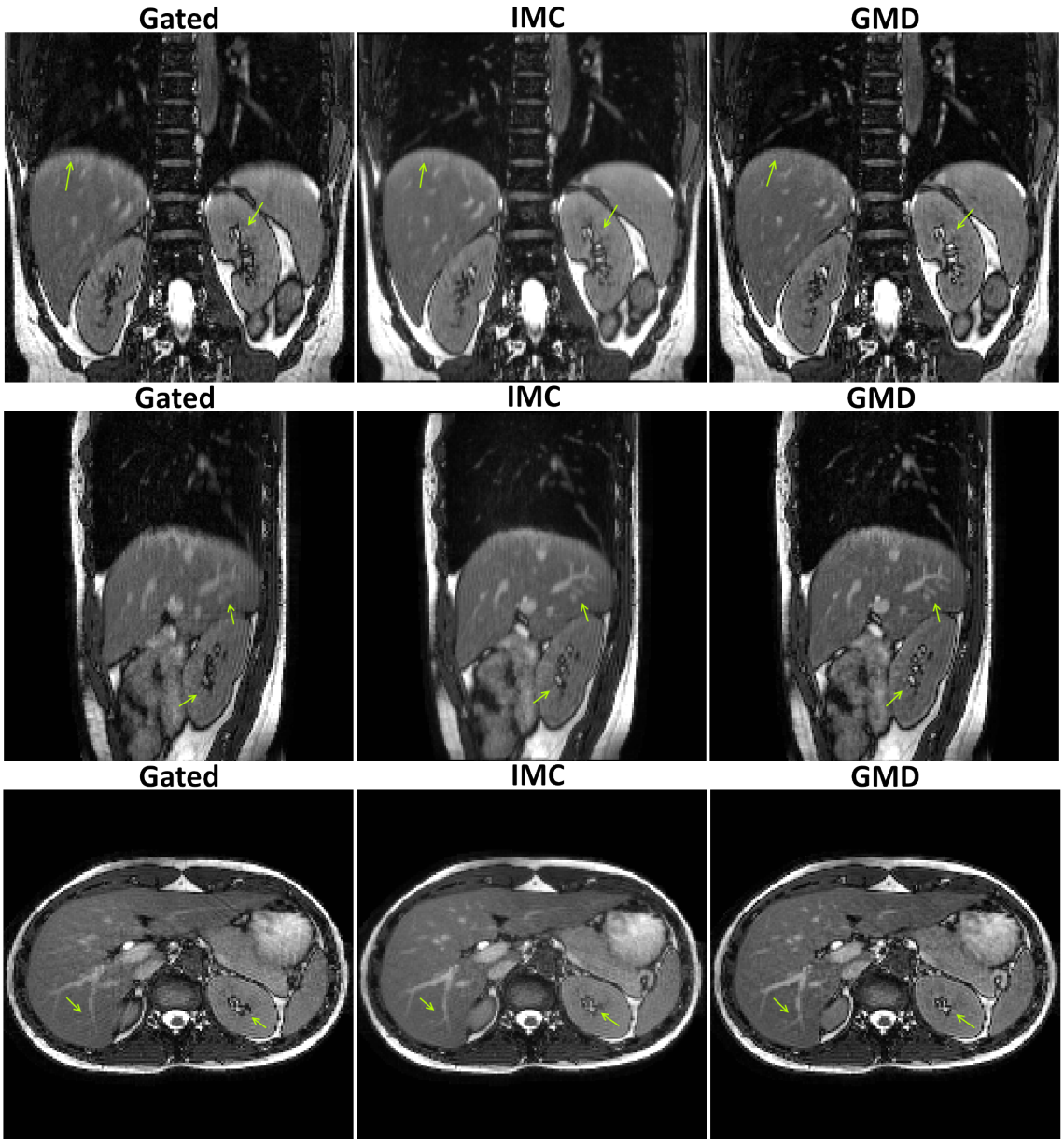

Figure 5.7: Coronal (**Top row**), sagittal (**Middle row**) and axial (**Bottom row**) slices for reconstructions with **Gated**, **IMC** and **GMD** in volunteer 1. Residual motion artefacts are visible in the 5 mm Gated reconstruction (arrows). Both IMC and GMD motion using 3 mm bins (on average) successfully correct the data, improving image quality. Additional blurring is introduced by IMC (arrows), but apparent SNR is also increased.

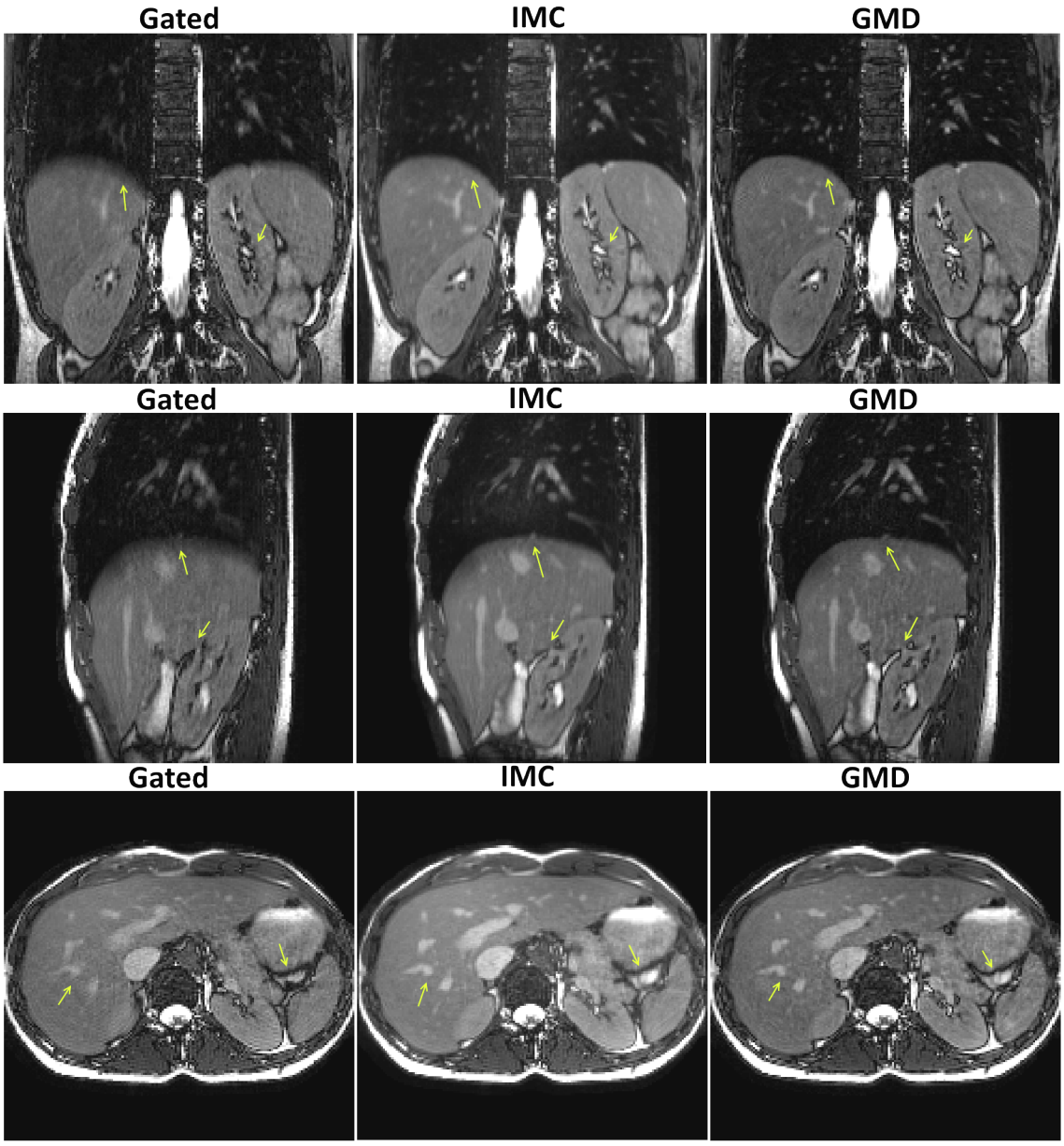

Figure 5.8: Coronal (**Top row**), sagittal (**Middle row**) and axial (**Bottom row**) slices for reconstructions with **Gated**, **IMC** and **GMD** in volunteer 2. Residual motion artefacts are visible in the 5 mm Gated reconstruction (arrows). Both IMC and GMD motion using 3 mm bins (on average) successfully correct the data, improving image quality. Additional blurring is introduced by IMC (arrows), but apparent SNR is also increased.

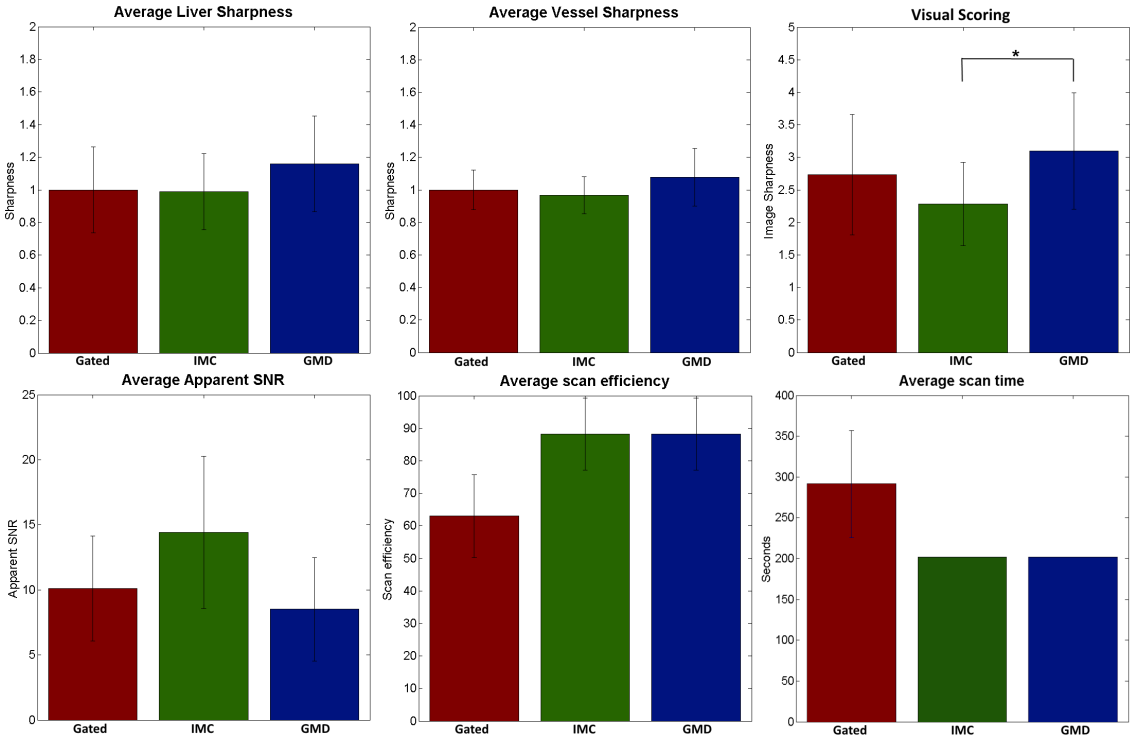

Figure 5.9: Bar plots comparing the Gated, IMC and GMD approaches in terms of liver sharpness (paired t-test), vessel sharpness (paired t-test), visual scoring (Wilcoxon test), apparent SNR (paired t-test), scan efficiency and scan time. The error bar denotes standard deviation. Statistically significant differences on a P-value < 0.05 are denoted by *.

5.5 Discussion

A comparison between image-based (IMC) and reconstrucion-based (GMD) motion correction in abdominal imaging was made. Both methods were also compared with standard 5 mm self-gated (Gated) reconstruction. Some motion artefacts remained in the 5 mm Gated reconstruction. In general, IMC and GMD achieved superior artefact reduction due to correcting motion to a finer range (3 mm bins on average). Additionally, the motion correction methods would benefit from a ≈25% reduction in scan time. Results indicate that the

GMD approach does not suffer from the limitations of the IMC approach, namely residual aliasing (shown in the simulations) and blurring (shown in vivo).

Simulations show that the IMC approach will contain aliasing artefacts if the undersampling factor for each motion state is too high. The GMD approach uses all the available data in a single reconstruction, with therefore lower undersampling factors. Indeed, for a fully sampled dataset, the effective undersampling factor of the GMD depends on the relationship between the motion and the sampling. In general, the undersampling factor R will be $1 \leq R \leq N_b$. On the other hand, the effective undersampling factor of the IMC will be proportional to the number of motion states N_b. Simulations demonstrate that the IMC can remove motion induced blurring, but may produce residual aliasing or blurring artefacts. For the same problem, the GMD approach can successfully remove motion related artefacts to a similar quality of the ideal motion-free image.

Blurring artefacts introduced by the IMC approach were confirmed with an in vivo study. Three different sharpness metrics (liver sharpness, vessel sharpness and blurring visual score) consistently rated IMC as the worst and GMD as the best (with Gated in the middle). The apparent blurring in the IMC is a consequence of the smoothing effect of averaging multiple images. Even if motion is perfectly estimated, the IMC will create blurring due to interpolation and av-

eraging.

The IMC approach had the highest apparent SNR. This effect is also a consequence of the final averaging step. The GMD approach presented with the lowest apparent SNR. It was shown in Chapter 4 that this reconstruction is ill-conditioned even for a fully sampled dataset (which was not the case for the in vivo experiments). Therefore, noise amplification is expected, particularly in the centre of the volume since it is the furthest away from the receive coils. As described in Chapter 4, this limitation can be addressed with regularization.

The reconstruction quality of the motion correction methods depend on the accuracy of the estimated motion. This is more so for the GMD approach, where errors in the forward model can manifest as noise amplification or aliasing artefacts. For the IMC, motion field errors will get smoothed out and the resulting artefacts may appear more benign. Therefore, it is important to obtain reliable and accurate motion estimation to guarantee successful motion correction. Further work will study the quality of the undersampled bin reconstructions and how they relate to accurate motion estimation via image registration.

Acceleration of the proposed framework is possible by further undersampling the data. However, aliasing in the bin reconstructions may compromise motion estimation. Furthermore, significant noise amplification may occur in the GMD reconstruction when high acceleration factors are considered. To address this limitation, the proposed GMD

framework will be combined with Compressed Sensing in the next Chapter. Both the bin reconstruction and GMD reconstruction can be regularized to ensure accurate motion and estimation and therefore a successful motion corrected reconstruction.

5.6 Conclusion

We have shown that the proposed GMD approach yields sharper images and correctly reconstructs small structures in comparison to the image warping and gated reconstructions, whereas image warping lead to higher apparent SNR. GMD shows an increase of ≈12% in Vessel Sharpness, ≈17% in Liver Sharpness and ≈36% in visual evaluation relative to the image warping approach. Both GMD and image warping approaches improve scan efficiency by ≈25% in comparison to the gated acquisition.

Chapter 6

Accelerated Motion Corrected Three-Dimensional Abdominal MRI Using Total Variation Regularized SENSE Reconstruction

6.1 Introduction

The previous Chapter introduced a novel framework to estimate and correct the data using only the data itself. Two approaches to the correction step were compared: an Image-based Motion Correction (IMC) and a reconstruction-based using the General Matrix Description (GMD). The image-based approach has two major limitations: 1) aliasing artifacts of each undersampled motion state are warped to the

common respiratory position and may persist in the final image, and 2) the averaging of multiple motion states may lead to blurring in the final image. The latter effect has been shown for abdominal images in the previous Chapter and for cardiac images in reference [156] when compared to the GMD approach.

GMD corrects motion directly during the reconstruction process; although a previous estimation of the motion is required. This motion has been estimated from low-resolution training acquisitions [226] or from a computationally expensive coupled motion reconstruction and motion estimation problem based on external sensors [149] or self-navigated models [148]. These approaches have been demonstrated for fully and over-sampled acquisitions only. Here, I propose a highly accelerated GMD-based method to correct non-rigid motion in under-sampled 3D isotropic abdominal images. Here, the GMD framework presented in Chapter 5 is combined with Compressed Sensing [124] to cope with higher undersampling factors.

The motion estimation step of the proposed approach is an extension of the framework proposed in the previous Chapter to account for undersampled acquisitions. Data is acquired under free breathing with a self-gated golden-radial phase encoding (G-RPE) trajectory [25, 167], enabling the reconstruction of highly undersampled images at various motion states (respiratory bins). Unlike in Chapter 5, where iterative SENSE reconstruction [168] was sufficient to independently

reconstruct the bins, here I propose to reconstruct all motion states simultaneously using a spatial and temporal total variation regularized iterative SENSE (TV-SENSE) approach, allowing reliable motion estimation from bins with higher undersampling factors than before. The proposed approach was tested on nine healthy volunteers and compared against a standard gated reconstruction.

6.2 Methods

The proposed framework can be divided into 5 steps (Figure 6.1b, Figure 6.1c). In the first step, data is acquired with a self-gated 3D golden-radial phase encoding (G-RPE) trajectory during free breathing. This data is sequentially assigned into different motion states using a self-navigated respiratory signal, yielding a set of highly undersampled k-spaces $\mathbf{K_b}$ at the completion of the acquisition (step 2). Each bin is reconstructed with TV-SENSE (step 3), producing undersampled respiratory resolved images $\mathbf{I_b}$. In the next step, non-rigid motion is estimated using image registration of $\mathbf{I_b}$. Finally, the estimated motion is used to reconstruct a motion corrected image using TV-GMD. Each step is described futher below.

6.2.1 Data acquisition

G-RPE [25, 167] combines a regularly sampled Cartesian readout (kx) in the foot-head (FH) direction with a radial phase encoding order

in the ky-kz plane, where radial profiles are separated by the golden angle $\theta_G = 111.25°$(Figure 6.1a, top). A G-RPE acquisition can be undersampled radially by skipping readouts within each radial profile and angularly by acquiring fewer radial profiles (Figure 6.1a, bottom).

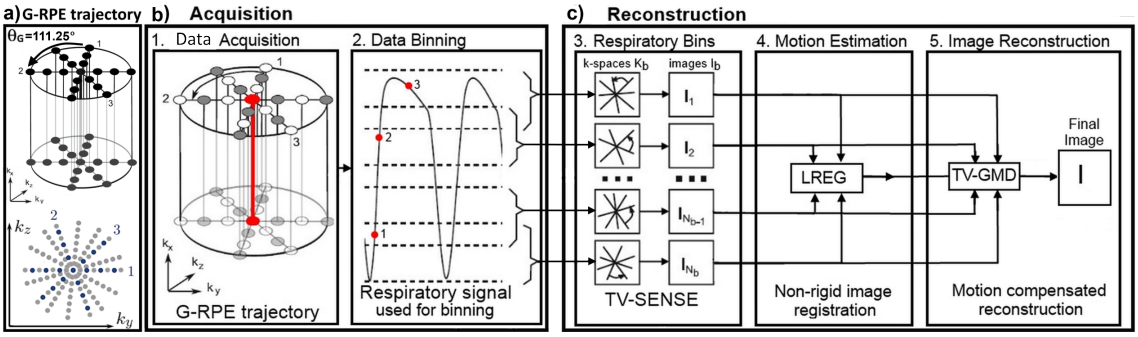

Figure 6.1: **a) Top:** Diagram of the golden radial phase encoding (GRPE) trajectory. Cartesian readouts (kx direction) are acquired with a radial order in the phase encoding plane (kykz). Consecutive radial profiles (numbered 1, 2 and 3) are separated by the golden angle $\theta_G = 111.25°$. **a) Bottom:** Diagram of GRPE undersampling in the phase encoding plane. Angular undersampling is achieved by skipping complete radial profiles (full grey radial profiles), while radial undersampling is performed along each radial profile by uniformly skipping readouts (grey readouts along radial profiles 1, 2 and 3). **c)** and **d)** Diagram of the proposed approach in 5 steps. The acquisition is comprised of two parts: step **1.** Image is acquired with 3D G-RPE; step **2.** The central k-space line yields a respiratory signal which is used to bin data. The reconstruction is divided into 3 parts: step **3.** Binned datasets are simultaneously reconstructed with TV-SENSE; step **4.** Motion is estimated by image registration (LREG) of the binned reconstructions; step **5.** The estimated motion is used in the motion corrected reconstruction. Only the acquired data is needed to produce a motion corrected image.

This trajectory provides a quasi-uniform k-space distribution regardless of the number of profiles used [227], ensuring an optimal distribution of profiles in k-space for different length of data acquisition. Additionally, the central k-space readout (red line in Figure 6.1b) is acquired every N x TR seconds where is N the number of readouts within a radial profile and TR is the repetition time, allowing for respiratory self-navigation. If the acquisition time for the radial profile

(N x TR) is fast enough, respiratory motion within the radial profile can be considered negligible and the central k-space readout can be used to navigate the entire radial profile.

6.2.2 Data binning

The respiratory position at which each radial profile was acquired is identified by inferring the diaphragm displacement in the (FH) readout direction as described in Chapter 5. This self-navigated respiratory signal is used to group the acquired data into different respiratory positions. During this process, referred as data binning, the radial profiles in each bin will not be equally spaced by the golden angle as they depend on the breathing cycle [33]. Therefore a quasi-uniform k-space distribution is not guaranteed for any bin. Gaps in k-space may generate artefacts in $\mathbf{I_b}$ and affect subsequent motion estimation. Thus, it is important to ensure that each bin has adequate coverage of k-space for reliable motion estimation. The artefact level in $\mathbf{I_b}$ is predicted using the maximum angle between two radial profiles (α).

To guarantee that the image quality of $\mathbf{I_b}$ is sufficient for reliable motion estimation an adaptive binning is performed (Figure 6.2). This strategy enforces each bin to have α_b (maximum angle between two radial profiles in bin b) smaller than a pre-determined α_{max} (determined empirically), in order to minimize undersampling artefacts.

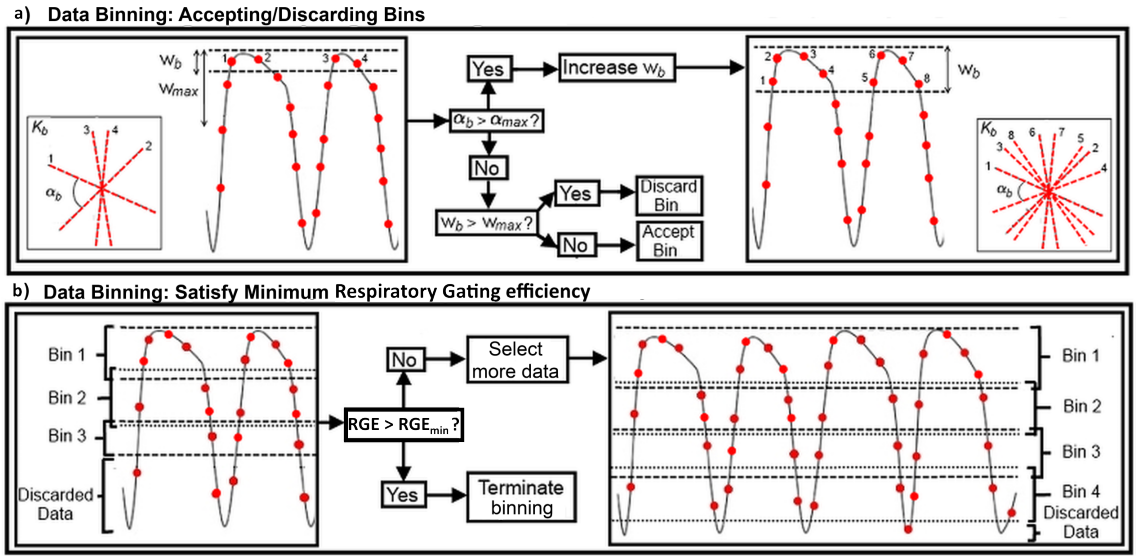

Figure 6.2: Adaptive data binning is performed in two steps: **a)** Each bin is initialized with a window size w_b. If α_b is larger than α_{max}, w_b is increased, providing additional data for this bin. This process is repeated until α_{max} is respected. If the final w_b is larger than w_{max}, the bin is discarded; otherwise it is accepted. **b)** Insufficient data causes a significant fraction of bins to be discarded, leading to a poor respiratory gating efficiency (RGE). If RGE is smaller than RGE_{min}, an additional radial profile is considered and the full dataset (including the newly considered radial profile) is re-binned. This process terminates when the RGE_{min}, α_{max} and w_{max} constraints are simultaneously respected.

Additionally, only bins with a bin window (w_b) smaller than a maximum bin window (w_{max}) are accepted, to minimize intra-bin motion. The adaptive binning process is controlled by 4 parameters: maximum overall undersampling factor (R_{max}), the maximum angle (α_{max}), the maximum bin window size (w_{max}) and the minimum gating efficiency (RGE_{min}). Respiratory gating efficiency (RGE) is given by:

$$RGE = \frac{AcceptedProfiles}{TotalProfilesAcquired} \tag{6.1}$$

Respiratory bins are chosen such that within each bin, $\alpha_b < \alpha_{max}$ (to limit reconstruction artifacts), and $w_b < w_{max}$ (to limit intra-bin mo-

tion). To limit undersampling artifacts in the final reconstruction of the complete dataset, a minimum amount of data to respect R_{max} is enforced. A potential bin is first generated at the end-exhale position with a bin window size equal to the image resolution. The bin window is increased until it has enough data to comply with the α_{max} constraint (Figure 6.2a). If the bin window size exceeds w_{max} the bin is discarded in order to minimize intra bin motion, otherwise it is accepted. A sliding window is used to initialize a potential bin in the next respiratory position and the process in Figure 6.2a is repeated.

Once the considered data thus far has been binned, the algorithm tests if the selected dataset satisfies the minimum gating efficiency. If the current gating efficiency is less than RGE_{min} (Figure 6.2b), then an additional radial profile is considered and the binning process is restarted (back to Figure 6.2a). Data binning terminates once enough motion states are adequately populated ($\alpha_b < \alpha_{max},\ w_b < w_{max}$) and the complete dataset satisfies the condition $RGE < RGE_{min}$.

6.2.3 Reconstruction of respiratory bins

The undersampled bins are simultaneously reconstructed with total variation regularized iterative SENSE (TV-SENSE) [124, 152] given by:

$$\hat{\mathbf{I}}_\mathbf{b} = arg\ min_{I_b} ||\mathbf{E}\ \mathbf{I_b} - \mathbf{K_b}||_2^2 + \lambda_s \mathbf{TV_s} + \lambda_t \mathbf{TV_t} \qquad (6.2)$$

where $\mathbf{K_b}$ is the acquired data at each bin b, $\mathbf{E}$ is the encoding matrix including coil sensitivities, gridding and Fourier transformation, $\mathbf{I_b}$ the binned images to be reconstructed, $\mathbf{TV_s}$ represents the 3D spatial total variation (intra-bin) and $\mathbf{TV_t}$ the temporal total variation in the respiratory direction (inter-bin). The L_2-norm is the data consistency term. $\mathbf{TV_s}$ is the sum of absolute differences in each bin; $\mathbf{TV_t}$ is the sum of absolute differences between adjacent bins. Both of these transforms are L_1-norms operating in image space, defined as:

$$\begin{aligned} \mathbf{TV_s} &= ||\nabla_s \mathbf{I_b}||_1 \\ \mathbf{TV_t} &= ||\nabla_t \mathbf{I_b}||_1 \end{aligned} \tag{6.3}$$

where ∇_s and ∇_t represent the 3D spatial gradient and the 1D temporal gradient, respectively. The parameters λ_s and λ_t define the balance between total variation regularization and data consistency. The $\mathbf{TV_s}$ term removes noise-like aliasing in the image and sharpens the main edges in the image, e.g. the diaphragm-lung boundary, allowing better image registration. Large λ_s values enhance these effects at the expense of additional blurring (due to over-smoothing). While blurring limits the accuracy of subsequent image registration, aliasing introduces errors in $\mathbf{I_b}$ that can make the registration fail altogether. Hence, we use a large value for λ_s to reconstruct artifact-free respiratory bins and allow reliable motion estimation.

The $\mathbf{TV_t}$ removes additional aliasing in areas where there is little mo-

tion, like the central part of the liver. Large λ_t values will introduce blurring in regions with large motion, e.g. diaphragm-lung boundary. Thus, we use small λ_t values to distinguish motion states. Here, the $\mathbf{TV_t}$ term amounts to a small regularization compared to $\mathbf{TV_s}$, yielding minor improvements in the reconstructed image. The values for λ_s and λ_t were determined empirically by inspecting the output reconstructions of four training datasets covering the expected range of undersampling factors and respiratory amplitudes and choosing values that removed the most background aliasing without significantly blurring the image.

To accelerate bin reconstruction, a data consistency reconstruction (i.e. λ_s and λ_t set to zero) is used as the starting estimate for TV-SENSE. This approach accelerates convergence and delivers a good approximation of the reconstructed image. These reconstructions are pre-conditioned [168] by intensity correction (from coil sensitivities) and a Voronoi based density compensation function [172], as the G-RPE is non-Cartesian.

6.2.4 Motion estimation

A 3D non-rigid respiratory motion model is obtained from image registration of reconstructed bin images to a common respiratory position. This is done using the LREG tool [34], which performs an intensity based registration through a succession of local affine registrations,

starting from a global affine down to small image blocks. The resulting deformation field is thus non-rigid.

6.2.5 Image reconstruction

The final undersampled image is reconstructed using a spatial total variation regularized GMD approach, based on the formalism introduced in [14]. The GMD approach is described by:

$$\mathbf{K} = \sum_{\mathbf{b}} \mathbf{A_b F S U_b I} = \mathbf{E\ I} \tag{6.4}$$

where $\mathbf{I}$ is the ideal (motionless) image, $\mathbf{U_b}$ are warping operators defined in the previous chapter that apply the spatial transformations for bin b (obtained with LREG), $\mathbf{S}$ are the coil sensitivities for all coils, $\mathbf{F}$ is the forward Fourier transform, $\mathbf{A_b}$ is a logical matrix that selects the k-space lines acquired for bin b, and $\mathbf{K}$ is the acquired multi-channel k-space data. Equation 6.4 is in the reference frame of the coils, where they are assumed to remain static. $\mathbf{I}$ may be obtained by inverting the encoding operator $\mathbf{E}$. Practical inversion of $\mathbf{E}$ is obtained with iterative methods such as the conjugate gradient (CG). The CG requires a symmetric positive-definite matrix, thus the method is applied to the equivalent normal equation:

$$\mathbf{E^H\ K} = (\mathbf{E^H E})\mathbf{I} \tag{6.5}$$

where $\mathbf{E^H}$ is the Hermitian transpose of $\mathbf{E}$.

The proposed approach uses undersampled data, which results in noise amplification in the reconstructed motion corrected images due to poor conditioning of the inversion. This happens for two reasons: firstly, if the object moves outside the field-of-view (FOV) then information is permanently lost; secondly, correcting for motion within the FOV may cause k-space inconsistencies, causing some samples to overlap and creating k-space gaps. This effectively increases the undersampling factor (R), which contributes to making Equation 6.5 undetermined [183]. Furthermore, in practice the motion is not known exactly and errors in motion estimation can further contribute to the poor conditioning of this problem. It has been shown how multiple channels improve the condition of the motion reconstruction problem for fully sampled images [183]. To reduce the effect of poor conditioning in undersampled datasets spatial total variation regularization is included in the GMD reconstruction (TV-GMD):

$$\hat{\mathbf{I}} = arg\ min_{\mathbf{I}}||\mathbf{E}\ \mathbf{I} - \mathbf{K}||_2^2 + \lambda_s \mathbf{TV_s} \tag{6.6}$$

This is solved with a non-linear conjugate gradient reconstruction using the solution to the non-regularized approach ($\lambda = 0$) as a starting estimate, similar to the previous description of the bin reconstruction. In the TV-GMD reconstruction, the $\mathbf{TV_s}$ term is used to remove

noise-like aliasing with small λ_s values. The λ_s for the TV-GMD was determined empirically by choosing a value that reduces the remaining artefacts without significantly affecting image sharpness.

6.2.6 Data acquisition

Nine volunteers were scanned under free-breathing on a 1.5T clinical scanner (Philips Achieva, Philips Healthcare, Best, The Netherlands) using a 32-channel cardiac coil. Written informed consent was obtained from all subjects according to institutional guidelines and the study ("Development of novel magnetic resonance techniques using healthy volunteers") was approved by the institutional review board. Data was acquired with a balanced steady state free precession sequence with the following parameters: 287 x 287 x 287 mm isotropic FOV, 1.75 x 1.75 x 1.75 mm isotropic resolution, TR/TE = 3/1.43 ms, flip angle 30. The self-navigation k-space central line was acquired every 246 ms. During acquisition, each radial profile was uniformly undersampled in the radial direction by a factor of 2. For the resulting reconstructed matrix size of 164 x 164 x 164, 256 radial profiles are needed to approximately fulfil the Nyquist criterion in the angular direction, assuming a quasi-uniform profile distribution. During the scan, 820 radial profiles were acquired to guarantee all volunteers provided enough data for different reconstruction approaches, including the self-gated reconstruction which has a low scan efficiency.

6.3 Experiments

The accuracy of motion estimation with different undersampling factors (in the bins) was initially analysed in a simulation study. Following, the motion estimated with the proposed TV-SENSE bin reconstruction was compared against the SENSE approach presented in the previous Chapter. Finally, in vivo experiments were performed to compare the the proposed method with a conventional self-gated acquisition (Gated).

6.3.1 Simulations

The proposed approach estimates motion from highly undersampled respiratory resolved bin reconstructions ($\mathbf{I_b}$). A pseudo-random distribution of radial profiles is sampled at each respiratory bin, depending on the breathing pattern. This may result in large k-space gaps that can introduce artefacts in the reconstructed images. Specifically, k-space gaps affect the image point spread function by broadening the main lobe / increasing side lobe amplitude, which results in blurring / aliasing artefacts [227]. Blurring and residual artifacts may hinder subsequent image registration, producing inaccurate motion fields. A simulation was conducted in one representative volunteer to study the relationship between the maximum angle between two radial profiles (α_{max}) and the accuracy of motion estimation. An end-inhale image

($\mathbf{I}$) was reconstructed with 25 different numbers of radial profiles (p), from fully sampled (256 profiles) to highly undersampled (26 profiles). The obtained undersampled images ($\mathbf{I_p}$) were registered to a reference fully sampled end-exhale image ($\mathbf{I_r}$). The obtained motion fields were then compared to the ground-truth: the registration between $\mathbf{I_r}$ and $\mathbf{I}$. We measure the average displacement error in the motion field $\epsilon(\alpha)$ similar to the strategy in reference [32]:

$$\epsilon(\alpha) = \frac{\sum_1^N \sqrt{(\mathbf{U}_{\alpha_{\mathbf{Kp}}}(\mathbf{n}) - \mathbf{U}_{\mathbf{Ir}}(\mathbf{n}))^2}}{N} \tag{6.7}$$

where $\mathbf{U}_{\alpha_{\mathbf{Kp}}}$ is the motion field between $\mathbf{I_p}$ and $\mathbf{I_r}$, $\mathbf{U}_{\mathbf{I_r}}$ is the motion field between $\mathbf{I}$ and $\mathbf{I_r}$, and the sum is taken over all the voxels (N being the total number of voxels in the image).

6.3.2 Comparison with image based motion compensation

A preliminary study was performed to compare the approach described in reference [33], hereby referred as image-based motion compensation (IMC) with the proposed TV-GMD. To evaluate the effects of blurring and residual artifacts in motion estimation, bin reconstructions using the α_{max} value, obtained via simulations, were performed using iterative SENSE (as in IMC) and with the proposed TV-SENSE. Motion fields between neighbouring bins of representative volunteers were obtained via LREG. A comparison of motion estimation obtained

from undersampled SENSE and TV-SENSE bin reconstructions was made by computing their displacement errors to motion fields obtained from a dataset 3x oversampled in the angular direction (considered as ground truth). Additionally, all nine datasets were reconstructed with IMC, using the same amount of data as the TV-GMD reconstruction. This resulted in a total of 160±37 acquired profiles for both TV-GMD and IMC reconstructions. IMC reconstruction was performed with iterative SENSE [168], taking approximately 1 hour. IMC and TV-GMD reconstructions were compared via measures of liver sharpness and gradient entropy. TV-GMD reconstruction and the comparison metrics are described in more detail in the following section.

6.3.3 In vivo experiments

The same acquired data was used retrospectively to produce a 2x undersampled non-motion corrected (NMC) reconstruction (2x undersampling in radial direction, no undersampling in angular direction), a 2x undersampled 5 mm self-gated reconstruction (2x undersampling in radial direction, no undersampling in angular direction) and a highly undersampled TV-GMD reconstruction (2x undersampling in radial direction, 1.8x undersampling in angular direction, on average). This resulted in a total of 256, 414±147 and 160±37 acquired profiles for the NMC, gated and TV-GMD reconstructions.

The following binning parameters were used: $\alpha_{max} = 13.75$ (deter-

mined according to the previous section); $w_{max} = 5$ mm (same value as the gating window); $RGE_{min} = 80\%$ (set to remove outliers in the respiratory cycle). Furthermore, to avoid remaining undersampling artifacts in the final motion corrected reconstruction a maximum undersampling factor (R_{max}) of 4 was used. Therefore, the proposed method was set to reconstruct a minimum of 128 radial profiles, equivalent to 2x angular undersampling and 2x radial undersampling. This resulted in data being grouped into 3-5 bins (varying per volunteer), with bin undersampling factors ranging from 5.2x to 18.9x (average of 9.5x). The motion corrected datasets were undersampled from a minimum of 2.1x to a maximum of 4x (average of 3.6x). Table 6.1 presents values for undersampling factors, gating efficiency, acquisition time, number of acquired profiles, number of profiles per bin, number of bins and bin window sizes.

Table 6.1: Acquisition and reconstruction information for non-motion corrected, Gated, GMD and the proposed TV-GMD reconstructions.

Method	NMC	Gated	GMD	TV-GMD
Number of bins	1	1	3-5	3-5
Bin windows (mm)	11.1±3.5	5.00	2.76±1.1	2.76±1.1
Number of profiles per bin	256	256	49±16	49±16
Number of profiles acquired	256	414±147	160±37	160±37
Number of profiles reconstructed	256	256	148±37	147±37
Acquisition time (s)	62.98	101.79±36.21	39.36±9.13	39.36±9.13
Gating efficiency (%)	100	67±15	93±7	93±7
Undersampling factor	2	2	3.6±0.5	3.6±0.5

The respiratory bins were reconstructed with TV-SENSE. The initial L_2-norm reconstruction ran with 10 iterations, with $\lambda_s = 0$ and $\lambda_t = 0$. This result was used as a starting estimate for the reconstruction with $\lambda_s = 0.2$ and $\lambda_t = 0.1$ (corresponding to $9.6x10^{-6}$ and $4.8x10^{-6}$, respectively, in terms of the average $||.||_\infty$ norm of the images), 3 iterations. The reconstructed bins were registered to estimate the motion for the TV-GMD reconstruction. The initial data consistency GMD reconstruction ran with 5 iterations, $\lambda_s = 0$. The following TV-GMD reconstruction used $\lambda_s = 0.0001$ (corresponding to $4.8x10^{-9}$, in terms of the average $||.||_\infty$ norm of the images) and 5 iterations. Additionally, data was reconstructed with GMD (4 iterations) for additional comparison with TV-GMD.

It took approximately 90 minutes to reconstruct bins (TV-SENSE) and an additional 90 minutes for the motion corrected reconstruction (TV-GMD) on a 12-core implementation. The gated and non-motion corrected images were reconstructed with iterative SENSE (23), both taking approximately 5 minutes to reconstruct. Coil sensitivities were estimated from a reference scan. All images were reconstructed using Matlab (The MathWorks, USA). In order to observe the effect of undersampling in the final motion corrected reconstruction, data from two representative volunteers was reconstructed with the proposed method with undersampling factors of 4x, 3x, 2x and 1x, using the same estimated motion as described above.

The proposed TV-GMD approach was compared with the gated reconstruction by means of liver sharpness, gradient entropy, visual image scoring and ranking [74]. The liver sharpness and gradient entropy metrics were computed on a set of 10 coronal slices. To compute liver sharpness, twenty five 1D profiles were manually selected across the liver-lung interface. The sharpness measure for each profile was obtained by the maximum gradient normalized to the maximum intensity, similar to what was proposed in reference [24]. Gradient entropy has previously been used in motion correction as an optimisation cost function that favours distinct boundaries and reduced artifacts and was ranked 1 out of 24 image quality metrics studied [135]. Here we use local gradient entropy as an image quality metric, similar to reference [212]. The total gradient entropy of the image is given by the mean of the local gradient entropies. All liver sharpness and gradient entropy values were normalized to the reference gated values. We present the gradient entropy results inverted to allow easier comparison with the other metrics (the higher the metric the better the image).

Two experts (a radiologist with 14 years of experience in MRI and an image processing researcher with 18 years of experience in MRI) were asked to score the sharpness of the main boundaries and features of the images on a scale of 0 (extreme blurring) to 4 (no blurring) and rank the overall image quality based on existing artifacts, ghosting and

blurring from 1 (worst) to 4 (best). Statistical significance of gradient entropy and liver sharpness was evaluated using a two-sided paired t-test (P-value < 0.01); statistical significance of expert sharpness score and quality rank was evaluated using a Wilcoxon signed rank test (P-value < 0.01).

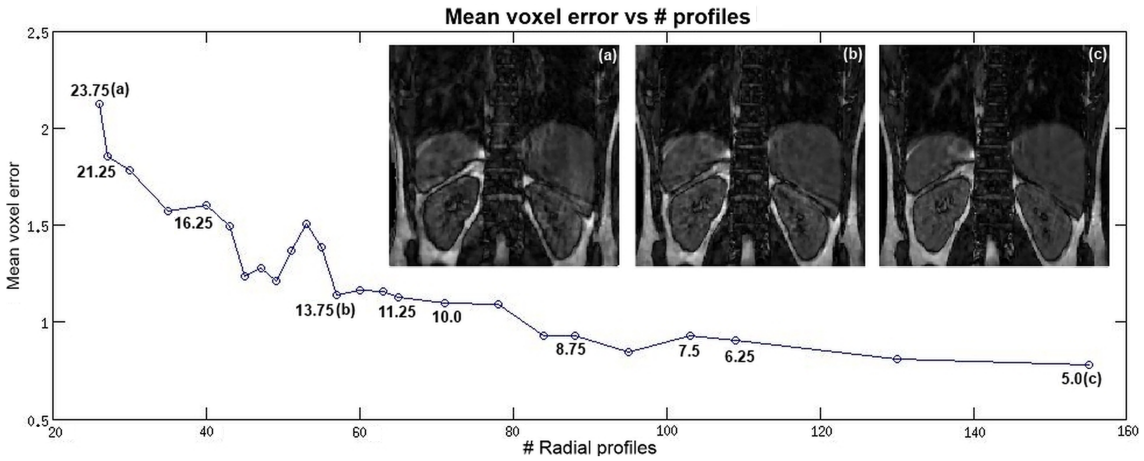

Figure 6.3: Plot of the mean motion field error as a function of the number of radial profiles used for bin reconstruction. Several α values are marked in the graph. Respiratory bin reconstruction for the volunteer studied for 3 different α values are shown: a) $\alpha = 5°$, b) $\alpha = 13.75°$and c) $\alpha = 16.25°$. For $\alpha \leq 13.75°$motion field errors are kept bellow 1.1 voxels.

6.4 Results

6.4.1 Simulations

Figure 6.3 shows the mean voxel error in the registration deformation field decreasing with the increasing number of radial profiles. Angular gaps values (α) resulting for different number of radial profiles are displayed throughout the graph. For values lower than $\alpha = 13.75°$the mean voxel error in the motion fields remains below 1.1 voxels. For α

values larger than 13.75°the error in the motion fields start increasing significantly. Based on this simulation, we chose to set $\alpha_{max} = 13.75°$.

6.4.2 Comparison with image based motion correction

Figure 6.4a-c shows bin images of volunteer 2 for a zero-filled reconstruction, iterative SENSE and TV-SENSE for resulting undersampling factors (R) of 11x, 15x and 19x for bins 1, 2 and 3, respectively. Iterative SENSE reconstruction, as used in [33], shows residual artifacts (Figure 6.4b). These artifacts are significantly reduced with a TV-SENSE reconstruction, while only introducing minor blurring (Figure 6.4c).

The improvement in motion estimation accuracy with the proposed TV-SENSE in comparison to previously shown iterative SENSE can be seen in Figure 6.5a-d), for two representative volunteers. Image registration of SENSE reconstructions can produce local errors (yellow-red regions in Figure 6.4b and Figure 6.4d) as the LREG algorithm attempts to register aliasing artifacts. TV-SENSE removes most of these artifacts, enabling reliable motion estimation (corresponding blue-green regions in Figure 6.4a and Figure 6.4c).

Figure 6.6 shows multiple slice orientations of two volunteers for image-based motion compensation (IMC) and TV-GMD reconstructions. If undersampling artifacts from different motion states fail to cancel out,

residual aliasing may arise in IMC as shown in Figure 6.6a for volunteer 2. This aliasing is significantly reduced with the TV-GMD (Figure 6.6b).

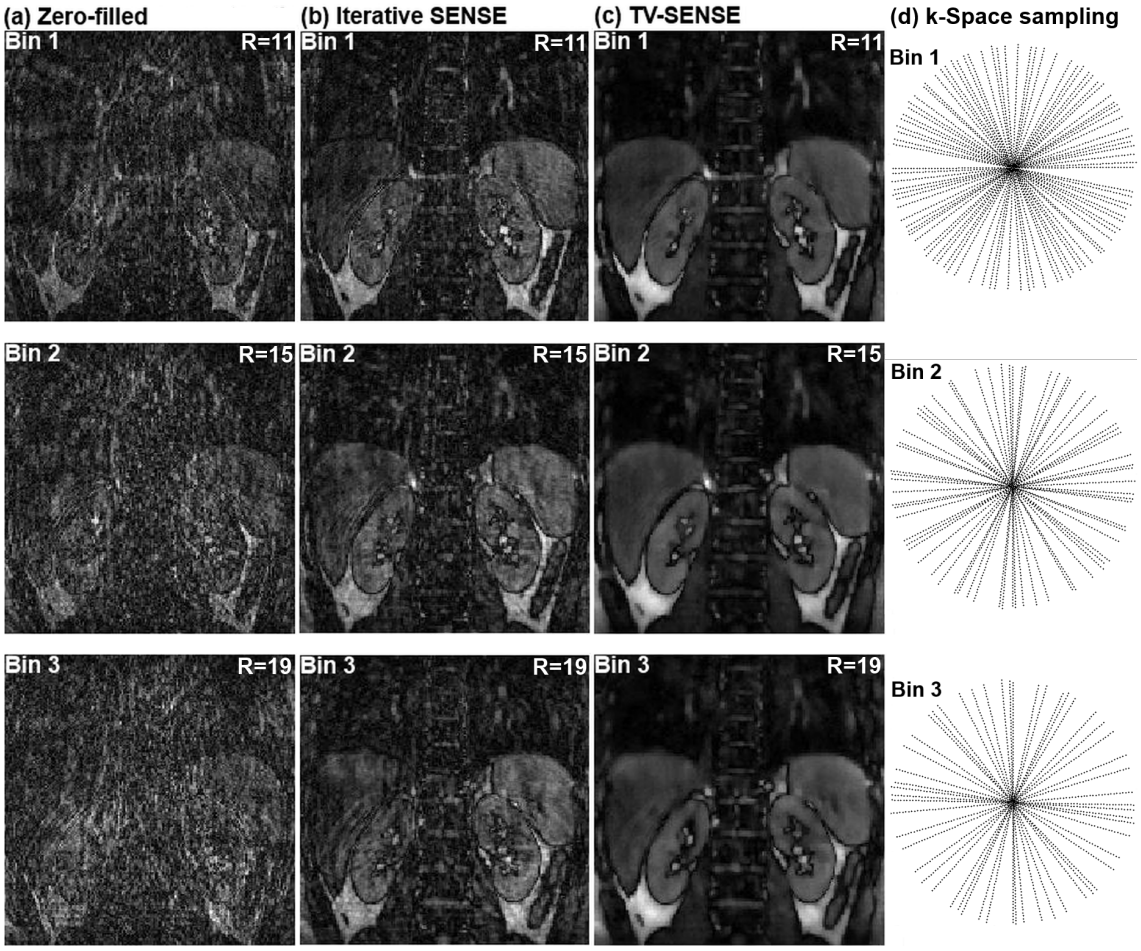

Figure 6.4: Reconstructions of bins 1, 2, and 3 with 46, 33 and 27 radial profiles (corresponding to undersampling factors R of 11, 15 and 19, respectively). **a)** Zero-filled reconstructions. **b)** Iterative SENSE used in [33], significant aliasing remains. **c)** TV-SENSE, most aliasing is eliminated. **d)** k-Space sampling locations in the phase encoding plane for bins 1, 2 and 3.

Results for volunteer 4 using IMC (Figure 6.6c) present less residual aliasing, but additional blurring is introduced (which can be seen in both volunteers). In contrast, the TV-GMD corrects motion without introducing this additional blurring (Figure 6.6d). TV-GMD and IMC presented liver sharpness values of 1.18 and 0.98, respectively and

gradient entropy values of 1.00 and 0.98, both statistically different with a P-value of 0.01.

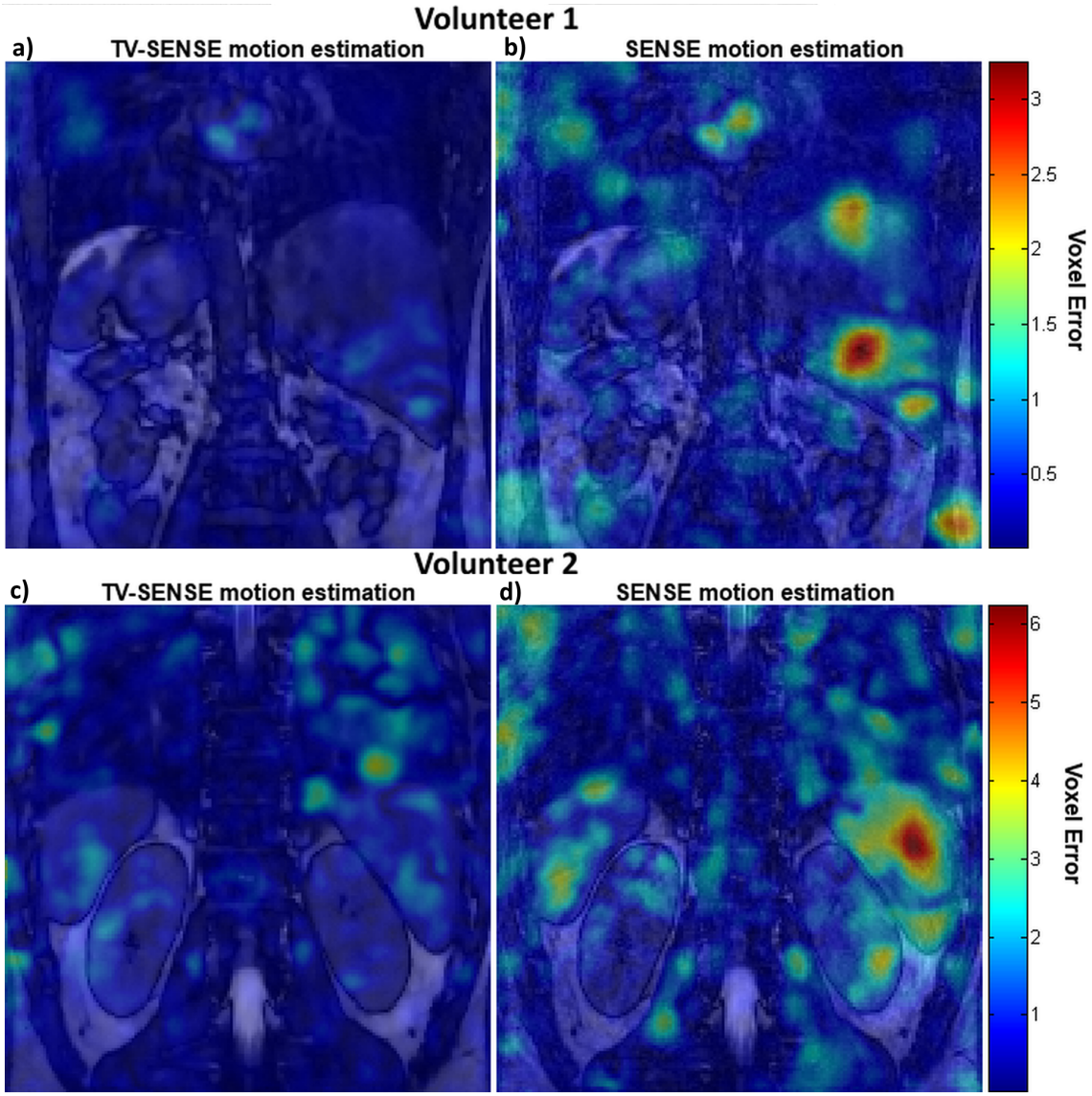

Figure 6.5: **a-d)** Motion estimation errors (in voxel units) between neighbouring bins for TV-SENSE and iterative SENSE bin reconstructions for two volunteers. Colour coded motion estimation errors are overlaid on the anatomical reconstruction. Iterative SENSE motion estimation **(b,d)** shows increased local errors, whereas TV-SENSE provides more reliable motion estimation **(a,c)**.

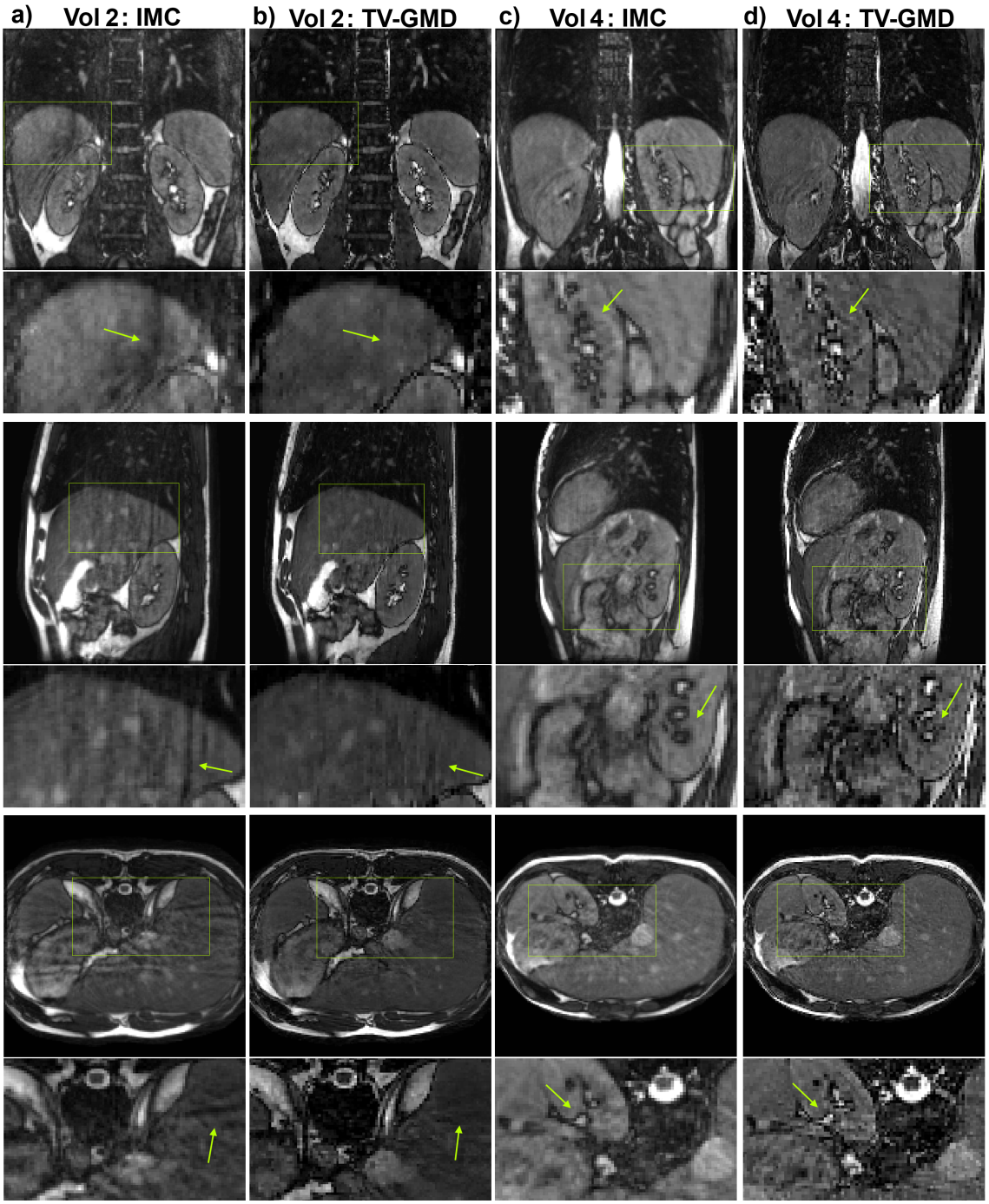

Figure 6.6: Coronal (top), sagittal (middle) and axial (bottom) slices for volunteers 2 and 4 (including zoom-in images, arrows point out some main differences). **a)** Image based motion correction (IMC) for volunteer 2 with 4x undersampling at 100% gating efficiency. Residual aliasing may be seen in all slice orientations (arrows). Additionally, some blurring is introduced by IMC (arrows). **b)** Proposed TV-GMD for volunteer 2 with 4x undersampling at 100% gating efficiency. Residual aliasing is reduced and image structures appear sharper when compared to IMC. **c)** IMC for volunteer 4 with 4x undersampling at 100% gating efficiency. Residual aliasing is not significant in this volunteer, but the IMC still introduces additional blurring to the image. **d)** TV-GMD for volunteer 4 with 4x undersampling at 100% gating efficiency. A sharper reconstruction is obtained with the TV-GMD.

6.4.3 In vivo experiments

Figure 6.7 shows multiple slice orientations for the non-motion corrected, gated, GMD and TV-GMD reconstructions for volunteer 1. It can be seen that TV-GMD and gated reconstructions yield images of similar quality, correcting most ghosting and blurring present in the non-motion corrected (NMC). The gated and NMC reconstructions have an undersampling factor of 2x, while the GMD and TV-GMD resulted in an undersampling of 3.5x for this volunteer. Remaining artifacts from undersampling and noise amplification can be observed in the GMD reconstruction (Figure 6.7). Comparison between GMD and TV-GMD highlights how TV regularization improves the conditioning of the reconstruction.

Figure 6.8 shows multiple slice orientations for volunteer 2, where the GMD and TV-GMD reconstructions resulted in an undersampling of 4x, compared to 2x for the gated and NMC. The TV-GMD presents a sharper reconstruction than the gated (Figure 6.8), due to the fact that the resulting binning windows were smaller (2.76 mm average) than the gating window (5 mm). Note that undersampling artifacts are stronger for this case, but still can be reduced by TV regularization.

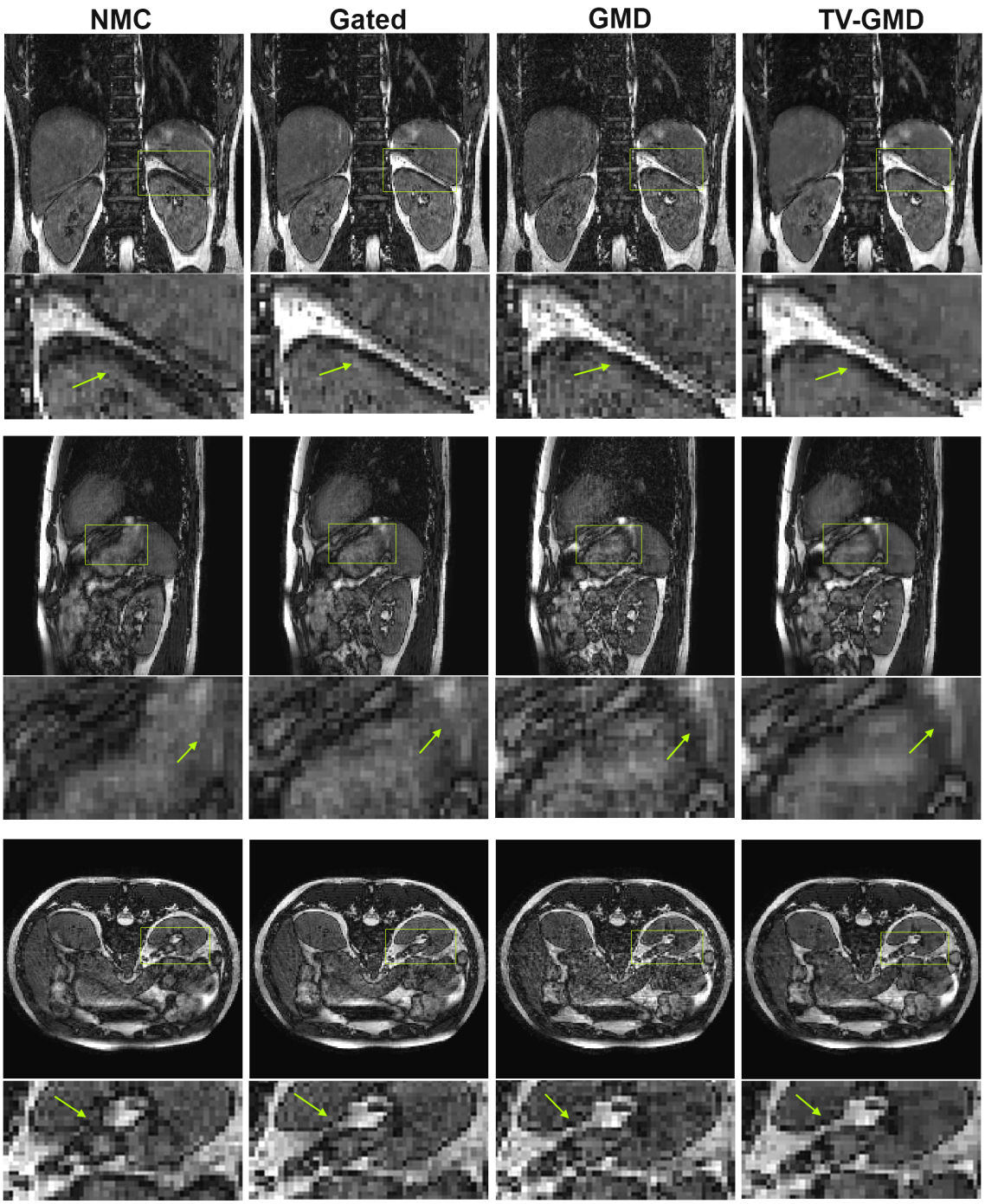

Figure 6.7: Coronal (top), sagittal (middle) and axial (bottom) slices for volunteer 1 with maximum respiratory amplitude of 14.8 mm (including zoom-in images, arrows point out some main differences). **NMC (non-motion corrected):** 2x undersampled at 100% gating efficiency. Several structures in the image are corrupted by motion. **Gated:** 2x undersampled at 60% gating efficiency. Most structures are sharper than the NMC. **GMD:** 3.5x undersampled at 80% gating efficiency. The GMD is sharper than the NMC, but presents remaining undersampling artifacts. **TV-GMD:** 3.5x undersampled at 80% gating efficiency. The total variation regularization improves undersampled reconstruction at the expense of minor blurring.

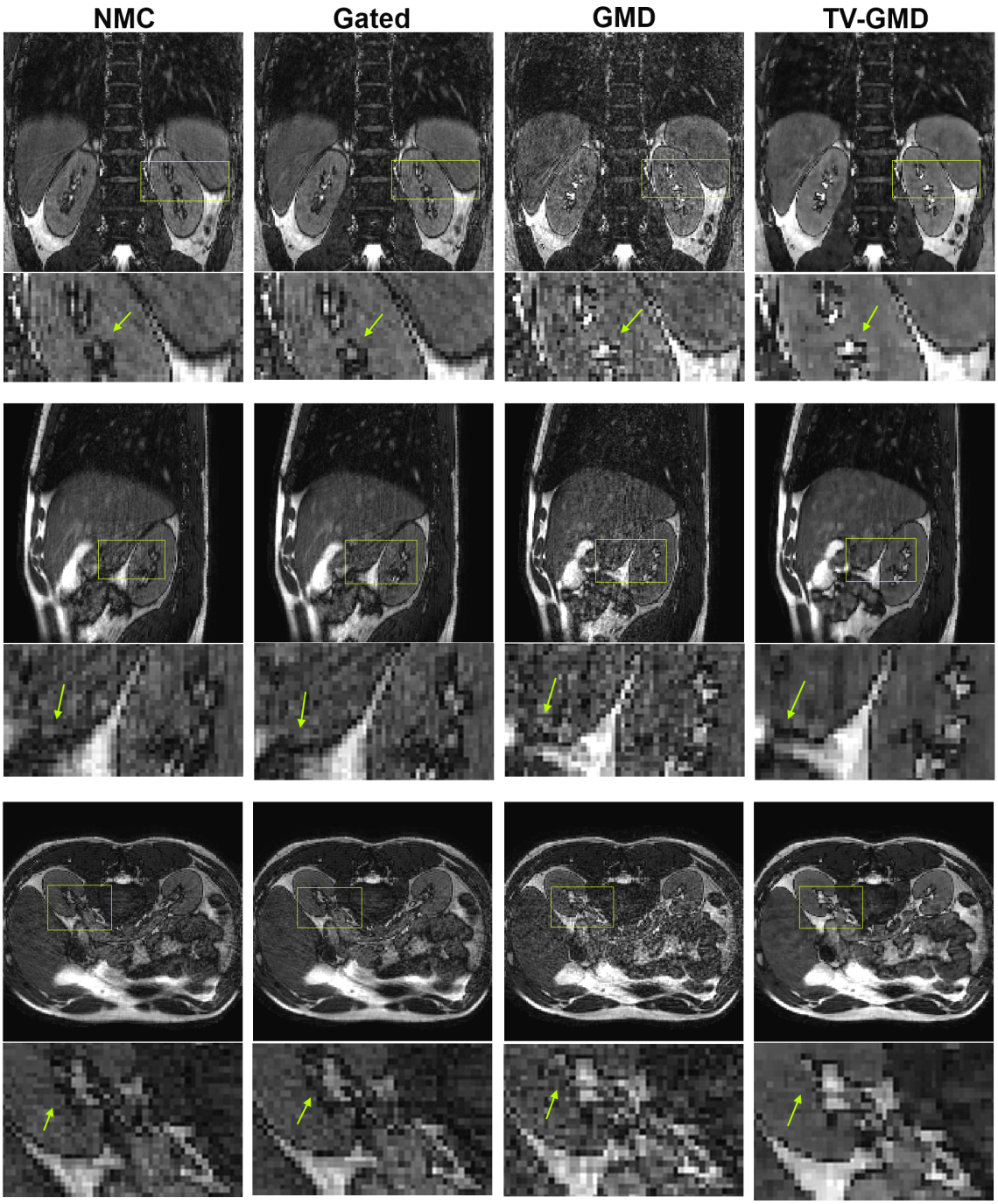

Figure 6.8: Coronal (top), sagittal (middle) and axial (bottom) slices for volunteer 2 with maximum respiratory amplitude of 8.2 mm (including zoom-in images, arrows point out some main differences). **NMC (non-motion corrected):** 2x undersampled at 100% gating efficiency. Some blurring is visible in image structures and the liver-lung border. **Gated:** 2x undersampled at 77% gating efficiency. There is no significant improvement, as the gated reconstruction uses a 5 mm window. **GMD:** 4x undersampled at 96% gating efficiency. The high undersampling creates a strong noise-like aliasing. **TV-GMD:** 4x undersampled at 96% gating efficiency. The total variation regularization improves GMD undersampled reconstruction at the expense of some minor blurring, despite using only 128 radial profiles.

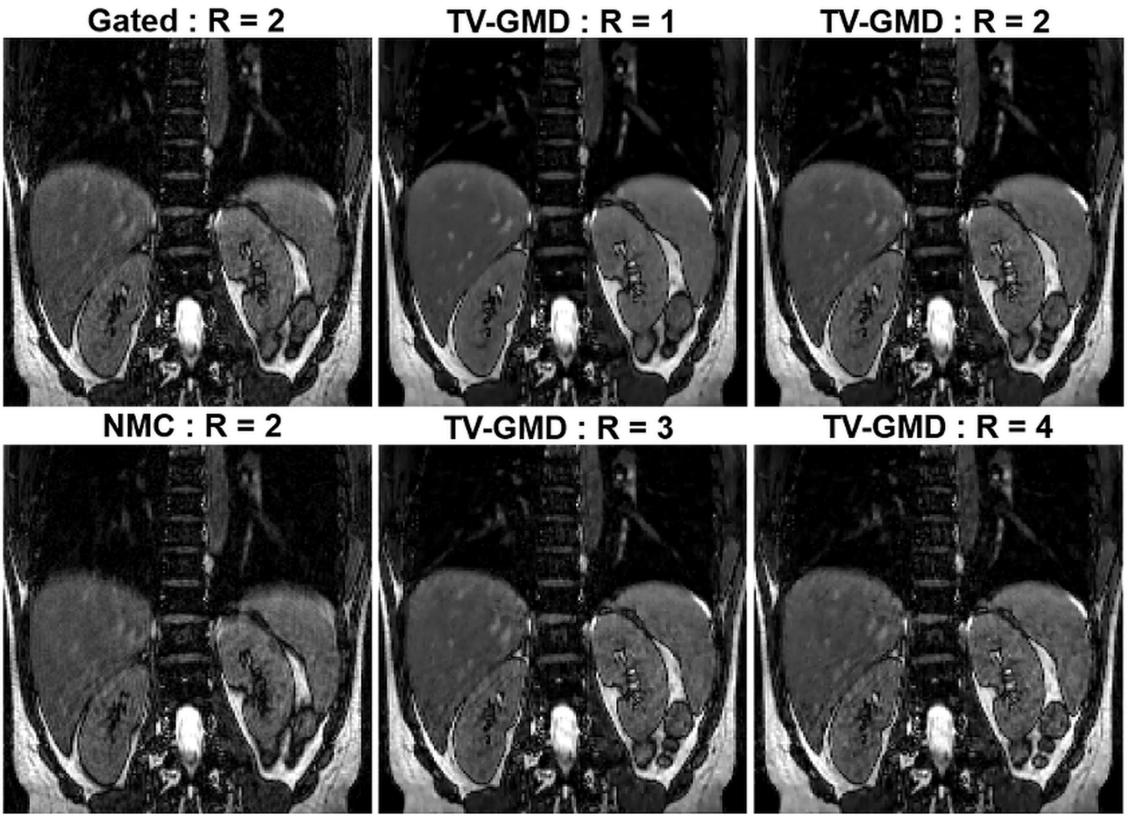

Figure 6.9: Coronal slices for volunteer 3 reconstructed with TV-GMD at undersampling factors (R) of 4x, 3x, 2x and 1x, corresponding to 128, 170, 256 and 512 radial profiles, respectively. The gated and non-motion corrected (NMC) reconstructions have an undersampling factor of 2. A signal-to-noise improvement is visible as more data is used for the reconstruction. Vessel features benefit particularly from this additional data.

Reconstructions for the TV-GMD at various undersampling factors in two volunteers are shown in Figures 6.9 and 6.10. As expected, undersampling artifacts decrease with increasing data used for reconstruction. The proposed method is flexible in the choice of the maximum undersampling factor of the reconstructed image which may be useful for clinical applications that require specific signal-to-noise ratios.

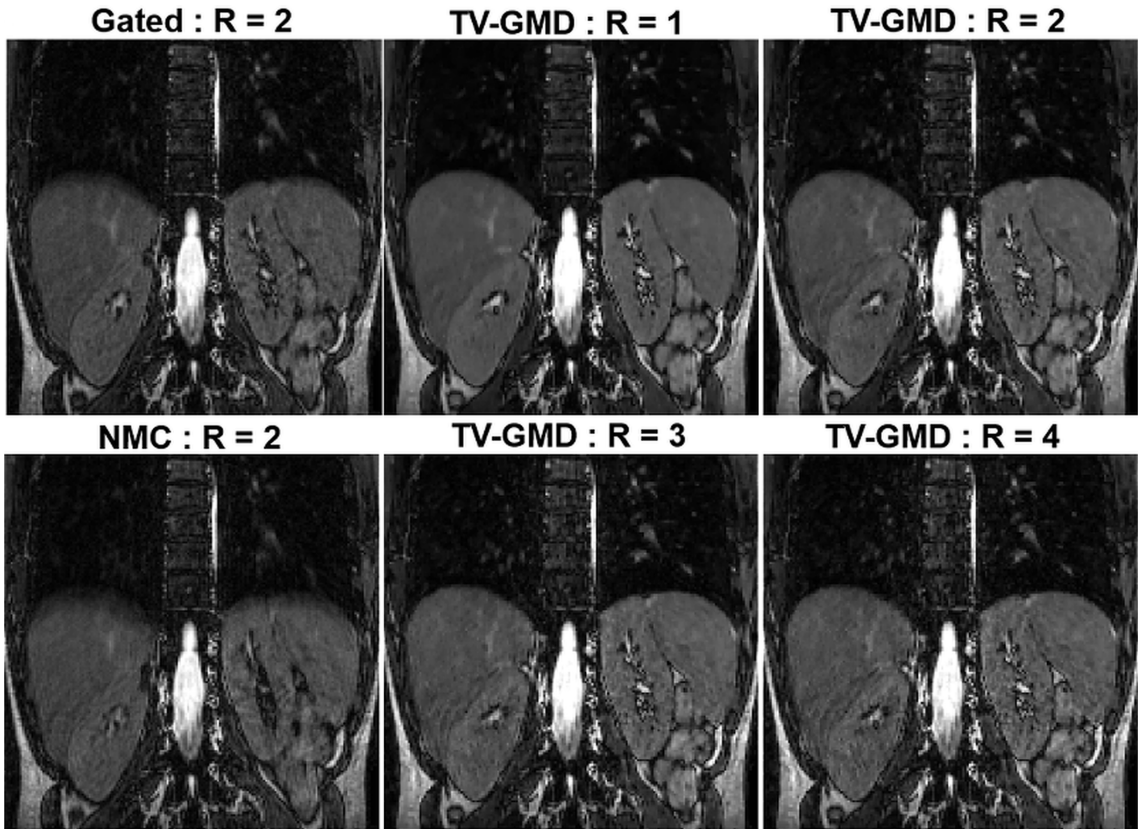

Figure 6.10: Coronal slices for volunteer 4 reconstructed with TV-GMD at undersampling factors (R) of 4x, 3x, 2x and 1x, corresponding to 128, 170, 256 and 512 radial profiles, respectively. The gated and non-motion corrected (NMC) reconstructions have an undersampling factor of 2. Small, low contrast features in the image are better defined with the TV-GMD reconstruction and benefit from the lower undersampling factors.

Bar plots of the average acquisition times, undersampling factors, gradient entropies, liver sharpness, sharpness visual score and image quality rank over all 9 volunteers are shown in Figure 6.11. When comparing with the gated reconstruction, the TV-GMD reconstruction reduces the average scan time from 101 to 34 seconds.

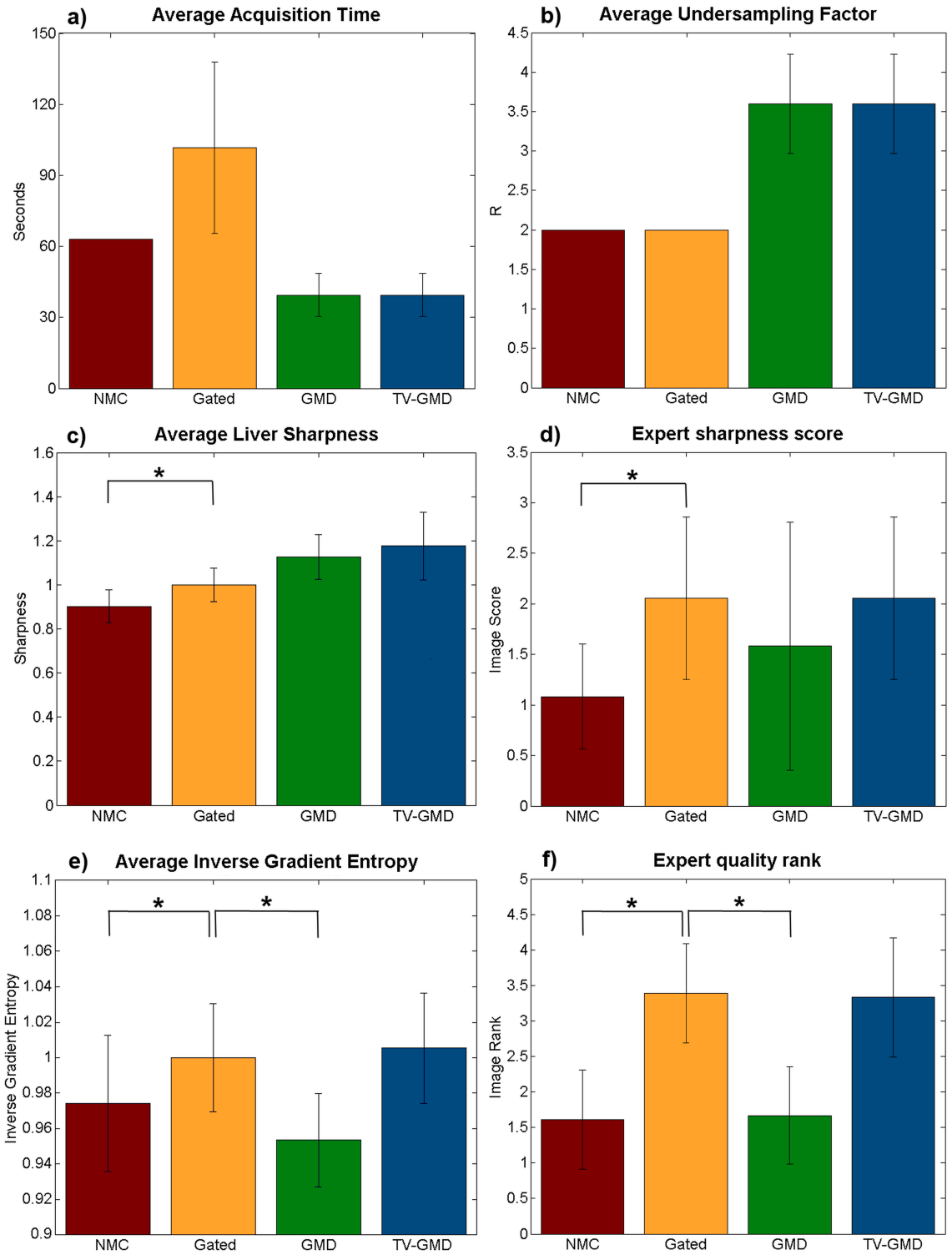

Figure 6.11: Bar plots comparing the performance of the non-motion corrected (NMC), gated, GMD and proposed TV-GMD reconstructions in terms of **a)** average acquisition time, **b)** average undersampling factor, **c)** average liver sharpness (paired t-test), **d)** expert sharpness score (Wilcoxon test) (0: extreme blurring to 4: no blurring), **e)** average (inverse) gradient entropy (paired t-test) and **f)** expert overall quality rank (Wilcoxon signed rank test) (1: worst to 4: best). Statistically different results with a P-value < 0.01 are marked with (*). Error bars denote standard deviation.

The gradient entropy indicates the TV-GMD and gated reconstructions have the best image quality (1.00 and 1.00, respectively), significantly better than NMC (0.97) and GMD (0.95). Image rank from visual assessment agreed with gradient entropy, marking TV-GMD (3.33) just below the gated (3.39), significantly better than NMC (1.61) and GMD (1.67). Image sharpness score from visual assessment yielded similar values between the TV-GMD (2.22) and gated (2.44), differentiating them from the NMC (1.17). Liver sharpness measures were not as sensitive as expert sharpness evaluation, but presented a similar behaviour, marking TV-GMD as the best (1.18), followed by GMD (1.12) and gated (1.00), significantly better than NMC (0.90).

6.5 Discussion

The proposed approach accelerates the acquisition via undersampling and 3D non-rigid motion correction, reducing the average scan time by 2.6x when compared to a gated acquisition. Here, motion is estimated from highly undersampled respiratory resolved images (TV-SENSE) and corrected in the reconstruction of the undersampled final data set (TV-GMD). Gradient entropy and image quality ranking present similar values for the TV-GMD and gated reconstructions, distinguishing them as superior to the NMC and GMD. The noise-like aliasing present in the GMD reconstruction is responsible for the worse values in gradient entropy. The liver sharpness and expert sharpness

score show TV-GMD removes motion-induced blurring (visible in the NMC) to a similar level as the gated reconstruction. In cases of uniform breathing the TV-GMD achieves sharper reconstructions than the gated as it uses binning windows (2.76 mm average) smaller than the gated window (5mm).

This experiment was carried out retrospectively to compare different approaches, but the decision to stop a running acquisition once enough data has been acquired could be performed prospectively. This process requires a 1D FFT and a cross-correlation (to obtain the self-navigation signal), followed by the adaptive binning algorithm, taking less than 3 ms to compute. One limitation of the proposed method is the 3 hour reconstruction time. Reconstruction times increase with both the amount of data used and the number of bins. The bottleneck in these reconstructions is the non-uniform Fourier transform, which may be accelerated by GPU implementations [198]. Another solution to this problem would be to use Cartesian trajectories with similar properties to the G-RPE, such as G-CASPR [57, 166] or VDRad [45].

Note that the proposed approach requires a superior-inferior readout for self-navigation and alternative navigation strategies will be needed for trajectories with readouts in other directions. Another limitation is error propagation from motion estimation. If the estimated motion is not accurate, this can lead to artefacts in the TV-GMD reconstruction (results not shown here). Here we force every bin to respect α_{max}

to guarantee accurate and reliable motion estimation. The proposed method is limited to inter-bin motion correction, thus a significant fraction of k-space remains uncorrected in the form of intra-bin motion. In this work, we perform motion corrected reconstructions with undersampling factors up to 4x. At high undersampling factors, over-regularization with total variation may create piecewise smoothing artefacts therefore an appropriate selection of a regularization parameter is needed.

It has been shown that GMD is capable of nearly perfect motion correction when the motion fields are known exactly [14]. Thus, future improvements should target the motion estimation. Firstly, self-navigation may be improved by using multiple coil information [148], as opposed to the single coil approach used here. Secondly, the number of bins may be increased by lowering the bin window size, w_{max}. This approach requires longer acquisitions and additional reconstruction time. However intra-bin motion and total variation artefacts of the motion corrected images should be reduced. Thirdly, bin quality may be improved by introducing pseudo-random sampling in the radial direction, which may improve both motion estimation and motion corrected reconstruction.

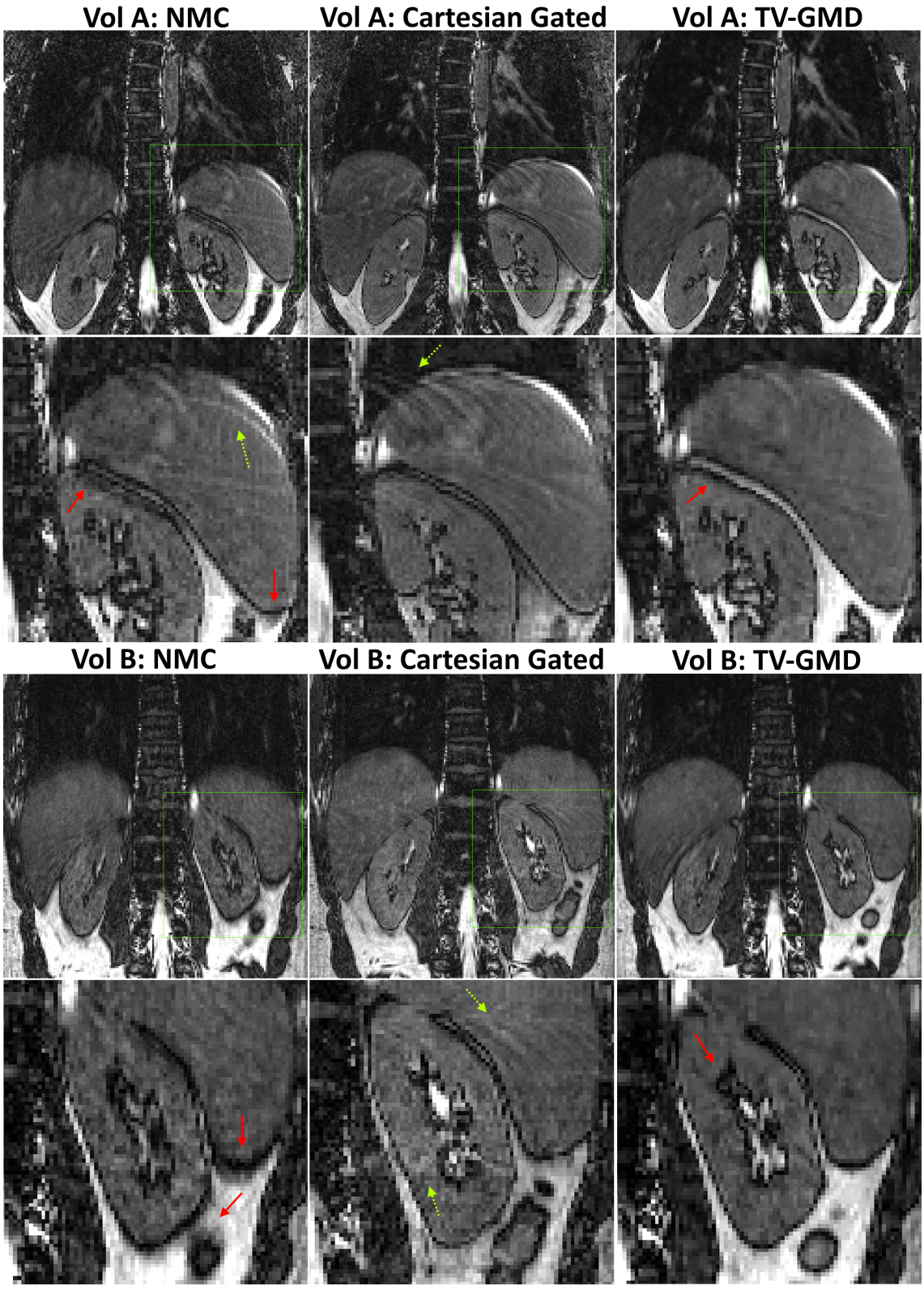

Figure 6.12: Coronal slices for a non-motion corrected **(NMC)** G-RPE 2x radially undersampled, Cartesian navigator **Gated** (5mm) 2x undersampled and **TV-GMD** G-RPE 2x radially undersampled for two volunteers. The Cartesian **Gated** and **TV-GMD** approaches compensate motion to a comparable degree. Residual motion is still present in the Cartesian **Gated** (ghosting, yellow dotted arrows) and **TV-GMD** (minor blurring, red full arrows).

The value α_{max} was determined from a single volunteer study and although it provided successful reconstructions for all nine volunteers, further investigation may provide a more optimal setting. Additional changes of the system due to breathing, such as B_0 and B_1 fields, should considered and studied in the future.

In this work, a self-gated reconstruction was used as reference to allow comparison of different methods using the same data. However, an additional comparison with a standard Cartesian gated acquisition is now warranted.

A preliminary study was performed to compare the proposed approach with a Cartesian gated acquisition. 2x undersampled Cartesian navigator gated (5 mm) and G-RPE datasets were acquired on two healthy volunteers using the same parameters as before.

Coronal slices for a non-motion corrected (NMC) G-RPE 2x radially undersampled, Cartesian gated 2x undersampled (AP direction) and TV-GMD G-RPE 2x radially undersampled are shown in Figure 6.12, for two volunteers. These initial results show that Cartesian gated and TV-GMD remove most motion artifacts present in the NMC images. However, residual motion in the Cartesian gated creates coherent ghosting, whereas in TV-GMD it creates blurring. Further studies comparing the proposed approach against a Cartesian gated scan in patients will be needed for clinical validation.

6.6 Conclusion

A motion corrected reconstruction framework for accelerated free-breathing 3D abdominal imaging has been presented. The proposed approach does not require additional training data or external sensors. Motion is estimated from highly undersampled data and incorporated into the reconstruction. In vivo results demonstrate the potential of the proposed method to provide similar image quality as a gated acquisition while reducing scan times by a factor of 2.6.

Chapter 7

Highly Efficient non-rigid Motion Corrected 3D Whole-Heart Coronary Vessel Wall Imaging

7.1 Introduction

Coronary magnetic resonance angiography (CMRA) has shown potential as a non-invasive diagnostic tool to assess location and degree of lumen stenosis in coronary heart disease [106]. CMRA can be used to detect and characterize atherosclerosis, a plaque accumulation that can develop in the vessels. The plaque narrows the cross-sectional area of the vessel, therefore impeding blood flow and potentially blocking it. A schematic of coronary atherosclerosis is depicted in Figure 7.1. As coronary atherosclerosis is not necessarily stenotic [201] due to outward remodelling of the vessel wall [150], both lumen and wall assessments are desirable to more comprehensively detect coronary

atherosclerosis. Atherosclerotic plaque burden increases as disease develops often without significant changes to the vessel lumen. Coronary plaque burden has been shown to correlate with risk of future coronary events [113] and thus direct and non-invasive visualization of both lumen and vessel wall is desired.

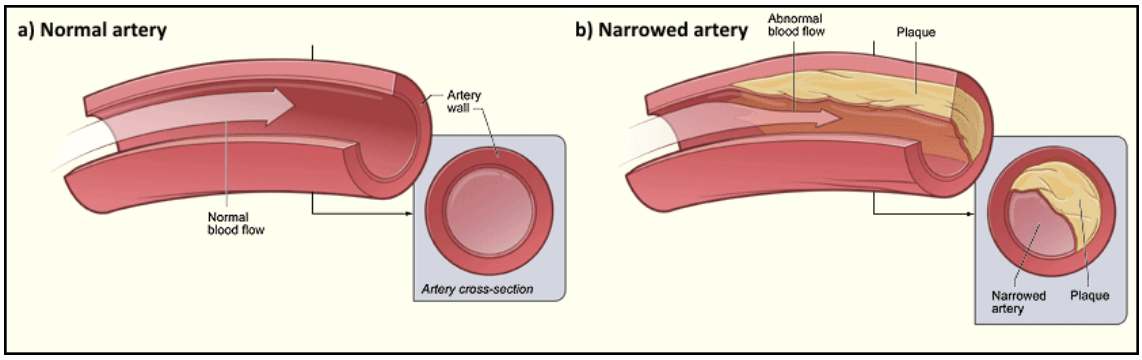

Figure 7.1: **a)** Normal, unobstructed artery with normal blood flow. **b)** Narrowed artery due to significant plaque accumulation, obstructing blood flow. Taken from www.nhlbi.nih.gov.

A 3D flow independent approach for vessel wall imaging was proposed recently [6], based on an interleaved acquisition and subtraction of data with (T2prep(+)) and without (T2prep(-)) a T2-preparation prepulse. This approach provides simultaneously coronary lumen (T2prep(+)) and vessel wall images, however the required subtraction is particularly sensitive to respiratory motion corruption. In the work by Andia and colleagues [6], respiratory motion was minimized using a 1D pencil-beam diaphragmatic navigator gating [218], with data being accepted only when both T2prep(+) and T2prep(-) acquisitions were within the same small gating window of the respiratory cycle. This leads to long and unpredictable acquisition times since only a fraction of

the acquired data was accepted for reconstruction (referred to as scan efficiency). Another limitation of 1D navigator gating is that only foot-head (FH) global translation can be corrected (using slice tracking). Thus, motion from anterior-posterior (AP), right-left (RL) and non-rigid components remain uncorrected, which has been shown to be significant in some subjects [133,191]. Additionally, heart motion is estimated indirectly from the right hemi-diaphragmatic displacement using a fixed linear correction factor of 0.6 [217]. It has been shown that the optimal factor varies for different regions of the heart and also for different subjects, meaning that motion artifacts may not be fully resolved if a fixed factor is used.

Recently, image navigators (iNAVs) have been introduced to directly estimate the respiratory motion of the heart and allow separation of static tissues from the moving heart [3, 19, 85, 87, 153, 154, 187]. Most of these approaches acquire a low-resolution image navigator before the actual CMRA acquisition to correct 2D or 3D translational respiratory motion in a beat-to-beat fashion [87, 187]. To account for more complex motion, respiratory binning techniques have been proposed [153, 166].

Beat-to-beat approaches usually provide high-temporal but low-spatial resolution motion estimation whereas binning approaches provide high-spatial but low-temporal motion estimation. In the binning approach, the acquired data is assigned into several states of the breathing cy-

cle or bins and afterwards corrected to a reference position using the motion estimated from the binned images. 3D affine motion can be estimated from these bins and corrected in either k-space [153] or directly in the reconstruction [166]. Reconstruction based non-rigid correction has also been applied to cardiac MR, using motion derived from training data [183] or coupled reconstruction problems [149]. An alternative approach to non-rigid correction has also been introduced in the form of localized autofocusing techniques [44, 91, 122].

A recently introduced approach combined beat-to-beat 2D translational correction with bin-to-bin 2D affine correction for coronary lumen imaging [3]. However, that approach does not correct for motion in the AP direction and only affine correction is performed in the other two directions, directly in the k-space. In this work, we propose a combined motion correction approach for coronary lumen and vessel wall imaging using beat-to-beat 2D translational motion correction and bin-to-bin 3D non-rigid motion correction. Motion corrected vessel wall images are obtained by acquiring a set of T2prep(+)/T2prep(-) data interleaved with a 2D iNAV in every heartbeat which is used for translation correction and binning. Bins are reconstructed with soft-gated [100] iterative SENSE [168] and non-rigid motion estimated via image registration [138] is incorporated into a motion corrected reconstruction [14]. Subsequently, vessel wall images are obtained by subtraction as described in [6], producing a set of motion corrected,

co-registered 3D coronary lumen and vessel wall images. The proposed method (2D translation + 3D non-rigid) was tested in ten healthy subjects and compared with a diaphragmatic gated and corrected coronary MR angiogram, 2D translational motion correction and no motion correction.

7.2 Methods

The proposed framework acquires two datasets simultaneously to produce vessel wall images. Both datasets undergo the same reconstruction framework described below.

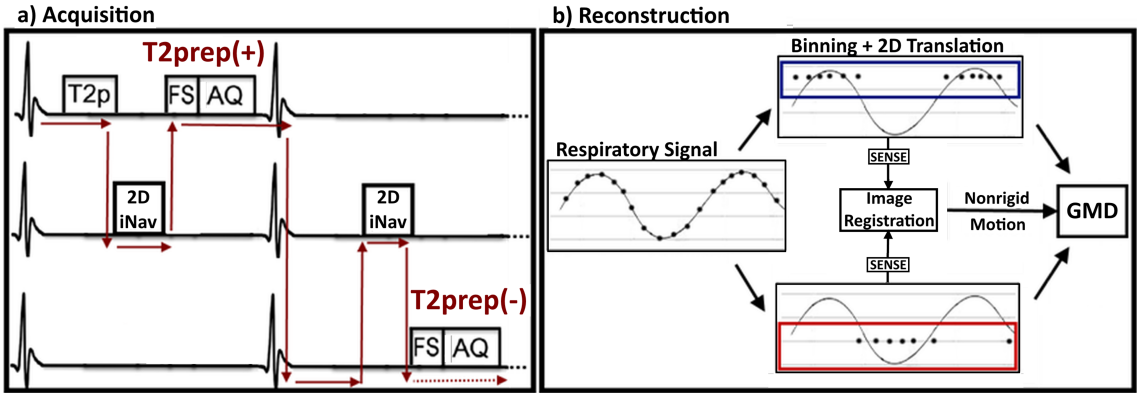

Figure 7.2: Framework of the proposed approach. **a)** Acquisition: data is acquired using interleaved scanning, allowing for datasets with/without T2 preparation (T2prep(+)/T2prep(-), respectively) to be acquired simultaneously with a 2D image navigator (2D iNAV). In each heartbeat, a T2 preparation prepulse (T2p) is applied (in the T2prep(+) case), followed by the 2D iNAV, a spectral fat saturation pulse (FS) and finally image acquisition (AQ). The arrows depict how the three sequences interleave at runtime. **b)** Reconstruction: takes place in two steps. First, foot-head translation of the heart obtained from the 2D iNAVs is used to derive a respiratory signal. Data is grouped into bins according to the respiratory position and beat-to-beat translational motion is corrected in k-space. Each binned dataset is reconstructed with iterative SENSE and the resulting images are registered to retrieve a non-rigid motion field. Second, the motion field is used in a General Matrix Description (GMD) reconstruction to correct inter-bin non-rigid motion.

7.2.1 Image acquisition

Data was acquired using an interleaved scanning framework [86]. Three scans were performed simultaneously: 3D segmented whole-heart with T2 preparation (T2prep(+)), 3D segmented whole-heart without T2 preparation (T2prep(-)) and 2D single shot golden-radial (GR) coronal image navigator (2D iNAV). The protocol was defined to acquire the T2prep(+) and T2prep(-) datasets at alternating heartbeats, with a 2D single shot GR iNAV being acquired every heartbeat (Figure 7.2a). In every other heartbeat, a T2 preparation pulse was applied (for T2prep(+)), followed by the 2D iNAV and a fat saturation pulse (FS), prior to 3D segmented data acquisition. The interleave scheme for the three scans is depicted in the sequence diagram of Figure 7.2a. The 2D iNAV used a low flip angle to minimize the effect on the magnetization prior to acquisition of the 3D high resolution data.

7.2.2 Motion estimation and correction

The framework for motion estimation and correction was performed in two steps: 2D beat-to-beat translational motion correction, followed by 3D bin-to-bin nonrigid motion correction, as shown in Figure 7.2b). T2prep(+) and T2prep(-) data were motion corrected separately and registered after motion correction.

7.2.3 Beat-to-beat translational motion estimation and correction

Beat-to-beat 2D translational motion was estimated from the iNAVs. Golden-radial iNAVs undergo a gridding reconstruction [77] using an iterative density compensation function [232], providing a set of low spatial, high temporal resolution images. A region-of-interest (ROI) was selected around the heart [3] and rigid image registration was performed [32] to estimate FH and RL global translational motion. Outliers due to deep breaths were removed prior to any corrections. The distribution of motion states was approximated as a Gaussian distribution. Even though this is not guaranteed to always be the case (as it depends on the subject breathing pattern), it provided satisfactory results in these experiments. K-space data with estimated FH motion $\mathbf{T_{FH}} > \mu \pm 2\sigma$ of the respiratory signal (μ being the average respiratory position, σ the corresponding standard deviation) were considered outliers and removed prior to reconstruction. Due to the difficulty of correcting and estimating motion in sparsely populated regions of the respiratory cycle, we opted to recover the ≈5% most motion corrupted data points (outliers) via parallel imaging [168]. The iNAV reference frame chosen for image registration corresponded to the average position at end-expiration. FH motion information was also used to bin the 3D data according to the position in the respiratory cycle. 2D global translational correction was applied within each

bin by the corresponding phase shift in k-space [26]:

$$\mathbf{K} = \mathbf{K}' exp(2\pi i \mathbf{k}' \cdot \mathbf{T}) \tag{7.1}$$

where $\mathbf{K}$ is the translation corrected k-space, $\mathbf{K}'$ the acquired k-space, $\mathbf{k}'$ the corresponding k-space trajectory and $\mathbf{T}$ the estimated 2D translation vector.

7.2.4 Bin-to-bin nonrigid motion estimation

Bin-to-bin 3D nonrigid motion is estimated from the data itself. After translational correction each 3D bin is reconstructed with a soft-gating [68,100] approach where data is weighted according to its FH distance to the centre of the bin, $\mathbf{T_{FH}}$. The binned, soft-gated reconstruction can be formulated as:

$$\hat{\mathbf{I}}_\mathbf{b} = arg\ min_{\mathbf{I_b}} ||\mathbf{W_b}(\mathbf{EI_b} - \mathbf{K_b})||_\mathbf{2}^\mathbf{2} \tag{7.2}$$

where $\mathbf{I_b}$ are the reconstructed bin volumes, $\mathbf{W_b}$ is a diagonal matrix containing data weights for bin b, $\mathbf{E}$ is the encoding matrix that includes the Fourier transform, coil sensitivities and sampling operations, and $\mathbf{K_b}$ is the acquired data at each bin. The diagonal elements of $\mathbf{W_b}$ were defined to be a linear function of the respiratory position of k-space data as follows:

$$\mathbf{w_k^b} = \begin{cases} 1 & ,if\ (\mathbf{R_{FH}}(b) - \mathbf{T_{FH}^b}(k) + r)/r > 1 \\ 0 & ,if\ (\mathbf{R_{FH}}(b) - \mathbf{T_{FH}^b}(k) + r)/r < 0 \\ (\mathbf{R_{FH}}(b) - \mathbf{T_{FH}^b}(k) + r)/r & ,\ otherwise \end{cases} \tag{7.3}$$

where $\mathbf{w_k^b}$ are the diagonal weights for data k at bin b, $\mathbf{R_{FH}}(b)$ is the radius of bin b (FH distance from the bin centre to the edge), $\mathbf{T_{FH}^b}(k)$ is the distance of k-space point k to the centre of bin b and r is a parameter defining the range of the soft-gate. Points within the bin have unity weight, decreasing linearly to zero as the distance of bin radius plus soft-gate range is reached. Increasing r reduces undersampling artefacts at the expense of minor blurring. Bins were reconstructed with iterative SENSE [168]. Image registration based on free-form deformations [138] was performed, using the end-expiration bin as reference [161], to estimate 3D nonrigid respiratory motion.

7.2.5 Translation plus non-rigid motion correction

Translational correction is applied directly in k-space to correct intra-bin motion, as described above in equation (7.1). Inter-bin motion is corrected using the General Matrix Description (GMD) introduced in [14]:

$$\begin{aligned} \hat{\mathbf{I}} &= arg\ min_{\mathbf{I}} ||\mathbf{EI} - \mathbf{K}||_{\mathbf{2}}^{\mathbf{2}} \\ \mathbf{E} &= \sum_{\mathbf{b}} \mathbf{A_b F S U_b} \end{aligned} \tag{7.4}$$

where $\hat{\mathbf{I}}$ is the motion corrected volume, $\mathbf{K}$ is the translation corrected k-space data, $\mathbf{A_b}$ is the sampling matrix for bin b, $\mathbf{F}$ is the Fourier transform, $\mathbf{S}$ are the coil sensitivities for all coils and $\mathbf{U_b}$ are the image warping operators defined in Chapter 5 that apply the non-rigid motion fields obtained via image registration. The GMD reconstruction was performed with a linear conjugate gradient method [89], using the relative residual as regularization to prevent noise amplification.

7.2.6 Coronary Vessel wall

The T2prep(+) and T2prep(-) complex datasets were subtracted to produce coronary vessel wall images as described in [6]:

$$I_{VW} = T2prep(-) \ - \ \lambda T2prep(+) \tag{7.5}$$

where I_{VW} is the vessel wall image, T2prep(-) and T2prep(+) are the motion corrected images without and with T2 preparation pulse, respectively. The parameter λ is used to achieve maximum cancelation of signal from arterial blood. T2prep(-) and T2prep(+) were registered using nonrigid deformation [138] prior to image subtraction to guarantee spatial alignment. The optimum value for λ can be computed as

a function of the heart rate and acquisition protocol as shown in [6]. In the presence of errors in the T2 preparation module it is possible to manually adjust the λ value to achieve the best vessel wall image quality.

7.3 Experiments

7.3.1 Acquisition

Ten subjects (ages 32±8 years) were scanned under free-breathing on a 1.5T clinical scanner (Philips Achieva, Philips Healthcare, Best, The Netherlands) using a 32-channel coil. Written informed consent was obtained from all subjects according to institutional guidelines and the study ("Development of novel magnetic resonance techniques using healthy volunteers") was approved by the institutional review board. T2prep(+), T2prep(-) and iNAV data were acquired using an interleaved scanning framework (31). T2prep(+) and T2prep(-) data were acquired with an ECG-triggered 3D balanced steady-state free precession sequence with the following parameters: coronal slices, RL phase encoding, 1 x 1 mm in-plane resolution, 2 mm slice thickness, 300 x 300 x 90 mm field of view, TR/TE = 5.3/2.6 ms, flip angle = 70, readout bandwidth (per pixel) = 433 Hz, subject specific acquisition window (ranging from 105.5 to 116.1 ms corresponding to 20-22 k-space lines acquired per heartbeat), spectral fat saturation prepulse,

subject specific mid-diastolic trigger and a low-high (centric) Cartesian acquisition with radial k-space order in ky and kz direction. The T2prep(+) acquisition included a T2 preparation pulse with a duration of 80 ms and two 180° adiabatic refocusing pulses. A 2D golden radial iNAV was acquired using a single shot spoiled gradient echo sequence with the following parameters: coronal slice (same geometry as the image data acquisition), 4 x 4 mm in-plane resolution, 25 mm slice thickness, 300 x 300 field of view, TR/TE = 2.4/1.07 ms, flip angle = 5°, acquisition window of 47.2 ms with 24 angular profiles per cardiac cycle. Additionally, an ECG-triggered 3D CMRA with diaphragmatic respiratory gating and tracking (6 mm gating window and scaling factor of 0.6) was performed for comparison, using the T2prep(+) protocol as described above. The acquisition order of the proposed approach and the gated and tracked CMRA scan was randomized. The 3D CMRA protocol had a nominal scan time of approximately 10 minutes at 60 beats per minute.

7.3.2 Reconstruction

Three reconstructions for coronary lumen and vessel wall were obtained from the same acquired data: (a) non-motion corrected (NMC), (b) 2D translational correction (TC), and (c) the proposed two step translational and nonrigid correction (TC+GMD). Additionally, the 3D CMRA with a hemi-diaphragmatic navigator and respiratory-gated

and corrected reconstruction (Gated) was used for comparison of coronary lumen images. The proposed method used the following (empirically chosen) parameters: 3 bins automatically defined such that every bin had the same amount of data; the soft-gate range (r) was set to 1 mm to keep any residual motion smaller than the voxel size; the minimum relative residual of the iterative reconstructions was set to 0.05%. Four of the acquired datasets were binned and reconstructed using three, four and five bins. All reconstructions presented similar results and therefore three bins were used in this work to reduce computational time. The stopping criterion (relative residual) was determined by inspecting the noise amplification through different iterations of these bin reconstructions.

Respiratory outliers were automatically removed before TC+GMD and TC reconstructions as described before. For the TC+GMD, each bin was translation corrected towards the central position of the bin. This translation corrected k-space (i.e. the group of bins) was reconstructed with the General Matrix Description (30) after non-rigid motion estimation. The TC approach used a 2D translational correction to a single reference followed by an iterative SENSE reconstruction, taking ≈120 seconds. The proposed TC+GMD required a set of 2D translational corrected soft-gated iterative SENSE bin reconstructions (≈490 seconds), followed by non-rigid image registration (≈170 seconds) and finally a motion corrected reconstruction (≈1020 seconds)

for a total of ≈1680 seconds. All reconstructions, image subtraction and post-processing were performed off-line in MATLAB (Mathworks, Natick, Massachusetts, USA) on a PC with 12 CPUs (Intel Xeon 3.07 GHz).

Coronary vessel wall images were obtained as described in [6], where a simulation study showed that the optimal λ for a balanced SSFP sequence lied between 1.21 and 1.27. Consequently, $\lambda = 1.25$ was used in this study for all subtractions. All reconstructions were reformatted onto a 2D plane using Soap-Bubble software [64], facilitating the visualization of the right (RCA) and left coronary arteries (LCA). All image metrics were evaluated on reformatted images after 4x zero-padding (0.25 x 0.25 mm in plane reconstructed resolution).

7.3.3 Data analysis

To evaluate the quality of motion correction, measures of vessel length, diameter and sharpness were performed using Soap-Bubble on the lumen of T2prep(+) images obtained with NMC, TC, TC+GMD and Gated reconstructions. Lumen vessel length and diameter were obtained by tracking the visible length of each coronary vessel. Lumen vessel sharpness was computed by taking the maximum gradient normalized to maximum centre line intensity of profiles along the visible portion of the vessel. Lumen vessel sharpness was normalized to the mean sharpness of the reference Gated acquisition. Lumen diameter

and sharpness metrics were measured for the proximal section (first four centimetres of the vessel) and the full length separately.

To evaluate the impact of motion correction on the vessel wall images, metrics of vessel wall thickness and sharpness were computed on vessel wall images for NMC, TC and TC+GMD. Vessel wall sharpness was obtained by taking the maximum gradient normalized to maximum intensity of profiles along the visible portion of the vessel wall, but tracking each side of the vessel wall of each coronary independently with Soap-Bubble. Vessel wall sharpness was measured on a smaller vessel length than lumen sharpness as the wall was not always visible in the distal sections of the vessel, particularly on TC and NMC images. Vessel wall thickness was computed by first manually defining twenty 1D profiles across the visible vessel wall of both RCA and LCA coronaries, in the proximal and mid sections of the vessel. Following, the average full width at half maximum (FWHM) of the selected profiles was computed to measure the vessel wall thickness. Vessel wall sharpness was normalized to the mean sharpness of the TC+GMD reconstruction.

Two experts (with 20 and 7 years of experience in CMRA) blinded to the reconstruction methods were asked to score the sharpness of the coronary vessels on the following scale: (0) extreme blurring, (1) significant blurring, (2) some blurring, (3) minor blurring and (4) no blurring. Visual assessment was performed on both T2prep(+) lumen

and vessel wall images. Statistical significance of the automated metrics (vessel sharpness, vessel diameter, vessel length and vessel thickness) was evaluated with a two-sided paired t-test (P-value < 0.01); statistical significance of the visual evaluations was performed with a Wilcoxon signed rank test (P-value < 0.01). This P-value is stricter than required by the Bonferroni correction on a P-value of 0.05 for the coronary lumen and vessel wall comparisons ($\approx$0.016 and 0.025, respectively). Statistical significance was tested against the Gated acquisition for lumen images and against TC+GMD reconstruction for vessel wall images.

7.4 Results

Scans were completed successfully in all subjects. Motion correction with insufficient quality to visualize the coronaries was obtained for one subject using TC and TC+GMD approaches. This is thought to be due to the large FH respiratory amplitude of 30.8 mm and considerable cardiac motion in this subject. The gated acquisition had a scan efficiency of 29% in this case and after two thirds of the scan all data were accepted due to low scan efficiency. This subject was treated as an outlier and its results were not included in the statistics. The minimum, maximum and average (and standard deviation) of the FH respiratory amplitude for the remaining subjects were 7.8 mm, 17.8 mm and 11.0$\pm$3.2 mm, respectively. The minimum, max-

imum and average (and standard deviation) scan efficiencies for the gated acquisitions were 40%, 70% and 59±11%. For the proposed TC+GMD, the bin sizes (millimetres) for end-expiration, mid-cycle and end-inspiration bins were, respectively: 2.49±0.91, 2.30±1.50 and 5.90±2.24. The corresponding undersampling factors for these bins were as follows: 2.51±0.42, 2.21±0.35 and 3.15±0.51.

Reformatted images for Gated, TC+GMD, TC and NMC with T2prep(+) for subjects 1-4 are shown in Figure 7.3. Motion artifacts are visible in both coronaries in NMC, which are reduced by both TC and TC+GMD, although TC+GMD provides higher vessel sharpness in both the LCA and RCA (magnified box in subjects 1 and 2). These improvements are particularly visible in the distal part of the vessels (arrows in subjects 1 and 2). A set of T2prep(+)/T2prep(-) with the corresponding vessel wall image for subject 5 is shown in Figure 7.4. Most of the vessel wall in NMC is obscured by motion artifacts (arrows). Motion correction improves both T2prep(+) and T2prep(-) images, making the vessel wall visible in TC and better delineated with TC+GMD (magnified).

Vessel wall images for TC+GMD, TC and NMC for subjects 1-4 are shown in Figure 7.5. Corresponding cross-section views in the line marked locations in Figure 7.5 are shown in Figure 7.6. In Figure 7.5, vessel wall for NMC appears blurred, whereas delineation of the vessel wall is considerably improved with TC and the sharpness of the wall

further improved by TC+GMD.

These improvements are clearly seen in the cross-section views in Figure 7.6. The wall is not visible in most cases for NMC, becomes visible for most cases with TC and appears sharper with TC+GMD. Residual artifacts are visible in the vessel wall images, originating from incomplete nulling of the blood pool in the subtraction. Inhomogeneities in the B0 and B1 fields cause the T2prep to be spatially dependent, leading to incomplete signal cancelation in some regions of the image.

Metrics for T2prep(+) coronary lumen evaluations are shown in Figure 7.7. Measured lumen vessel lengths were very similar for Gated and TC+GMD, with lower values for TC and NMC. Significant differences were found between Gated and NMC for both coronaries. Lumen vessel length indicates reduced visibility of the distal part of both RCA and LCA when no motion compensation method is employed (NMC), showing gradual improvements with TC, TC+GMD and Gated. Similar results are found for lumen vessel sharpness, with significant differences between Gated and NMC for both coronaries. TC+GMD had the smallest lumen diameter for both coronaries, whereas NMC had the largest due to blurring effects of respiratory motion.

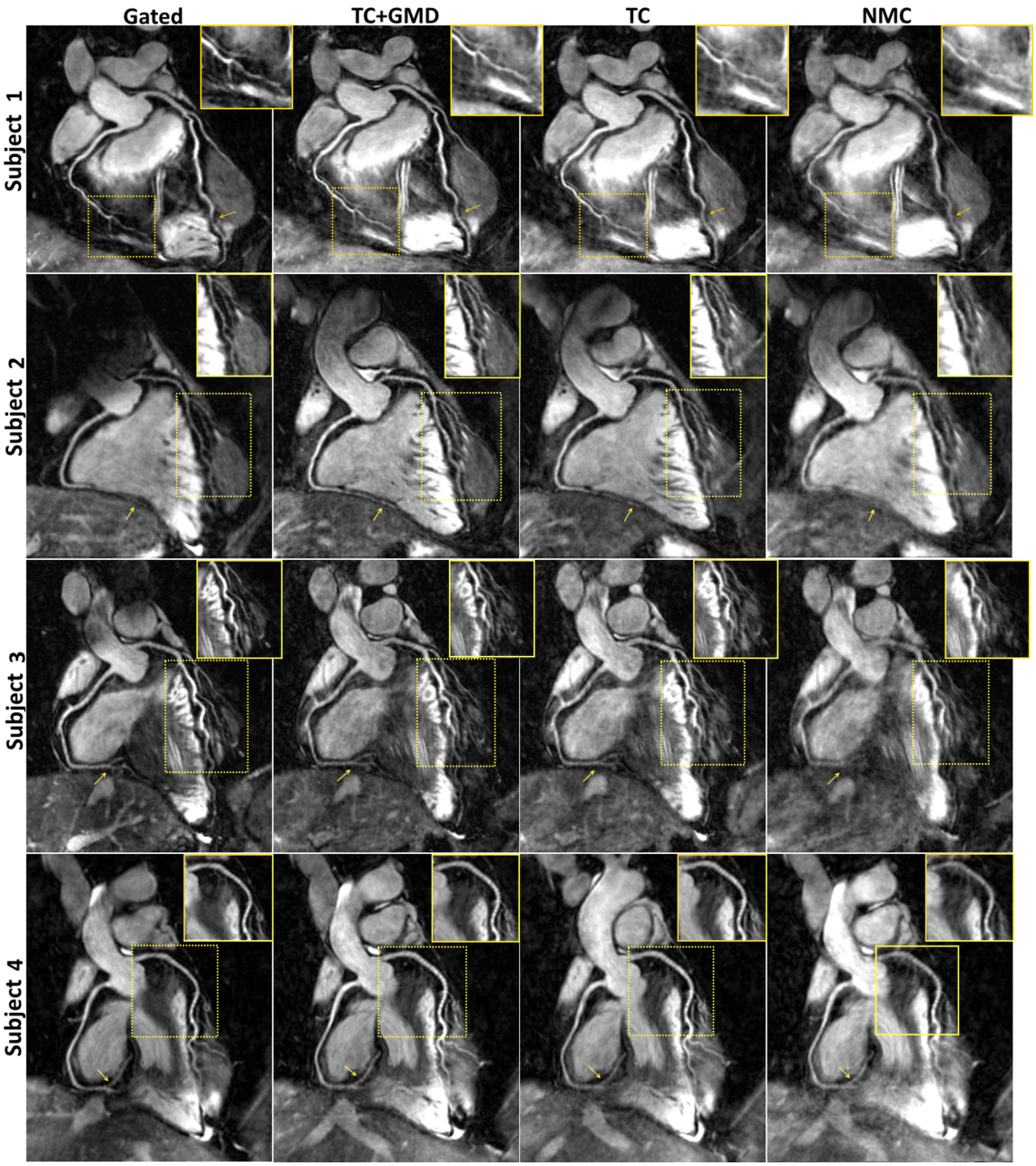

Figure 7.3: Reformatted coronary lumen images (T2prep(+)) for Gated, the proposed translation plus General Matrix Description correction (TC+GMD), translation correction (TC) and no motion correction (NMC) for subjects 1-4. Blurring present in the NMC images is reduced with TC and sharpness further increased with TC+GMD (magnified boxes). The distal part of both coronaries is particularly affected by motion (arrows). Note that TC and TC+GMD have similar image quality to the Gated.

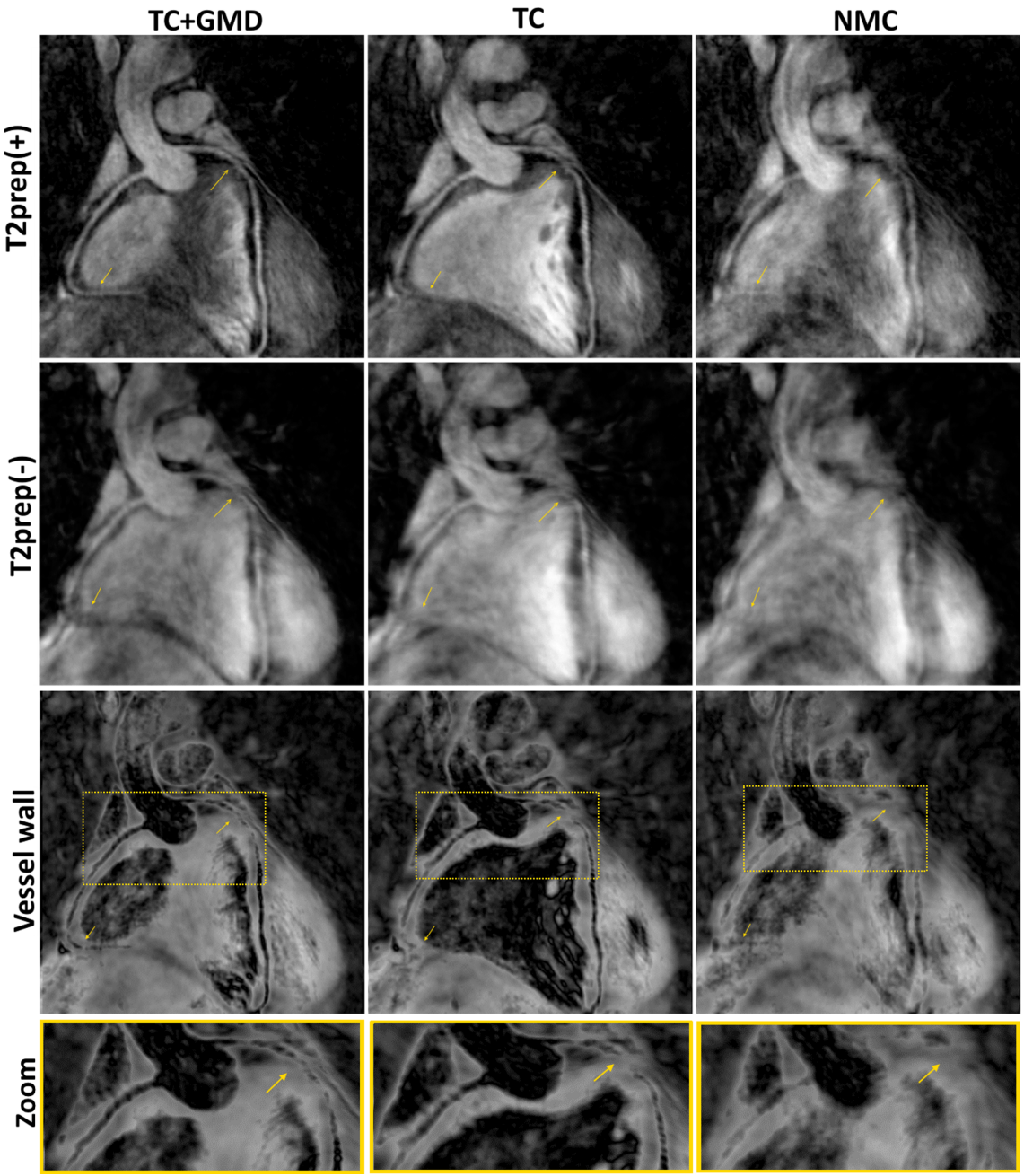

Figure 7.4: Reformatted vessel wall images for the proposed translation plus General Matrix Description correction (TC+GMD), translation correction (TC) and no motion correction (NMC) for subject 5. T2 prepared (T2prep(+)) images are shown on top, images without T2 preparation (T2prep(-)) in the middle and vessel wall images on the bottom. Significant motion artifacts can be seen in all NMC images. Most artifacts are removed with TC and further corrected with TC+GMD (arrows). Residual artifacts in either T2prep(+) or T2prep(-) will contribute to blurring of the vessel wall and may fully obscure it (magnified box).

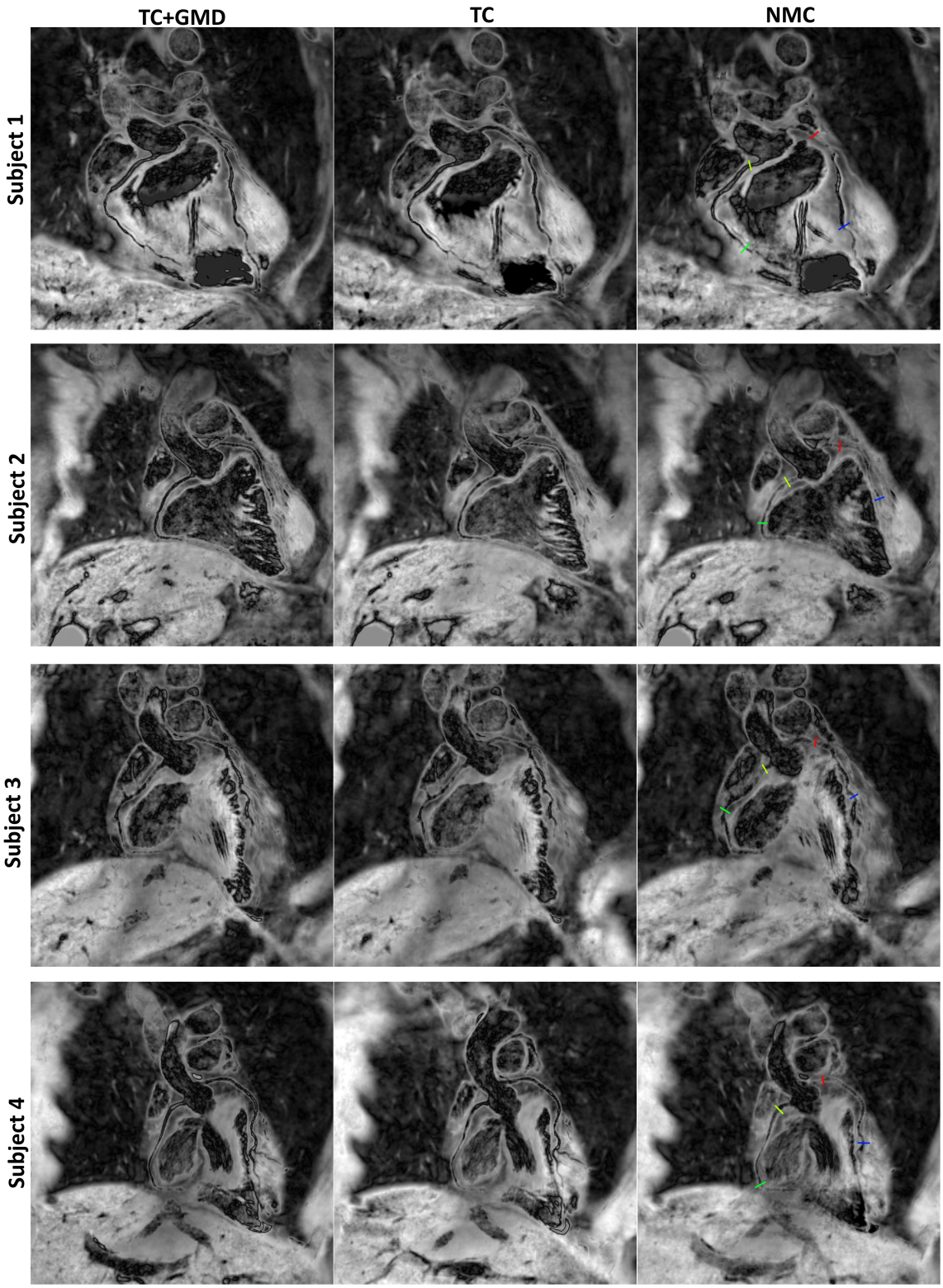

Figure 7.5: Reformatted vessel wall images for the proposed translation plus General Matrix Description correction (TC+GMD), translation correction (TC) and no motion correction (NMC) for subjects 1-4. The vessel wall is obscured in the NMC images. A significant improvement is obtained with TC, although small blurring remains. Vessel wall sharpness is further improved with TC+GMD. Coloured lines in the NMC images mark the locations of the corresponding cross-sectional views in Figure 7.6 for TC+GMD, TC and NMC.

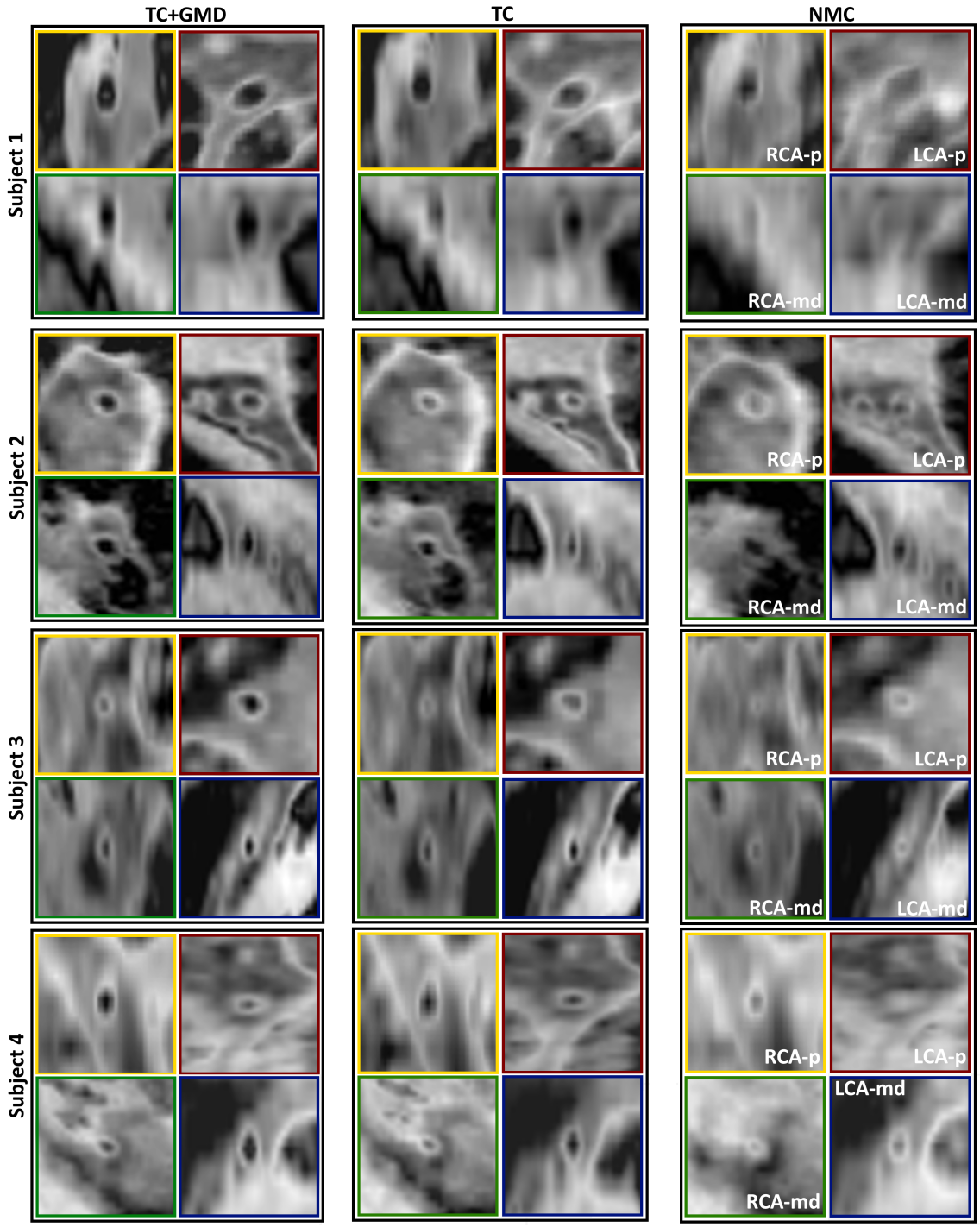

Figure 7.6: Cross-section views of vessel wall images for TC+GMD, TC and NMC for the corresponding subjects shown in Figure 7.5. For each subject, the RCA proximal (RCA-p) is shown in the top left box (yellow), the RCA mid/distal (RCA-md) is shown in the bottom left box (green), the LCA proximal (LCA-p) is shown in the top right box (red), the LCA mid/distal (LCA-md) is shown in the bottom right box (blue). The vessel locations of the cross-sections are shown in corresponding colours in Figure 7.5

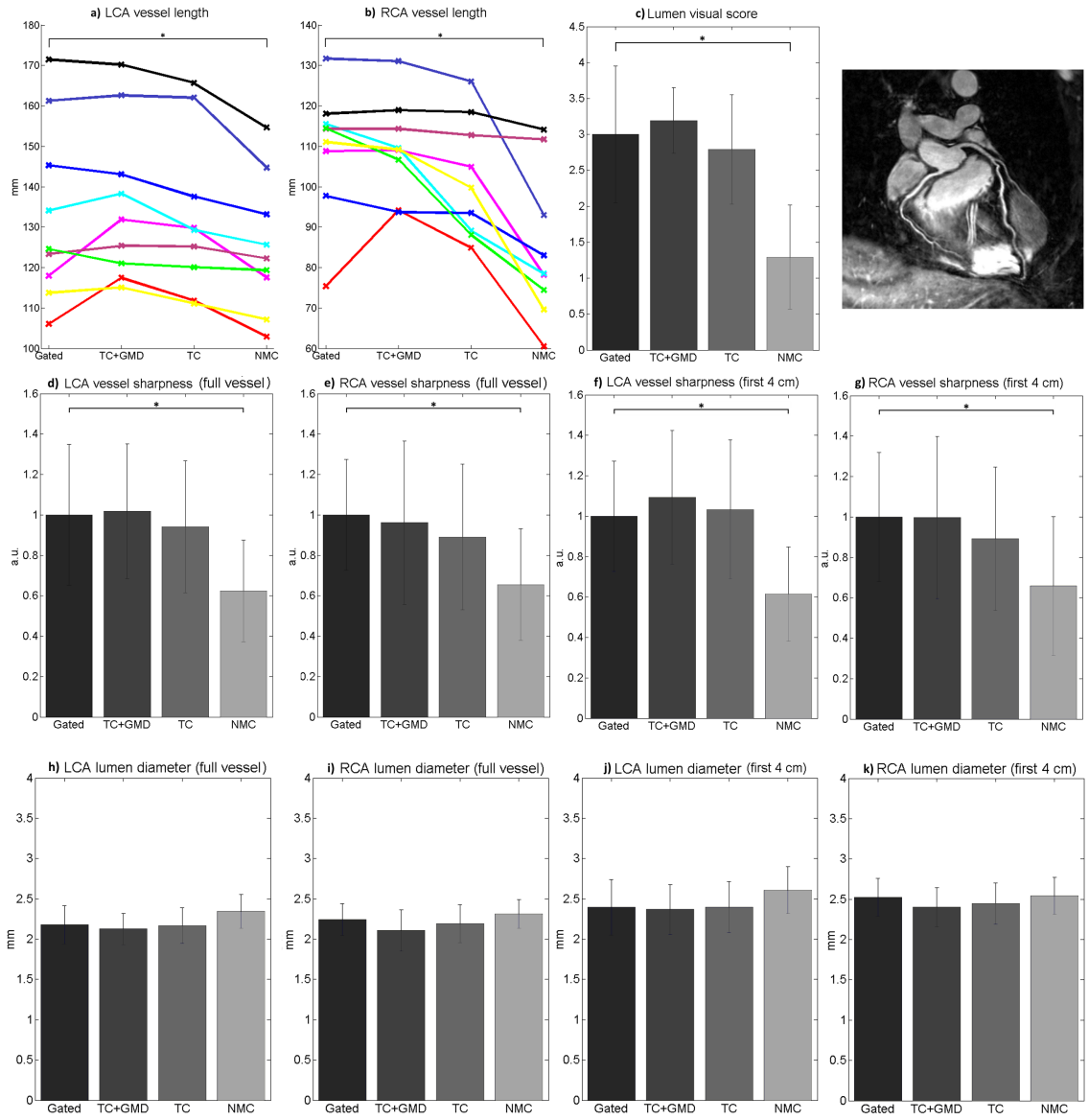

Figure 7.7: Image metrics for coronary lumen for 9 subjects for Gated, the proposed translation plus General Matrix Description correction (TC+GMD), translation correction (TC) and no motion correction (NMC). Statistically significant differences on a P-value < 0.01 are marked with (*). a) Vessel length along the left coronary artery for 9 subjects (coloured). b) Vessel length along the right coronary artery for 9 subjects (coloured). c) Visual score of the coronary lumen images (Wilcoxon test). d) Vessel sharpness for the full length of the left coronary artery (paired t-test). e) Vessel sharpness for the full length of the right coronary artery (paired t-test). f) Vessel sharpness for the first 4 centimetres of the left coronary artery (paired t-test). g) Vessel sharpness for the first 4 centimetres of the right coronary artery (paired t-test). h) Lumen diameter for the full length of the left coronary artery (paired t-test). i) Lumen diameter for the full length of the right coronary artery (paired t-test). j) Lumen diameter for the first 4 centimetres of the left coronary artery (paired t-test). k) Lumen diameter for the first 4 centimetres of the right coronary artery (paired t-test). Error bars indicate standard deviation.

No significant differences were found in lumen diameter measurements. Lumen visual score results were as follows: 3.00±0.95 for Gated, 3.19±0.46 for TC+GMD, 2.79±0.76 for TC, 1.29±0.72 for NMC. NMC was significantly different from Gated according to lumen visual score. The Gated acquisition had an acquisition time of 1051±66 seconds; NMC, TC and TC+GMD had a fixed acquisition time of 620 seconds.

Metrics for coronary vessel wall analysis are shown in Figure 7.8. Blurring due to motion resulted in increased vessel wall thickness, as can be seen for NMC. Vessel wall thickness in NMC was not measured in 2 out of 9 cases, as it was not visible. The measured vessel wall thickness (millimetres) for the LCA and RCA, respectively, were: 1.20±0.20 and 1.08±0.16 for TC+GMD, 1.27±0.26 and 1.21±0.13 for TC, 1.80±0.39 and 1.42±0.14 for NMC.

Table 7.1: Image metric results for lumen and vessel wall imaging. (*) denotes a significant difference to the Gated with a P-value < 0.01. (**) denotes a significant difference to the TC+GMD with a P-value < 0.01.

Image Metrics	Gated	TC+GMD	TC	NMC
LCA lumen vessel length (mm)	133.1±22.1 (*)	136±19.6	132.5±19.7	125.3±16.7 (*)
RCA lumen vessel length (mm)	109.7±15.6 (*)	109.6±11.6	101.9±14.6	84.7±18.3 (*)
LCA lumen sharpness (full length) (a.u.)	1.00±0.35 (*)	1.02±0.33	0.94±0.33	0.63±0.25 (*)
RCA lumen sharpness (full length) (a.u.)	1.00±0.27 (*)	0.96±0.40	0.89±0.36	0.65±0.28 (*)
LCA lumen sharpness (first 4 cm) (a.u.)	1.00±0.27 (*)	1.09±0.33	1.03±0.34	0.61±0.23 (*)
RCA lumen sharpness (first 4 cm) (a.u.)	1.00±0.32 (*)	0.99±0.40	0.89±0.35	0.65±0.34 (*)
LCA lumen diameter (full length) (mm)	2.18±0.24	2.13±0.20	2.17±0.22	2.36±0.21
RCA lumen diameter (full length) (mm)	2.24±0.20	2.11±0.25	2.19±0.24	2.32±0.18
LCA lumen diameter (first 4 cm) (mm)	2.40±0.35	2.37±0.31	2.40±0.31	2.61±0.29
RCA lumen diameter (first 4 cm) (mm)	2.52±0.24	2.40±0.25	2.45±0.26	2.54±0.23
Lumen visual score	3.00±0.95 (*)	3.19±0.46	2.79±0.76	1.29±0.72 (*)
LCA vessel wall sharpness (full length) (a.u.)	N/A	1.00±0.17 (**)	0.93±0.19	0.51±0.15 (**)
RCA vessel wall sharpness (full length) (a.u.)	N/A	1.00±0.29 (**)	0.87±0.30 (**)	0.65±0.34 (**)
LCA vessel wall sharpness (first 4 cm) (a.u.)	N/A	1.00±0.17 (**)	0.95±0.17	0.53±0.15 (**)
RCA vessel wall sharpness (first 4 cm) (a.u.)	N/A	1.00±0.30 (**)	0.85±0.30 (**)	0.62±0.35 (**)
LCA vessel wall thickness (mm)	N/A	1.20±0.2 (**)	1.27±0.16	1.80±0.39 (**)
RCA vessel wall thickness (mm)	N/A	1.08±0.16 (**)	1.21±0.13 (**)	1.42±0.14 (**)
Vessel wall visual score	N/A	2.54±0.49 (**)	2.15±0.64 (**)	1.00±0.60 (**)
Scan efficiency (%)	59±11	96±2	96±2	100

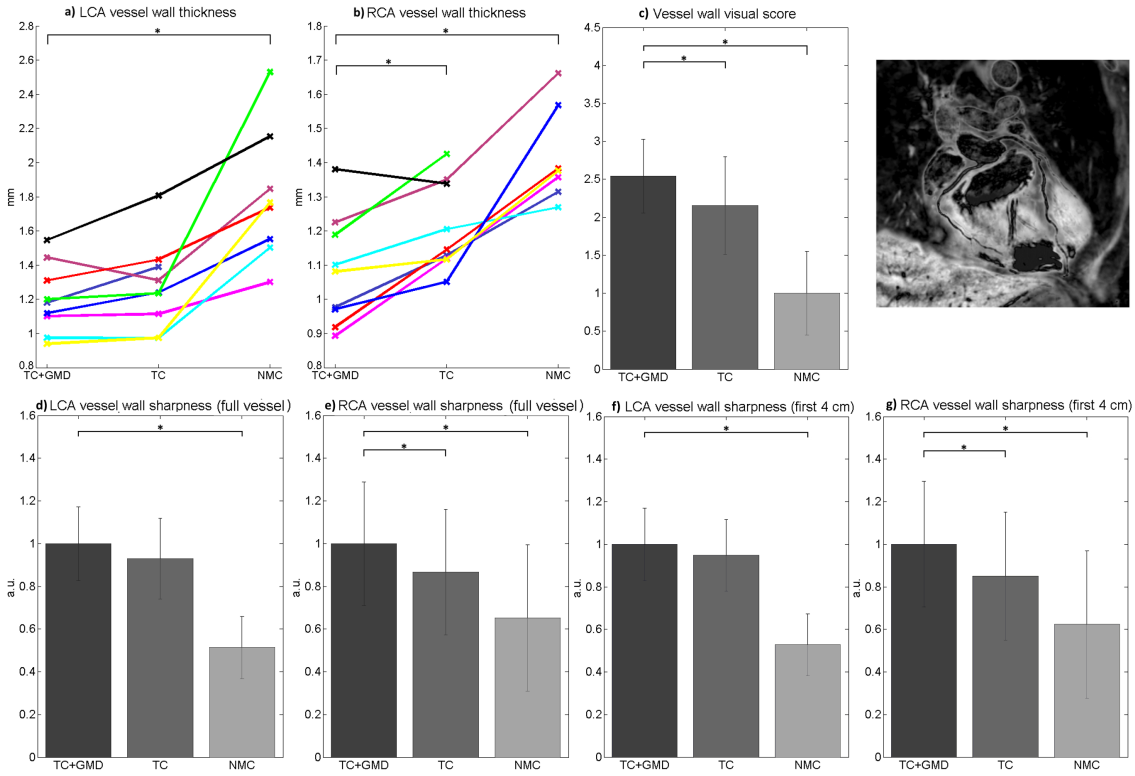

Figure 7.8: Image metrics for vessel wall images for 9 subjects the proposed translation plus General Matrix Description correction (TC+GMD), translation correction (TC) and no motion correction (NMC). Statistically significant differences on a P-value of 0.01 are marked with (*). a) Vessel wall thickness along the left coronary artery for 9 subjects (coloured) (paired t-test). b) Vessel wall thickness along the right coronary artery for 9 subjects (coloured) (paired t-test). c) Visual score of the vessel wall images (Wilcoxon test). d) Vessel wall sharpness for the full visible length of the left coronary artery (paired t-test). e) Vessel wall sharpness for the full visible length of the right coronary artery (paired t-test). f) Vessel wall sharpness for the first 4 centimetres of the left coronary artery (paired t-test). g) Vessel wall sharpness for the first 4 centimetres of the right coronary artery (paired t-test). Error bars denote standard deviation.

Significant differences were found between TC+GMD and NMC for both coronary arteries and between TC+GMD and TC for the RCA. Vessel wall sharpness measures were in agreement with lumen vessel sharpness metrics, however significant differences were found between TC+GMD and NMC for both coronaries and between TC+GMD and TC for the RCA using full vessel length. Similar results were found for the vessel wall visual score: 2.54±0.49 for TC+GMD, 2.15±0.64 for

TC, 1.00±0.60 for NMC. Significant differences were found between TC+GMD and NMC and between TC+GMD and TC. Detailed results for all metrics are shown in Table 7.1.

7.5 Discussion

A novel approach for nonrigid respiratory motion correction for 3D whole-heart coronary MRI has been proposed and validated for simultaneous coronary lumen and vessel wall imaging. The proposed method uses a combined approach to motion correction: small amplitude motion is corrected with high temporal resolution intra-bin translational corrections; large amplitude motion is corrected with low temporal resolution inter-bin nonrigid motion correction. Translational motion is estimated from a golden radial 2D iNAV while nonrigid motion is estimated from the data itself via binning and image registration. This approach was combined with an interleaved T2prep(+)/T2prep(-) acquisition, yielding motion corrected, co-registered, 3D coronary lumen and vessel wall images in a user defined fixed scan time.

Bin-to-bin 3D nonrigid motion correction was performed with the proposed TC+GMD approach after 2D (RL and FH) beat-to-beat intra-bin translational correction. TC approach corrects only for 2D (RL and FH) beat-to-beat translational motion and thus AP motion remained uncorrected. Both approaches were compared against a stan-

dard Gated reconstruction. TC+GMD approach in lumen imaging (T2prep(+)) shows improvements over TC and similar image quality to Gated, while ensuring a predictable and highly efficient scan. No significant differences were found between Gated and TC+GMD for lumen imaging. While the proposed framework has a predictable scan time of approximately 1240 seconds (≈20 minutes) for a T2prep(+) and T2prep(-) dataset (i.e. lumen and vessel wall imaging), the corresponding Gated approach [6] would be expected to require at least 2x(1009±68) seconds (≈35 minutes at 60 beats per minute) plus additional time required for dual gating. For this reason, only a Gated T2prep(+)data set was acquired in this study. The performance of the proposed TC+GMD on vessel wall imaging was compared with TC and NMC, showing improvements over both approaches. Significant differences were found between TC+GMD and TC for vessel wall imaging in terms of vessel wall visual score, RCA vessel wall thickness and RCA vessel wall sharpness.

The proposed TC+GMD measured vessel wall thickness of 1.20±0.20 mm and 1.08±0.16 for the LCA and RCA, respectively. According to previous studies [75, 157], the coronary vessel wall is expected to be approximately 1.0 - 1.1 mm thick. The reason for the slight overestimation of wall thickness may be two-fold: first, residual motion will manifest as blurring, increasing the apparent width of the vessels (and consequently the wall that is obtained by subtraction); second,

the acquired spatial resolution (1x1x2 mm) may be insufficient to fully visualise the vessel wall and partial volume effects may occur, particularly in the distal part. Residual non-rigid motion may be addressed by increasing the number of bins in the framework. For high number of bins, additional regularization in the bin reconstruction may be required (e.g. Compressed Sensing) to guarantee the reconstructions have sufficient quality for reliable motion estimation.

The vessel wall was also partially obscured in some regions due to incomplete nulling of the blood pool. Field inhomogeneities may cause the T2 preparation to vary in space [96], thus leading to an imperfect subtraction. This problem could be improved by optimizing parameter for each subject. If estimates of the B0 [97] and B1 [51] fields are available, then that information could be incorporated into a spatially varying λ. Alternatively, this issue could be alleviated by reducing the duration of the T2 preparation or employing additional 180° refocusing pulses during the T2 preparation. The last solution will produce a more spatially uniform subtraction at the expense of contrast in the vessel wall image.

In one subject with large respiratory amplitude (≈31 mm, subject 10) and considerable cardiac motion, the proposed motion correction approach was not successful in removing all respiratory motion artefacts for both coronary lumen and vessel wall images. To tackle cases of large respiratory amplitudes, the proposed method could be com-

bined with some level of gating while still maintaining high scan efficiencies. A coronal iNAV was acquired to match the geometry of the T2prep(+)/T2prep(-), simplifying the planning of the acquisition, but in general any geometry and protocol can be used for interleaved scanning [86].

The current framework uses a 2D iNAV, meaning that beat-to-beat translational correction is unavailable in one dimension (this was AP for the experiments performed). This limitation can be overcome by extending the proposed approach to acquire a low-resolution 3D iNAV before or after image acquisition. A preliminary study by Powell and colleagues [165] indicated that reliable motion estimation may be obtained from a 3D iNAV with a spatial resolution of 5 x 10 x 10 mm, acquired in ≈81 milliseconds. Long duration iNAVs could compromise the efficacy of preparation pulses, however compressed sensing may also be used to reduce the acquisition time of the 3D iNAV. Arrhythmia rejection was not implemented for the current version of the framework. Therefore residual cardiac motion due to respiratory sinus arrhythmia [174] may be still present, however arrhythmia rejection will be implemented in future work. Compressed sensing could be used alternatively to reconstruct undersampled data due to cardiac motion in order to maintain the same scan time.

Future work will explore more isotropic spatial resolution to measure the vessel wall with increased accuracy. The increased acquisition

time will be addressed by combining accelerated reconstruction with motion correction to tolerate higher undersampling factors in both the binning and motion corrected coronary lumen and vessel wall reconstructions, as recently proposed for 3D abdominal imaging [50]. Further study on optimal values is desired to produce more homogenous blood nulling in the vessel wall image. Future work will validate the proposed method in patient scans and compare against alternative motion correction approaches.

7.6 Conclusion

A framework for nonrigid respiratory motion correction of simultaneous coronary lumen and vessel wall imaging has been introduced, using an interleaved scanning and a combination of 2D translational and 3D nonrigid motion correction. The proposed method allowed for 96% scan efficiency on average, reducing scan times by ≈1.6x on average relative to a gated acquisition, while maintaining similar image quality. No significant differences were observed in coronary lumen images between the proposed approach and the reference gated scans. Significant improvements in the RCA vessel wall sharpness and vessel wall visual score were observed when comparing the proposed approach with translational motion correction alone.

Chapter 8

3D Whole-Heart Water Fat Coronary MRA at 3T with 100% Scan Efficiency

8.1 Introduction

Chapter 2 introduced coronary magnetic resonance angiography (MRA) as a non-invasive tool to assess coronary lumen integrity. T_2 preparation pulses significantly improve contrast between myocardium and vessels [24, 28]. Additionally, fat suppression is required to allow visualization of the coronary arteries, as they are embedded in epicardial fat [134].

Recent work has shown that cardiac fat may provide important diagnostic information [104]. Specifically, it has been shown that fatty infiltrations in the myocardium are correlated with sudden death [35]

and thus fat visualization may be desirable. Fat suppression could be used to detect fat as it creates signal voids compared to an image with no fat suppression. However, in regions of low fat concentration it may be difficult to distinguish signal loss due to fat from signal loss due to other effects.

Alternatively, Dixon-based methods yield both water and fat images [56]. The Dixon method requires two or more images aquired at different echo times (TE). The original solution [56] with two echoes acquired one in-phase (IP) image and one out-of-phase (OP) image, however this two-point approach is sensitive to B_0 field inhomogeneities (which create fluctuations in the resonant frequency). This limitation can be addressed with a three-point Dixon strategy [73] to estimate the off-resonance map, in addition to the water and fat images.

Dixon-based methods have shown superior fat suppression when compared with spectral methods [17] and have recently been used to produce attenuation maps for simultaneous PET-MR imaging [213]. However, respiratory motion is a major problem in whole-heart 3D water/fat Dixon MRI as motion artefacts may compromise water-fat separation. Respiratory gating is commonly used to minimize respiratory-induced motion, however this increases scan time. Moreover, translational correction of respiratory motion may be of limited use as it may introduce ghosting artefacts from static fat tissue present in the in-phase and out-of-phase images. I hypothesize that errors may prop-

agate to the final water and fat images and that they may be avoided with non-rigid motion correction.

Here, the acquisition and motion correction framework proposed in the previous chapter is adapted for free-breathing 3D whole-heart water/fat Dixon coronary MRA. In this work, the motion correction step uses the total variation regularized General Matrix Description (TV-GMD), as introduced in Chapter 6. The approach proposed uses all the acquired data for reconstruction (100% scan efficiency) and therefore has a predictable scan time. The proposed approach was compared with a 2D translational correction (TC) and no motion correction (NMC) in a preliminary study in four subjects.

8.2 Methods

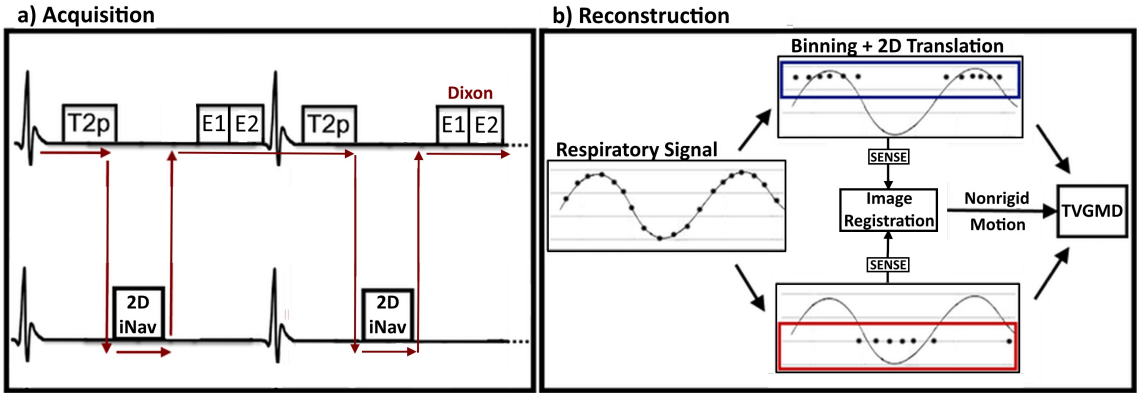

Figure 8.1: Proposed acquisition scheme for 3D coronary Dixon motion correction. **a)** Acquisition: Data is acquired using interleaved scanning, allowing for a dual-echo Dixon dataset ($E1/E2$) to be acquired simultaneously with a 2D image navigator (2D iNAV). **b)** Reconstruction: 2D iNAV-based beat-to-beat translational motion correction followed by 3D bin-to-bin nonrigid motion correction incorporated in the reconstruction (TV-GMD).

The proposed approach uses a dual-echo acquisition, producing two datasets. Both datasets undergo the same motion correction process.

8.2.1 Image acquisition

Similarly to the framework presented in the previous chapter, data was acquired using an interleaved scanning framework [86]. In this work, two scans were obtained in alternated fashion: a 3D segmented Cartesian whole-heart dual-echo Dixon and a 2D single shot golden-radial coronal image navigator (2D iNAV). A schematic for this acquisition is depicted in Figure 8.1a), where the red line denotes the scan ordering at run-time.

8.2.2 Beat-to-beat motion estimation and correction

The same approach for beat-to-beat motion estimation as proposed in the previous chapter was used here. The golden-radial iNAVs were reconstructed with gridding [77] and beat-to-beat 2D translational motion extracted via image registration [32]. The foot-head (FH) motion component was used for respiratory binning. 2D translational motion correction was applied in k-space [26], correcting each bin towards its' central position, as before:

$$\mathbf{K} = \mathbf{K}' exp(2\pi i \mathbf{k}' \cdot \mathbf{T}) \tag{8.1}$$

where $\mathbf{K}$ is the translation corrected k-space, $\mathbf{K}'$ the acquired k-space, $\mathbf{k}'$ the corresponding k-space trajectory and $\mathbf{T}$ the estimated 2D translation vector.

8.2.3 Bin-to-bin motion estimation and correction

Following respiratory binning, datasets were reconstructed with a soft-gated [100], iterative SENSE [168] reconstruction, as described in the previous chapter:

$$\hat{\mathbf{I}}_\mathbf{b} = arg\ min_{\mathbf{I_b}} ||\mathbf{W_b}(\mathbf{EI_b} - \mathbf{K_b})||_\mathbf{2}^\mathbf{2} \tag{8.2}$$

where $\mathbf{I_b}$ are the reconstructed bin volumes, $\mathbf{W_b}$ is a diagonal matrix containing data weights for bin b, $\mathbf{E}$ is the encoding matrix that includes the Fourier transform, coil sensitivities and sampling operations, and $\mathbf{K_b}$ is the acquired data at each bin. The weights $\mathbf{W_b}$ were a linear function of the FH location of the data in the respiratory cycle, as before. Here, the OP data were binned, reconstructed and used for non-rigid motion estimation. The signal cancellation at boundaries with equal water and fat content in OP delineates structures and facilitates intensity-based image registration. Non-rigid motion estimation [138] was performed using the end-expiration bin as reference to retrieve dense motion fields.

Non-rigid bin-to-bin motion correction was performed with a Total

Variation regularized General Matrix Description (TV-GMD), as introduced in chapter 6:

$$\begin{aligned} \hat{\mathbf{I}} &= arg\ min_{\mathbf{I}} ||\mathbf{E}\ \mathbf{I} - \mathbf{K}||_2^2 + \lambda_s \mathbf{TV_s} \\ \mathbf{E} &= \sum_{\mathbf{b}} \mathbf{A_b F S U_b} \\ \mathbf{TV_s} &= ||\nabla_s \mathbf{I}||_1 \end{aligned} \tag{8.3}$$

where $\hat{\mathbf{I}}$ is the motion corrected volume, $\mathbf{K}$ is the translation corrected k-space data. $\mathbf{E}$ is the encoding operator: $\mathbf{A_b}$ is the sampling matrix for bin b, $\mathbf{F}$ is the Fourier transform, $\mathbf{S}$ are the coil sensitivities for all coils and $\mathbf{U_b}$ are the non-rigid motion field operators obtained via image registration. Δ_s is the 3D spatial gradient. The TV-GMD was performed for IP and OP independently, using the same motion fields (estimated from OP bin reconstructions).

TV regularization not only manages noise amplification in the GMD reconstruction, but also suppresses incoherent motion artefacts that may arise from the beat-to-beat translational correction. Stationary tissue is expected to produce strong aliasing artefacts when the translational correction for the heart is applied. Although, the proposed approach relies only on small intra-bin translational corrections, some incoherent artefacts are expected to arise from high intensity static fat signal. These artefacts may occur in either the IP or OP images and propagate into the water/fat images. Therefore, TV regularization can suppress residual artefacts and is expected to produce superior

water/fat separation.

8.2.4 Water/fat separation

Water/fat separation was performed following the motion corrected reconstructions of IP and OP datasets as described above. Water and fat images were obtained as described in [17]. The water **H** and fat **L** components of the complex images $\mathbf{S_1}$ and $\mathbf{S_2}$ acquired at TE_1 and TE_2 (respectively) can be modelled by:

$$\begin{aligned} \mathbf{S_1} &= (\mathbf{H} + \alpha_1 \mathbf{L})\theta \\ \mathbf{S_2} &= (\mathbf{H} + \alpha_2 \mathbf{L})\theta\Delta_\theta \end{aligned} \tag{8.4}$$

where θ is the phase of the water signal at TE_1 and Δ_θ is the phase accumulation between TE_1 and TE_2 due to static field inhomogeneities. The parameters α_n are given by:

$$\alpha_n = exp(-i2\pi\gamma B_0 \delta TE_n - \nu TE_n) \tag{8.5}$$

where γ is the gyromagnetic ratio, δ is the fat chemical shift, ν is the inverse of TE_2^*. The phase term θ is expected to be spatially smooth and can be accurately estimated from the low resolution k-space data using a sequential tree re-weighted message-passing algorithm [214]. ν can be known a priori [38] or estimated from the data itself [230]. If

θ and ν are known, the problem in equation (8.4) is fully determined and may be written in matrix from as:

$$\begin{bmatrix} Re(\mathbf{S_1}/\theta) \\ Im(\mathbf{S_1}/\theta) \\ Re(\mathbf{S_2}/(\theta\Delta_\theta)) \\ Im(\mathbf{S_2}/(\theta\Delta_\theta)) \end{bmatrix} = \begin{bmatrix} 1 & Re(\alpha_1) \\ 0 & Im(\alpha_1) \\ 1 & Re(\alpha_2) \\ 0 & Im(\alpha_2) \end{bmatrix} \begin{bmatrix} \mathbf{H} \\ \mathbf{L} \end{bmatrix} \tag{8.6}$$

$$\mathbf{S} = \mathbf{D} \begin{bmatrix} \mathbf{H} \\ \mathbf{L} \end{bmatrix}$$

where $\mathbf{D}$ contains the parameters α_n for the Dixon water/fat separation. Equation (8.6) may be solved in the least-squares sense via the Moore-Penrose pseudoinverse:

$$(\mathbf{D^T D})^{-1}\mathbf{D^T S} = \begin{bmatrix} \mathbf{H} \\ \mathbf{L} \end{bmatrix} \tag{8.7}$$

8.3 Experiments

Four healthy subjects were scanned free-breathing on a 3T Philips scanner using a 32-channel coil. Written informed consent was obtained from all subjects according to institutional guidelines and the study ("Development of novel magnetic resonance techniques using healthy volunteers") was approved by the institutional review board.

Dual-echo Dixon data was acquired with an ECG-triggered 3D Cartesian spoiled gradient echo: 1x1 mm in-plane resolution, 2 mm slice thickness, 300x300x80 mm FOV, TR/TE1/TE2 = 4.0/1.44/2.6 ms, flip angle = 20°, T2prep duration = 40 ms, subject specific acquisition window and a low-high (centric) Cartesian acquisitions with a radial-like k-space order in k_y and k_z. The data acquisition was interleaved with a 2D golden radial iNAV spoiled gradient echo sequence 4x4 mm in-plane resolution, 25 mm slice thickness, 300x300 FOV, TR/TE = 2.4/1.07 ms, flip angle = 5°.

Non-motion correction (NMC), 2D translational correction (TC) and the proposed translation plus nonrigid (TC+TVGMD) reconstructions were obtained from these data. None of the subjects presented with deep breathing, hence no outlier removal was employed for the reconstruction. For the TC+TVGMD, 5 bins were used to estimate and correct non-rigid motion. A higher number of bins was used here (than in the previous work, Capter 7) to reduce the amplitude of translational correction performed, which can introduce residual artefacts from static signal. Soft-gated bin reconstructions used a soft-gate range of 1 mm. All reconstructions terminated when the relative residual threshold of 0.05% was reached. For TC+TVGMD, the regularization weight λ_s was set to $5 \times 10^4 ||.||_\infty$ of the k-space data. Tools from the Fat-Water Toolbox (http://ismrm.org/workshops/FatWater12/) were used to perform the water/fat separation according to [17]. Coro-

nary vessel sharpness of the water separated images was computed using the method proposed in reference [64], as in the previous Chapter.

8.4 Results

Scans were sucessfully completed in all subjects. Coronal slices for the out-of-phase (OP) and in-phase (IP) images using the non-motion corrected (NMC), 2D translation corrected (TC) and proposed translation plus Total Variation regularized General Matrix Description (TC+TVGMD) reconstructions are presented in Figure 8.2. Motion artefacts due to respiratory motion are visible for NMC in both echoes. TC brings into focus structures inside the heart as seen in the arrows in Figure 8.2. However, this global k-space translational correction will be incorrect for static fat signal present in echoes 1 and 2, potentially introducing significant aliasing. These artefacts are indeed present in both echoes, manifesting as incoherent spurious signal (also marked with arrows in Figure 8.2).

The proposed approach corrects respiratory-induced motion in the heart without introducing these artefacts. The TC+TVGMD combines intra-bin (i.e. small) translational correction with inter-bin non-rigid correction. Therefore, both moving and static tissues are adequately motion corrected with GMD and residual incoherent aliasing suppressed with total variation regularization. Aliasing artefacts in

the OP and IP images will appear in the water and fat images after separation.

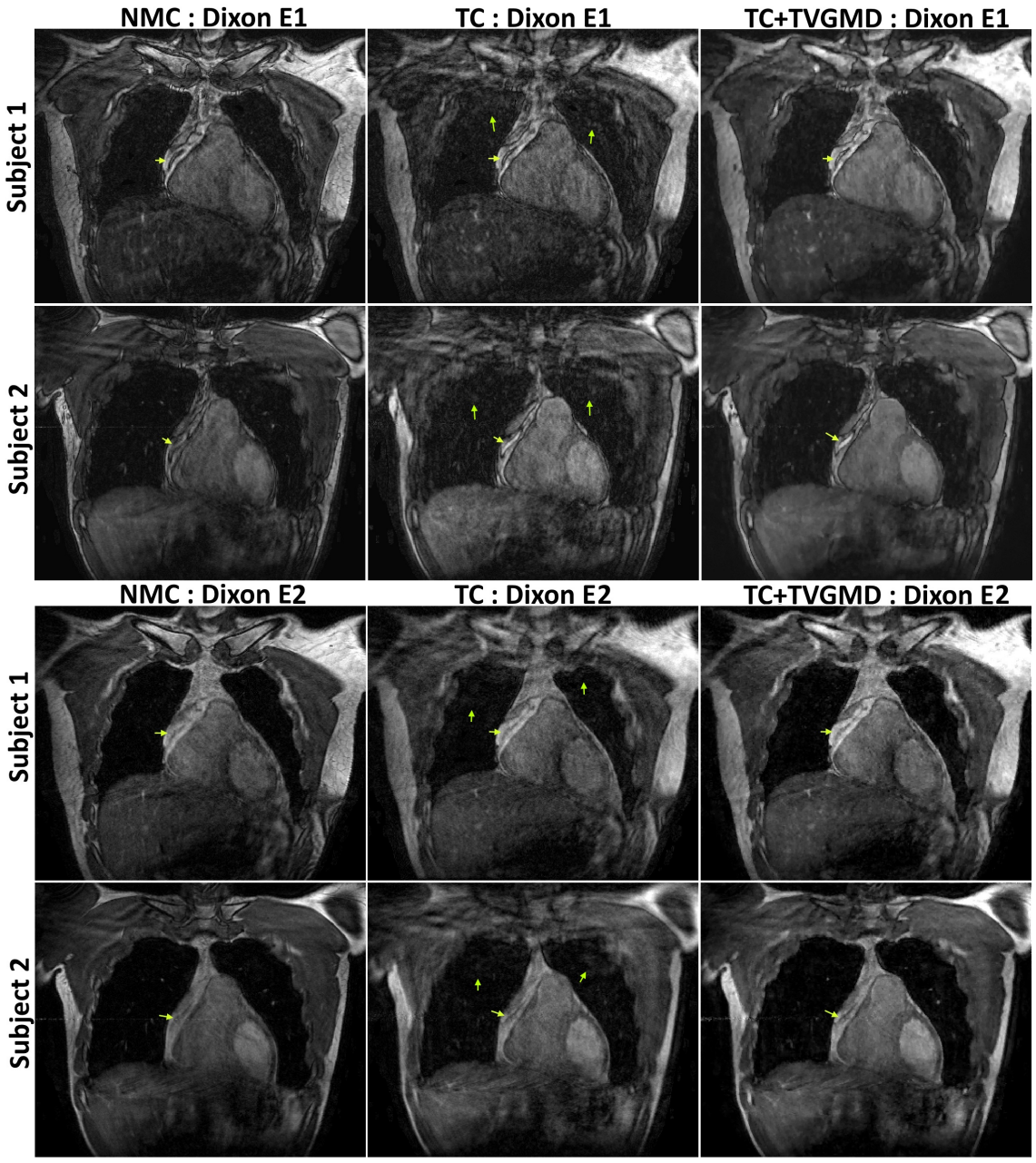

Figure 8.2: Coronal slices for echo 1 (E1, out-of-phase) and echo 2 (E2, in-phase) with no motion correction (NMC), translational correction (TC) and the proposed nonrigid approach (TC+TVGMD) for two subjects. TC reduces blurring in NMC, but introduces ghosting artefacts from static fat signal. The proposed method further improved motion correction minimising ghosting artefacts from static tissue (arrows).

Water and fat images reformatted along the right and left coronary

arteries (RCA and LAD) are shown in Figure 8.3 for the NMC, TC and the proposed TC+TVGMD. In the reformatted coronary images it is easier to observe progressive improvements in motion correction from the NMC to TC to TC+TVGMD, particularly in the distal sections of the vessels. Since the base and apex of the heart will not usually share the same translational motion, it is unlikely that the TC succeed in both regions of the heart.

Despite the motion artefact reduction from NMC to TC, it can be seen on Figure 8.3 that additional spurious signal is introduced with TC. These are predominantly originating from static fat signal that has been incorrectly displaced due to translation correction. The TC+TVGMD only applies small amplitude translational corrections (intra-bin) in addition to non-rigidly correcting both moving and static tissues. Residual incoherent artefacts or noise amplification are suppressed with the total variation regularization. Residual errors from imperfect water/fat separation can be seen in all reconstructions, likely caused by static field inhomogeneities.

Vessel sharpness for the left and right coronary arteries (LCA and RCA, respectively) are shown in Figure 8.4 for each subject separately. For each subject and each coronary, the sharpness metric has been normalized to the TC+TVGMD.

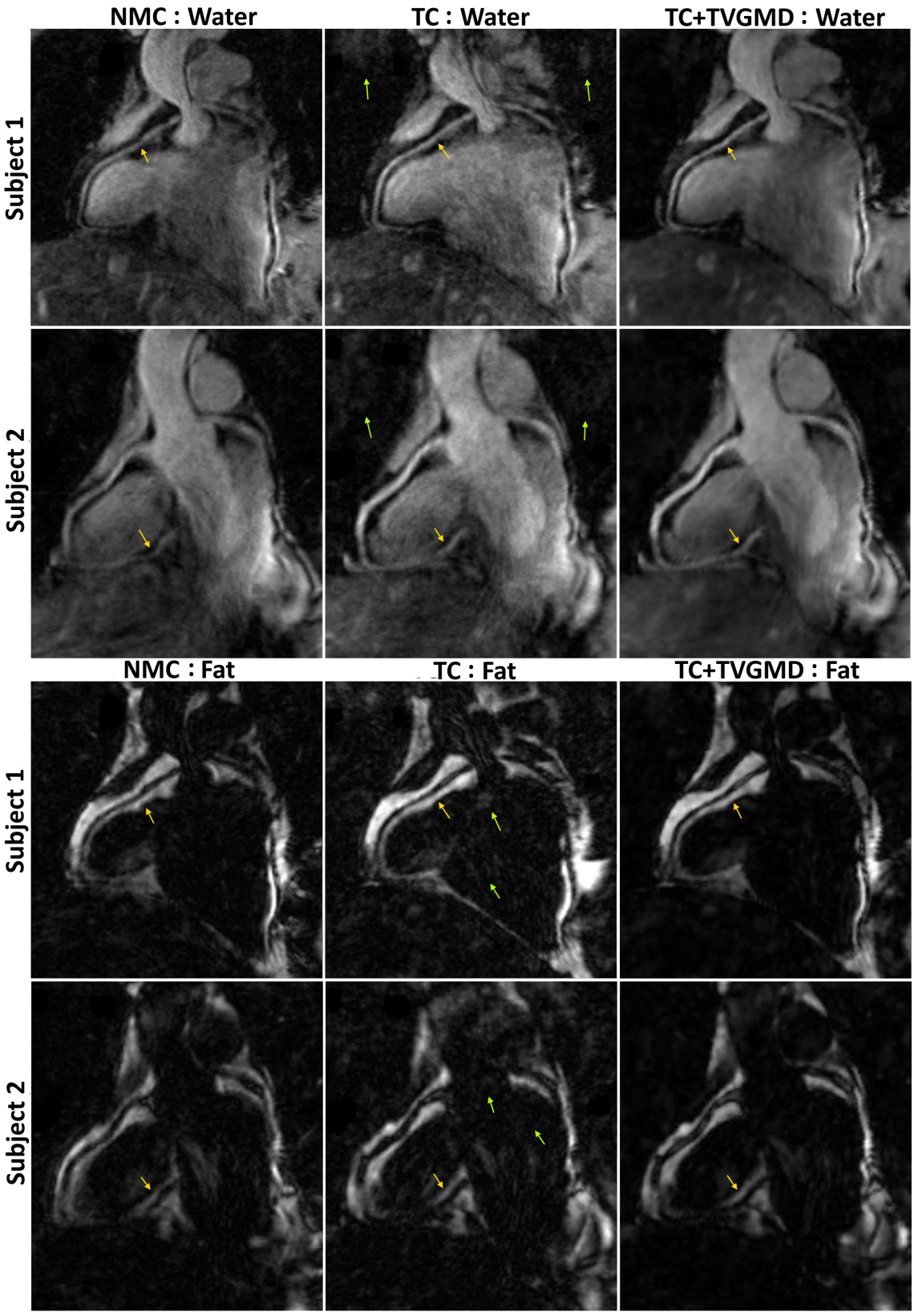

Figure 8.3: Reformated water and fat separated CMRA with no motion correction (NMC), translational correction (TC) and the proposed non-rigid approach (TC+TVGMD) for two subjects. Coronaries in NMC are obscured by motion artefacts (arrows). TC reduces some blurring, but introduces ghosting from static fat signals (arrows). TC+TVGMD further improves motion correction whilst avoiding the spurious signal introduced by TC (arrows).

The proposed TC+TVGMD obtained the highest vessel sharpness for both coronaries in all four subjects, followed by the TC and finally NMC. While the TC is expected to improve sharpness compared to the NMC, it is also likely to provide suboptimal corrections in different regions of the heart due to the different displacements caused by respiratory motion. The proposed TC+TVGMD uniformly improves the TC with more localized, non-rigid corrections, as verified visually in Figure 8.3 and the plots in Figure 8.4.

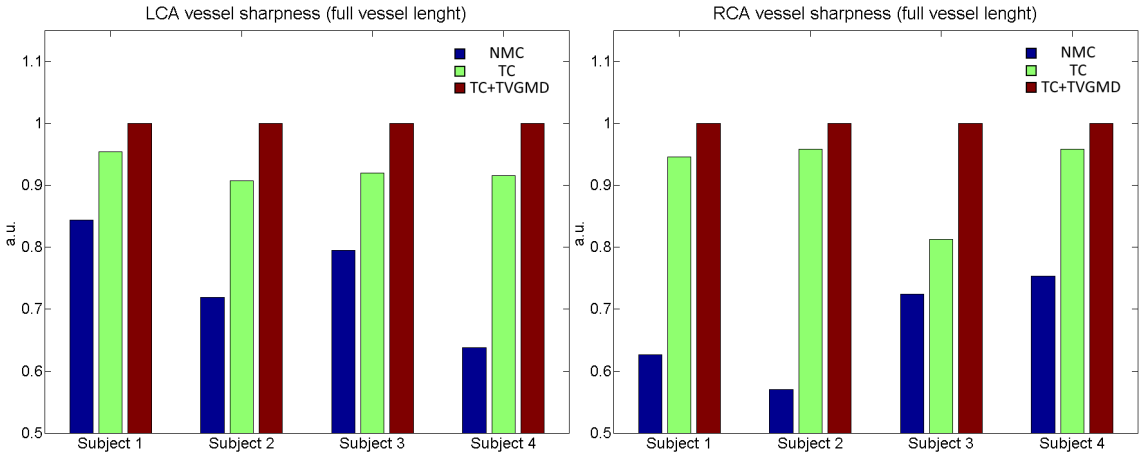

Figure 8.4: Bar plots for the left and right coronary artery (LCA and RCA) vessel sharpness using the full vessel length. Sharpness has been normalized to the TC+TVGMD in each subject. The proposed TC+TVGMD consistently achieved the best vessel sharpness. Results on both coronaries indicate a loss in sharpness in about 5-15% if only TC is employed. A significant loss in sharpness, up to 40%, may occur if no motion correction is employed.

8.5 Discussion

A framework for non-rigid respiratory motion correction has been proposed for 3D water/fat Dixon coronary MRA. Initial results on three subjects indicate that the proposed approach bypasses the fundamental limitations of translational correction (TC) when fat suppression

is not deployed. Whereas TC will introduce aliasing artefacts from static signal (specially static fat), the proposed TC+TVGMD avoids this problem by applying small translation corrections whilst improving motion correction with non-rigid corrections.

Non-rigid motion estimation was obtained from out-of-phase reconstructed bins. However, water and fat separated respiratory bins could be better for motion estimation. This consideration will be studied in future work. The TC+TVGMD approach currently uses a 2D coronal iNAV, meaning that AP beat-to-beat motion is uncorrected for. This limitation can be addressed by employing a 3D iNAV as previously demonstrated [165]. Although a significant increase in iNAV acquisition time is to be expected, this can be managed by reduced spatial resolution, Parallel Imaging and Compressed Sensing reconstruction. Long duration iNAVs may compromise the efficacy of prepulses and motion estimation, and may not be possible at faster heart rates.

An additional solution would be to split the iNAV into two iNAV acquisitions before and after the image acquisition. Small duration iNAVs will be closer to image acquisition, which has shown to have a meaningful impact on image quality [199], specially at higher resolutions (Figure 2.10). These data (before and after iNAVs) may be inconsistent due to motion during the ≈100 ms image acquisition window. This problem can easily be addressed with autofocus [9] since it amounts to a simple two motion-state problem with a very small

search space. A double iNAV autofocus approach would enable motion measurements at both the beginning and end of the image acquisition window. This motion information could be interpolated to correct every k-space point independently, therefore enabling intra-beat translational motion correction. Correcting intra-beat motion would further improve image quality and/or enable longer acquisition windows (Figure 2.8).

In the current approach, both Dixon echoes are reconstructed independently before the water fat separation. Both the motion corrected reconstruction and the water/fat separation are linear processes that can be combined into a single problem. Combining equations (8.3) and (8.7) (where $\mathbf{S} = \mathbf{I}$ and $\mathbf{K}$ contains k-space data from both echoes) produces:

$$\sum_{\mathbf{b}} \mathbf{A_b F S_c U_b D} \begin{bmatrix} \mathbf{H} \\ \\ \mathbf{L} \end{bmatrix} = \mathbf{K} \tag{8.8}$$

which could be solved to produce motion corrected water and fat images directly from corrupted k-space datasets. The water and fat images contain different physiological information and have different contrast. However, both images correspond to the same structures and should have some similarities in their high frequency k-space information. Despite the different contrasts, water and fat images are expected to have a similar representation in the spatial gradient do-

main, as shown in Figure 8.5 for subject 3. This information could be enforced into the reconstruction described above as sparse regularization $||\nabla_{\mathbf{H}} - \nabla_{\mathbf{L}}||_{\mathbf{1}}$, for example, or enforcing specific sparsifying transforms for water and fat, as proposed in [58].

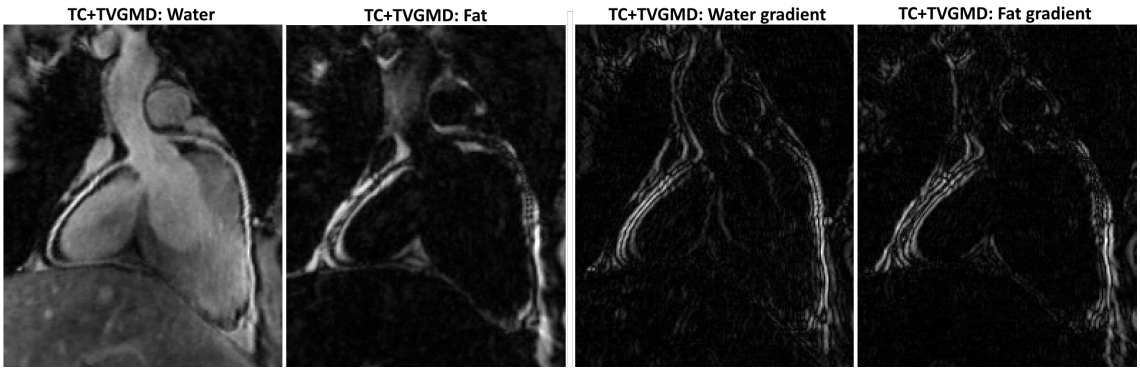

Figure 8.5: Reformated water and fat separated CMRA with the proposed non-rigid approach (TC+TVGMD) for subject 3. Water and fat images have different physiological information. However, they have similar representations in the spatial gradient domain.

Residual artefacts from water/fat separation errors are present in some regions of the reconstructed images, likely due to field inhomogeneities. An off-resonance map may be estimated from the data [23], however three-point Dixon approaches are also possible [73].

8.6 Conclusion

A framework for 3D water/fat Dixon coronary MRA with non-rigid motion correction has been proposed. The proposed approach corrects non-rigid motion of the heart, thereby minimising ghosting from static fat tissue and thus solving a fundamental limitation of translational correction. The proposed approach also allows 100% scan efficiency,

enabling shorter and predictable scan times than a gated acquisition would. Future work will focus on comparison of the proposed approach with standard navigator-gated acquisition in additional subjects.

Chapter 9

Conclusion and future work

9.1 Conclusion

This thesis introduced novel methods for respiratory motion correction in 3D abdominal and cardiac imaging. The proposed methods estimate dense motion fields from the data itself to enable correction. The motion corrected reconstruction [14] was combined with Compressed Sensing [124], enabling higher acceleration factors and improved SNR. These characteristics enabled the proposed frameworks to significantly reduce scan time in abdominal and cardiac imaging relative to the standard gated acquisition, whilst maintaining similar image quality.

Chapter 5 compared image-based (IMC) and reconstruction-based (GMD) motion correction methods for abdominal imaging. It was demonstrated that the IMC does not guarantee aliasing cancellation and some ghosting may remain in the motion corrected image. Also, this approach introduces some blurring during motion correction. The

GMD approach did not present these limitations. Additionally, these methods were compared with a 5 mm self-gated reconstruction, showing superior (albeit non-significant) image sharpness for the GMD as well as improved scan efficiency. This work also demonstrated the feasibility of a self-dependent motion estimation framework for the IMC and GMD. The proposed motion estimation framework used self-navigation to enable respiratory resolved reconstructions, which in turn allowed motion estimation via image registration.

Chapter 6 combined the GMD framework proposed in Chapter 5 with Compressed Sensing to enable higher acceleration factors. Although reliable motion estimation may be obtained from binned reconstructions of a fully-sampled dataset, this is not guaranteed for the undersampled case due to residual aliasing. Therefore, spatial and temporal (along the respiratory dimension) gradient sparsity was enforced to obtain accurate and reliable motion estimation in highly undersampled binned reconstructions (5x-19x). Spatial gradient sparsity was also used to prevent noise amplification in the proposed TV-GMD. The IMC approach was evaluated for undersampled datasets, showing residual aliasing and blurring, which were significantly reduced with the proposed TV-GMD. When compared with a 5 mm self-gated reconstruction, the TV-GMD presented similar image quality. However, a scan time reduction of 2.6x was obtained with the proposed method (when compared to the gated acquisition) due to superior scan effi-

ciency and higher undersampling factor.

Chapter 7 extended the GMD framework with a combination beat-to-beat and bin-to-bin respiratory motion correction for coronary vessel wall imaging. A 2D image navigator (iNAV) was interleaved with data acquisition to provide beat-to-beat translation information. In this Translation Correction plus GMD (TC+GMD) approach, motion correction is split into two problems: low amplitude, intra-bin, beat-to-beat translational motion is corrected before reconstruction; following, high amplitude, inter-bin, bin-to-bin non-rigid motion is corrected with the GMD motion corrected reconstruction. This work demonstrated the usage of soft-gating to enable accurate motion estimation from undersampled binned reconstructions. The proposed approach was compared with TC only and 6 mm gated (and tracked) acquisition for coronary lumen, showing similar image quality to gated and superior (albeit non-significant) metric values to TC only. TC+GMD showed statistically significant improvements in vessel wall sharpness of the right coronary artery, vessel wall thickness of the right coronary artery and expert visual score of vessel wall images when compared with TC. Once again, a significant improvement in scan efficiency (from 59% to 96%) was observed between gated and the proposed approach.

Chapter 8 extended the previous framework to water/fat coronary imaging. Non-rigid motion correction should be particularly useful in

non fat suppressed imaging, which are susceptible to significant errors when simpler models are used. Indeed, significant aliasing is expected with a translational correction due to incorrect displacement of the static fat signal. The TC+GMD framework introduced in Chapter 7 was combined with total variation regularization (as introduced in Chapter 6 for abdominal imaging) to non-rigidly correct respiratory motion whilst suppressing residual incoherent artefacts that may affect water/fat separation. Initial results in four subjects showed superior motion correction for the proposed TC+TVGMD when compared to TC only. Additionally, the proposed approach avoided aliasing artefacts from static tissue otherwise introduced by TC only.

9.2 Future work

The field of magnetic resonance imaging has seen significant developments in recent years. Advances in acquisition and reconstruction methodologies have enabled faster acquisitions with superior image quality. Regardless, patient motion has remained a challenge in many MR applications.

The works in this dissertation focused on respiratory motion correction methods to reduce scan times. In cardiac imaging, cardiac-induced motion was minimized with (a scan inefficient) ECG. The methods developed here could be extended for cardiac-induced motion correction. The challenge, however, lies in obtaining highly accurate, high spatial

and especially high temporal resolution motion estimates. A possible solution was hinted in Chapter 8 to address intra-beat motion correction, using information in the acquisition and reconstruction steps. In general, improvements in motion correction will likely be associated with improvements in motion estimation.

Future advances in motion correction should be distributed between the acquisition and the reconstruction. Specifically, the optimal solutions should come from a combination of prospective and retrospective motion correction methods. As described in Chapter 4, retrospective motion correction is often an underdetermined problem (even for a fully sampled dataset). This limitation can be addressed using prospective motion correction, however the prospective approach is limited to affine corrections. Therefore, a robust solution could rely on prospective corrections to address large displacements approximated by an affine model, followed by a finer retrospective non-rigid correction. The practical challenges to this approach will be two-fold: acquiring and processing high spatial and temporal resolution motion information for prospective correction, and solving computationally expensive reconstructions in a timely fashion for the retrospective correction. If timely prospective correction is difficult, then it is possible to simply detect and re-acquire k-space segments that contain significant motion. Slow motion corrected reconstructions may be managed by the number of motion states, providing a trade-off between residual

motion artefacts and reconstruction speed. Naturally, these solutions require an estimate of the motion that occurs during the scan. This problem has been tackled using many different ideas: navigator echoes, self-navigation, image registration, image navigators, in-bore cameras, RF probes and ultrasound measurements. Research and development of these approaches should continue to further improve the accuracy and robustness of motion estimation.

In recent years, significant advances have been made in accelerated imaging strategies such as Parallel Imaging and Compressed Sensing. These methods (and others such as motion correction or partial Fourier) may not share similar sampling requirements during acquisition. From the acquisition side, study on optimal sampling strategies for specific applications and methodologies should be considered in the future. Optimized sampling patters for accelerated acquisitions will effectively be more scan efficient. From the reconstruction side, Parallel Imaging is now relatively mature, but additional developments for Compressed Sensing can be expected. In particular, development of novel application specific sparsifying transforms (dictionary based or otherwise) could enable higher acceleration factors.

From the reconstruction point of view, motion is additional information that can be incorporated into the inverse problem, similar to Parallel Imaging, Compressed Sensing or partial Fourier. Chapter 6 combined motion, Parallel Imaging and Compressed Sensing into a

single reconstruction framework, but additional information could be added to the reconstruction process. Such an example has been suggested in Chapter 8 for water/fat motion corrected separation. Despite all the physical-based information that has been introduced into the reconstruction, it should also be possible to incorporate other types of information, such as patient specific information. A large scale analysis of patient gender, age and medical history, for instance, could help tailor patient specific acquisitions and reconstructions. On a subject specific scale, previously acquired data could potentially reduce the sampling requirements in new acquisitions, for the same patient. Additional information can also come from alternative modalities, such as Positron Emission Tomography (PET), which is in fact currently under study using simultaneous PET-MR [143]. This strategy leverages complementary information from both systems to improve the output of both of them and therefore produce additional diagnostic information with superior quality. Future work will extend the works developed in this thesis to PET-MR imaging to improve clinical throughput and diagnostic confidence.

This dissertation developed novel motion correction approaches for abdominal and cardiac imaging. Nonetheless, these approaches can be extended to any MR application where motion is a problem to improve clinical throughput. The feasibility of these methods were demonstrated using healthy subjects, therefore clinical studies with

patients are now warranted.

9.3 Publications

The works presented in this thesis are based on the following publications:

- Cruz G, Atkinson D, Kolbitsch C, Schaeffter T, Prieto C. Comparison of non-rigid motion compensated reconstructions for 3D abdominal MRI. In Proceedings of the 22nd Annual Meeting of ISMRM, Milan, Italy, 2014. Abstract number 4385.

- Cruz G, Atkinson D, Buerger C, Schaeffter T, Prieto C. Accelerated motion corrected three-dimensional abdominal MRI using total variation regularized SENSE reconstruction. Magn Reson Med 2015;75: 14841498. Full paper.

- Cruz G, Atkinson D, Schaeffter T, Prieto C. Navigation-based motion model for motion compensated reconstruction in 3D abdominal MRI. In Proceedings of the 23rd Annual Meeting of ISMRM, Toronto, Canada, 2015. Abstract number 1274.

- Cruz G, Atkinson D, Henningsson M, Botnar RM, Prieto C. Highly Efficient Nonrigid Motion Corrected 3D Whole-Heart Coronary Vessel Wall Imaging. Magn Reson Med 2016. doi:10.1002/mrm.26274. Full paper.

- Cruz G, Botnar RM, Prieto C. 3D Whole-Heart Water Fat Coronary MRA at 3T with 100% Scan Efficiency. In Proceedings of the 24th Annual Meeting of ISMRM, Singapore, 2016. Abstract number 5145.

Glossary

1D - One-dimensional

2D - Two-dimensional

3D - Three-dimensional

A - Sampling operator

ACQ - Acquisition

ADC - Apparent Diffusion Coefficient

AP - Anterior-Posterior

ARA - Accept-Reject Algorithm

$\mathbf{B_0}$ - Static magnetic field

$\mathbf{B_1}$ - Radio-frequency rotation magnetic field

b-SSFP - Balanced Steady State Free Precession

C - Condition number

C - Coil sensitivities operator

CAD - Coronary Artery Disease

CE - Contrast Enhanced

CG - Conjugate Gradient

CMR - Cardiovascular Magnetic Resonance

CMRA - Coronary Magnetic Resonance Angiography

COPE - Centrally Ordered Phase Encoding

CT - Computed Tomography

CS - Compressed Sensing

D - Dixon operator

DCE - Dynamic Contrast Enhanced

DCF - Density Compensation Function

DVA - Diminishing Variance Algorithm

DWI - Diffusion Weighted Imaging

$\mathbf{E}$ - Encoding operator

ECG - Electrocardiogram

$\mathfrak{F}$ - Fourier transform

$\mathbf{F}$ - Fourier operator

FFT - Fast Fourier Transform

FID - Free Induction Decay

FH - Foot-Head

FHN - Focular Nodular Hyperplasia

FOV - Field Of View

$\mathbf{G}$ - Magnetic field gradient

$\mathbf{G_{FE}}$ - Frequency encoding gradient

$\mathbf{G_{PE}}$ - Phase encoding gradient

$\mathbf{G_{SS}}$ - Slice selection gradient

GMD - General Matrix Description

G-RPE - Golden Radial Phase Encoding

GE - Gradient Echo

GR - Golden Radial

$\hbar$ - Planck's constant normalized

$\mathbf{H}$ - Water image

HCC - Hepatocellular Carcinoma

HOPE - Hybrid Ordered Phase Encoding

$\mathbf{I}$ - Reconstructed Image

IHCC - Intrahepatic Cholangiocarcinoma

IMC - Image-based Motion Correction

iNAV - Image Navigator

IP - In Phase

J - Angular momentum

k - Boltzmann constant

k - k-Space position

K - k-Space data

L - Fat image

LCA - Left Coronary Artery

LGE - Late gadolinium enhancement

LR - Left-Right

LV - Left ventricle

M - Net magnetization

m - Reconstructed image

M_0 - Net magnetization before RF pulse

M_z - Net longitudinal magnetization

M_{xy} - Net transverse magnetization

MRA - Magnetic Resonance Angiography

MRI - Magnetic Resonance Imaging

NAV - Navigator

N_{down} - Number of spins anti-parallel to $\mathbf{B_0}$

NMC - Non-Motion Corrected

NMR - Nuclear Magnetic Resonance

NUFFT - Non-Uniform Fast Fourier Transform

N_{up} - Number of spins parallel to $\mathbf{B_0}$

OOP - Out Of Phase

P - Coil sensitivities RSS

PAWS - Phase Encoding with Automatic Window Selection

PC - Phase Contrast

PD - Proton Density

PET - Positron Emission Tomography

PI - Parallel Imaging

ppm - Part Per Million

PSF - Point Spread Function

Q - Affine matrix

R - Undersampling factor

$\mathbf{R}(\mathbf{k})$ - Non-Cartesian sample position

r - Spatial position

RCA - Right Coronary Artery

RF - Radio-Frequency

RGE - Respiratory Gating Efficiency

ROI - Region Of Interest

ROPE - Respiratory Ordered Phase Encoding

RSS - Square Root Sum Of Squares

RV - Right ventricle

S - Signal produced by an MR experiment

$\mathbf{S_c}$ - Coil sensitivities operator

s - Vectorized k-space data

SAR - Specific Absorption Rate

SE - Spin echo

SENSE - Sensitivity Encoding

SNR - Signal-to-Noise Ratio

SPECT - Single Photon Emission Computed Tomography

SPIR - Spectral Inversion Recovery

STIR - Short Tau Inversion Recovery

SVD - Singular Value Decomposition

$\mathbf{t}$ - Temporal position

$\mathbf{T}$ - Translation vector

T - Temperature

T_1 - Spin-lattice relaxation time

T_2 - Spin-spin relaxation time

T_2^* - Spin-spin relaxation time under field inhomogeneities

T_2prep - T_2 preparation pulse

TC - Translation correction

TE - Echo Time

TR - Repetition Time

TV - Total Variation

TTE - Transthoracic Echocardiogram

$\mathbf{U}$ - Motion operator

VDRU - Variable Density Random Undersampling

$\mathbf{W}$ - Diagonal weighting operator

Π - Top hat function

III - Dirac comb function

$\mathbf{\Delta_k}$ - k-Space sample spacing

$\mathbf{\Delta r}$ - Spatial resolution

$\Delta\epsilon$ - Energy difference between spin states

γ - Gyromagnetic ratio

λ - Regularization weight

μ - Magnetic moment

ϕ - Spin phase

Φ - Magnetic flux

Ψ - Sparsifying operator

ψ - Noise channel correlation

$\rho\mathbf{k}$ - k-Space Sample density

σ - Noise

τ - Singular value

ω - Spatially dependent Larmor frequency

$\omega_\mathbf{0}$ - Larmor frequency

$\omega_\mathbf{1}$ - Transverse rotational frequency

Bibliography

[1] Hassan Abdel-Aty, Anja Zagrosek, Jeanette Schulz-Menger, Andrew J Taylor, Daniel Messroghli, Andreas Kumar, Michael Gross, Rainer Dietz, and Matthias G Friedrich. Delayed enhancement and t2-weighted cardiovascular magnetic resonance imaging differentiate acute from chronic myocardial infarction. *Circulation*, 109(20):2411–2416, 2004.

[2] ACR. http://www.acr.org/quality-safety/standards-guidelines/practice-guidelines-by-modality/mri.

[3] Andrew P Aitken, Markus Henningsson, Rene M Botnar, Tobias Schaeffter, and Claudia Prieto. 100% efficient three-dimensional coronary mr angiography with two-dimensional beat-to-beat translational and bin-to-bin affine motion correction. *Magnetic resonance in medicine*, 74(3):756–764, 2015.

[4] Osama Al-Kwifi, Jeffrey Stainsby, Warren D Foltz, Marshall S Sussman, Yuexi Huang, and Graham A Wright. Characterizing coronary motion and its effect on mr coronary angiographyinitial

experience. *Journal of Magnetic Resonance Imaging*, 24(4):842–850, 2006.

[5] Khaled Alfakih, Sven Plein, Holger Thiele, Tim Jones, John P Ridgway, and Mohan U Sivananthan. Normal human left and right ventricular dimensions for mri as assessed by turbo gradient echo and steady-state free precession imaging sequences. *Journal of Magnetic Resonance Imaging*, 17(3):323–329, 2003.

[6] Marcelo E Andia, Markus Henningsson, Tarique Hussain, Alkystis Phinikaridou, Andrea Protti, Gerald Greil, and Rene M Botnar. Flow-independent 3d whole-heart vessel wall imaging using an interleaved t2-preparation acquisition. *Magnetic resonance in medicine*, 69(1):150–157, 2013.

[7] Ravi G Assomull, Sanjay K Prasad, Jonathan Lyne, Gillian Smith, Elizabeth D Burman, Mohammed Khan, Mary N Sheppard, Philip A Poole-Wilson, and Dudley J Pennell. Cardiovascular magnetic resonance, fibrosis, and prognosis in dilated cardiomyopathy. *Journal of the American College of Cardiology*, 48(10):1977–1985, 2006.

[8] RC Aster, B Borchers, and C Thurber. Parameter estimation and inverse problems. 2005.

[9] David Atkinson, Derek LG Hill, Peter NR Stoyle, Paul E Summers, Stuart Clare, Richard Bowtell, and Stephen F Keevil. Au-

tomatic compensation of motion artifacts in mri. *Magnetic Resonance in Medicine*, 41(1):163–170, 1999.

[10] Ahmed Ba-Ssalamah, Martin Uffmann, Sanjai Saini, Nina Bastati, Christian Herold, and Wolfgang Schima. Clinical value of mri liver-specific contrast agents: a tailored examination for a confident non-invasive diagnosis of focal liver lesions. *European radiology*, 19(2):342–357, 2009.

[11] Judith L Babar, Robert G Jones, Lucy Hudsmith, Richard Steeds, and Peter Guest. Application of mr imaging in assessment and follow-up of congenital heart disease in adults. *Radiographics*, 30(4):e40, 2010.

[12] DR Bailes, DJ Gilderdale, GM Bydder, AG Collins, and DN Firmin. Respiratory ordered phase encoding (rope): a method for reducing respiratory motion artefacts in mr imaging. *Journal of computer assisted tomography*, 9(4):835–838, 1985.

[13] Ceyla Basaran, Musturay Karcaaltincaba, Deniz Akata, Nevzat Karabulut, Devrim Akinci, Mustafa Ozmen, and Okan Akhan. Fat-containing lesions of the liver: cross-sectional imaging findings with emphasis on mri. *American Journal of Roentgenology*, 184(4):1103–1110, 2005.

[14] PG Batchelor, D Atkinson, P Irarrazaval, DLG Hill, J Hajnal, and D Larkman. Matrix description of general motion correction

applied to multishot images. *Magnetic resonance in medicine*, 54(5):1273–1280, 2005.

[15] Philip Beatty and Michael Hansen. Ismrm 2013 parallel imaging sunrise course, 2013.

[16] Philip J Beatty, Dwight G Nishimura, and John M Pauly. Rapid gridding reconstruction with a minimal oversampling ratio. *Medical Imaging, IEEE Transactions on*, 24(6):799–808, 2005.

[17] Johan Berglund, Håkan Ahlström, Lars Johansson, and Joel Kullberg. Two-point dixon method with flexible echo times. *Magnetic resonance in medicine*, 65(4):994–1004, 2011.

[18] Matt A Bernstein, Kevin F King, and Xiaohong Joe Zhou. *Handbook of MRI pulse sequences*. Elsevier, 2004.

[19] Himanshu Bhat, Lan Ge, Sonia Nielles-Vallespin, Sven Zuehlsdorff, and Debiao Li. 3d radial sampling and 3d affine transform-based respiratory motion correction technique for free-breathing whole-heart coronary mra with 100% imaging efficiency. *Magnetic resonance in medicine*, 65(5):1269–1277, 2011.

[20] Oliver Bieri and Klaus Scheffler. Fundamentals of balanced steady state free precession mri. *Journal of Magnetic Resonance Imaging*, 38(1):2–11, 2013.

[21] Jan Bogaert, Steven Dymarkowski, Andrew Taylor, and Vivek Muthurangu. *Clinical Cardiac MRI*. Springer, 2012.

[22] HG Bogren, BM Lantz, RR Miller, and DT Mason. Effect of respiration on cardiac motion determined by cineangiography. implications concerning three-dimensional heart reconstruction using computer tomography. *Acta radiologica: diagnosis*, 18(6):609–620, 1977.

[23] Joseph A Borrello, Thomas L Chenevert, Charles R Meyer, AM Aisen, and GM Glazer. Chemical shift-based true water and fat images: regional phase correction of modified spin-echo mr images. *Radiology*, 164(2):531–537, 1987.

[24] René M Botnar, Matthias Stuber, Peter G Danias, Kraig V Kissinger, and Warren J Manning. Improved coronary artery definition with t2-weighted, free-breathing, three-dimensional coronary mra. *Circulation*, 99(24):3139–3148, 1999.

[25] Redha Boubertakh, Claudia Prieto, PG Batchelor, Sergio Uribe, David Atkinson, Holger Eggers, Thomas Sangild Sørensen, Michael Schacht Hansen, RS Razavi, and Tobias Schaeffter. Whole-heart imaging using undersampled radial phase encoding (rpe) and iterative sensitivity encoding (sense) reconstruction. *Magnetic resonance in medicine*, 62(5):1331–1337, 2009.

[26] RN Bracewell, Ku-Young Chang, Alok K Jha, and Yu-Huan Wang. Affine theorem for two-dimensional fourier transform. *Electronics Letters*, 29(3):304, 1993.

[27] Edward D Brandner, Andrew Wu, Hungcheng Chen, Dwight Heron, Shalom Kalnicki, Krishna Komanduri, Kristina Gerszten, Steve Burton, Irfan Ahmed, and Zhenyu Shou. Abdominal organ motion measured using 4d ct. *International Journal of Radiation Oncology* Biology* Physics*, 65(2):554–560, 2006.

[28] Jean H. Brittain, Bob S. Hu, Graham A. Wright, Craig H. Meyer, Albert Macovski, and Dwight G. Nishimura. Coronary angiography with magnetization-prepared t2 contrast. *Magnetic Resonance in Medicine*, 33(5):689–696, 1995.

[29] Robert W Brown, Y-C Norman Cheng, E Mark Haacke, Michael R Thompson, and Ramesh Venkatesan. *Magnetic resonance imaging: physical principles and sequence design*. John Wiley & Sons, 2014.

[30] Alfred M Bruckstein, David L Donoho, and Michael Elad. From sparse solutions of systems of equations to sparse modeling of signals and images. *SIAM review*, 51(1):34–81, 2009.

[31] Robert W Buccigrossi and Eero P Simoncelli. Image compression via joint statistical characterization in the wavelet domain. *Image Processing, IEEE Transactions on*, 8(12):1688–1701, 1999.

[32] Christian Buerger, Rachel E Clough, Andrew P King, Tobias Schaeffter, and Claudia Prieto. Nonrigid motion modeling of the liver from 3-d undersampled self-gated golden-radial phase en-

coded mri. *Medical Imaging, IEEE Transactions on*, 31(3):805–815, 2012.

[33] Christian Buerger, Claudia Prieto, and Tobias Schaeffter. Highly efficient 3d motion-compensated abdomen mri from undersampled golden-rpe acquisitions. *Magnetic Resonance Materials in Physics, Biology and Medicine*, 26(5):419–429, 2013.

[34] Christian Buerger, Tobias Schaeffter, and Andrew P King. Hierarchical adaptive local affine registration for fast and robust respiratory motion estimation. *Medical image analysis*, 15(4):551–564, 2011.

[35] Allen P Burke, Andrew Farb, Gerti Tashko, and Renu Virmani. Arrhythmogenic right ventricular cardiomyopathy and fatty replacement of the right ventricular myocardium are they different diseases? *Circulation*, 97(16):1571–1580, 1998.

[36] GM Bydder and IR Young. Mr imaging: clinical use of the inversion recovery sequence. *Journal of computer assisted tomography*, 9(4):659–675, 1985.

[37] Mark Bydder, David J Larkman, and Joseph V Hajnal. Detection and elimination of motion artifacts by regeneration of k-space. *Magnetic resonance in medicine*, 47(4):677–686, 2002.

[38] Mark Bydder, Takeshi Yokoo, Gavin Hamilton, Michael S Middleton, Alyssa D Chavez, Jeffrey B Schwimmer, Joel E Lavine,

and Claude B Sirlin. Relaxation effects in the quantification of fat using gradient echo imaging. *Magnetic resonance imaging*, 26(3):347–359, 2008.

[39] Jose Caballero, Anthony N Price, Daniel Rueckert, and Joseph V Hajnal. Dictionary learning and time sparsity for dynamic mr data reconstruction. *Medical Imaging, IEEE Transactions on*, 33(4):979–994, 2014.

[40] Paul T. Callaghan. *Principles of nuclear magnetic resonance microscopy*. Oxford University Press on Demand, 1993.

[41] Paolo G Camici, Sanjay Kumak Prasad, and Ornella E Rimoldi. Stunning, hibernation, and assessment of myocardial viability. *Circulation*, 117(1):103–114, 2008.

[42] Emmanuel J Candes and Justin K Romberg. Signal recovery from random projections. In *Electronic Imaging 2005*, pages 76–86. International Society for Optics and Photonics, 2005.

[43] Emmanuel J Candes, Justin K Romberg, and Terence Tao. Stable signal recovery from incomplete and inaccurate measurements. *Communications on pure and applied mathematics*, 59(8):1207–1223, 2006.

[44] Joseph Y Cheng, Marcus T Alley, Charles H Cunningham, Shreyas S Vasanawala, John M Pauly, and Michael Lustig. Nonrigid motion correction in 3d using autofocusing withlocalized

linear translations. *Magnetic resonance in medicine*, 68(6):1785–1797, 2012.

[45] JY Cheng, M Uecker, MT Alley, SS Vasanawala, JM Pauly, and M Lustig. Free-breathing pediatric imaging with nonrigid motion correction and parallel imaging. In *Proceedings of the 21th scientific meeting. International Society for Magnetic Resonance in Medicine, Salt Lake City, UT, USA*, volume 1506, 2013.

[46] Vivian L Clark and James A Kruse. Clinical methods: the history, physical, and laboratory examinations. *JAMA*, 264(21):2808–2809, 1990.

[47] Mark A Clifford, Filip Banovac, Elliot Levy, and Kevin Cleary. Assessment of hepatic motion secondary to respiration for computer assisted interventions. *Computer Aided Surgery*, 7(5):291–299, 2002.

[48] James W Cooley and John W Tukey. An algorithm for the machine calculation of complex fourier series. *Mathematics of computation*, 19(90):297–301, 1965.

[49] Simone Coppo, Davide Piccini, Gabriele Bonanno, Jérôme Chaptinel, Gabriella Vincenti, Hélène Feliciano, Ruud B van Heeswijk, Juerg Schwitter, and Matthias Stuber. Free-running 4d whole-heart self-navigated golden angle mri: Initial results. *Magnetic resonance in medicine*, 74(5):1306–1316, 2015.

[50] Gastao Cruz, David Atkinson, Christian Buerger, Tobias Schaeffter, and Claudia Prieto. Accelerated motion corrected three-dimensional abdominal mri using total variation regularized sense reconstruction. *Magnetic resonance in medicine*, 2015.

[51] Charles H Cunningham, John M Pauly, and Krishna S Nayak. Saturated double-angle method for rapid b1+ mapping. *Magnetic Resonance in Medicine*, 55(6):1326–1333, 2006.

[52] Yu-Hong Dai and Yaxiang Yuan. A nonlinear conjugate gradient method with a strong global convergence property. *SIAM Journal on Optimization*, 10(1):177–182, 1999.

[53] Peter G Danias, Michael V McConnell, Vaibhav C Khasgiwala, Michael L Chuang, Robert R Edelman, and Warren J Manning. Prospective navigator correction of image position for coronary mr angiography. *Radiology*, 203(3):733–736, 1997.

[54] SC Davies, AL Hill, RB Holmes, M Halliwell, and PC Jackson. Ultrasound quantitation of respiratory organ motion in the upper abdomen. *The British journal of radiology*, 67(803):1096–1102, 1994.

[55] André De Troyer and Marc Estenne. Coordination between rib cage muscles and diaphragm during quiet breathing in humans. *Journal of Applied Physiology*, 57(3):899–906, 1984.

[56] W Thomas Dixon. Simple proton spectroscopic imaging. *Radiology*, 153(1):189–194, 1984.

[57] M Doneva, C Stehning, K Nehrke, and P Börnert. Improving scan efficiency of respiratory gated imaging using compressed sensing with 3d cartesian golden angle sampling. In *Proc Intl Soc Mag Reson Med*, volume 19, page 641, 2011.

[58] Mariya Doneva, Peter Börnert, Holger Eggers, Alfred Mertins, John Pauly, and Michael Lustig. Compressed sensing for chemical shift-based water–fat separation. *Magnetic resonance in medicine*, 64(6):1749–1759, 2010.

[59] David L Donoho. Compressed sensing. *Information Theory, IEEE Transactions on*, 52(4):1289–1306, 2006.

[60] Holger Eggers and Peter Brnert. Chemical shift encoding-based waterfat separation methods. *Journal of Magnetic Resonance Imaging*, 40(2):251–268, 2014.

[61] Richard L Ehman and Joel P Felmlee. Adaptive technique for high-definition mr imaging of moving structures. *Radiology*, 173(1):255–263, 1989.

[62] Richard Lorne Ehman, MT McNamara, M Pallack, H Hricak, and CB Higgins. Magnetic resonance imaging with respiratory gating: techniques and advantages. *American journal of Roentgenology*, 143(6):1175–1182, 1984.

[63] Michael Elad and Michal Aharon. Image denoising via sparse and redundant representations over learned dictionaries. *Image Processing, IEEE Transactions on*, 15(12):3736–3745, 2006.

[64] Alex Etienne, René M Botnar, Arianne van Muiswinkel, Peter Boesiger, Warren J Manning, and Matthias Stuber. soap-bubble visualization and quantitative analysis of 3d coronary magnetic resonance angiograms. *Magnetic Resonance in Medicine*, 48(4):658–666, 2002.

[65] Silvana C Faria, Karthik Ganesan, Irene Mwangi, Masoud Shiehmorteza, Barbara Viamonte, Sameer Mazhar, Michael Peterson, Yuko Kono, Cynthia Santillan, Giovanna Casola, et al. Mr imaging of liver fibrosis: Current state of the art 1. *Radiographics*, 29(6):1615–1635, 2009.

[66] David A Feinberg, Daniel Giese, D Andre Bongers, Sudhir Ramanna, Maxim Zaitsev, Michael Markl, and Matthias Günther. Hybrid ultrasound mri for improved cardiac imaging and real-time respiration control. *Magnetic Resonance in Medicine*, 63(2):290–296, 2010.

[67] Jeffrey Fessler, Bradley P Sutton, et al. Nonuniform fast fourier transforms using min-max interpolation. *Signal Processing, IEEE Transactions on*, 51(2):560–574, 2003.

[68] Christoph Forman, Davide Piccini, Robert Grimm, Jana Hutter, Joachim Hornegger, and Michael O Zenge. Reduction of respiratory motion artifacts for free-breathing whole-heart coronary mra by weighted iterative reconstruction. *Magnetic Resonance in Medicine*, 73(5):1885–1895, 2015.

[69] Alejandro Forner, Ramón Vilana, Carmen Ayuso, Lluís Bianchi, Manel Solé, Juan Ramón Ayuso, Loreto Boix, Margarita Sala, Maria Varela, Josep M Llovet, et al. Diagnosis of hepatic nodules 20 mm or smaller in cirrhosis: prospective validation of the noninvasive diagnostic criteria for hepatocellular carcinoma. *Hepatology*, 47(1):97–104, 2008.

[70] Sohrab Fratz, Taylor Chung, Gerald F Greil, Margaret M Samyn, Andrew M Taylor, Emanuela R Valsangiacomo Buechel, Shi-Joon Yoo, Andrew J Powell, et al. Guidelines and protocols for cardiovascular magnetic resonance in children and adults with congenital heart disease: Scmr expert consensus group on congenital heart disease. *J Cardiovasc Magn Reson*, 15(1):51, 2013.

[71] Zhuo Wu Fu, Yi Wang, Roger C Grimm, Phillip J Rossman, Joel P Felmlee, Stephen J Riederer, and Richard L Ehman. Orbital navigator echoes for motion measurements in magnetic resonance imaging. *Magnetic Resonance in Medicine*, 34(5):746–753, 1995.

[72] GH Glover and JM Pauly. Projection reconstruction techniques for reduction of motion effects in mri. *Magnetic Resonance in Medicine*, 28(2):275–289, 1992.

[73] GH Glover and E Schneider. Three-point dixon technique for true water/fat decomposition with b0 inhomogeneity correction. *Magnetic resonance in medicine*, 18(2):371–383, 1991.

[74] Walter F Good, Jules H Sumkin, Nilima Dash, Christopher M Johns, Margarita L Zuley, Howard E Rockette, and David Gur. Observer sensitivity to small differences: a multipoint rank-order experiment. *AJR. American journal of roentgenology*, 173(2):275–278, 1999.

[75] Irmina Gradus-Pizlo, Brian Bigelow, Yousuf Mahomed, Stephen G Sawada, Karen Rieger, and Harvey Feigenbaum. Left anterior descending coronary artery wall thickness measured by high-frequency transthoracic and epicardial echocardiography includes adventitia. *The American journal of cardiology*, 91(1):27–32, 2003.

[76] Luigi Grazioli, Michael P Federle, Giuseppe Brancatelli, Tomoaki Ichikawa, Lucio Olivetti, and Arye Blachar. Hepatic adenomas: Imaging and pathologic findings 1. *Radiographics*, 21(4):877–892, 2001.

[77] Leslie Greengard and June-Yub Lee. Accelerating the nonuniform fast fourier transform. *SIAM review*, 46(3):443–454, 2004.

[78] Mark A Griswold, Peter M Jakob, Robin M Heidemann, Mathias Nittka, Vladimir Jellus, Jianmin Wang, Berthold Kiefer, and Axel Haase. Generalized autocalibrating partially parallel acquisitions (grappa). *Magnetic resonance in medicine*, 47(6):1202–1210, 2002.

[79] E Mark Haacke and John L Patrick. Reducing motion artifacts in two-dimensional fourier transform imaging. *Magnetic resonance imaging*, 4(4):359–376, 1986.

[80] A Haase, J Frahm, W Hanicke, and D Matthaei. 1h nmr chemical shift selective (chess) imaging. *Physics in medicine and biology*, 30(4):341, 1985.

[81] Okka W Hamer, Diego A Aguirre, Giovanna Casola, Joel E Lavine, Matthias Woenckhaus, and Claude B Sirlin. Fatty liver: Imaging patterns and pitfalls 1. *Radiographics*, 26(6):1637–1653, 2006.

[82] Per Christian Hansen. *Discrete inverse problems: insight and algorithms*, volume 7. Siam, 2010.

[83] Per Christian Hansen. *Discrete inverse problems: insight and algorithms*, volume 7. Siam, 2010.

[84] Markus Henningsson and Rene M Botnar. Advanced respiratory motion compensation for coronary mr angiography. *Sensors*, 13(6):6882–6899, 2013.

[85] Markus Henningsson, Peter Koken, Christian Stehning, Reza Razavi, Claudia Prieto, and René M Botnar. Whole-heart coronary mr angiography with 2d self-navigated image reconstruction. *Magnetic resonance in medicine*, 67(2):437–445, 2012.

[86] Markus Henningsson, Giel Mens, Peter Koken, Jouke Smink, and Rene M Botnar. A new framework for interleaved scanning in cardiovascular mr: Application to image-based respiratory motion correction in coronary mr angiography. *Magnetic Resonance in Medicine*, 73(2):692–696, 2015.

[87] Markus Henningsson, Claudia Prieto, Amedeo Chiribiri, Ghislain Vaillant, Reza Razavi, and René M Botnar. Whole-heart coronary mra with 3d affine motion correction using 3d image-based navigation. *Magnetic Resonance in Medicine*, 71(1):173–181, 2014.

[88] Markus Henningsson, Jouke Smink, Reza Razavi, and René M Botnar. Prospective respiratory motion correction for coronary mr angiography using a 2d image navigator. *Magnetic Resonance in Medicine*, 69(2):486–494, 2013.

[89] Magnus Rudolph Hestenes and Eduard Stiefel. Methods of conjugate gradients for solving linear systems. 1952.

[90] Geoffrey Hugo, Carlos Vargas, Jian Liang, Larry Kestin, John W Wong, and Di Yan. Changes in the respiratory pattern during radiotherapy for cancer in the lung. *Radiotherapy and oncology*, 78(3):326–331, 2006.

[91] R Reeve Ingle, Holden H Wu, Nii Okai Addy, Joseph Y Cheng, Phillip C Yang, Bob S Hu, and Dwight G Nishimura. Nonrigid autofocus motion correction for coronary mr angiography with a 3d cones trajectory. *Magnetic resonance in medicine*, 72(2):347–361, 2014.

[92] John Jackson, Craig H Meyer, Dwight G Nishimura, Albert Macovski, et al. Selection of a convolution function for fourier inversion using gridding [computerised tomography application]. *Medical Imaging, IEEE Transactions on*, 10(3):473–478, 1991.

[93] John I Jackson, Dwight G Nishimura, and Albert Macovski. Twisting radial lines with application to robust magnetic resonance imaging of irregular flow. *Magnetic resonance in medicine*, 25(1):128–139, 1992.

[94] Cosima Jahnke, Ingo Paetsch, Stephan Achenbach, Bernhard Schnackenburg, Rolf Gebker, Eckart Fleck, and Eike Nagel. Coronary mr imaging: Breath-hold capability and patterns,

coronary artery rest periods, and beta-blocker use 1. *Radiology*, 239(1):71–78, 2006.

[95] Cosima Jahnke, Ingo Paetsch, Stephan Achenbach, Bernhard Schnackenburg, Rolf Gebker, Eckart Fleck, and Eike Nagel. Coronary mr imaging: Breath-hold capability and patterns, coronary artery rest periods, and beta-blocker use 1. *Radiology*, 239(1):71–78, 2006.

[96] Elizabeth R Jenista, Wolfgang G Rehwald, Enn-Ling Chen, Han W Kim, Igor Klem, Michele A Parker, and Raymond J Kim. Motion and flow insensitive adiabatic t2-preparation module for cardiac mr imaging at 3 tesla. *Magnetic resonance in medicine*, 70(5):1360–1368, 2013.

[97] Peter Jezzard and Robert S Balaban. Correction for geometric distortion in echo planar images from b0 field variations. *Magnetic resonance in medicine*, 34(1):65–73, 1995.

[98] P Jhooti, PD Gatehouse, J Keegan, NH Bunce, AM Taylor, and DN Firmin. Phase ordering with automatic window selection (paws): a novel motion-resistant technique for 3d coronary imaging. *Magnetic resonance in medicine*, 43(3):470–480, 2000.

[99] Permi Jhooti, Frank Wiesmann, Andrew M Taylor, Peter D Gatehouse, Guang Z Yang, Jennifer Keegan, Dudley J Pennell, and David N Firmin. Hybrid ordered phase encoding (hope): an

improved approach for respiratory artifact reduction. *Journal of Magnetic Resonance Imaging*, 8(4):968–980, 1998.

[100] Kevin M Johnson, Walter F Block, Scott Reeder, Alexey Samsonov, et al. Improved least squares mr image reconstruction using estimates of k-space data consistency. *Magnetic resonance in medicine*, 67(6):1600–1608, 2012.

[101] Bernd Jung, Daniela Föll, Petra Böttler, Steffen Petersen, Jürgen Hennig, and Michael Markl. Detailed analysis of myocardial motion in volunteers and patients using high-temporal-resolution mr tissue phase mapping. *Journal of Magnetic Resonance Imaging*, 24(5):1033–1039, 2006.

[102] Eleni Kaldoudi, Steve CR Williams, Gareth J Barker, and Paul S Tofts. A chemical shift selective inversion recovery sequence for fat-suppressed mri: theory and experimental validation. *Magnetic resonance imaging*, 11(3):341–355, 1993.

[103] Aya Kamaya, Katherine E Maturen, Grace A Tye, Yueyi I Liu, Naveen N Parti, and Terry S Desser. Hypervascular liver lesions. In *Seminars in Ultrasound, CT and MRI*, volume 30, pages 387–407. Elsevier, 2009.

[104] Peter Kellman, Diego Hernando, Saurabh Shah, Sven Zuehlsdorff, Renate Jerecic, Christine Mancini, Zhi-Pei Liang, and Andrew E Arai. Multiecho dixon fat and water separation method

for detecting fibrofatty infiltration in the myocardium. *Magnetic resonance in medicine*, 61(1):215–221, 2009.

[105] Raymond J Kim, Timothy SE Albert, James H Wible, Michael D Elliott, John C Allen, Jennifer C Lee, Michele Parker, Alicia Napoli, Robert M Judd, Gadoversetamide Myocardial Infarction Imaging Investigators, et al. Performance of delayed-enhancement magnetic resonance imaging with gadoversetamide contrast for the detection and assessment of myocardial infarction an international, multicenter, double-blinded, randomized trial. *Circulation*, 117(5):629–637, 2008.

[106] W Yong Kim, Peter G Danias, Matthias Stuber, Scott D Flamm, Sven Plein, Eike Nagel, Susan E Langerak, Oliver M Weber, Erik M Pedersen, Matthias Schmidt, et al. Coronary magnetic resonance angiography for the detection of coronary stenoses. *New England Journal of Medicine*, 345(26):1863–1869, 2001.

[107] W Yong Kim, Matthias Stuber, Peter Börnert, Kraig V Kissinger, Warren J Manning, and René M Botnar. Three-dimensional black-blood cardiac magnetic resonance coronary vessel wall imaging detects positive arterial remodeling in patients with nonsignificant coronary artery disease. *Circulation*, 106(3):296–299, 2002.

[108] YS Kim, CW Mun, and ZH Cho. Chemical-shift imaging with large magnetic field inhomogeneity. *Magnetic resonance*

in medicine, 4(5):452–460, 1987.

[109] Kei Kitamura, Hiroki Shirato, Yvette Seppenwoolde, Tadashi Shimizu, Yoshihisa Kodama, Hideho Endo, Rikiya Onimaru, Makoto Oda, Katsuhisa Fujita, Shinichi Shimizu, et al. Tumor location, cirrhosis, and surgical history contribute to tumor movement in the liver, as measured during stereotactic irradiation using a real-time tumor-tracking radiotherapy system. *International Journal of Radiation Oncology* Biology* Physics*, 56(1):221–228, 2003.

[110] Christoph Kolbitsch. *Advanced techniques for cardiovascular magnetic resonance imaging in cases of irregular motion.* PhD thesis, King's College London (University of London), 2012.

[111] Kimio Konno and Jere Mead. Measurement of the separate volume changes of rib cage and abdomen during breathing. *Journal of Applied Physiology*, 22(3):407–422, 1967.

[112] Hope W Korin, Richard L Ehman, Stephen J Riederer, Joel P Felmlee, and Roger C Grimm. Respiratory kinematics of the upper abdominal organs: a quantitative study. *Magnetic resonance in medicine*, 23(1):172–178, 1992.

[113] Takashi Kubo, Toshio Imanishi, Shigeho Takarada, Akio Kuroi, Satoshi Ueno, Takashi Yamano, Takashi Tanimoto, Yoshiki Matsuo, Takashi Masho, Hironori Kitabata, et al. Assessment of

culprit lesion morphology in acute myocardial infarction: ability of optical coherence tomography compared with intravascular ultrasound and coronary angioscopy. *Journal of the American College of Cardiology*, 50(10):933–939, 2007.

[114] R Lalloo et al. Global, regional, and national age-sex specific all-cause and cause-specific mortality for 240 causes of death, 1990-2013: a systematic analysis for the global burden of disease study 2013. 2015.

[115] Andrew C Larson, Richard D White, Gerhard Laub, Elliot R McVeigh, Debiao Li, and Orlando P Simonetti. Self-gated cardiac cine mri. *Magnetic Resonance in Medicine*, 51(1):93–102, 2004.

[116] Paul C Lauterbur et al. Image formation by induced local interactions: examples employing nuclear magnetic resonance. *Nature*, 242(5394):190–191, 1973.

[117] Gerald W Lenz, E Mark Haacke, and Richard D White. Retrospective cardiac gating: a review of technical aspects and future directions. *Magnetic resonance imaging*, 7(5):445–455, 1989.

[118] Debiao Li, Shantanu Kaushikkar, E Mark Haacke, Pamela K Woodard, Paritosh J Dhawale, Randall M Kroeker, Gerhard Laub, Yasuaki Kuginuki, and Femando R Gutierrez. Coronary

arteries: three-dimensional mr imaging with retrospective respiratory gating. *Radiology*, 201(3):857–863, 1996.

[119] Zhi-Pei Liang and Paul C Lauterbur. *Principles of magnetic resonance imaging: a signal processing perspective*. The Institute of Electrical and Electronics Engineers Press, 2000.

[120] Jan-Ray Liao, John M Pauly, Thomas J Brosnan, and Norbert J Pelc. Reduction of motion artifacts in cine mri using variable-density spiral trajectories. *Magnetic resonance in medicine*, 37(4):569–575, 1997.

[121] Christopher J Lisanti and David B Douglas. Effects of breath-hold and cardiac cycle on the mri appearance of the aorta and inferior vena cava in t2 abdominal imaging. *American Journal of Roentgenology*, 192(5):1348–1358, 2009.

[122] Alexander Loktyushin, Hannes Nickisch, Rolf Pohmann, and Bernhard Schölkopf. Blind retrospective motion correction of mr images. *Magnetic resonance in medicine*, 70(6):1608–1618, 2013.

[123] M Louis Lauzon and Brian K Rutt. Generalized k-space analysis and correction of motion effects in mr imaging. *Magnetic resonance in medicine*, 30(4):438–446, 1993.

[124] Michael Lustig, David Donoho, and John M Pauly. Sparse mri: The application of compressed sensing for rapid mr imaging. *Magnetic resonance in medicine*, 58(6):1182–1195, 2007.

[125] Michael Lustig, David L Donoho, Juan M Santos, and John M Pauly. Compressed sensing mri. *Signal Processing Magazine, IEEE*, 25(2):72–82, 2008.

[126] Michael Lustig and John M Pauly. Spirit: Iterative self-consistent parallel imaging reconstruction from arbitrary k-space. *Magnetic Resonance in Medicine*, 64(2):457–471, 2010.

[127] Julian Maclaren, Brian SR Armstrong, Robert T Barrows, KA Danishad, Thomas Ernst, Colin L Foster, Kazim Gumus, Michael Herbst, Ilja Y Kadashevich, Todd P Kusik, et al. Measurement and correction of microscopic head motion during magnetic resonance imaging of the brain. *PLOS one*, 7(11):e48088, 2012.

[128] Kurt Majewski, Oliver Heid, and Thomas Kluge. Mri pulse sequence design with first-order gradient moment nulling in arbitrary directions by solving a polynomial program. *Medical Imaging, IEEE Transactions on*, 29(6):1252–1259, 2010.

[129] John Mallard. http://www.bshr.org.uk/mallard.html.

[130] Lazar Mandinov, Franz R Eberli, Christian Seiler, and Otto M Hess. Diastolic heart failure. *Cardiovascular research*, 45(4):813–825, 2000.

[131] Santhi Maniam and Janio Szklaruk. Wjr. *World*, 2(8):309–322, 2010.

[132] Dirk Manke, Kay Nehrke, and Peter Börnert. Novel prospective respiratory motion correction approach for free-breathing coronary mr angiography using a patient-adapted affine motion model. *Magnetic Resonance in Medicine*, 50(1):122–131, 2003.

[133] Dirk Manke, Kay Nehrke, Peter Börnert, Peter Rösch, and Olaf Dössel. Respiratory motion in coronary magnetic resonance angiography: a comparison of different motion models. *Journal of Magnetic Resonance Imaging*, 15(6):661–671, 2002.

[134] Warren J Manning, Wei Li, Noel G Boyle, and Robert R Edelman. Fat-suppressed breath-hold magnetic resonance coronary angiography. *Circulation*, 87(1):94–104, 1993.

[135] Kiaran P McGee, Armando Manduca, Joel P Felmlee, Stephen J Riederer, and Richard L Ehman. Image metric-based correction (autocorrection) of motion effects: Analysis of image metrics. *Journal of Magnetic Resonance Imaging*, 11(2):174–181, 2000.

[136] Charles A McKenzie, Ernest N Yeh, Michael A Ohliger, Mark D Price, and Daniel K Sodickson. Self-calibrating parallel imaging

with automatic coil sensitivity extraction. *Magnetic Resonance in Medicine*, 47(3):529–538, 2002.

[137] Kate McLeish, Derek LG Hill, David Atkinson, Jane M Blackall, and Reza Razavi. A study of the motion and deformation of the heart due to respiration. *Medical Imaging, IEEE Transactions on*, 21(9):1142–1150, 2002.

[138] Marc Modat, Gerard R Ridgway, Zeike A Taylor, Manja Lehmann, Josephine Barnes, David J Hawkes, Nick C Fox, and Sébastien Ourselin. Fast free-form deformation using graphics processing units. *Computer methods and programs in biomedicine*, 98(3):278–284, 2010.

[139] James CC Moon, Emma Reed, Mary N Sheppard, Andrew G Elkington, SiewYen Ho, Margaret Burke, Mario Petrou, and Dudley J Pennell. The histologic basis of late gadolinium enhancement cardiovascular magnetic resonance in hypertrophic cardiomyopathy. *Journal of the American College of Cardiology*, 43(12):2260–2264, 2004.

[140] Krishna S Nayak, Pedro A Rivas, John M Pauly, Greig C Scott, Adam B Kerr, Bob S Hu, and Dwight G Nishimura. Real-time black-blood mri using spatial presaturation. *Journal of Magnetic Resonance Imaging*, 13(5):807–812, 2001.

[141] Kay Nehrke and Peter Börnert. Prospective correction of affine motion for arbitrary mr sequences on a clinical scanner. *Magnetic resonance in medicine*, 54(5):1130–1138, 2005.

[142] Kay Nehrke, Peter Bornert, Dirk Manke, and Johannes C Bock. Free-breathing cardiac mr imaging: Study of implications of respiratory motioninitial results 1. *Radiology*, 220(3):810–815, 2001.

[143] Felix Nensa, Thorsten D Poeppel, Karsten Beiderwellen, Juliane Schelhorn, Amir A Mahabadi, Raimund Erbel, Philipp Heusch, Kai Nassenstein, Andreas Bockisch, Michael Forsting, et al. Hybrid pet/mr imaging of the heart: feasibility and initial results. *Radiology*, 268(2):366–373, 2013.

[144] Thanh D Nguyen, Pascal Spincemaille, Matthew D Cham, Jonathan W Weinsaft, Martin R Prince, and Yi Wang. Free-breathing 3-dimensional steady-state free precession coronary magnetic resonance angiography: comparison of four navigator gating techniques. *Magnetic resonance imaging*, 27(6):807–814, 2009.

[145] Thoralf Niendorf, Lukas Winter, and Tobias Frauenrath. *Electrocardiogram in an MRI environment: clinical needs, practical considerations, safety implications, technical solutions and future directions*. INTECH Open Access Publisher, 2012.

[146] Douglas C Noll, Dwight G Nishimura, and Albert Macovski. Homodyne detection in magnetic resonance imaging. *Medical Imaging, IEEE Transactions on*, 10(2):154–163, 1991.

[147] Freddy Odille, Nicolae Cîndea, Damien Mandry, Cédric Pasquier, Pierre-André Vuissoz, and Jacques Felblinger. Generalized mri reconstruction including elastic physiological motion and coil sensitivity encoding. *Magnetic resonance in medicine*, 59(6):1401–1411, 2008.

[148] Freddy Odille, Sergio Uribe, Philip G Batchelor, Claudia Prieto, Tobias Schaeffter, and David Atkinson. Model-based reconstruction for cardiac cine mri without ecg or breath holding. *Magnetic Resonance in Medicine*, 63(5):1247–1257, 2010.

[149] Freddy Odille, Pierre-André Vuissoz, Pierre-Yves Marie, and Jacques Felblinger. Generalized reconstruction by inversion of coupled systems (grics) applied to free-breathing mri. *Magnetic Resonance in Medicine*, 60(1):146–157, 2008.

[150] Hiroyuki Okura, Yoshio Kobayashi, Satoru Sumitsuji, Mitsuyasu Terashima, Toru Kataoka, Motomaru Masutani, Mitsumasa Ohyanagi, Kenei Shimada, Haruyuki Taguchi, Yuji Yasuga, et al. Effect of culprit-lesion remodeling versus plaque rupture on three-year outcome in patients with acute coronary syndrome. *The American journal of cardiology*, 103(6):791–795, 2009.

[151] John N Oshinski, Lennart Hofland, Srinivasan Mukundan Jr, W Thomas Dixon, W James Parks, and Roderic I Pettigrew. Two-dimensional coronary mr angiography without breath holding. *Radiology*, 201(3):737–743, 1996.

[152] Ricardo Otazo, Daniel Kim, Leon Axel, and Daniel K Sodickson. Combination of compressed sensing and parallel imaging for highly accelerated first-pass cardiac perfusion mri. *Magnetic Resonance in Medicine*, 64(3):767–776, 2010.

[153] Jianing Pang, Himanshu Bhat, Behzad Sharif, Zhaoyang Fan, Louise EJ Thomson, Troy LaBounty, John D Friedman, James Min, Daniel S Berman, and Debiao Li. Whole-heart coronary mra with 100% respiratory gating efficiency: Self-navigated three-dimensional retrospective image-based motion correction (trim). *Magnetic resonance in medicine*, 71(1):67–74, 2014.

[154] Jianing Pang, Behzad Sharif, Reza Arsanjani, Xiaoming Bi, Zhaoyang Fan, Qi Yang, Kuncheng Li, Daniel S Berman, and Debiao Li. Accelerated whole-heart coronary mra using motion-corrected sensitivity encoding with three-dimensional projection reconstruction. *Magnetic resonance in medicine*, 73(1):284–291, 2015.

[155] Jianing Pang, Behzad Sharif, Zhaoyang Fan, Xiaoming Bi, Reza Arsanjani, Daniel S Berman, and Debiao Li. Ecg and navigator-free four-dimensional whole-heart coronary mra for simultaneous

visualization of cardiac anatomy and function. *Magnetic resonance in medicine*, 72(5):1208–1217, 2014.

[156] Nadia K Paschke, Olaf Dössel, Tobias Schaeffter, Claudia Prieto, and Christoph Kolbitsch. Comparison of image-based and reconstruction-based respiratory motion correction for golden radial phase encoding coronary mr angiography. *Journal of Magnetic Resonance Imaging*, 42(4):964–971, 2015.

[157] Rebecca Perry, Majo X Joseph, Derek P Chew, Philip E Aylward, and Carmine G De Pasquale. Coronary artery wall thickness of the left anterior descending artery using high resolution transthoracic echocardiography–normal range of values. *Echocardiography*, 30(7):759–764, 2013.

[158] Steffen E Petersen, Michael Jerosch-Herold, Lucy E Hudsmith, Matthew D Robson, Jane M Francis, Helen A Doll, Joseph B Selvanayagam, Stefan Neubauer, and Hugh Watkins. Evidence for microvascular dysfunction in hypertrophic cardiomyopathy new insights from multiparametric magnetic resonance imaging. *Circulation*, 115(18):2418–2425, 2007.

[159] Steffen E Petersen, Bernd A Jung, Frank Wiesmann, Joseph B Selvanayagam, Jane M Francis, Juergen Hennig, Stefan Neubauer, and Matthew D Robson. Myocardial tissue phase mapping with cine phase-contrast mr imaging: regional wall mo-

tion analysis in healthy volunteers 1. *Radiology*, 238(3):816–826, 2006.

[160] Caroline Petitjean, Nicolas Rougon, and Philippe Cluzel. Assessment of myocardial function: a review of quantification methods and results using tagged mri. *Journal of Cardiovascular Magnetic Resonance*, 7(2):501–516, 2005.

[161] Davide Piccini, Gabriele Bonanno, Giulia Ginami, Arne Littmann, Michael O Zenge, and Matthias Stuber. Is there an optimal respiratory reference position for self-navigated whole-heart coronary mr angiography? *Journal of Magnetic Resonance Imaging*, 2015.

[162] James G Pipe. An optimized center-out k-space trajectory for multishot mri: Comparison with spiral and projection reconstruction. *Magnetic resonance in medicine*, 42(4):714–720, 1999.

[163] James G Pipe and Padmanabhan Menon. Sampling density compensation in mri: rationale and an iterative numerical solution. *Magnetic Resonance in Medicine*, 41(1):179–186, 1999.

[164] Johannes C Post, Albert C van Rossum, Jean GF Bronzwaer, Carel C de Cock, Mark BM Hofman, Jacob Valk, and Cees A Visser. Magnetic resonance angiography of anomalous coronary arteries a new gold standard for delineating the proximal course? *Circulation*, 92(11):3163–3171, 1995.

[165] Jonathan Powell, Claudia Prieto, Markus Henningsson, Peter Koken, and Rene Botnar. Cmra with 100% navigator efficiency with 3d self navigation and interleaved scanning. *Journal of Cardiovascular Magnetic Resonance*, 16(Suppl 1):O8, 2014.

[166] Claudia Prieto, Mariya Doneva, Muhammad Usman, Markus Henningsson, Gerald Greil, Tobias Schaeffter, and Rene M Botnar. Highly efficient respiratory motion compensated free-breathing coronary mra using golden-step cartesian acquisition. *Journal of Magnetic Resonance Imaging*, 41(3):738–746, 2015.

[167] Claudia Prieto, Sergio Uribe, Reza Razavi, David Atkinson, and Tobias Schaeffter. 3d undersampled golden-radial phase encoding for dce-mra using inherently regularized iterative sense. *Magnetic resonance in medicine*, 64(2):514–526, 2010.

[168] Klaas P Pruessmann, Markus Weiger, Peter Börnert, and Peter Boesiger. Advances in sensitivity encoding with arbitrary k-space trajectories. *Magnetic Resonance in Medicine*, 46(4):638–651, 2001.

[169] Klaas P Pruessmann, Markus Weiger, Markus B Scheidegger, Peter Boesiger, et al. Sense: sensitivity encoding for fast mri. *Magnetic resonance in medicine*, 42(5):952–962, 1999.

[170] Mike Puddephat. Principles of magnetic resonance imaging, 2010.

[171] Marcony Queiroz-Andrade, Roberto Blasbalg, Cinthia D Ortega, Marco AM Rodstein, Ronaldo H Baroni, Manoel S Rocha, and Giovanni G Cerri. Mr imaging findings of iron overload 1. *Radiographics*, 29(6):1575–1589, 2009.

[172] Volker Rasche, Roland Proksa, R Sinkus, P Börnert, and Holger Eggers. Resampling of data between arbitrary grids using convolution interpolation. *Medical Imaging, IEEE Transactions on*, 18(5):385–392, 1999.

[173] Matthias Regenfus, Dieter Ropers, Stephan Achenbach, Christian Schlundt, Winfried Kessler, Gerhard Laub, Werner Moshage, and Werner G Daniel. Comparison of contrast-enhanced breath-hold and free-breathing respiratory-gated imaging in three-dimensional magnetic resonance coronary angiography. *The American journal of cardiology*, 90(7):725–730, 2002.

[174] Stijntje D Roes, Grigorios Korosoglou, Michael Schär, Jos J Westenberg, Matthias JP van Osch, Albert de Roos, and Matthias Stuber. Correction for heart rate variability during 3d whole heart mr coronary angiography. *Journal of Magnetic Resonance Imaging*, 27(5):1046–1053, 2008.

[175] Torsten Rohlfing, Calvin R Maurer Jr, Walter G ODell, and Jianhui Zhong. Modeling liver motion and deformation during

the respiratory cycle using intensity-based nonrigid registration of gated mr images. *Medical physics*, 31(3):427–432, 2004.

[176] Todd S Sachs, Craig H Meyer, Bob S Hu, Jim Kohli, Dwight G Nishimura, and Albert Macovski. Real-time motion detection in spiral mri using navigators. *Magnetic resonance in medicine*, 32(5):639–645, 1994.

[177] Todd S Sachs, Craig H Meyer, Pablo Irarrazabal, Bob S Hu, Dwight G Nishimura, and Albert Macovski. The diminishing variance algorithm for real-time reduction of motion artifacts in mri. *Magnetic resonance in medicine*, 34(3):412–422, 1995.

[178] Todd S Sachs, Craig H Meyer, John M Pauly, Bob S Hu, Dwight G Nishimura, and Albert Macovski. The real-time interactive 3-d-dva for robust coronary mra. *Medical Imaging, IEEE Transactions on*, 19(2):73–79, 2000.

[179] Claudio Santelli, Reza Nezafat, Beth Goddu, Warren J Manning, Jouke Smink, Sebastian Kozerke, and Dana C Peters. Respiratory bellows revisited for motion compensation: preliminary experience for cardiovascular mr. *Magnetic resonance in medicine*, 65(4):1097–1102, 2011.

[180] Klaus Scheffler and Jrgen Hennig. Is truefisp a gradient-echo or a spin-echo sequence? *Magnetic Resonance in Medicine*, 49(2):395–397, 2003.

[181] Klaus Scheffler and Jürgen Hennig. Reduced circular field-of-view imaging. *Magnetic resonance in medicine*, 40(3):474–480, 1998.

[182] Klaus Scheffler and Stefan Lehnhardt. Principles and applications of balanced ssfp techniques. *European radiology*, 13(11):2409–2418, 2003.

[183] Johannes FM Schmidt, Martin Buehrer, Peter Boesiger, and Sebastian Kozerke. Nonrigid retrospective respiratory motion correction in whole-heart coronary mra. *Magnetic resonance in medicine*, 66(6):1541–1549, 2011.

[184] Lawrence H Schwartz. Rc semelkaabdominal–pelvic mri2nd ed2006wileyhoboken (nj) 0471692735 [1427 pages, 1500 illustrations]. *Clinical Imaging*, 30(3):221, 2006.

[185] Juerg Schwitter, Christian M Wacker, Albert C van Rossum, Massimo Lombardi, Nidal Al-Saadi, Hakan Ahlstrom, Thorsten Dill, Henrik BW Larsson, Scott D Flamm, Moritz Marquardt, et al. Mr-impact: comparison of perfusion-cardiac magnetic resonance with single-photon emission computed tomography for the detection of coronary artery disease in a multicentre, multivendor, randomized trial. *European heart journal*, 2008.

[186] Andrew D Scott, Jennifer Keegan, and David N Firmin. Motion in cardiovascular mr imaging 1. *Radiology*, 250(2):331–351, 2009.

[187] Andrew D Scott, Jennifer Keegan, and David N Firmin. Beat-to-beat respiratory motion correction with near 100% efficiency: a quantitative assessment using high-resolution coronary artery imaging. *Magnetic resonance imaging*, 29(4):568–578, 2011.

[188] Yvette Seppenwoolde, Hiroki Shirato, Kei Kitamura, Shinichi Shimizu, Marcel van Herk, Joos V Lebesque, and Kazuo Miyasaka. Precise and real-time measurement of 3d tumor motion in lung due to breathing and heartbeat, measured during radiotherapy. *International Journal of Radiation Oncology* Biology* Physics*, 53(4):822–834, 2002.

[189] Puneet Sharma, Hiroumi D Kitajima, Bobby Kalb, and Diego R Martin. Gadolinium-enhanced imaging of liver tumors and manifestations of hepatitis: pharmacodynamic and technical considerations. *Topics in Magnetic Resonance Imaging*, 20(2):71–78, 2009.

[190] John T Sharp, Norma B Goldberg, Walter S Druz, and J Danon. Relative contributions of rib cage and abdomen to breathing in normal subjects. *Journal of Applied Physiology*, 39(4):608–618, 1975.

[191] Guy Shechter, Cengizhan Ozturk, Jon R Resar, and Elliot R McVeigh. Respiratory motion of the heart from free breathing coronary angiograms. *Medical Imaging, IEEE Transactions on*, 23(8):1046–1056, 2004.

[192] Jonathan Richard Shewchuk. An introduction to the conjugate gradient method without the agonizing pain, 1994.

[193] Shinichi Shimizu, Hiroki Shirato, Hidefumi Aoyama, Seiko Hashimoto, Takeshi Nishioka, Akira Yamazaki, Keinji Kagei, and Kazuo Miyasaka. High-speed magnetic resonance imaging for four-dimensional treatment planning of conformal radiotherapy of moving body tumors. *International Journal of Radiation Oncology* Biology* Physics*, 48(2):471–474, 2000.

[194] Alvin C Silva, James M Evans, Ann E McCullough, Mashal A Jatoi, Hugo E Vargas, and Amy K Hara. Mr imaging of hypervascular liver masses: A review of current techniques 1. *Radiographics*, 29(2):385–402, 2009.

[195] Surachate Siripongsakun, Jeong K Lee, Steven S Raman, Myron J Tong, James Sayre, and David S Lu. Mri detection of intratumoral fat in hepatocellular carcinoma: potential biomarker for a more favorable prognosis. *American Journal of Roentgenology*, 199(5):1018–1025, 2012.

[196] Daniel K Sodickson and Warren J Manning. Simultaneous acquisition of spatial harmonics (smash): fast imaging with radiofrequency coil arrays. *Magnetic Resonance in Medicine*, 38(4):591–603, 1997.

[197] Ruitian Song, Aaryani Tipirneni, Perry Johnson, Ralf B Loeffler, and Claudia M Hillenbrand. Evaluation of respiratory liver and kidney movements for mri navigator gating. *Journal of Magnetic Resonance Imaging*, 33(1):143–148, 2011.

[198] Thomas Sangild Sorensen, Tobias Schaeffter, Karsten Østergaard Noe, and Michael Schacht Hansen. Accelerating the nonequispaced fast fourier transform on commodity graphics hardware. *Medical Imaging, IEEE Transactions on*, 27(4):538–547, 2008.

[199] Elmar Spuentrup, Warren J Manning, René M Botnar, Kraig V Kissinger, and Matthias Stuber. Impact of navigator timing on free-breathing submillimeter 3d coronary magnetic resonance angiography. *Magnetic resonance in medicine*, 47(1):196–201, 2002.

[200] RE Steiner, GM Bydder, A Selwyn, J Deanfield, DB Longmore, RH Klipsten, and D Firmin. Nuclear magnetic resonance imaging of the heart. current status and future prospects. *British heart journal*, 50(3):202–208, 1983.

[201] Gregg W Stone, Akiko Maehara, Alexandra J Lansky, Bernard de Bruyne, Ecaterina Cristea, Gary S Mintz, Roxana Mehran, John McPherson, Naim Farhat, Steven P Marso, et al. A prospective natural-history study of coronary atherosclerosis. *New England Journal of Medicine*, 364(3):226–235, 2011.

[202] Matthias Stuber, René M Botnar, Peter G Danias, Kraig V Kissinger, and Warren J Manning. Submillimeter three-dimensional coronary mr angiography with real-time navigator correction: Comparison of navigator locations 1. *Radiology*, 212(2):579–587, 1999.

[203] Tarinee Tangcharoen, Cosima Jahnke, Uwe Koehler, Bernhard Schnackenburg, Christoph Klein, Eckart Fleck, and Eike Nagel. Impact of heart rate variability in patients with normal sinus rhythm on image quality in coronary magnetic angiography. *Journal of Magnetic Resonance Imaging*, 28(1):74–79, 2008.

[204] DS Taubman and MW Marcellin. Image compression fundamentals, standards and practice: Jpeg2000, 2002.

[205] Andrew M Taylor, Jennifer Keegan, Permi Jhooti, David N Firmin, and Dudley J Pennell. Calculation of a subject-specific adaptive motion-correction factor for improved real-time navigator echo-gated magnetic resonance coronary angiography. *Journal of Cardiovascular Magnetic Resonance*, 1(2):131–138, 1999.

[206] Chi-Ming Tsai and Dwight G Nishimura. Reduced aliasing artifacts using variable-density k-space sampling trajectories. *Magnetic resonance in medicine*, 43(3):452–458, 2000.

[207] Muhammad Usman, David Atkinson, Freddy Odille, Christoph Kolbitsch, Ghislain Vaillant, Tobias Schaeffter, Philip G Batch-

elor, and Claudia Prieto. Motion corrected compressed sensing for free-breathing dynamic cardiac mri. *Magnetic resonance in medicine*, 70(2):504–516, 2013.

[208] Behroze Vachha, Maryellen RM Sun, Bettina Siewert, and Ronald L Eisenberg. Cystic lesions of the liver. *American Journal of Roentgenology*, 196(4):W355–W366, 2011.

[209] Ties van Brussel. Anatomy of the human abdomen, 2010.

[210] Curtis R Vogel and Mary E Oman. Fast, robust total variation-based reconstruction of noisy, blurred images. *Image Processing, IEEE Transactions on*, 7(6):813–824, 1998.

[211] M Von Siebenthal, U Gamper, P Boesiger, A Lomax, Ph Cattin, et al. 4d mr imaging of respiratory organ motion and its variability. *Physics in medicine and biology*, 52(6):1547, 2007.

[212] Pierre-André Vuissoz, Freddy Odille, Brice Fernandez, Maelene Lohezic, Adnane Benhadid, Damien Mandry, and Jacques Felblinger. Free-breathing imaging of the heart using 2d cine-grics (generalized reconstruction by inversion of coupled systems) with assessment of ventricular volumes and function. *Journal of Magnetic Resonance Imaging*, 35(2):340–351, 2012.

[213] Gudrun Wagenknecht, Hans-Jürgen Kaiser, Felix M Mottaghy, and Hans Herzog. Mri for attenuation correction in pet: methods

and challenges. *Magnetic resonance materials in physics, biology and medicine*, 26(1):99–113, 2013.

[214] Martin J Wainwright, Tommi S Jaakkola, and Alan S Willsky. Map estimation via agreement on trees: message-passing and linear programming. *Information Theory, IEEE Transactions on*, 51(11):3697–3717, 2005.

[215] David O Walsh, Arthur F Gmitro, and Michael W Marcellin. Adaptive reconstruction of phased array mr imagery. *Magnetic Resonance in Medicine*, 43(5):682–690, 2000.

[216] Yi Wang, Roger C Grimm, Joel P Felmlee, Sephen J Riederer, and Richard L Ehman. Algorithms for extracting motion information from navigator echoes. *Magnetic resonance in medicine*, 36(1):117–123, 1996.

[217] Yi Wang, Stephen J Riederer, and Richard L Ehman. Respiratory motion of the heart: kinematics and the implications for the spatial resolution in coronary imaging. *Magnetic Resonance in Medicine*, 33(5):713–719, 1995.

[218] Yi Wang, Phillip J Rossman, Roger C Grimm, Stephen J Riederer, and Richard L Ehman. Navigator-echo-based real-time respiratory gating and triggering for reduction of respiration effects in three-dimensional coronary mr angiography. *Radiology*, 198(1):55–60, 1996.

[219] Yi Wang, Erez Vidan, and Geoffrey W Bergman. Cardiac motion of coronary arteries: Variability in the rest period and implications for coronary mr angiography 1. *Radiology*, 213(3):751–758, 1999.

[220] Heidi A Ward, Stephen J Riederer, Roger C Grimm, Richard L Ehman, Joel P Felmlee, and Clifford R Jack. Prospective multiaxial motion correction for fmri. *Magnetic Resonance in Medicine*, 43(3):459–469, 2000.

[221] Elisabeth Weiss, Krishni Wijesooriya, S Vaughn Dill, and Paul J Keall. Tumor and normal tissue motion in the thorax during respiration: Analysis of volumetric and positional variations using 4d ct. *International Journal of Radiation Oncology* Biology* Physics*, 67(1):296–307, 2007.

[222] Arnold M Weissler, Willard S Harris, and Clyde D Schoenfeld. Systolic time intervals in heart failure in man. *Circulation*, 37(2):149–159, 1968.

[223] Edward Brian Welch, Armando Manduca, Roger C Grimm, Heidi A Ward, and Clifford R Jack Jr. Spherical navigator echoes for full 3d rigid body motion measurement in mri. *Magnetic resonance in medicine*, 47(1):32–41, 2002.

[224] Edward Brian Welch, Phillip J Rossman, Joel P Felmlee, and Armando Manduca. Self-navigated motion correction using mo-

ments of spatial projections in radial mri. *Magnetic resonance in medicine*, 52(2):337–345, 2004.

[225] John Burnard West. *Respiratory physiology: the essentials*. Lippincott Williams & Wilkins, 2012.

[226] MJ White, DJ Hawkes, A Melbourne, DJ Collins, C Coolens, M Hawkins, MO Leach, and D Atkinson. Motion artifact correction in free-breathing abdominal mri using overlapping partial samples to recover image deformations. *Magnetic resonance in medicine*, 62(2):440–449, 2009.

[227] Stefanie Winkelmann, Tobias Schaeffter, Thomas Koehler, Holger Eggers, and Olaf Doessel. An optimal radial profile order based on the golden ratio for time-resolved mri. *Medical Imaging, IEEE Transactions on*, 26(1):68–76, 2007.

[228] Michael L Wood and R Mark Henkelman. Mr image artifacts from periodic motion. *Medical physics*, 12(2):143–151, 1985.

[229] www.nzuaa.org. Coronary artery anatomy, 2016.

[230] Huanzhou Yu, Ann Shimakawa, Charles A McKenzie, Ethan Brodsky, Jean H Brittain, and Scott B Reeder. Multiecho water-fat separation and simultaneous r 2* estimation with multifrequency fat spectrum modeling. *Magnetic resonance in medicine*, 60(5):1122–1134, 2008.

[231] Yan Zhang, Masafumi Uchida, Toshi Abe, Hiroshi Nishimura, Naofumi Hayabuchi, and Yutaka Nakashima. Intrahepatic peripheral cholangiocarcinoma: comparison of dynamic ct and dynamic mri. *Journal of computer assisted tomography*, 23(5):670–677, 1999.

[232] Nicholas R Zwart, Kenneth O Johnson, and James G Pipe. Efficient sample density estimation by combining gridding and an optimized kernel. *Magnetic resonance in medicine*, 67(3):701–710, 2012.